Towards Quantum gas mixture of neutral Sodium and Potassium atoms

Raman Research Institute

Bangalore-560080, India



Thesis submitted for the degree of

Doctor of Philosophy

to

Jawaharlal Nehru University

New Delhi-110067, India

by

Sagar Sutradhar

Supervisor: **Saptarishi Chaudhuri**

June, 2023

Declaration of Original and Sole Authorship

I, Sagar Sutradhar, declare that this thesis entitled **"Towards Quantum gas mixture of neutral Sodium and Potassium atoms"** and the data presented in it are original and my own work under the supervision of Dr. Saptarishi Chaudhuri. I confirm that, the work presented here has not been submitted for the award of any other degree, diploma, membership, associateship, fellowship, etc. of any other University or Institute. I further confirm that, references to work of others have been clearly acknowledge. I have also run the thesis through "Ouriginal" software.

(Signature of the student)

Sagar Sutradhar

Date: June 23, 2023

(Signature of the supervisor)

Dr. Saptarishi Chaudhuri

Date: June 23, 2023

Certificate

This is to certify that, the work contained in the thesis titled **"Towards Quantum gas mixture of neutral Sodium and Potassium atoms"**, submitted by **Sagar Sutradhar** (Enrollment No.- RRI/2014/008) to **Jawaharlal Nehru University** for the award of the degree of **Doctor of Philosophy** in Physical Sciences, is bonafied record of original work carried out by the candidate from July 2014-May 2023, under my guidance and supervision at the **Raman Research Institute**, Bengaluru, India. The results embodied in the thesis have not been submitted to any other University or Institute for the award of any degree or diploma.

(Signature of the supervisor)

Dr. Saptarishi Chaudhuri

Date: June 23, 2023

(Signature of the director)

Prof. Tarun Souradeep Ghosh

Date: June 23, 2023

Acknowledgment

I would like to express my deepest appreciation and gratitude to all those who have contributed to the completion of this Ph.D. thesis. Without their support, guidance, and encouragement, this achievement would not have been possible.

First and foremost, I am immensely grateful to my supervisor, Dr. Saptarishi Chaudhuri, for his invaluable guidance, expertise, and unwavering support throughout this research journey. My supervisor's insightful feedback, constructive assessment, and dedication to academic excellence have been instrumental in shaping this thesis and pushing me to strive for greater heights. I am truly fortunate to have had the opportunity to work under his guidance.

I am also grateful to Dr. Sanjukta Roy, for the scientific and technical discussions and sharing her knowledge with us. Her expertise in the field has greatly enhanced the quality and rigor of this research.

I am also indebted to the members of my thesis committee, Prof. Reji Philip and Prof. Andal Narayanan for their valuable insights, scholarly advice, and thorough review of this research. Their expertise and constructive suggestions have played a pivotal role in refining the quality and rigor of this thesis.

I would like to acknowledge the contributions of my colleagues and fellow researchers: Anirban Misra, Gourab Pal, and Sayari Majumder, for their stimulating discussions, and valuable insights. Their support and collaboration have enriched my academic experience and broadened my perspective.

I thank my other lab members Silpa, Shovan, and Swarnava for their help and support.

My sincere appreciation to Mr. Mohammed Ibrahim and his team for providing us an enormous amount of support with all the workshop facility during setting up this experiment.

I thank Mrs. Meena and Mrs. Sujatha for their support with all the electronics need. I would like to thank our secretary Mrs. Savitha for taking care of the official matters. I am grateful to the support of Mr. Sachin Belvadi, Mr. Muneswaran, Mr. Chethan, and all other 'E and B' staffs for all the supports.

I would like to extend my gratitude to Mr. Naresh VS, and all other members of administration and purchase for providing me with the opportunity to pursue my academic journey and complete this thesis. The support and resources offered by RRI have been instrumental in the successful completion of this research.

I acknowledge RRI computing facility, especially for allowing us to use the high performance computing resources which were very helpful to analysis our experimental data.

I acknowledge the Ministry of Electronics and Information Technology (MeitY), Government of India, through the Center deppestfor Excellence in Quantum Technology, under Grant4(7)/2020-ITEA for the financial support during the thesis work.

I would like to thank my friends and juniors Maheswar, Kaushik, Subhajit, Dipak, Bapan for all of their supports and help during this long journey.

My deepest and sincere thanks to my family. Their love, encouragement, and belief in me have been the driving force behind my perseverance.

Dedication

To Maa, Baba, Didi, and Bunu.

Ph.D. synopsis

Introduction

This thesis reports design, construction, implementation, and full characterisation of a state-of-the-art experimental facility. This system will be used to produce a quantum degenerate mixture of sodium and potassium atoms to study the Bose-Bose and Bose-Fermi mixture, and eventually will be used to produce ground-state NaK molecules. This experimental facility is the first of its kind in the country.

The experimental observations of Bose-Einstein condensate (BEC) [1–3] and Fermi degeneracy [4, 5] in dilute atomic gases have revolutionized the field of atomic physics. A degenerate cloud of atoms is a giant coherent matter wave. There has been enormous progress in the field at an incredible pace since its discovery. Many experiments have been performed focused on the coherent and superfluid nature of the BECs. This includes the observation of the interference between two BECs [6], formation of quantized vortices in rotating BECs [7–9], observation of long range coherence in BEC [10], the realization of time-resolved formation of condensate [11] and atom laser [12], observation of excitation of collective modes in condensate [13], and the propagation of sound wave in Bose-Einstein condensate [14].

The theoretical predictions [15] envisioned that ultracold quantum gases in optical lattices are a promising tool to investigate and explore quantum phases observed in condensed matter systems. The experimental observation of the quantum phase transition of ultracold atoms in optical lattices is a remarkable achievement [16] in the field. This experiment paved the way for simulating the underlying theoretical models that describe

many phenomena observed in condensed matter systems [17].

One of the long-standing interests and yet unresolved topic in the community is the understanding of the High-temperature (T_C) superconductivity. One would like to understand the mechanism behind this phenomenon and predict materials with higher critical temperatures, eventually at room temperature. The observation of BEC-BCS crossover [18, 19] in fermionic gases simulates the physics behind this phenomenon.

The realization of the remarkable experiments with cold atoms and molecules has opened the door to a plethora of exciting and unexplored regimes of physics [17, 20–23]. Our new experimental system described in this thesis will contribute to a deeper understanding of the related concepts. To explore new physics experimentally, one would like to have best possible signal-to-noise ratio. For cold atoms experiments, a large number of cold-trapped atoms aids in this endeavor. As described in the thesis, we developed an efficient experimental system that simultaneously loads a multi-species cold atom trap in a very short time. This development will help in achieving a high signal-to-noise ratio for the future experiments, as well as a high repetition rate of the measurements.

Quantum degenerate gases

The field of research on ultracold atoms had been started with the revolutionary experimental observation of laser cooling and trapping of neutral atoms [24] in a Magneto-optical trap (MOT). The spontaneous emission of photons associated with each absorption from the cooling laser limits the lowest temperature (few hundreds of μK) and maximum density that can be achieved in a MOT. New cooling mechanism models had been introduced [25], and experiments along this line [26] observed the temperature of the atoms below the Doppler limit. Many revolutionary experiments were employed, and the atoms can be cooled to even temperatures below recoil limit: velocity selective coherent population trapping (VSCPT) [27], and Raman sideband cooling [28]. The density of atoms in a MOT is typically limited to less than $\sim 10^{11}$ atoms/cm^{-3}. The implementation of dark-spot MOT [29] increased the density up to 10^{12} atoms/cm^{-3} and enhanced the Phase

Space Density (PSD) by up to 50 folds. The evaporative cooling technique [30, 31], when employed on alkali atoms, reduces the temperature of the atoms and increases the phase space density by a few orders of magnitude [32]. The success of these efforts led to the observation of BEC in alkali atoms [1–3] in 1995.

Quantum degenerate gas mixtures

The experimental realization of the quantum degeneracy of alkali atoms paved the way for studying quantum degenerate mixtures of two different atomic species. There has been a growing interest in the quantum degenerate mixtures both from the experimental [33–35] and theoretical [36–38] perspectives. The quantum degenerate mixture experiments [39, 40], offer a well-controlled system to simulate condensed matter physics [41].

In real life, solid-state materials are not defects free. Therefore, studying the physics of impurities in a superfluid of quantum degenerate mixtures [42] would be highly interesting. This system could be a testbed to explore the physics behind the localization of electrons surrounding the defects in the ionic structure. Experimentally, the underlying situation can be simulated by tightly confining an atomic species (minority) using optical potentials in the superfluid bath of the other species (majority).

A quantum mixtures in 2D optical lattices [43] could mimic the strongly correlated electron systems and explain the origin of the quasi 2D unconventional superconductor with high critical temperature for transition to the superconducting state. In addition, quantum degenerate mixtures are expected to form new magnetic phases [44] and super-solid phases [45].

The quantum gas mixtures also open possibilities for studying the chemical reaction in a controlled way [46]. This can reveal the underlying processes, such as the quantum states of the atoms, the quantum statistics, the interaction potentials, and so on that determine the reaction dynamics.

Ultracold heteronuclear molecules in their absolute ground state exhibit large electric dipole moment of the order of a few Debye, for the specific case of NaK ground state

molecule, the dipole moment is $\sim$ 2.72 Debye [47]. The ground state polar molecules with long-range anisotropic dipole-dipole interactions are ideal testbed to study strongly correlated many-body dynamics and exhibit exotic quantum phases [48]. Ultracold polar molecules in optical lattices are promising candidates to simulate the condensed matter systems [17].

Aim of the work

The production of Bose-Einstein condensate requires the sample to be cooled to extremely low temperatures ($\sim$ sub-micro Kelvin). This is achieved by employing the evaporative cooling technique: this process deterministically removes higher energy atoms from the trap and subsequently thermalizes the remaining atoms to lower temperatures. This cooling technique causes a significant loss of atoms from the trap. Therefore, it is necessary to start with a very large number of atoms in the MOT to obtain a large number of atoms in the condensate.

The collision between the background thermal atoms with the cooled and trapped atoms is one of the major reasons for the limited lifetime of the trapped atoms. By reducing the background pressure, we can minimize these collisions, reducing the atom loss from the trap. Therefore, it is necessary to create an ultra-high vacuum environment.

We have carefully designed the vacuum system to reconcile the need for fast loading with the need for an ultra-high vacuum environment.

We have developed two independent two dimensional magneto-optical traps ($2D^+$MOTs) for ^{23}Na and ^{39}K as a source of low velocity, intense source of the cold atomic beam to load the three dimensional (3D) MOT.

The cold atomic beam is generated in $2D^+$ MOT in a separated region of the vacuum system maintaining a high vapor pressure (10^{-9}-10^{-7} mbar) of the alkali atoms, and directed through a differential pumping tube to the 3DMOT chamber. This differential pumping tube could maintain a pressure difference better than 1000 times between the $2D^+$ MOT region and the 3DMOT region. In our vacuum manifold, we could maintain a

base pressure $\sim 7 \times 10^{-11}$ mbar at the operating condition of the MOT.

This thesis reports the design, construction, and characterization of a compact, versatile experimental setup, which will be used to experimentally study a dual-species ultracold, quantum gas mixture.

In Chapter 1, I will describe the present state-of-the-art of experimental and theoretical developments with cold atoms and cold atomic mixtures. I shall also introduce the basic concepts to convey the cooling and trapping mechanisms, as well as give the basic descriptions of the instruments and techniques used to perform experiments described in this thesis.

In Chapter 2, I shall give a through and comprehensive description of the state-of-the-art experimental system that I have built during the course of this thesis work. This includes the design and installation of the ultrahigh vacuum system, the description of the laser systems for laser cooling and trapping of neutral sodium (^{23}Na) and potassium (^{39}K) atoms

In Chapter 3, I shall give a overview on the mechanism of the laser cooling and trapping of neutral atoms in a magneto-optical trap(MOT). I have given a detailed description of the numerical simulation we have performed to model the cold and collimated atomic beams sources: 2D^{+}MOTs for sodium and potassium atoms.

In Chapter 4, I shall describe the detection schemes I have implemented to observe the cold atoms of sodium and potassium atoms. In the following discussion, I have described our experimental observation of the characterization of the system. I have described the experimental study of the light-assisted interspecies collisional dynamics of cold and trapped sodium and potassium atoms.

In chapter 5, I described in detailed the design, construction, and installation of a magnetic transport assembly. The magnetic transport scheme aims to transfer the cold and trapped cold atoms from our three dimensional MOT (3DMOT) ultra-high vacuum chamber to the "science cell" for the future experiments.

Brief introduction to laser cooling and trapping of neutral atoms

The cooling and trapping of atoms in a magneto-optical trap (MOT) [24, 49] is a powerful tool for preparing an ensemble of ultracold atoms at temperatures down to several hundreds of micro Kelvin. It depends on the radiative scattering force that uses the momentum transfer between the atoms and the near-resonant radiation field by exploiting the Doppler effect. The radiative scattering force experienced by the atoms is proportional to $\frac{s}{1+s+(\frac{2\delta}{\Gamma})^2}$ [50], where s is the saturation parameter for the transition, δ is the detuning between the laser frequency and the atomic transition frequency, Γ the is the natural linewidth of the transition, typically ranged between (1-10) MHz for alkali atoms.

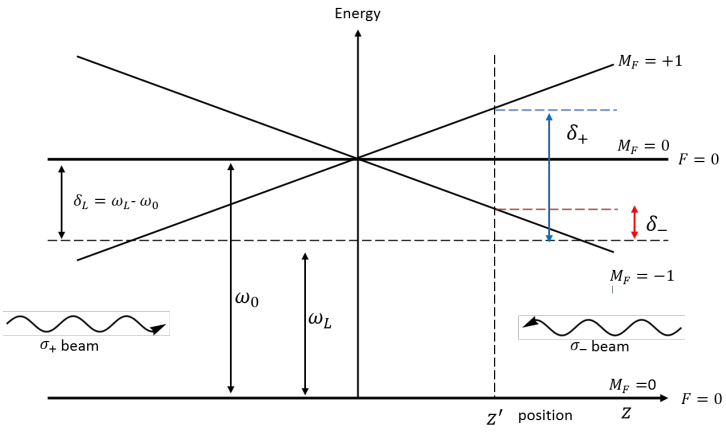


Figure 1: The schematic diagram of the arrangement of a MOT in 1D. The horizontal dashed line (black) represents the laser frequency seen by an atom at rest at the center of the trap. The radiative force in the presence of an inhomogeneous magnetic field becomes velocity and space-dependent and pushes the atoms toward the center.

We can illustrate the principle of a MOT by considering a simple two-level atomic system with hyperfine quantum numbers, $F = 0$ in the ground state and $F = 1$ in the excited state as shown in Figure-1. In a weak inhomogeneous magnetic field, $B(z) = bz$, where b is the gradient along $\hat{z}$ direction, the energy levels are Zeeman split by an amount $\Delta E(z) = \mu_B m_F B(z)$, where μ_B is the Bohr magneton. We assume the quantization axis is along $+\hat{z}$ direction. Consider a collimated laser beam with σ^- polarization propagating along $-z$ direction and a counter-propagating laser beam with σ^+ polarization propagat-

ing along $+z$ direction. The frequency (ω_L) (black dashed line) of both the laser beams is tuned below the atom's resonance frequency (ω_0) (in the absence of the magnetic field). For the atoms at the position z', the radiative force will be more by σ^- photons than σ^+ photons, because the laser frequency is closer to $|F = 0, m_F = 0\rangle \rightarrow |F = 1, m_F = -1\rangle$ transition frequency. As a result, the atoms will feel a net time-averaged force toward the center. For the atoms at $z < 0$ position, the Zeeman shifts are reversed, and the radiative force will be more by σ^+ photons (ω_L closer to $|F = 0, m_F = 0\rangle \rightarrow |F = 1, m_F = +1\rangle$ transition) and the net force will be directed towards the center again. Thus in a MOT, the velocity of the atoms is reduced by the well-directed counter-propagating laser beams; at the same time, they are pushed towards the zero magnetic field position yielding the trapping.

The experimental system

Ultra-high vacuum setup

A high flux atomic source must be used to load a MOT quickly. The schematic 3D view of the experimental system is shown in Figure-2. The system is segmented into two parts. In the first one, we have two independent 2D$^+$MOT sections, each for sodium and potassium atomic species. The other is a Ultra High Vacuum (UHV) section, which includes a 3DMOT chamber, magnetic transport, and a science cell. The system has five ion pumps and one titanium sublimation (Ti-sub) pump.

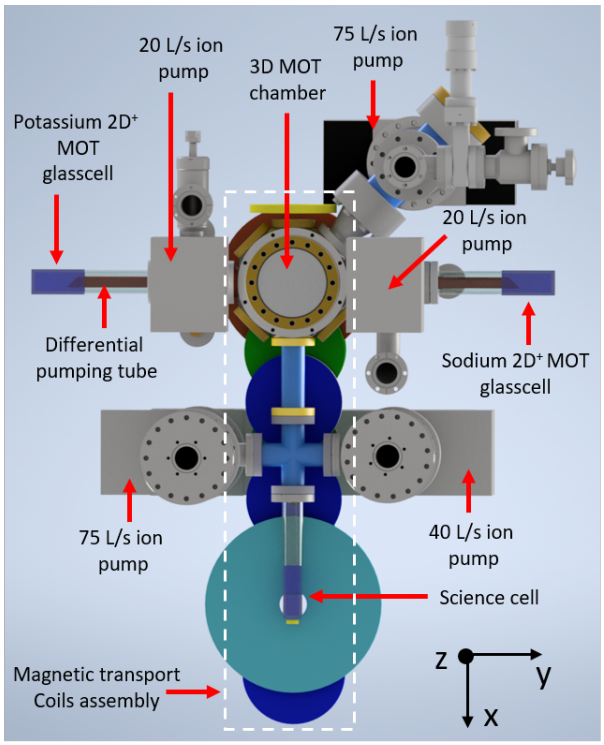


Figure 2: A 3D drawing of the experimental setup. It consists of a UHV manifold and magnetic coils assembly for magnetic transport. Two well collimated atomic beams load the 3DMOT from two spatially separated $2D^{+}$MOT of ^{23}Na and ^{39}K atoms. The trapped atoms at the 3DMOT region will be adiabatically transported over ~ 51 cm to the science cell. This will be achieved by dynamically shifting the magnetic trap center towards the science cell by varying the currents in the static ensemble of magnetic coils.

Laser and optical systems

The presence of a single valence electron at the outer shell of alkali atoms makes them a suitable candidate for laser cooling and trapping experiments by providing strong optical transitions. We have used stable and narrow linewidth lasers in external cavity diode lasers. We have used TA-SHG pro laser system (Toptica) for the cooling and trapping of sodium atoms. For potassium atoms, we have used Toptica DLpro and DL100 laser for cooling and repumping transitions, respectively.

We have used commercially available Acousto-optic modulators (AOMs) to tune the frequency of the laser beams to the atomic transitions and to control the power of the

laser beams.

The frequency of the emitted light from a diode laser is determined by the energy band gap of the semiconductor material being used. The bandgap depends on the temperature of the laser diode and the current passing through it.

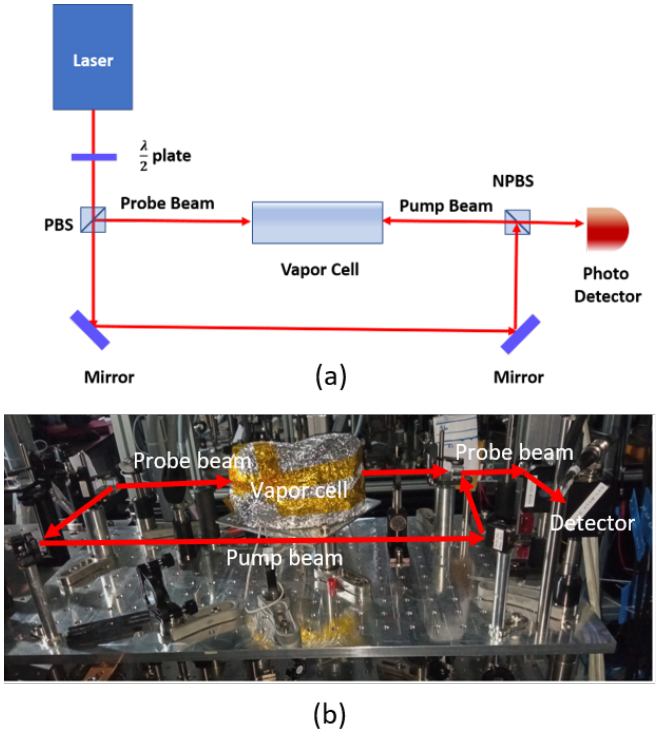


Figure 3: (a) A schematic diagram of Saturation Absorption Spectroscopy (SAS) setup. A laser beam is divided into a low-intensity (probe) and high-intensity (pump) beam, with a ratio $\sim \frac{1}{5}$. The probe beam goes through the vapor cell and falls on the detector. The pump beam overlaps with the probe beam inside the vapor cell (b) the photograph of SAS setup for ^{23}Na atoms. The blue plots show the transmission of the probe through the vapor cell in the absence of the pump beam, while the red plots show the same in the presence of the pump beam.

Therefore, the temperature drift and current fluctuations could change the frequency of the laser light over time. The scattering rate of photons from an atom depends on the detuning of the laser light frequency from the atomic transition frequency. Therefore, the fluctuation of the laser frequency causes inefficient laser cooling. We stabilize the frequency of the laser light relative to the atomic transition frequencies, obtained by

saturation-absorption spectroscopy (SAS) techniques, which yields a frequency stability better than 10^{-10}.

Atomic source

A MOT has a finite depth ($\sim$ few Kelvin). Therefore, for the atoms having a velocity that is less than the MOT's characteristic velocity, the so-called capture velocity of the MOT (typically, 30-100 m/s) can only be captured. Furthermore, the collisions of the trapped atoms with the residual background atoms present inside the UHV system limit the lifetime and steady-state number of the trapped atoms in a MOT. Achieving a degenerate cloud of ultracold atoms involves an evaporation cooling stage, where the higher velocity atoms are forcefully removed from the trap. To obtain a large atoms number in the degenerate atoomic cloud, it is necessary to start with a large number of atoms in the 3DMOT in a UHV environment.

So far, two classes of atomic sources are proven to be efficient for high fluxes of cold atoms in ultracold atom experiments. In the first kind, a Zeeman slower: a flux of atoms is slowed down by using a counter-propagating red-detuned laser beam in the presence of a spatially inhomogeneous magnetic field. The phenomenon of the Zeeman shift of the magnetic sub-levels of the atoms in the presence of a magnetic field is exploited here. The spatial inhomogeneous magnetic field keeps the atoms in resonance with the laser beam while they are decelerating [51]. The second kind of source is based on a two-chamber design. In one of the chambers, containing vapor at high pressure (10^{-8}-10^{-6} mbar), the atoms are cooled and trapped directly from the vapor and subsequently transferred to the final trapping chamber. These two chambers are separated by a differential pumping tube, which typically maintains a few orders of magnitude pressure difference between the high-pressure region and the final trapping chamber. Two different classes of the source were developed on this principle: low-velocity intense source (LVIS) implemented by Lu et. al. [52] and two-dimensional magneto-optical trap ($2D$MOT). [53].

For our experiment, we have opted to develop two spatially separated $2D^{+}$MOT for

^{23}Na and ^{39}K.

Design of the $2D^{+}$MOT The $2D^{+}$MOT vacuum system consists of a UHV grade glass cell (dimensions: 40 mm x 40 mm x 85 mm) connected to a standard CF40 flange through a metal-to-glass connector, as shown in Figure-4. An Oxygen free high conductive (OFHC) copper tube with a centered hole is inserted into the glass cell along its long axis which separates the $2D^{+}$MOT chamber from the rest of the vacuum system. One of the sides of the tube, which is inside the glass cell, has 45^{o} degree angle cut: this surface is polished to make it highly reflective for one of the longitudinal laser beams.

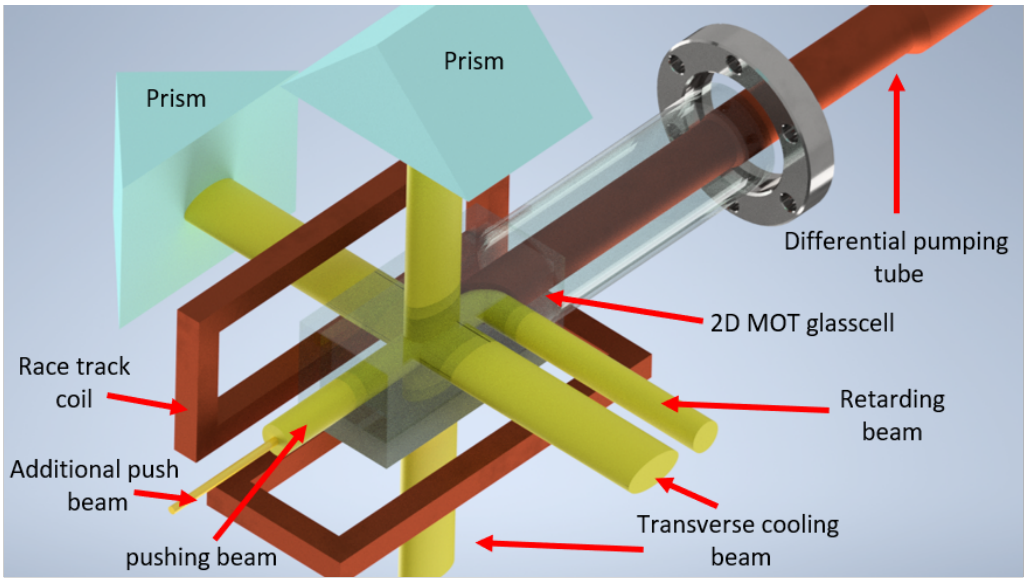


Figure 4: A schematic diagram of $2D^{+}$MOT configuration. It consists of a UHV-compatible glasscell, and one differential pumping tube is inserted inside the glasscell. The differential tube has a 45^{o} cut at the surface, which is inside the glass cell. A pair of racetrack coils (all of them are not shown for the image clarity) generates a 2D quadrupole magnetic field configuration. The transverse cooling beams, upon retro-reflected from the prisms, form the transverse cooling and trapping volume. The pushing and the retarding beams overlapped in the cooling volume form the longitudinal optical molasses. An additional push beam is aligned along the the longitudinal direction enhancing the atomic flux through the differential pumping hole to the 3DMOT chamber.

The center hole starts with a diameter of 2mm at the angled surface and continues over a distance of 20 mm. The hole then stepwise widens up to 14 mm (12mm) over a

total length of 270 mm for ^{23}Na (^{39}K) source. These differential pumping tubes maintain a pressure ratio better than 10^3 between the $2D^+$MOTs and the 3DMOT chamber.

In 2D$^+$MOT, two orthogonal pairs of counter-propagating laser beams are shone into a vapor cell in combination with a two-dimensional quadrupole magnetic field. This configuration creates a restoring force along the transverse directions towards the line of zero magnetic field (y-axis). The atoms which are entering the cooling volume are slowed down in the transverse direction and are compressed onto the longitudinal direction (y-axis). A pushing beam along the y-axis, pushes out the atoms from the 2D$^+$ cooling volume towards the 3DMOT through a differential tube connecting the 2D-MOT section and the 3DMOT chamber. In $2D^+$MOT, one more beam, the retardation beam, is introduced along the longitudinal direction counter-propagating to the pushing beam. The polished 45^o surface of the differential pumping tube overlaps the retarding beam with the pushing beam. The pushing and the retarding beams create optical molasses along the longitudinal direction. The optical molasses reduces the longitudinal velocity of the atoms inside the cooling volume; this increases the interaction time of the atoms with the transverse cooling beams. As a result, the atoms are more confined on the transverse plane, which eases their passage through the differential pumping tube and increases the flux of the atoms. The retarding beam, upon reflection from the 45^o degree surface, creates a central dark cylinder, creating an imbalance between the radiation forces originating from the pushing and the retarding beam. Therefore, the atoms cooled and confined in the transverse direction once they enter this dark region are pushed out towards the 3DMOT chamber and form the cold atomic beam. In our setup, we have introduced one more beam, the additional pushing beam, having independent control over intensity and frequency, aligned along the pushing beam. The additional pushing beam enhances the atomic flux by a significant amount.

Detection technique

In a 3DMOT, an atom absorbs photons from well-directed laser beams; each absorption of photons is associated with a subsequent spontaneous emission of a photon. Therefore, by measuring the total power emitted by the atoms trapped in a MOT by spontaneous emission, we can determine the total number of atoms in the MOT. This measurement technique is termed Fluorescence Imaging (F.I). The trapped atoms emit the photons isotropically over 4π solid angle.

Total power emitted by the atoms trapped in the MOT is given by the relation, $P = N_{MOT}\ \hbar\omega_{ge}\Gamma\rho_e$, where N_{MOT} is the number of trapped atoms in the MOT, $\hbar\omega_{ge}$ is the energy of the transition, Γ is the natural line-width of the transition, and ρ_e is the excited state population. The value of ρ_e is expressed by the relation, $\rho_e = \frac{1}{2}\frac{s}{1+s+(2\delta/\Gamma)^2}$, where s is the saturation parameter, and δ is the detuning of the 3DMOT cooling laser frequency from the atomic transition frequency.

Typically the imaging system is placed outside the UHV chamber and we could only measure a fraction of the total power emitted by the trapped atoms in the MOT. The fraction of the power is proportional to the solid angle subtended by the first lens of the imaging system onto the position of the MOT. A schematic diagram of the detection system is shown in Figure-5.

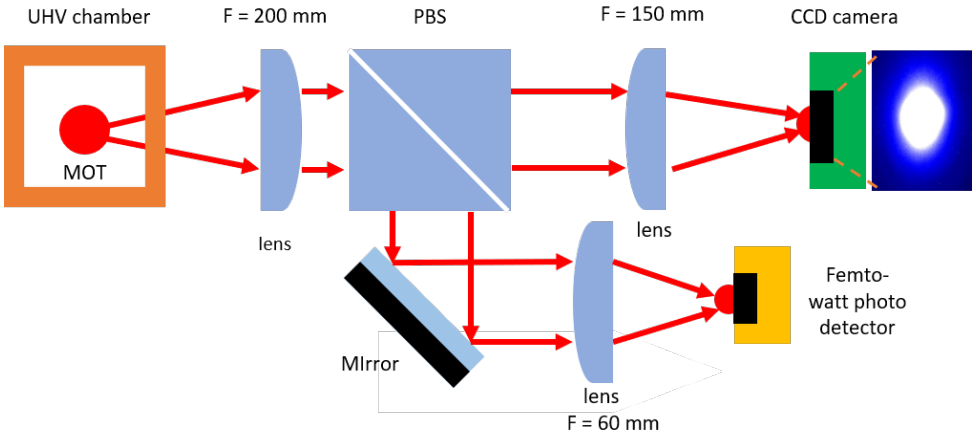


Figure 5: A schematic diagram of fluorescence imaging setup. The first lens captures the fluorescence emitted by the cloud of atoms. The first lens is placed such that the MOT is located at its focal length. The collimated fluorescence output is divided into two arms by a polarization beam splitter. The transmitted arm of the PBS is followed by a lens that falls on the CCD camera. The reflected arm, followed by one mirror reflection and a lens, incident on a Femtowatt detector.

The solid angle subtended by the first lens to the MOT is given by-

$$\Omega = \frac{\pi r^2}{F^2} \tag{1}$$

where, r is the radius of the lens and F is the focal length of the lens.

Therefore, the fraction of the power falling on the detector (either CCD camera or photo-diode) is given by-

$$P_{det} = \frac{\Omega}{4\pi} P \tag{2}$$

The second lens of the imaging system focuses the captured fluorescence on the Charge Coupled Device (CCD) camera and the photo-detector.

In the CCD camera, the incident fluorescence falls on an array of pixels. The number of electron counts generated in each pixel depends on the number of photons that fall on the pixels; thus, the CCD camera would be able to give us the intensity dependence of the fluorescence emitted from the MOT. The spatial distribution of the fluorescence,

which maps with the spatial distribution of the number of trapped atoms in the MOT, is captured by the CCD camera. To determine the number of atoms trapped in the MOT, we need to calculate the total count, which is the addition of the counts produced by all pixels for the given exposure time of the camera. From our calibration of the CCD camera, we know the dependence of the total count on the power of the incident light. So, from the above consideration, we can determine the number of trapped atoms in the MOT.

The photo-detector, converts the incident power in voltage and we observed the signal in the oscilloscope. The voltage (V_{det}) generated by the photo-detector for the incident fluoresence power (P_{det}) is related by the equation, $V_{det} = \kappa P_{det}$, where κ is the proportionality factor having the unit $\frac{V}{W}$. κ is obtained by the calibration of the photo-detector (provided by the manufacturer). The combination of all the above described equations yields the expression of N_{MOT},

$$N_{MOT} = \frac{4\pi}{\Omega} \frac{V_{det}}{\hbar \omega_{eg} \Gamma \rho_e \kappa} \tag{3}$$

In the above equation, once we provide all the experimental parameters, we obtain the number of atoms trapped in the MOT.

Figure-6(a) and Figure-6(b) show MOT loading characteristics captured by the photo-detector (Femto watt) and the CCD camera.

Characterization of the system

We load the 3DMOT by the cold atomic beams produced by the respective $2D^{+}$MOTs of ^{23}Na and ^{39}K atoms. Figure-6 shows the loading characteristics of the atoms in the 3DMOT. We measure fluorescence emitted by the atoms as the MOT grows and calculate the number of atoms trapped in the 3DMOT using the Eqn.4.12.

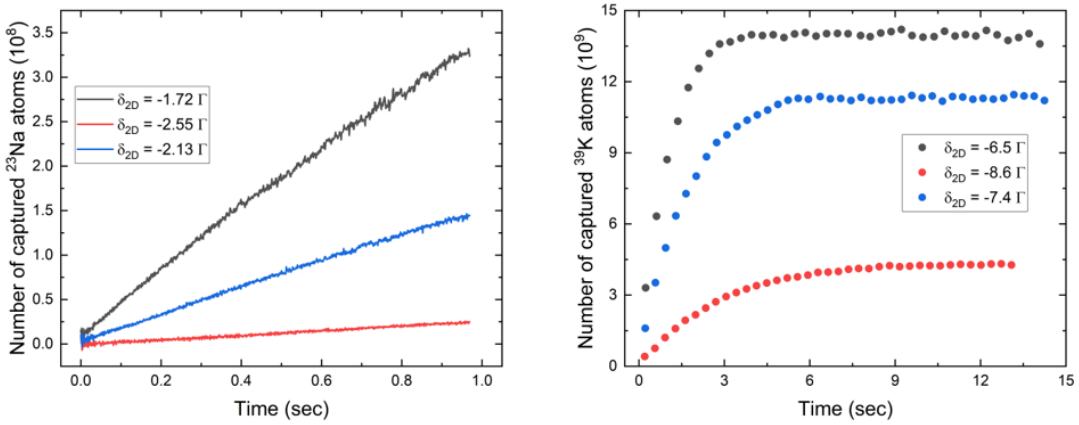


Figure 6: The loading characteristics of the 3DMOT for different detunings of the $2D^{+}$MOT cooling beams for (a) ^{23}Na and (b) ^{39}K atoms. In (a), we measure the fluorescence using a Femtowatt detector, while in (b), we measure the same using a CCD camera.

Magnetic transport and pathway to dual-species BEC

In Figure-2, I have shown the vacuum manifold and the magnetic transport assembly designed to accommodate the requirements of the experiment. We have designed the experimental system carefully keeping in mind the requirements of Ultra-High Vacuum (UHV) and sufficient optical access for the quantum degenerate clouds. In this setup, the 3DMOT is loaded from two independent 2D^{+}MOTs for ^{23}Na and ^{39}K atoms. To increase the lifetime of the degenerate clouds, we would like to trap the atoms in a much better vacuum as compared to the 3DMOT chamber. The presence of a large number of optical components near the 3DMOT chamber for the dual-species MOT makes limited access for the high-resolution imaging setup. All these considerations demand that we need to transfer the trapped atomic cloud to a much more convenient region where the Vacuum must be better by at least by an order of magnitude. At the same time, we should be able to place the high-resolution imaging system very close to the atomic cloud. In our

design, we have extended the vacuum manifold from the 3DMOT chamber in a direction normal to the atomic jets emerging from the two 2D$^+$MOTs. The extended arm ends up in a small UHV grade glasscell, and we termed it a 'science cell' (dimension: 30 mm x 30 mm x 85 mm). In the future, we will perform experiments on quantum degenerate gases in the science cell. At the science cell end, two more large-capacity ion pumps and one Titanium sublimation pump are connected, which ensures a much better vacuum. At the same time, the smaller dimension of the science cell allows placing the high-resolution imaging system much closer to the trapped cloud.

We have decided to implement a magnetic transport based on a static ensemble of coils. The current in each coil will be dynamically varied to transfer the position of the magnetic trap center. Principle In this section, I will present the principle of magnetic transport and the algorithm that calculates the current in the coils. In our system, the atoms will be transported along the x-axis, as shown in Figure-2.

We want to impose and control the shape of the magnetic trap and the position of the magnetic trap center. Thus we need to control four parameters, trap position (x^*) and the magnetic field gradients along the three axes (x, y, and z). The magnetic field gradients determine the shape of the trapped cloud. The three gradients (b_x, b_y, and b_z) are linked through the Maxwell's equation-

$$\widehat{\nabla}.\widehat{B} = 0 \tag{4}$$

With all the above considerations we can define the following three independent parameters-

1. centre position of the trap: x^*

2. $b_y = \frac{\partial B}{\partial y}$, magnetic field gradient along $\hat{y}$ axis

3. Aspect ratio, $\frac{b_x}{b_z}$

For instance, in a spherical quadrupole configuration (such as the magnetic field configuration for the MOT), the value of A is -0.5, as it has cylindrical symmetry with respect to the axial direction ($\hat{z}$). During the transport sequence, several coils operate simultaneously, so the cylindrical symmetry is broken. Therefore the value of A also varies during transport.

Simulation Our numerical simulation then yields the variation of the current required in each coil over the transport distance.

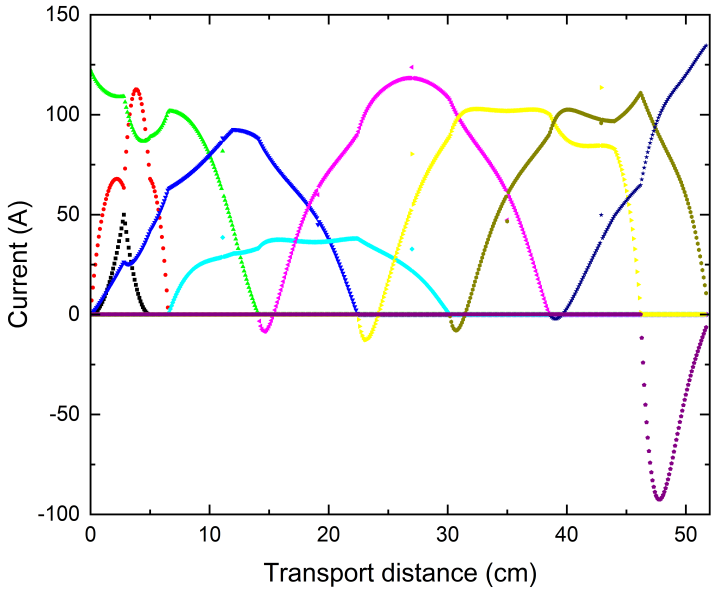


Figure 7: The variation of the current required in each coil over the transport distance. The different coloured graphs indicate currents through different sets of coils: green - MOT coils, black - push coil, red - additional coils, blue - T_1, cyan - T_2, magenta - T_3, yellow - T_4, dark green - T_5, dark blue - quadrupole, and violet - T_6.

According to the 3D design and numerical simulation, we have home built the magnetic field coils. We have used a hollow core copper tube for the quadrupole coils to facilitate cold water flow for cooling them. Other transport coils are disk-shaped; we made them using an enameled copper strip (1 mm x 5mm).

Publication and conference presentations

Publications

1. Sagar Sutradhar, Anirban Misra, Gourab Pal, Sayari Majumder, Sanjukta Roy, and Saptarishi Chaudhuri. Fast loaded dual species magneto optical trap of cold sodium and potassium atoms with light-assisted inter-species interaction. AIP Advances,13(6), 06 2023. 065317 (Editor's pick, featured article).

Conference presentations

1. **Design and performance of an experimental set-up for simultaneous laser cooling of ^{23}Na and ^{39}K atoms towards quantum degeneracy**, Physics with Trapped Atoms, Molecules and Ions (HYBRID), 9-13 May, 2022, International Centre for Theoretical Sciences (ICTS), Bangalore, India

2. **'Simultaneous trapping and cooling of sodium and potassium atoms towards quantum degeneracy'**, The 27th International Conference on Atomic Physics (ICAP), 17-22 July, 2022, Toronto, Canada (selected to present a poster).

3. **'Towards a Sodium-Potassium Ultra-cold Gas Mixture Experiment to Explore Many-body Physics with Long-Range Dipolar Interaction's,** Dynamics of Ultracold Systems with Embedded Highly-excited Rydberg Atoms (DUSSEHRA), 22-24 October, 2018, IISER Bhopal, India.

4. **'A Quantum gas mixture experiment to explore long-range dipolar interactions'**, DST-SERB School on Frontiers in Quantum Optics, 1 - 19 December, 2017, IIT Guwahati, India.

Contents

1 Introduction **1**

1.1 Instrumentation 18

1.1.1 Acousto-optic modulator 18

1.1.2 Electro-optic modulator 21

1.1.3 CMOS camera 24

1.2 Automation of the experiment 24

1.3 Aim of this thesis 27

2 Construction of the sodium-potassium cold atom experiment **28**

2.1 Philosophy behind the system design 29

2.2 The ultra high vacuum system 31

2.2.1 Importance of the differential pumping tubes 38

2.2.2 Achieving the ultra high vacuum 40

2.3 The laser system 44

2.3.1 Laser system for cooling and trapping of potassium atoms 46

2.3.2 Laser system for cooling and trapping of sodium atoms 47

2.4 Laser frequency stabilization 50

2.4.1 Saturation Absorption Spectroscopy 50

2.4.2 Frequency stabilization using Pound-Drever-Hall (PDH) locking techniques 54

2.4.3 Frequency stabilization using side-of-fringe technique 56
2.5 Optical layout 58
2.6 Atomic beam source 62
2.7 Magnetic field coils 73
2.8 Fast switching of the current in the magnetic coils 74

3 Laser cooling and trapping of neutral alkali atoms 76
3.1 Laser cooling of neutral atoms 77
3.2 The cooling and trapping atoms in a MOT 82
3.3 Modelling of the cold atomic beam flux of the $2D^+$MOT 85

4 Experimental realization of a dual-species magneto-optical trap 90
4.1 The description of the experimental arrangement of the magneto-optical trap 91
4.2 Experimental arrangement to determine number of atoms trapped in the 3DMOT 96
4.2.1 Determination of atoms number using CCD camera 99
4.2.2 Determination of atoms number from Femtowatt detector signal . . 102
4.3 Optimization of $2D^+$MOT of potassium and sodium 103
4.3.1 3DMOT capture rate vs $2D^+$MOTs' cooling beam detuning 104
4.3.2 3DMOT capture rate vs $2D^+$MOTs' cooling beam intensity 106
4.3.3 Capture rate of 3DMOT vs $2D^+$MOTs repumper and cooling beam intensity ratio 108
4.3.4 3DMOT capture rate vs $2D^+$MOTs intensity ratio of push and retardation beam 110
4.3.5 the capture rate in the 3DMOT vs the magnetic field gradient of $2D^+$MOTs 111
4.3.6 The capture rate in the 3DMOT vs the vapor pressure of the $2D^+$MOTs 113
4.4 Collisional dynamics of cold atoms in a MOT 116
4.4.1 Collisional dynamics of cold atoms in a single species 3DMOT . . . 121

4.5 Interspecies collisional dynamics of spatially overlapped ^{39}K and ^{23}Na MOTs 123

5 Magnetic trap and magnetic transport 135

5.1 Magnetic trap . . . 136

5.2 Realization of a magnetic transport . . . 138

5.2.1 Principle . . . 140

5.2.2 Dynamics . . . 146

5.3 Construction of the magnetic transport assembly . . . 155

5.4 Majorana losses from the quadrupole traps . . . 159

5.5 Quadrupole-Ioffe configuration (QUIC) trap . . . 165

Conclusion and Outlook 175

Bibliography 177

A Ultra-high vacuum system and 2D$^+$MOT 207

A.1 Calculations to design a ultra-high vacuum system . . . 207

A.2 UHV compatible glasscells of the vacuum setup . . . 214

A.3 Two dimensional (2D) quadrupole magnetic field for the 2D$^+$MOT . . . 216

B Fast switching of current in the magnetic coils based on IGBT 219

C Opto-coupler 222

D 3DMOT 224

D.1 Calibration of the total number of counts generated by the CCD camera for an incident laser beam . . . 225

D.2 Determine the atoms number from the counts of the CCD pixel . . . 226

D.3 Determination the intraspecies collisional loss rate for single species 3DMOT 228

D.4 Determination of interspecies collisional loss rate 229
D.5 Determination of the excited state population of the potassium atoms in K-3DMOT 232

E Magnetic transport **242**

List of Figures

1 The schematic diagram of the arrangement of a MOT in 1D. The horizontal dashed line (black) represents the laser frequency seen by an atom at rest at the center of the trap. The radiative force in the presence of an inhomogeneous magnetic field becomes velocity and space-dependent and pushes the atoms toward the center. xii

2 A 3D drawing of the experimental setup. It consists of a UHV manifold and magnetic coils assembly for magnetic transport. Two well collimated atomic beams load the 3DMOT from two spatially separated $2D^{+}$MOT of ^{23}Na and ^{39}K atoms. The trapped atoms at the 3DMOT region will be adiabatically transported over $\sim$ 51 cm to the science cell. This will be achieved by dynamically shifting the magnetic trap center towards the science cell by varying the currents in the static ensemble of magnetic coils. xiv

3 (a) A schematic diagram of Saturation Absorption Spectroscopy (SAS) setup. A laser beam is divided into a low-intensity (probe) and high-intensity (pump) beam, with a ratio $\sim \frac{1}{5}$. The probe beam goes through the vapor cell and falls on the detector. The pump beam overlaps with the probe beam inside the vapor cell (b) the photograph of SAS setup for ^{23}Na atoms. The blue plots show the transmission of the probe through the vapor cell in the absence of the pump beam, while the red plots show the same in the presence of the pump beam. xv

4 A schematic diagram of $2D^{+}$MOT configuration. It consists of a UHV-compatible glasscell, and one differential pumping tube is inserted inside the glasscell. The differential tube has a 45^{o} cut at the surface, which is inside the glass cell. A pair of racetrack coils (all of them are not shown for the image clarity) generates a 2D quadrupole magnetic field configuration. The transverse cooling beams, upon retro-reflected from the prisms, form the transverse cooling and trapping volume. The pushing and the retarding beams overlapped in the cooling volume form the longitudinal optical molasses. An additional push beam is aligned along the the longitudinal direction enhancing the atomic flux through the differential pumping hole to the 3DMOT chamber. xvii

5 A schematic diagram of fluorescence imaging setup. The first lens captures the fluorescence emitted by the cloud of atoms. The first lens is placed such that the MOT is located at its focal length. The collimated fluorescence output is divided into two arms by a polarization beam splitter. The transmitted arm of the PBS is followed by a lens that falls on the CCD camera. The reflected arm, followed by one mirror reflection and a lens, incident on a Femtowatt detector. xx

6 The loading characteristics of the 3DMOT for different detunings of the $2D^{+}$MOT cooling beams for (a) ^{23}Na and (b) ^{39}K atoms. In (a), we measure the fluorescence using a Femtowatt detector, while in (b), we measure the same using a CCD camera. xxii

7 The variation of the current required in each coil over the transport distance. The different coloured graphs indicate currents through different sets of coils: green - MOT coils, black - push coil, red - additional coils, blue - T_1, cyan - T_2, magenta - T_3, yellow - T_4, dark green - T_5, dark blue - quadrupole, and violet - T_6. xxiv

1.1 Behavior of Bosons and Fermions in harmonic trap at different temperatures. At high temperatures, both type of particles behave classically. At lower temperature the the quantum statistical nature comes into play and the particles follow different quantum statistics. 5

1.2 The schematic diagram showing geometry of the dipole-dipole interactions. (a) un-polarized case: the dipoles are interacting without the presence of applied field (b) polarized case: the interaction of the dipoles in presence of the applied field, the direction of the applied field is the quantization axis of the system (c) Two polarized dipole placed side-by-side repel each other. (d) Two polarized dipoles placed in a head-to-tail geometry attract each other. 10

1.3 The comparison of the strength of the dipole-dipole interaction (DDI) in magnetic atoms (dot), laser-cooled molecules (star), and the hetero-nuclear molecules in their absolute ground state(triangle). The DDI strength has been expressed in terms of the characteristic length in the units of the Bohr radius (a_0). To put it in a perspective, the lattice spacing of a 1064 nm optical lattice is $532nm \approx 10^4 a_0$. 12

1.4 The schematic of Radio frequency(RF) evaporation of the atoms trapped in a magnetic trap. The atoms in $M_F = +1$ states are trapped, while $M_F = -1$ is the anti-trapping state, here we have assumed $g_F > 0$. A RF field flips the spin of the atoms from $M_F = 1$ to $M_F = -1$ state. Atoms with higher kinetic energy execute a larger orbit in the trap. Therefore, the RF evaporative cooling is initiated at a higher frequency and gradually reducing the frequency, as a result the atoms with higher K.E. are deterministically removed from the trap and remaining atoms re-thermalized to a lower temperature. (b)The evaporative cooling is chopping out the higher distribution tail of the Maxwell-Boltzmann distribution and resulting in lower temperature. 17

1.5 A schematic of an AOM. An RF signal produces a acoustic wave in the material which generates a dynamical grating in the material and the incident light gets diffracted into different orders. 18
1.6 A Schematic of the double pass configuration using AOM. The reflected beam of a PBS is injected into an AOM. The first-order diffracted beam has been retraced back through the AOM using a combination of a lens and a mirror. The quarter-waveplate changes the phase of the polarization of the retraced beam by an amount π. Therefore, the retraced beam is out-coupled from the transmission arm of the PBS. 19
1.7 The image of the customize AOM driver circuit consisting of VCO, VVA, RF switch, RF amplifier. 20
1.8 The phase modulator EOM that we have employed in the experiment to generate the repumper frequency for the sodium atoms. 22
1.9 A schematic diagram of a phase modulation of incident light by an EOM. The phase-modulated beam from the EOM is injected into a Febry-Perot interferometer for characterization. 23
1.10 The transmission signal of FPI100. The Phase phase-modulated light from the EOM (PM-Na23-1.7-M3, QUBIG) is injected into the EOM. The carrier and the two sidebands are shown . The x-axis scaling has been done relative to the frequency of the incident beam and sidebands have been generated at $\pm 1725\,\mathrm{MHz}$. 23
1.11 The CMOS CCD camera used in the measurements of the 3DMOTs. . . . 24
1.12 The automation layout of the experiment. We use the LabVIEW interfacing software from a host PC, which controls all the analog and digital cards installed in the PXIe chassis. The generated analog and digital voltages in turn controls the AOM's driver circuit, gate of the IGBT for switching the current in the MOT coils, the CCD camera and so on. 25
1.13 Control panel of the sodium MOT in the LabVIEW. 26

1.14 Control panel of the potassium MOT in the LabVIEW. 26

2.1 A 3D model of the vacuum setup. The dual-species 3D MOT is loaded from two counter-propagating $2D^+$ MOTs. A single-arm magnetic transport transfers the trapped atoms to the science cell. 33

2.2 The top view of the 3D model of the vacuum setup. The dual-species 3D MOT is loaded from two counter-propagating $2D^+$ MOTs. A single-arm magnetic transport transfers the trapped atoms to the science cell. 34

2.3 Schematic of the $2D^+$MOT section. An atomic sample is kept inside the DN16CF I. The desired vapor pressure is obtained by heating the DN16CF I using heating tapes. The DN16CF gate valve controls the flow of the vapor into the $2D^+$MOT glasscell, where an atomic beam is realized from the filled vapor. 35

2.4 A schematic of 3DMOT section. A $75\,l/s$ ion pump and an ion gauge is connected to the 3DMOT chamber. Two $2D^+$ MOTs are connected to the chamber from two opposite DN40CF viewports. 37

2.5 The UHV system during the baking process. We wrapped the all the components using heating as describe in the text. 40

2.6 A schematic diagram showing the sequence of the pumps operation. The diagram outlined condition; the pressure range over which different vacuum pumps operate. 41

2.7 The variation of the pressure inside at the 3DMOT chamber measured by an ion-gauge during the bakeout procedure. 42

2.8 The hyperfine energy level structure for the $^2S_{1/2}$ ground state and the $^2P_{3/2}$ excited state of the D_2 transition line of (a) potassium and (b) sodium atoms. The hyperfine energy splittings are given in MHz. 44

2.9 A schematic diagram of an external cavity diode laser. The schematic shows that a lens collimates a divergent beam from an AR-coated diode laser. The length of the diode laser is L_D. The collimated light is incident on the reflective grating. The piezo actuator attached behind the grating pushes the grating back and forth. This mechanism rotates the grating around the pivot point. The grating angle is kept so that the -1^{th} order is coupled back into the laser diode. Thus the rear facet of the laser diode and the grating surface forms an external cavity. The length of the cavity is given by L_{ext}. 45

2.10 Laser system for cooling and trapping of potassium atoms. (a) cooling beam is derived from the DL pro and followed by the BoosTA pro and (b) the repumper beam is derived from DL 100 and subsequently amplified by another BoosTA pro. 46

2.11 Laser system for cooling and trapping of sodium atoms. (a) TA-SHG pro laser system and (b) a schematic diagram of the TA SHG pro laser system. The master laser (DLpro) emits 1178 nm light beam, and the beam is injected into a Tapered amplifier. The amplified light beam is passed through an EOM and injected into a Bow-tie cavity. An intensity-stabilized continuous wave laser beam at 589 nm is out-coupled through the cavity mirror M4. 47

2.12 TA-SHG intra-cavity leakage (aqua) and the PDH error (pink) signals. A ramp voltage from PID110 module is applied to the piezos behind mirrors M2 in Figure-2.11 and changes the length of the SHG cavity. The intra-cavity power is measured by the detector behind the mirror M3, and the error signal is generated from the modulated reflected light that falls on the PDH photo-detector. 48

2.13 A schematic diagram of the saturation absorption spectroscopy setup. The laser beam is divided into probe and pump beams. The probe and pump beams are made to overlap inside the vapor cell. The vapor cell is heated at the required temperature using heating tapes. The transmitted power of the probe beam incident into the photodiode. 51

2.14 Experimental arrangements to observe the saturation absorption spectroscopy signals of (a) potassium and (b) sodium atoms. 51

2.15 Saturation absorption spectroscopy signal of (a) potassium and (b) sodium atoms. The blue plots show the transmission of the probe through the vapor cell in the absence of the pump beam, while the red plots show the same in the presence of the pump beam. 52

2.16 A schematic diagram of saturation absorption spectroscopy set up and the frequency stabilization scheme using the PDH technique. The spectroscopy signal from the photodiode is fed into the Digilock module. The feedback signals from the Digilock module are fed to the laser via the operating current and the piezo driving voltage. A wavelength meter (WSU2, Highfiness) monitors the laser's wavelength during the experiment. 55

2.17 Sodium laser frequency locking technique. (a) Saturation absorption spectroscopy of sodium $D2$ transition. The black plot shows the SAS signal and the red plot shows corresponding PDH error signal. (b) The locking stability of the laser using the PDH locking technique. The red plot shows the wavelength of the laser while the laser is locked to the atomic transition line using PDH locking technique. The blue plot shows the wavelength variation of the laser light when free running. 56

2.18 The schematic diagram is showing the frequency stabilization of the sodium and potassium lasers using the side-of-the-fringe locking technique. The SAS signal of the atomic species is sent to Toptica Digilock module and the frequency is stabilized by choosing a set point on the SAS signal (as described in the text). 57

2.19 The layout of the potassium laser system. Each of the outputs of the Dl pro and DL 100 is split into two beams using the combination of half-waveplates and the PBSs. One of the beams is sent to respective tapered amplifiers. The amplified output beam from the respective tapered amplifiers is split into a series of beams, and each beam is sent to respective AOMs. The double pass output of the AOMs is injected into their individual PM fiber. The remaining beam of Dl100 is sent to an AOM, and the double pass output beam is sent to the SAS setup. In the case of DL pro, the remaining beam is split into two more beams; both beams are sent to AOMs. The double pass output of one of the AOMs is sent to the SAS setup, while the double pass output of the other AOM is tuned to imaging transition and injected into the respective PM fiber. 59

2.20 Sodium laser system. The output beam from TA SHG pro is split into a number of beams. A series of AOM double pass configurations tuned and controlled the frequencies and intensities of these beams. One of the double pass beam is directed to the saturation absorption spectroscopy (SAS) setup. 61

2.21 A schematic diagram of 2D+MOT configuration. It consists of a UHV-compatible glasscell, and one differential pumping tube is inserted inside the glasscell. The differential tube has a 45deg cut at the surface; this surface is placed inside the glass cell. A pair of racetrack coils (all of them are not shown for image clarity) generates a 2D quadrupole magnetic field configuration. The transverse cooling beams and the retro-reflected beam from the prisms form the transverse cooling and trapping volume. The pushing and the retarding beams overlapped in the cooling volume to form the longitudinal optical molasses. An additional push beam is aligned along the longitudinal direction, enhancing the atomic flux through the differential pumping hole to the 3DMOT chamber. 66

2.22 The image of UHV glasscell and the differential pumping tube of K-2D$^+$MOT. 67

2.23 The schematic diagram of sodium 2D$^+$MOT experimental arrangement. The collimated output from the fiber collimator of diameter 12 mm is divided by several half-waveplate and PBS combinations. I indicate the ratio of the $\frac{1}{e^2}$ diameter of the beam on the XZ plane to the $\frac{1}{e^2}$ diameter of the beam on the XY plane at a given position. For example, quantity 1:1 corresponds to a laser beam of a circular cross-section diameter of 12 mm. In comparison, quantity 2:2 corresponds to a laser beam circular cross-section of diameter 24 mm. The white arrows indicate the direction of the current flow in the 2D$^+$MOT magnetic coils. 70

2.24 The schematic diagram shows a laser beam retro-reflected from a prism. The laser beam preserves the helicity of the circular polarization experiencing two total internal reflections. 71

2.25 The schematic diagram of potassium 2D$^+$MOT experimental arrangement. The collimated output from the fiber collimator of diameter 12 mm is divided by a number of half-waveplate and PBS combinations. I indicate the ratio of the $\frac{1}{e^2}$ diameter of the beam on the XZ plane to the $\frac{1}{e^2}$ diameter of the beam on the XY plane at a given position. For example, quantity 1:1 corresponds to a laser beam circular cross-section of diameter 12 mm. In comparison, the quantity 2:3 corresponds to a laser beam with an elliptical cross-section of minor and major axes diameter of 24 mm and 36 mm, respectively. The white arrows indicate the direction of the current flow in the 2D$^+$MOT magnetic coils. 72

2.26 The image of the 2D$^+$MOT of potassium atoms. The glasscell and the racetrack coils to generate 2D quadrupole magnetic field configuration is indicted. 73

2.27 Schematic of IGBT based fast switching circuit for magnetic coils 74

2.28 The switching characteristics of current in the MOT coil using the IGBT based switching circuit. (a) Rise and (b) fall dynamics of the current. . . . 75

3.1 A resonant laser beam interacts with a two-level atomic system. The atom absorbs a photon from the laser beam and gets a momentum kick by an amount $\hbar k$ towards the direction of the laser beam. (b) The excited atom emits a photon via spontaneous emission. The direction of the spontaneously emitted photon is random and could be directed in any direction. . 77

3.2 (a) Two counter-propagating red detune laser beams interacting with a two-level atom at rest. The atom absorbs a photon from the laser beam and gets a momentum kick by an amount $\hbar k$ towards the direction of the laser beam. (b) The atom is moving with a velocity v along $\hat{z}$ direction. Due to Doppler shift the atom encounter more scattering from the laser beam moving counter-propagating compared to the laser beam co-propagating with the atom. 79

3.3 The force on an atom in optical molasses. The force experienced by the atom from the co-propagating laser beam is denoted by F_+, while the force acting on the atom by the counter-propagating laser beam is indicated by F_-. The damping of the atomic motion is governed by the slope of the resultant force (F) at $v = 0$. 80

3.4 The arrangement of a MOT in 1D. The horizontal dashed line(black) represents the laser frequency seen by an atom at rest in the trap's center. The Zeeman shifts of the atomic transition frequencies in the inhomogeneous magnetic field $B(z) = bz$. Therefore, atoms at $z = z'$ are closer to resonance with the σ^- laser beam than with the σ^+ beam and are therefore driven toward the center of the trap. 82

3.5 A schematic diagram of a 3DMOT. Three pairs of circularly polarized counter-propagating lasers beam are directed towards the position of zero magnetic field of a three dimensional quadrupole magnetic configuration. . 84

3.6 A schematic diagram of a 3DMOT loaded by the cold and collimated atomic beam produced by the 2D$^+$MOT. 85

3.7 The trajectories of the atoms emerging from the 2D$^+$MOT. 88

3.8 The distribution of the atoms emerging from the 2D$^+$MOT on the transverse plane at the position of the 3DMOT. 89

4.1 The top view of the layout of the experimental arrangement of sodium and potassium 3DMOTs. The laser beams required for the 3DMOT are out-coupled from the PM fibers. In the case of potassium, we merged the cooling and the repumper beams using PBS, while for sodium, we have a single fiber. The output beam of respective fiber collimators is divided into three beams using half-waveplates. Each of the beams is sent through a telescopic expansion and directed along three orthogonal directions. The sodium and potassium beams are made to overlap using a dichroic before injecting into the 3DMOT chamber along three orthogonal directions. . . . 91

4.2 The side view of the layout of the experimental arrangement of sodium and potassium 3DMOTs. This projection shows the configuration and path of the 3DMOT beams along the vertical direction. The prepared vertical beams of sodium and potassium 3DMOTs are made to overlap using a dichroic mirror before injecting into the vacuum chamber. 92

4.3 The arrangement of the 3DMOT on the experimental table for both the species: sodium and potassium. 94

4.4 Images of (a) potassium and (b) Na-3DMOT in the 3DMOT chamber. The images were capture through the 'science cell' by a smartphone. 95

4.5 Schematic diagram of fluorescence imaging setup. The first lens captures the fluorescence emitted by the cloud of atoms. The first lens is placed such that the MOT is located at its focal length. The collimated output of the fluorescence is divided into two arms by a polarization beam splitter. The transmitted arm, followed by a lens, falls on the CCD camera. The reflected component, followed by one mirror reflection and a lens incident on a Femtowatt detector. 97

4.6 The captured fluorescence image of the 3DMOT in the CCD camera. The CCD camera has 1920 pixels along the X-axis and 1080 pixels along the Y-axis. The heat map shows the generated counts in each pixel. 99

4.7 A typical loading curve of K-3DMOT. The atom number is calculated from the counts of the CCD camera for the given exposure time. Each point on the curve corresponds to a captured fluorescence image in the CCD camera. 100

4.8 A typical 3DMOT loading signal is obtained from the Femtowatt photo-detector. The incident photons from fluorescence of the 3DMOT, generates a photo-current, which in turn produces a voltage signal across the load resistance of the oscilloscope. Using the calibration factor, we determine the loading rate and number of atoms trapped in the the steady state of the 3DMOT. 102

4.9 The loading dynamics of (a) potassium and (b) sodium atoms in respective 3DMOT. The loading dynamics are represented at different detuning of the $2D^{+}$MOT cooling beam detuning. 105

4.10 The variation of the capture rate of (a) potassium and (b) sodium 3DMOTs at different $2D^{+}$MOT cooling beam detunings. We obtained a maximum capture rate at detunings of -6.5Γ and -1.8Γ of the potassium and sodium $2D^{+}$MOT cooling beams. 105

4.11 The experimental observations and the comparison with the numerical simulation of the variation of the capture rate of (a) potassium and (b) sodium atoms in their respective 3DMOTs with the intensity of the $2D^{+}$MOT cooling beams. As we increased the intensity of the cooling beam we observed an increase of the the capture rate. At higher intensities the rate of increase of capture rate slows down. At much higher intensities the capture rate expected to saturate as described in the text. 107

4.12 The variation of the capture rate in the 3DMOT of (a) potassium and (b) sodium atoms with the intensity ratio of repumper and cooling beams of respective 2D$^+$MOTs. As we increase the ratio, we observed a rapid increment in the capture rate in both the 3DMOTs. At higher values of the ratio, the capture rate is saturated. We can see a stark difference between the values at which the saturation of the capture rate occurs in potassium and sodium. The higher value of the ratio in the case of potassium atoms is attributed to the fact that the energy splitting of the excited state is less(factor $\sim$3) compared to the same of the sodium atoms. As a result, the atoms are more likely to get transferred into the dark hyperfine state $|F = 1\rangle$. Therefore, it required more repumper power in comparison to the sodium atoms to get the saturation in the capture rate. 108

4.13 The variation of the capture rate in the 3DMOT of (a) potassium and (b) sodium atoms with the intensity ratio of the pushing and retardation beams of 2D$^+$MOTs. 110

4.14 The experimental observations and the comparison with numerical simulation of the capture rate in the 3DMOT of (a) potassium and (b) sodium atoms with the magnetic field gradient of 2D$^+$MOTs. 112

4.15 The variation of the capture rate in the 3DMOT of (a) potassium and (b) sodium atoms with the vapor pressure of 2D$^+$MOTs. 113

4.16 The Na-2D$^+$MOT is wrapped by the heat-insulation blanket and the layers of aluminium foils. 114

4.17 A schematic of excite state -ground state collision between two atoms of species 'A' and 'B'in a dual-species MOT. An atom of the species 'A' adsorbs a photon of energy $h\nu_A$ and makes a transition to the excited state $A(P_{3/2})$ at the interatomic distance R_0. The atoms in the excited state $A(P_{3/2})$ and ground state $B(S_{1/2})$ approach each other in the attractive potential. Over the duration of the lifetime of the excited state (τ) atoms approach an interatomic distance R' and the atom 'A' is de-excited to the ground state by emitting a photon of energy $h\nu'_A$ ($< h\nu_A$). The difference of the energy, $\Delta E = h\nu_A - h\nu'_A$, converted to the kinetic energy of the atoms 'A' and 'B'. 119

4.18 The density evolution of the 3DMOT of (a) potassium and (b) sodium atoms. During the initial part of the loading, the density gradually increases. In the case of potassium 3DMOT, the density saturates after $t \sim$10 sec, while for Na-3DMOT, it happens after $\sim$40 sec. The loading of 3DMOT in this regime is termed 'constant density limit'. 122

4.19 The loading dynamics of sodium atoms in the 3DMOT in the absence and the presence of potassium 3DMOT. We obtain a steady state atoms number in the Na-3DMOT, and after that, allow the loading of the potassium 3DMOT. We observed a significant loss of sodium atoms as large as 50%. . 125

4.20 The schematic diagram of the sequence of the measurement of the number of trapped sodium atoms in the absence and the presence of the trapped potassium atoms in the 3DMOT. During the entire sequence, we observe the fluorescence of the Na-3DMOT by placing the band pass filter (FB590-10, Thorlabs) before the Femto Watt detector. 128

4.21 The variation of the 'survival probability ^{23}Na' with the 'Mixture ratio'. The survival probability decreases as the 'Mixture ratio' increases. As more potassium atoms are trapped in the dual-species 3DMOT, the collisional rate has also increased. The 'survival probability' saturates beyond the 'Mixture ratio' value of 5. 129

4.22 The variation of the 'survival probability of ^{23}Na' w.r.t the excited state population of the potassium atoms in the 3DMOT. As we increase the excited state population, there is a decrease in the survival probability. At higher values of the excited state population beyond 1.75%, the survival probability increases. 131

4.23 The schematic diagram shows the measurement scheme of the excited state population of the potassium atoms in the 3DMOT. We send the first pulse, 'probe 1' in the steady state of the 3DMOT. The transmission of the probe is shown by the photodiode signal(green). The distribution of the atoms in different hyperfine states is shown in the inset. Afterward, we turned off the cooling beam of the 3DMOT, and after 50 μs, we turned off the repumper beam of the 3DMOT. This scheme optically transfers the atoms in the hyperfine state $|F = 1\rangle$ to $|F = 2\rangle$. After 100 μs, we sent another pulse, 'probe 2', through the atomic cloud. The transmission of the probe is shown by the photodiode signal(green). The difference(ΔV) between the two consecutive signals is a measure of the optically pumped atoms to $|F = 2\rangle$. 133

5.1 Trapping of an atom in a quadrupole magnetic field. (a) The magnetic field generated by a pair of coils in anti-Helmholtz configuration, the white arrows show the direction of the current flow and the blue line shows the variation of the field with the distance from the center and red arrows indicate the direction of the local magnetic field. (b) The potential energy of the atoms in the quadrupole magnetic field. The atoms could be trapped when, $\sim K_B T < V_{trap}$. 137

5.2 The magnetic transport assembly around the UHV chamber. A large number of coils are placed from the 3DMOT chamber towards the "science cell". 139

5.3 A side view of the magnetic transport assembly. A series of static coils are shown. After obtaining the atoms in the 3DMOT, the atoms would be trapped in the quadrupole magnetic trap of MOT coils by increasing the current in the MOT coils. Thereafter, dynamically varying the currents in the subsequent coils T_1, T_2, T_3 and so on, the magnetic trap would be dynamically moved towards the quadrupole coil(Q). The atoms would adiabatically follow the magnetic trap and would be transferred to the final quadrupole coil (Q) at a distance $x = 51.8$ cm in the "science cell". 140

5.4 We have defined (a) the magnetic field gradient along y-axis and (b) the aspect ratio over the transport length. The numerical simulation determines the required current in each of the magnetic coils in order to obtained these defined y-gradient and aspect ratio over the transport length. 142

5.5 The solution of the numerical simulation. The current in each of the coils required in order obtained the defined y-gradient and the aspect ration as shown in Figure-5.4. The different coloured graphs indicate currents through different sets of coils: green - MOT coils, black - push coil, red - additional coils, blue - T_1, cyan - T_2, magenta - T_3, yellow - T_4, dark green - T_5, dark blue - quadrupole, and violet - T_6. The coil definition is given in Appendix-E. 144

5.6 Magnetic field component along transport direction of T_1 coil. The magnetic field varies linearly over a distance $\sim$ 5 cm, beyond this point the non-linearity starts to appear. 148

5.7 The potential of the magnetic trap at the position $x = L_P$ on the transport axis (a) at static condition, and (b) with different acceleration at which the trap is moved. At higher acceleration, the trap range of the trap is significantly reduced on $x' < 0$ region. 150

5.8 Position of the centre of trap during the transport. 153

5.9 (a) The velocity and (b) acceleration of the centre of the trap during the transport. 154

5.10 Winding of the MOT coil. We wrapped the capillary tube with a Nomex tape, then we wound the tube on a aluminium structure. 155

5.11 One of the prepared MOT coil is mounted in the aluminium frame just before the installation to the transport assembly. 156

5.12 We have wound all of our magnetic transport coils in this specialized arrangement made by the RRI workshop. 157

5.13 One of the transport coil and its mounting frame. 157

5.14 The stage-1 of magnetic transport assembly before installation. 158

5.15 Stage-2 of the magnetic transport assembly. 158

5.16 The installation of the magnetic transport stage-2 to the experiment. . . . 159

5.17 An atom with magnetic dipole moment μ is precessing around the external magnetic field with the Larmor frequency Ω_L. 160

5.18 The schematic showing the Majorana spin flip. An atom which is exhibiting an orbit of spatial extension $x0$, follows the magnetic field orientation adiabatically. When the atoms is directly crossing the center of the quadrupole trap, the magnetic moment could not follow the direction of the local magnetic field direction. As a result, the atom transfer to the anti-trapping states on $z < 0$ region and the atom escape from the trap. 161

5.19 A QUIC trap set up. Two pair of coils with symmetry axis along z -axis produces a quadrupole trap in anti-Helmholtz configuration. The Ioffe coil is placed, with its axis of symmetry along the transport direction. The current in the Ioffe coil produces a curvature and offset magnetic field along x-axis.Turning on the current in the Ioffe coil converts the quadrupole trap into a QUIC trap with the trap center moving towards the Ioffe coil along the x-axis. 165

5.20 Schematic of the QUIC trap coils assembly. x=0 position corresponds to the center of the quadrupole trap. The Ioffe coil is placed with its symmetry axis along the x direction. 166

5.21 The radial magnetic field of the quadrupole trap and the axial magnetic field of Ioffe coil along the transport axis(x-axis).The black arrows represent the magnetic field direction of the quadrupole field and the red arrow is that of the axial field of the Ioffe coil. 167

5.22 The evolution of a quadrupole trap into a QUIC one. The graphs are showing the absolute value of the magnetic field along the x-axis with 95 amps of current in the quadrupole coils and (a) 0 amps, (b) 40 Amps, (c) 75 Amps, (d) 85 Amps, (e) 90 Amps, and (f) 95 Amps of current in the Ioffe coil. 169

5.23 The magnitude of the magnetic field of the QUIC trap along the transport direction . The arrows represent the magnetic field direction of axial field along the transport axis. 171

5.24 A close view of Figure-5.23 around the minimum field position. We have fitted the curve over two different spatial extensions. The blue curve represent the fitting over range below 12 Gauss ($500\,\mu K$) magnetic field while the green curve represents the fitting over the extension below 6 Gauss ($100\,\mu K$) magnetic field. 172

5.25 The fitting parameters $b0$ and $b2$ at different Ioffe coils current with (a) 90 Amperes and (b) 95 Amperes of current in the quadrupole coil. 173

5.26 The magnetic field components along (a) y-axis and (b) z-axis of the QUIC trap. 174

A.1 A schematic diagram of a vacuum setup. The higher pressure and low pressure chambers are separated by a differential pumping tube. 208

A.2 A simplified schematic diagram of the vacuum setup. 209

A.3 The engineering drawing of differential pumping tube of the sodium $2D^+$MOT. 212

A.4 The engineering drawing of differential pumping of the potassium $2D^+$MOT 213

A.5 Engineering drawing of the $2D^+$MOT glasscell. 215

A.6 Engineering drawing of the 'science cell'. 215

A.7 The dimension of the frame of the $2D^+$MOT racetrack coils. 216

A.8 The experimentally measured magnetic field of the $2D^+$MOT racetrack coils along one of the transverse axis ($\hat{x}$). The fitting of the experimental data points by a linear function yields a magnetic field gradient $\sim$ 19Gauss/cm at 1 Ampere of current. 217

B.1 The schematic of the circuit diagram of IGBT based switching circuit of current in magnetic coils 219

B.2 A simplified schematic diagram of the switching circuit. 220

C.1 The circuit diagram of the opto-coupler. The output voltage from the NI 1062Q is send though a current buffer followed by the opto-coupler circuit. 222

C.2 The response of the opto-coupler to the (a) rise and (b) fall to a square voltage signal. 223

D.1 A probe laser beam is incident on the CCD camera. We measure the power of the laser beam in front of the CCD camera and determine the total count generated by the CCD camera. 225

D.2 The density evolution of the atoms in (a) potassium and (b) sodium 3DMOTs. We fit Eqn.D.7 to the data of (a) and (b) and obtained the respective intra-species collisional rates (β). 229

D.3 The loading dynamics of sodium atoms in the 3DMOT in the absence and the presence of K-3DMOT. We load Na-3DMOT from the atomic beam from the Na-2D$^+$MOT and obtain a steady state at $\sim$20 sec. We allowed the K-3DMOT loading at $\sim$95sec and observed a gradual decrease of sodium atoms. We obtained a steady state of the Na-3DMOT again at $\sim$120 sec. We observed a significant loss of sodium atoms as large as 50%. N_{Na} and N'_{Na} are the steady state number of the sodium atoms in the Na-3DMOT in the absence and presence of the potassium 3DMOT. . . 230

D.4 The schematic diagram shows the distribution of atoms in different hyperfine states. The cooling beam is tuned to the transition $|F = 2\rangle \rightarrow |F' = 3\rangle$. While interacting with the cooling beam, the atoms could make a transition to the hyperfine state $|F = 1\rangle$ and would be out of the cooling transition. Therefore, the repumper beam is employed, which is tuned to the transition $|F = 1\rangle \rightarrow |F' = 2\rangle$. The repumper beam is optically pumps the atoms again to the hyperfine state $|F = 2\rangle$. 232

D.5 The schematic diagram shows the measurement scheme of the excited state population of the potassium atoms in the 3DMOT. We send the first pulse, 'probe 1' in the steady state of the 3DMOT. The transmission of the probe is shown by the photodiode signal(green). The distribution of the atoms in different hyperfine states is shown in the inset. Afterward, we turned off the cooling beam of the 3DMOT, and after 50 μs, we turned off the repumper beam of the 3DMOT. This scheme optically transfers the atoms in the hyperfine state $|F = 1\rangle$ to $|F = 2\rangle$. After 100 μs, we sent another pulse, 'probe 2', through the atomic cloud. The transmission of the probe is shown by the photodiode signal(green). The difference(ΔV) between the two consecutive signals is a measure of the optically pumped atoms to $|F = 2\rangle$. 235

D.6 The schematic diagram of the experimental arrangement. We first aligned the probe beam through the center of the atomic cloud. Thereafter, we sent the two pulses of the probe beams as describe in the text. The transmission of the pulses of the probe beam has been measured by a fast photodiode. The blue dashed lines shows the path traversed by the probe beam and blue solid block represent the pulse of the probe beam. 236

D.7 The enhancement in the absorption of the 'probe 2' pulse w.r.t the 'probe 1' pulse as we varied the intensity of the 3DMOT repumper beams. 237

D.8 The additional number of photons absorbed after the optical pumping (black) and the number of photons emitted from the trapped atoms in the 3DMOT due to the fluorescence(red). 239

D.9 The additional number of photons absorbed after the optical pumping, calculated from the linear fitting as mentioned in the text and the number of photons emitted from the trapped atoms in the 3DMOT due to the fluorescence. 240

D.10 The variation of the excited state population of the potassium atoms in K-3DMOT with the power of the repumper beams. 241

E.1 A schematic of a current carrying single loop generating magnetic field at position $P(x, y, z)$ in the cylindrical cor-ordinate. The loop has a radius R and carrying current I and $\rho = \sqrt{x^2 + y^2}$, is the radial distance of the point. 243

E.2 A schematic of a current carrying single loop generating magnetic field at position $P(x, y, z)$ in the cylindrical cor-ordinate. The loop has a radius R and carrying current I and $\rho = \sqrt{x^2 + y^2}$, is the radial distance of the point. 244

E.3 The arrangement for the measurement of the magnetic field generated by the coils in anti-Helmholtz configuration. 246

E.4 The measured magnetic field and the comparison of the magnetic field components along (a) x-axis, (b) y-axis, and (c) z-axis of the additional coils at 10 Amps of current. 247

E.5 The measured magnetic field and the comparison of the magnetic field components along (a) x-axis, (b) y-axis, and (c) z-axis of the MOT coils at 10 Amps of current. 249

E.6 The measured magnetic field and the comparison of the magnetic field components along (a) x-axis, (b) y-axis, and (c) z-axis of the T1 coils at 10 Amps of current. 251

E.7 The measured magnetic field and the comparison of the magnetic field components along (a) x-axis, (b) y-axis, and (c) z-axis of the T2 coils at 10 Amps of current. 253

E.8 The measured magnetic field and the comparison of the magnetic field components along (a) x-axis, (b) y-axis, and (c) z-axis of the T3 coils at 10 Amps of current. 255

E.9 The measured magnetic field and the comparison of the magnetic field components along (a) x-axis, (b) y-axis, and (c) z-axis of the T4 coils at 10 Amps of current. 257

E.10 The measured magnetic field and the comparison of the magnetic field components along (a) x-axis, (b) y-axis, and (c) z-axis of the T5 coils at 10 Amps of current. 259

E.11 The measured magnetic field and the comparison of the magnetic field components along (a) x-axis, (b) y-axis, and (c) z-axis of the Quadrupole coils at 10 Amps of current. 261

E.12 The measured magnetic field and the comparison of the magnetic field components along (a) x-axis, (b) y-axis, and (c) z-axis of the T6 coils at 10 Amps of current. 263

List of Tables

1.1 The description of the chemical stability, dipole moment in absolute ro-vibration ground state of the hetero-nuclear polar molecules. The dipole-dipole interaction length has been calculated using Eqn.1.3 and represented in terms of the Bohr radius, $a_0 = .052 \times 10^{-9}$m. 14

1.2 Lists of the components used in the AOM driver. 21

2.1 Typical value of the parameters of the potassium light beams prepared for the 2DMOT and 3DMOT. The detuning and the power delivered to the main experimental table. The power has been Measured after the respective fiber collimators. 60

2.2 Typical value of the parameters of the sodium light beams prepared for the 2DMOT and 3DMOT. The detuning and the power delivered to the main experimental table. The power has been Measured after the respective fiber collimators. 62

4.1 The optimized parameters of the $2D^{+}$MOT for maximum capture rate of potassium and sodium atoms in the respective 3DMOTs. 115

4.2 The experimental values of the parameters of employed for potassium and sodium 3DMOTs. 116

5.1 Summarizing the sequence and the characteristic lengths involve in magnetic transport. 146

5.2 Summarizing the characteristic timescale involve in the Magnetic transport scheme. 153

5.3 The field gradients along y and z axes. For 95 Amps of current in the quadrupole coils and different currents in the Ioffe coil. 174

A.1 The dimensions of the vacuum components and their conductance. 210

A.2 The dimensions of the vacuum components and their conductance. 211

A.3 The dimensions of different parts of the differential pumping tube of the sodium 2D$^+$MOT. 212

A.4 The dimensions of different parts of the differential pumping tube of the sodium 2D$^+$MOT. 213

B.1 The list of the components have been used in the IGBT based switching circuit. 220

D.1 The calibration of the CCD camera. We are listing the experimentally obtained conversion factor of the number of photons to the counts generated by the CCD camera. 226

D.2 The value of the solid angle subtended by the imaging system and the properties of the cooling beams of K-3DMOT. 227

D.3 The value of the solid angle subtended by the imaging system and the properties of the cooling beams of Na-3DMOT. 228

E.1 parameters of the magnetic transport coils 245

E.2 Magnetic field gradients of additional coils pair at 10 Amperes of current . 248

E.3 Magnetic field gradients of MOT coils pair at 10 Amperes of current 250

E.4 Magnetic field gradients of T1 coils pair at 10 Amperes of current 252

E.5 Magnetic field gradients of T2 coils pair at 10 Amperes of current 254

E.6 Magnetic field gradients of T3 coils pair at 10 Amperes of current 256

E.7 Magnetic field gradients of T4 coils pair at 10 Amperes of current 258

E.8 Magnetic field gradients of T5 coils pair at 10 Amperes of current 260

E.9 Magnetic field gradients of Quadrupole coils pair at 10 Amperes of current 262

E.10 Magnetic field gradients of T6 coils pair at 10 Amperes of current 264

E.11 parameters of the Ioffe coils of the QUIC trap. 264

Chapter 1

Introduction

The advancement achieved through the realization of the experimental observation of Bose-Einstein condensations (BECs) [1–3] and Fermi degeneracy [4, 5] in dilute atomic gases has revolutionized the field of atomic physics. This has opened up the door to a plethora of new exciting and unexplored regimes of physics [17, 20–23]. The theoretical proposal of the ultracold atoms in an optical lattices [15] is an ideal system to simulate Hubbard model . The Hubbard model is at the heart in exploring the quantum dynamics of the electrons in a condensed matter system. The experimental realization of superfluid-to-Mott insulator transition [16] has unveiled the true potential of ultracold quantum gases in an optical lattices . Afterwards it has emerged as a new tool to investigate and explore quantum many body systems, in particular, to simulate condensed matter systems [17,54–58]. The observation of Feshbach resonances [59] between the same atomic species [60,61] and different atomic species [62–66], has given the experimentalists a knob to tune the interactions between the neutral atoms. It allows to vary the nature of interactions from repulsive to attractive, and vice versa, as well as it can be used to control the strength of the interactions. The field of ultracold atoms has become one of the most prominent avenues of research in modern physics due to the precise and unprecedented control over the degrees of freedom of the system. The study of the ultracold atoms is not only restricted to single species, the precise control enables to extend the exploration

over multi-species together. The ultracold atomic system has become a novel testbed to explore the superfluid-Mott insulator transition [15, 16] and to determine the underlying physics behind the interaction induced insulator behaviour. The exceptional experimental controllability of the ultracold atoms has enabled the study of the physics of disorder induced localization of matter waves [67, 68] - Anderson localization, originally proposed for the phenomenon of the localization of electrons in disordered materials [69].

BEC-BCS crossover [18, 19, 70–72] is also a very important physical phenomena studied conclusively using ultracold atoms with tunable interactions. Exploring the polaron physics with ultracold atoms offers a unique opportunity to study the behaviour of the quasi-particle in a highly controllable manner [73], which is difficult to perform in solid-state materials. A polaron is a quasi-particle consisting of an electron or hole in a solid-state material interacting with its surrounding lattice of atoms [74]. The study of polaron physics is of fundamental interests, they are key objects to understand the dynamics of impurity in a High-T_c superconductor [73, 75].

Ultracold polar molecules are relatively new area of research in the field of atomic, molecular and optical (AMO) physics. The large electric dipole moment of the ultracold hetero-nuclear polar molecules [76–80] manifest the long-range and anisotropic interactions. These extraordinary properties feature strongly correlated many-body system [21, 81, 82] and exhibit exotic quantum phases [83–85].

Simulating condensed matter systems using ultracold polar molecules is an active area of research. The condensed matter systems are typically made up of a large numbers of interacting particles: electrons, ions exhibiting complex behavior. At the same time, it is not possible to tune the interactions between the particles. Therefore, the inaccessibility of the control of the interactions and the number of particles in a bulk sample hinders the deep understanding of the underlying dynamics in condensed matter systems. In comparison, ultracold polar molecules paved the way for simulating the complex condensed matter system in a controlled way [17, 82, 86, 87].

The tunability of the interactions between the polar molecules using an external field

allows studying a wide range of condensed matter phenomena. Among a plethora of such possibilities, to name a few: superfludity [48], high-T_c superconductivity: the dipole-dipole attraction between the polar molecules confined in bilayer optical potentials lead to the formation of paired superfluid phase (PSP) [88, 89]. This yields a model system to gain insights into the underlying dynamics of high-T_c superconductivity in cuprates. Ultracold polar molecules are the new avenue to study quantum magnetism [90–92].

A detailed study of the underlying dynamics behind a chemical reaction is of fundamental importance in the AMO community. An ultracold system, with practically zero transnational motion and excellent control over the preparation of the quantum states [46, 93], provides a unique platform to study the chemical reactions in a controlled way. It is possible to determine the quantum state-controlled chemical reactions [94–96], and it becomes possible to obtain a deep insight into how the law of quantum mechanics governs the reaction dynamics. The collisional dynamics determine the efficiency of evaporative cooling and the lifetime of an ultracold atomic or molecular system. A deep understanding of the process of the chemical reactions is very important to determine the inelastic collisions involved in the process. Therefore, engineered systems could be devised to suppress the inelastic collisions to obtain a ultracold system with long life-time, which is fundamental for the quantum information [97] and the quantum simulation studies [98]. For example, the chemical reaction could be tuned by Feshbach resonance [99, 100] and controlling the geometry of the systems the inelastic collisions could be suppressed [101, 102].

Ultracold polar molecules are promising candidates in the field of quantum computation. The long-range dipolar interactions make them particularly useful for the quantum gate operations [103–106]. The nuclear spin states of the singlet ro-vibrational ground state of hetero-nuclear polar molecules have been employed to encode and store quantum information. The hyperfine states of the rotational ground state of the $^1\Sigma^+$ molecules of NaCs have been proposed for the qubit operations and to be employed for qubit storage [105]. The long-range dipolar interactions have been exploited to perform a controlled

quantum computation operation. The experimental techniques have been demonstrated to precisely control the quantum states, specifically, the hyperfine states of the ro-vibrational state of the polar molecules have been demonstrated [46,93,107,108] . These experimental achievements are important steps toward the preparing the quantum gates with a high degree of fidelity. Ultracold polar molecules confined in an optical tweezer array [109] has been demonstrated as a promising model system for quantum computation operations. Some specific superpositions of the hyperfine states of a singlet ro-vibrational ground state are insensitive to the magnetic field fluctuations as well as immune to the non-uniform optical potential. These properties result in a large coherence time between the ultracold polar molecules' quantum states, which is required for robust storage of qubits. A large coherence time between the quantum states is the key to perform a high-fidelity quantum computation. A long coherence time between the nuclear spin-sates has been observed for the hetero-nuclear polar molecules [110]. Enormous efforts have been put forward to minimize all the possible sources of the decoherence in ultracold polar molecules, and a large storage time of the quantum information has been observed [97, 111].

After the breakthrough in the field of ultracold polar molecules, it is a prime time for the quantum simulation employing polar molecules. A series of exceptional experimental achievements: the creation of ultracold polar molecules in their absolute ground state [76, 78, 112], quantum state control of the ground state polar molecules [46, 93, 108], and the trapping of dipolar molecules in optical lattices [77, 101], make very promising advancement for the quantum simulation using hetero-nuclear polar molecules. The development of the single site and single-atom resolved quantum gas microscopy for bosons [113, 114], fermions [115–117], and for the molecules [118] is an accomplishment for the field.

Ultracold atoms are typically million times thinner than the air at standard atmospheric pressure. The dilute nature of the cloud of the ultracold atoms assists in reaching quantum degeneracy without forming a crystal. Still, it comes at a cost: the atoms required to be cooled to extremely low temperatures. A standard laser cooling and trapping

method is employed to reduce the temperature of neutral atoms to ∼100 μK in a magneto-optical trap (MOT) [24, 49, 119] from the room temperature atomic vapors. A subsequent evaporative cooling [120] stage of atoms in conservative traps brings the atoms to much lower temperatures (≈ 100-500 nK) to enter into the quantum degeneracy. For ultracold atoms, a conservative trap can be realized using a magnetic trap [121] or a far-detuned optical trap [122]. In the conservative trap, the atoms with higher kinetic energies are forced to leave the trap, and the atomic cloud obtains a new equilibrium with a lower mean velocity. When a sufficient amount of energy has been extracted from the system, the remaining atoms become cold enough to enter quantum degeneracy. In a magnetic trap, the evaporative cooling is performed using radio frequency (RF) [1–3, 121], and in an optical trap, this is realized by reducing the power of the trapping beams [123, 124].

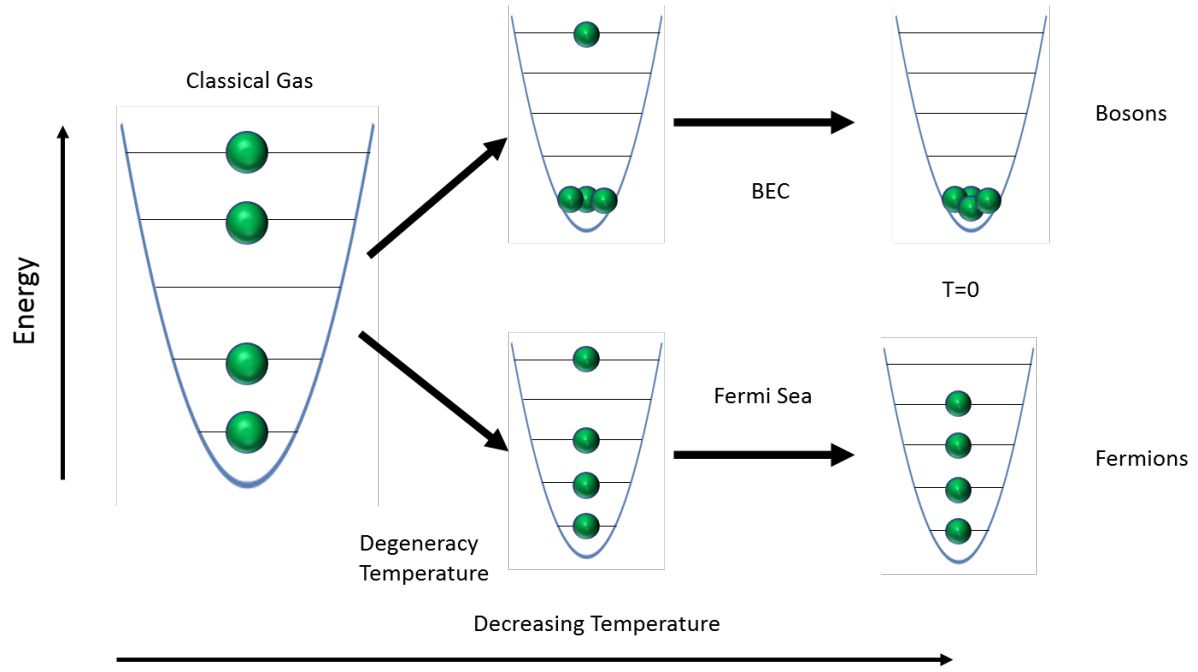


Figure 1.1: Behavior of Bosons and Fermions in harmonic trap at different temperatures. At high temperatures, both type of particles behave classically. At lower temperature the the quantum statistical nature comes into play and the particles follow different quantum statistics.

Quantum degenerate gases

Indian physicist Satyendra Nath Bose published an article on photon statistics [125] in 1924. Following this work, Albert Einstein predicted a new state of matter: Bose-Einstein condensate. In a system of ideal Bose gas, when cooled below a critical temperature, a significant number of atoms occupies the lowest possible quantum state. Frtiz London emphasized that the observation of superfluidity in liquid Helium [126] below 2.19 K is the manifestation of Bose-Einstein condensation. This study was a strong evidence of the fact that the BECs could occur in real systems, where inter-particle interactions are ubiquitous.

The journey of the ultracold atoms has been started with the revolutionary idea of laser cooling and trapping of neutral atoms [24]. The first demonstration of laser cooling was awarded with a set of Nobel prizes in 1997. It was soon realized that the spontaneous emissions and absorptions of photons associated with the absorptions of the near-resonant laser light imposed limitations on the lowest possible temperature and maximum density that can be achieved in a MOT [127]. In the following years, many important developments took place to overcome these limitations. The realization of the temperatures of the laser-cooled atoms below the Doppler cooling limit was reported in [127]. The experimental techniques which demonstrated that the atoms could be cooled to temperatures below recoil limit are velocity selective coherent population trapping [27] and Raman cooling [28] in two dimensions. The realization of dark-spot MOT [29] demonstrated that the density of the atoms could be increased up to 10^{12} atoms/cm^3, which was limited typically around 10^{11} atoms/cm^3 in a standard MOT. The evaporative cooling technique [30, 31], when employed on alkali atoms, reduces the temperature of the atoms and increases the phase space density by a few orders of magnitude [128]. All these years of efforts culminated in the accomplishment of the observation of BEC in alkali atoms [1–3] in 1995 which was rewarded with the Nobel prize in 2001.

After realizing BEC, intensive efforts were put forward to obtain degeneracy in Fermi

gases. One of the major challenges in reaching the quantum degeneracy in Fermi gases is the breakdown of the evaporative cooling scheme for single-species spin-polarized fermions. This phenomenon occurs due to the vanishing s-wave collisional cross-section for identical fermions in the same spin state and makes the evaporative cooling of single species of fermions ineffective. The community's dream became true through the pioneering work by DeMarco and D. Jin in JILA in 1998, the group first time observed Fermi degeneracy [4]. The Fermi degeneracy has been realized by using the concept of s-wave collisions between a mixture of two spin states of fermionic ^{40}K atoms, which is permissible according to the Pauli exclusion principle. Another experimental route to obtain Fermi degeneracy is to trap the fermions with bosons and evaporatively cool the bosonic species. The non-zero collisional cross-section between bosons and fermions re-thermalizes the fermionic cloud and reduces their kinetic energy, which is known as sympathetic cooling. When the fermions are cooled below the Fermi temperature, they enter into Fermi degeneracy [5].

Quantum degenerate gas mixtures

The experimental discoveries of the quantum degeneracy of alkali atoms paved the way for studying quantum degenerate mixtures of two different atomic species. There has been a growing interest in the quantum degenerate mixtures both in experimental [33–35,65,129,130] and theoretical [36–38] perspectives. The Bose-Fermi quantum degenerate mixture systems are ubiquitous in nature. The quantum degenerate mixture experiments [39, 40] offer a well-controlled system to simulate and investigate the phenomena present in condensed matter physics.

Specifically, a quantum degenerate Bose-Fermi mixture offers to study a plethora of quantum many-body phases [131]. The bosons-mediated pairing of fermions via the Bose-Fermi interactions can also be studied [131–135]. It has been proposed that the Bose-Fermi interspecies interactions could enhance the critical temperature for the BCS transition [133]. Intensive experimental efforts have been put forward to precisely control the interspecies interactions in the Bose-Fermi mixtures [129, 136, 137]. Therefore, a mix-

ture of the Bose-Fermi ultracold system is a potential system to simulate the underlying dynamics of the phonon-mediated pairing of electrons.

A self-bound system is a unique field to study, which is quite common in the universe. It ranges over a vast scale, from the nanoscale to the cosmological scale, such as the atomic nuclei to the astronomical objects like neutron stars [138]. The stabilization mechanism of a droplet is universal: it is an interplay of an attractive force and a repulsive force that stabilizes these exotic self-bound phases. A quantum droplet is a very recent development in the field of ultracold atoms. The formation of a quantum droplet manifests a delicate balance between an attractive force between the atoms, which holds them together, and a repulsion, which stabilizes the atoms against collapse. This exotic quantum phase is beyond the scope of a single species quantum degenerate gas of atoms, where the underlying interactions are either repulsive or attractive in nature. In the seminal paper [139], Petrov predicted a self-bound quantum droplet phase in a quantum degenerate mixture of Bose-Bose atoms. The attraction originates from a mean-field term, and beyond mean-field effects arise due to quantum fluctuations, which stabilizes the droplet against the collapse, to first order it leads to Lee-Huang-Yang (LHY) repulsive energy [140].

The experimental realizations of the quantum droplets [141,142] in the quantum degenerate mixture of ^{39}K atoms is a direct demonstration of the scenario suggested by Petrov. In the experiments, the mixture of ^{39}K atoms is prepared in the two hyperfine states of the absolute ground state, namely $|F = 1, M_F = 0\rangle$ (state-1) and $|F = 1, M_F = -1\rangle$ (state-2). The intraspecies scattering lengths a_{11} and a_{22} are positive (repulsive interaction), while interspecies scattering length a_{12} is negative (attractive interaction). The magnitude of the scattering lengths is tuned by employing magnetic Feshbach resonances. The magnetic field is tuned to a value such that the LHY correction term is comparable to the mean field interaction, which results in the formation of the self-bound quantum droplet. Experimentally, the occurrence of the quantum droplet was verified by measuring the size of the droplet. Without any trapping, the droplet retains its size over $\sim 20\,\mathrm{ms}$.

The Quantum droplet phases have been predicted in a Bose-Fermi mixture [143]. In a Bose-Fermi mixture, the attraction between boson and fermion would be balanced by the repulsive Fermi pressure, which corresponds to the LHY correction. This would result in the formation of the quantum droplet in the quantum degenerate Bose-Fermi mixture. Recently, quantum droplet phases have been realized in hetero-nuclear Bose-Bose mixture of ^{23}Na and ^{87}Rb [144].

Real condensed matter systems are not defect free. The impurities are one of the main reasons for the dissipation of the conductivity in a superconductor [145]. A quantum degenerate mixture offers an exceptional model system to explore impurity physics. In an optical lattice, one of the atomic species (majority) could be made superfluid by carefully choosing the wavelength of the optical lattice, tuning the interactions using Feshbach resonances, and the lattice depth. By adding the other species (minority) in a controlled way in the given optical lattices, it could be made localized (depending on the atomic species). The interspecies interactions between majority and minority species result in a change in the trapping potential at the position of the minority atoms. The change of the potential trapping acts as a defect to the bath of the superfluid [146]. Therefore, a quantum degenerate mixture offers the study of the phenomena of the disorder induced localization in a controlled way.

The dimension of a system plays an important role in the underlying dynamics of the system and in reduced dimensionality, quantum degenerate mixtures predict novel quantum phases to occur, such as charge density wave [43, 147–149], supersolidity [150], and boson induced unconventional superfluidity [151].

Till now we have been considering the quantum phases realized in a quantum degenerate mixture of atoms, where the underlying dynamics is governed by the short-ranged interactions, $\sim \frac{1}{R^6}$, where R is the interatomic distance.

On the other hand, there is an ever-growing interest in the field of AMO physics in studying the long-range interactions. One way to introduce the long-range interactions is the dipole-dipole interactions, where the interparticle interaction goes as $\sim \frac{1}{R^3}$. A

plethora of exciting exotic quantum phases [17,21,85,152] have been predicted in quantum degenerate systems with dipole-dipole interactions. The interaction potential between two dipoles is read as [21],

$$V_{dd} = \frac{C_{dd}}{4\pi}\frac{1-3cos^2(\theta)}{R^3} \tag{1.1}$$

Where C_{dd} is the dipole-dipole coupling constant, θ is the angle between the direction of quantization axes and the relative separation between the dipoles, and d^2 is the dipole-dipole coupling constant. In the case of electric dipoles, C_{dd} will be $\frac{d^2}{\epsilon_0}$, where d is the electric dipole moment of the particle and ϵ_0 is the permittivity of the free space. While in the case of magnetic dipoles, C_{dd} will be $\mu_0\mu^2$, where μ_0 is the permeability of the free space and μ is the magnetic dipole moment of the particle.

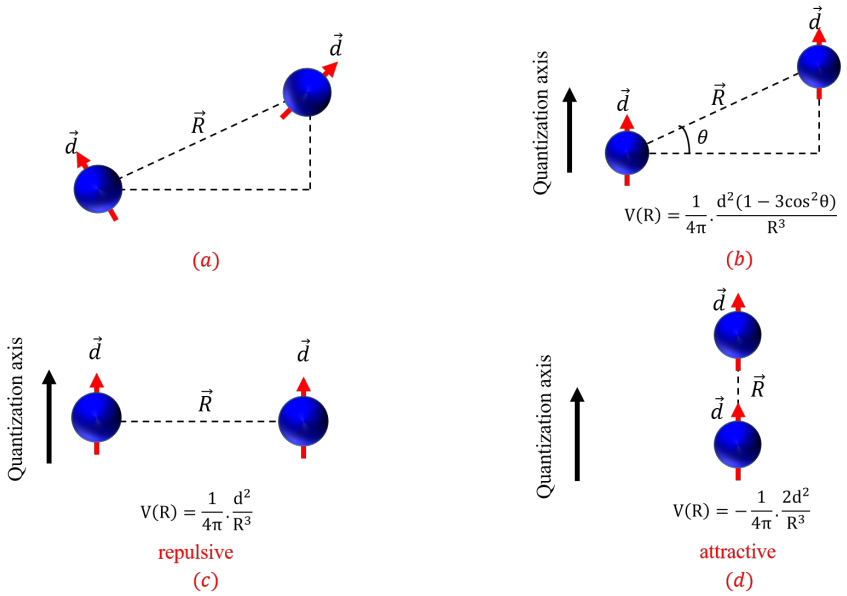


Figure 1.2: The schematic diagram showing geometry of the dipole-dipole interactions. (a) un-polarized case: the dipoles are interacting without the presence of applied field (b) polarized case: the interaction of the dipoles in presence of the applied field, the direction of the applied field is the quantization axis of the system (c) Two polarized dipole placed side-by-side repel each other. (d) Two polarized dipoles placed in a head-to-tail geometry attract each other.

The main characteristics of the dipole-dipole interaction are the long-range ($\sim \frac{1}{R^3}$) and the anisotropic nature of the interactions. The strength of the dipole-dipole interaction is represented in terms of a length scale: dipole-dipole interaction (DDI) length [153],

$$a_{dd} = \frac{C_{dd} m_r}{4\pi\hbar^2} \tag{1.2}$$

Where m_r is the reduced mass of the pair of particles. This length scale quantifies the spatial range of dipole-dipole interaction. In the case of the hetero-nuclear polar molecules, we have,

$$a_{dd} = \frac{d^2}{4\pi\epsilon_0} . \frac{m_r}{\hbar^2} \tag{1.3}$$

Fully polarized NaK molecules [154] in the absolute ground state has the electric dipole moment, $d = 2.72$ Debye [47]. The dipolar length corresponds to $a_{dd} \approx 1.5\,\mu m$. To put this value into perspective, let us consider the lattice spacing of an optical lattice created from a 1064 nm laser; the lattice spacing is 532 nm or $\sim 0.5\,\mu$m. This comparison gives a flavor that trapped polarized ultracold polar molecules in an optical lattice would exhibit few to many body-body interaction dynamics.

There have been intensive experimental activities in the recent past to produce degenerate quantum gas of the alkaline earth (chromium) [155] and rare-earth metals: Dysprosium [156] and Erbium [157]. These atoms possess very large magnetic moments, making them promising candidates for magnetic dipole-dipole interactions. Experimental observations of the quantum magnetism [158], quantum droplets [159], ferrofluid [160], and supersolidity [159] phases have realized by employing the degenerate quantum gas of these magnetic atoms.

The dipole-dipole interactions originating from the internal magnetic moment of the atoms are relatively weak compared to the electric dipole moment of the absolute ground state molecules. For example, we can take the ratio of the coupling constants of the electric and magnetic dipole-dipole interaction, which provides the relative strength of the interactions. We use the expression, $\eta = \frac{\frac{d_e^2}{\epsilon_0}}{\mu_0 \mu^2}$ to compare the strength of the interac-

tions. Dysprosium has magnetic dipole moment $\mu \sim 10\,\mu_B$, and for typical electric dipole moment of $d \sim 1\,\text{Debye}$, we obtain $\eta \approx 100$.

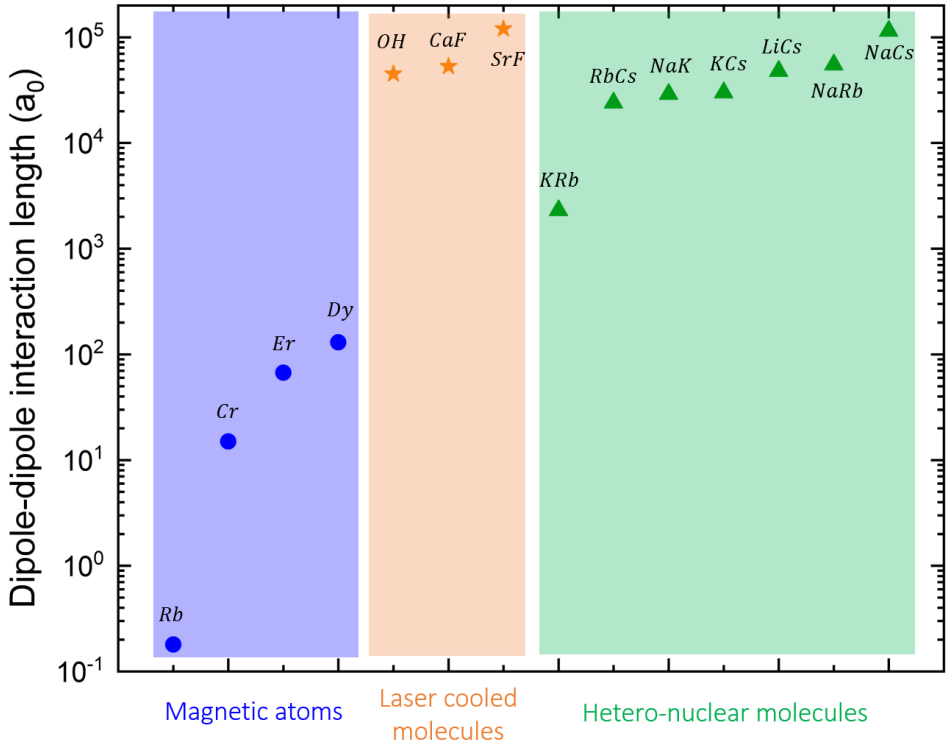


Figure 1.3: The comparison of the strength of the dipole-dipole interaction (DDI) in magnetic atoms (dot), laser-cooled molecules (star), and the hetero-nuclear molecules in their absolute ground state(triangle). The DDI strength has been expressed in terms of the characteristic length in the units of the Bohr radius (a_0). To put it in a perspective, the lattice spacing of a 1064 nm optical lattice is $532nm \approx 10^4 a_0$.

Figure-1.3 shows the comparison of the dipole-dipole strength in terms of the characteristic length scale: dipole-dipole interaction(DDI) length. We have compared the DDI length of the magnetic atoms(Cr, Sr, and Dy, etc.), the laser-cooled molecules(e.g., OH, CaF, etc.), and the hetero-nuclear polar molecules (KRb, Nak, etc.) in their absolute ground state. To estimate the length scales, we have compared the DDI lengths with the optical lattice spacing of a 1064 nm laser, which corresponds to $10000a_0$. The above

comparison shows that the electric DDI strength is orders of magnitude higher than the magnetic DDI strength.

Therefore, ultracold molecules in their absolute ground state are the holy grail in exploring the many-body quantum dynamics. A considerable amount of progress is going on to cool and trap the molecules, such as CaF [161], SrF [162] and so on. Numerous amount of techniques have been demonstrated in cooling the molecules: buffer gas cooling [163], stark [164] and Zeeman deceleration [165]. Direct laser cooling and trapping of molecules have been realized in magneto-optical trap [162, 166]. In addition, trapping of the molecules has been achieved in magnetic trap [167] and in pure optical trap [168]. The temperature and the phase-space density achieved in the cooling and trapping of the molecules are at present far from the quantum degeneracy limit. The evaporative cooling of the molecules has been employed [161, 169] to cool the molecules further. Therefore, the recent progress in the field is very promising.

The electric dipole-dipole interaction in hetero-nuclear molecules has a very large strength as shown in Figure-1.3. The electric dipole moment in a hetero-nuclear molecule is not permanent. The dipole moment could be induced in the presence of an external electric field [154]. This property of the hetero-nuclear molecules has a significant implication in the experiments and provides the experimentalist a knob to tune the interaction strengths.

The experimental realization of the creation of the ultracold polar molecules in the absolute ground state has taken a different route rather than the direct cooling of the molecules. This remarkable experimental technique was first pioneered in JILA by the Jun Ye and Deborah Jin group to create KRb molecules in their absolute ground state [76]. The typical procedure followed is as followed. A Feshbach resonance [63] is employed to a quantum or near quantum degenerate mixture of atoms, which creates a weakly bound molecular state, followed by a STImulated Raman Adiabatic Passage (STIRAP) [170]. The STIRAP is a coherent two-photon process that transfers the weakly bound molecules to the deeply bound molecules in its absolute ro-vibrational ground state [76].

An enormous amount of experimental progress have been made with many combinations of the alkali atoms to produce the hetero-nuclear molecules in their absolute ground state: LiCs [171], RbCs [77, 172], fermionic NaK [78, 173], NaRb [174], bosonic NaK [79], and NaCs [112].

Molecules	Chemically stable	Dipole moment (Debye)	Dipolar length (a_0)
KRb	× [175, 176]	0.56 [76, 81]	2.3 $\times 10^3$
LiCs	× [175, 176]	5.5 [81, 177]	4.8×10^4
RbCs	✓ [175]	1.28 [172, 177]	2.4×10^4
NaRb	✓ [175]	3.3 [81, 178]	5.5×10^4
NaK	✓ [175]	2.72 [47, 178]	3 $\times 10^4$
NaCs	✓ [175]	4.6 [178]	11 $\times 10^4$
KCs	✓ [175]	1.9 [81, 177]	3 $\times 10^4$

Table 1.1: The description of the chemical stability, dipole moment in absolute ro-vibration ground state of the hetero-nuclear polar molecules. The dipole-dipole interaction length has been calculated using Eqn.1.3 and represented in terms of the Bohr radius, $a_0 = .052 \times 10^{-9}$m.

The hetero-nuclear KRb molecules in their absolute ground state are not chemically stable: the collision resulting $K_2 + Rb_2$. This chemical reaction is exothermic, leading to a significant loss of the ultracold KRb molecules from the trap [95]. Zuchowski et al. [175] studied the collisional dynamics of alkali-metal dimers and predicted stable hetero-nuclear ultracold polar molecules: NaK, NaRb, NaCs, KCs, and RbCs. Table-1.1 lists the chemical stability, electric dipole moment, and the dipolar length of the hetero-nuclear polar molecules.

In particular, the ultracold NaK in their absolute ro-vibrational ground state is stable against the dissociative chemical reaction, i.e., $2NaK \neq Na_2 + K_2$. Therefore, they display a large lifetime [179] (few seconds) in optical potential, which is of fundamental

importance for quantum computation and quantum simulation studies. In addition to the longer lifetime, the NaK molecules in their absolute ro-vibrational ground state exhibit a large induced electric dipole moment, ∼2.7 Debye [47]. The large dipole moment corresponds to a large interaction energy in the cloud of the ultracold NaK molecular system. Therefore, the dynamics of the system is governed by long-range dipole-dipole interactions. A detailed study of the spectrum of the Feshbach resonances has been performed for both fermionic [129, 180] and the bosonic [65] NaK molecules. Intense experimental efforts have been given to demonstrate an effective pathway for the two-photon STIRAP protocol to transfer the weakly bound Feshbach NaK molecules to the deeply bound absolute ground state for both fermionic [173,179] and the bosonic [181] NaK molecules. Years of hard work paid off with experimental observation of the absolute ro-vibrational ground state for both fermionic [78] and bosonic [79] NaK molecules. The quantum degenerate cloud of hetero-nuclear ground state polar molecules [102,182,183] has been achieved very recently. This opens up the door to the study of quantum ferrofluid [90], dipolar superfluid [184], quantum droplet and dipolar supersolidity [185] and many other unexplored exotic quantum phases.

Experimental pathways towards the quantum degenerate gases

Laser cooling and trapping technique [24] has become a powerful tool for preparing an ensemble of ultracold atoms at temperatures down to micro Kelvin. It depends on the radiative scattering force that uses the momentum transfer between a near-resonant radiation field and an atom by exploiting the Doppler effect. The radiative scattering force, in the presence of a near-resonant light field and an anti-Helmholtz magnetic field, can be made velocity and position-dependent.

Due to the spontaneous emissions, the photon recoil opposes the cooling process in a MOT which leads to the diffusion in the velocity space and, therefore, heating the atom. This heating mechanism balances the above-described cooling, which restricts the temperature of the atoms in a MOT to a limit.

The temperature of the atoms is further reduced in a conservative trap by employing evaporative cooling [120]. The most simple conservative magnetic trap can be constructed by using quadrupole magnetic field configuration, which has a zero field at the center. When atoms go to the region near the zero field, a Majorana spin-flip occurs and the atom is lost from the trap. Therefore, to prevent the atom loss, modified magnetic trap geometry is typically used. The first BEC experiment [1], carried out at the JILA, employed a time-averaged orbiting potential (TOP) trap, where a rapidly rotating uniform bias magnetic field is superimposed onto the quadrupole magnetic field. The time average of the resulting instantaneous potential yielded a harmonic-like potential. In MIT, the BEC experiment [3] has been performed in a plugged trap, where a repulsive potential has been superimposed with a quadrupole magnetic trap so that the atoms will be repelled from the trap center. This trap configuration is realized by focusing a blue-detuned laser beam through the center of the quadrupole trap. Many groups had employed modified magnetic traps for the degenerate experiments, namely Ioffe-Pritchard trap [186], Quadrupole -Ioffe configuration (QUIC) trap [121, 187].

The mechanism of evaporative cooling is based on the preferential removal of atoms

with energies higher than the average energy of a trapped sample and the re-thermalization of the remaining atoms by elastic collisions. The basic mechanism of evaporative cooling is as follows: the total energy of an atom in a magnetic trap is the sum of kinetic and potential energy. As the atom moves away from the trap's center, the kinetic energy is converted to potential energy. The atoms with higher total energy have turning points in the regions of the trap further away from the center. Driving the atomic transitions at this energy, from trapped to untrapped states, removes the hotter atoms from the trap. The system must re-thermalize to a lower temperature before iterating the process. This process of continuously decreasing the temperature of the sample as shown in Figure-1.4, at the expense of losing higher energy atoms, is known as forced evaporation.

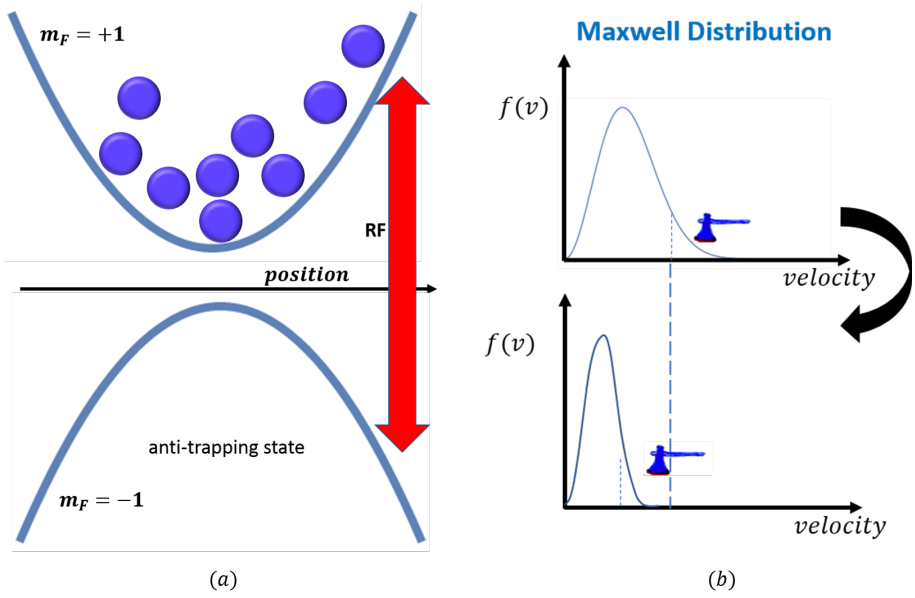


Figure 1.4: The schematic of Radio frequency(RF) evaporation of the atoms trapped in a magnetic trap. The atoms in $M_F = +1$ states are trapped, while $M_F = -1$ is the anti-trapping state, here we have assumed $g_F > 0$. A RF field flips the spin of the atoms from $M_F = 1$ to $M_F = -1$ state. Atoms with higher kinetic energy execute a larger orbit in the trap. Therefore, the RF evaporative cooling is initiated at a higher frequency and gradually reducing the frequency, as a result the atoms with higher K.E. are deterministically removed from the trap and remaining atoms re-thermalized to a lower temperature. (b)The evaporative cooling is chopping out the higher distribution tail of the Maxwell-Boltzmann distribution and resulting in lower temperature.

1.1 Instrumentation

Ultra cold atom experiments are challenging by its nature. These experiments employ a plethora of highly sophisticated and sensitive instruments. In this section, I will give a general overview of some of the instruments we routinely use in the laboratory to conduct a ultracold atomic physics experiment.

1.1.1 Acousto-optic modulator

An acoustic-optic modulator (AOM) is used to precisely control and modulate the frequency and intensity of a laser beam. An AOM also provides a fast switching time for the laser beams. An AOM is made of an optically transparent material (e.g., TeO2, PbMo4) to which a piezoelectric transducer is attached. A RF signal drives the transducer to vibrate, which generates a traveling acoustic wave through the material.

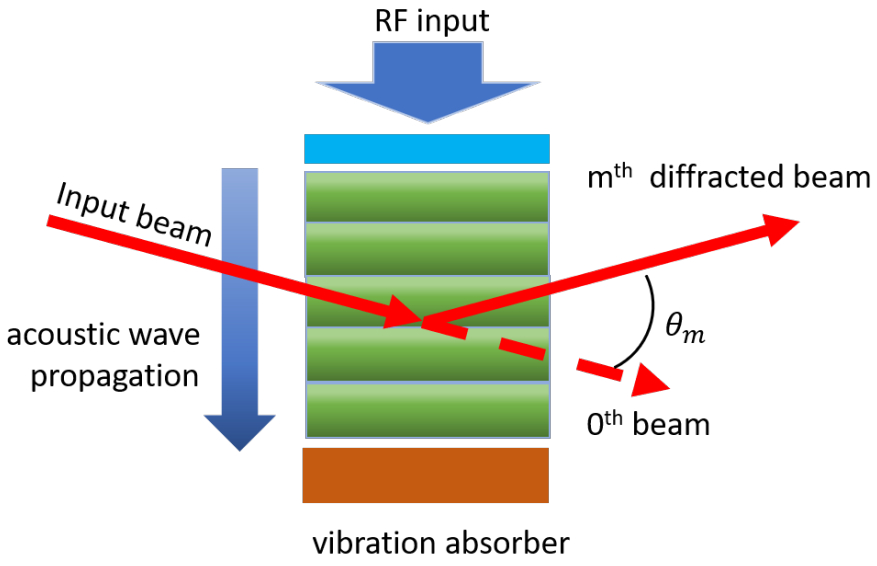


Figure 1.5: A schematic of an AOM. An RF signal produces a acoustic wave in the material which generates a dynamical grating in the material and the incident light gets diffracted into different orders.

The oscillating mechanical pressure of the acoustic waves induces a variation in the refractive index of the medium: thus, the AOM acts as a moving diffraction grating. If an

incident light beam of frequency ω_L interacts with an AOM operating at radio frequency Ω, the frequency of the mth order diffraction beam is given by-

$$\omega_{\pm m} = \omega_L \pm m\,\Omega \tag{1.4}$$

The beam diffracted at an angle θ_m, given by the Bragg formula,

$$\sin(\theta_m) = \frac{m\lambda}{2\Lambda} \tag{1.5}$$

Where Λ is the wavelength of the acoustic wave (depends on the frequency of the applied RF signal), and λ is the wavelength of the incident laser light, $\lambda = \frac{2\pi c}{\omega_L}$.

Double pass configuration

The frequency and intensity of the laser beam can be precisely tuned by changing the frequency and amplitude of the RF signal. The angle of diffraction also changes with the applied RF frequency, which makes it very inconvenient to use the first-order diffracted beam in the laser cooling experiments. To circumvent this issue, a double pass configuration has been implemented, as shown in Figure-1.6

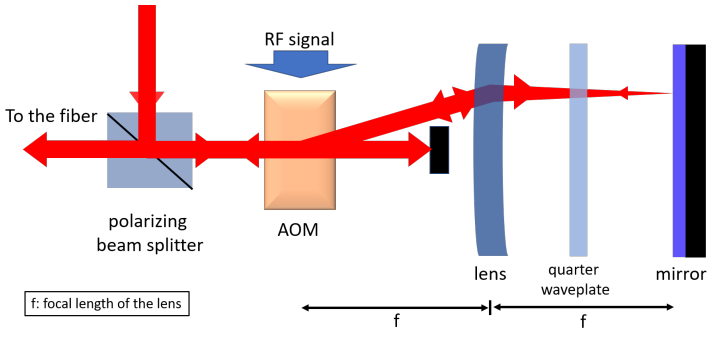


Figure 1.6: A Schematic of the double pass configuration using AOM. The reflected beam of a PBS is injected into an AOM. The first-order diffracted beam has been retraced back through the AOM using a combination of a lens and a mirror. The quarter-waveplate changes the phase of the polarization of the retraced beam by an amount π. Therefore, the retraced beam is out-coupled from the transmission arm of the PBS.

In this configuration, the first order diffracted beam is again sent through the AOM. The diffracted beam path is retraced back using a combination of a lens and a mirror. The alignment of the output beam doesn't change with the applied RF frequency, but the frequency of the output beam is shifted by an amount 2Ω. Therefore, this scheme allows a dynamical tuning of the frequency by varying the applied RF signal without changing the alignment.

Driver circuit for the acousto-optic modulators

Laser cooling and trapping of atoms require a precise control over the frequency and intensity of the laser beams used in the experiment. This is achieved by sending the laser beams through AOMs. The frequency and intensity of the diffracted beams are determined by operating frequency and the power of the applied RF signal to the AOMs. In our lab, the RF signal is generated by a customized driver circuit, the image of circuit is the shown in Figure-1.7. lists the components that comprised the AOM driver circuit.

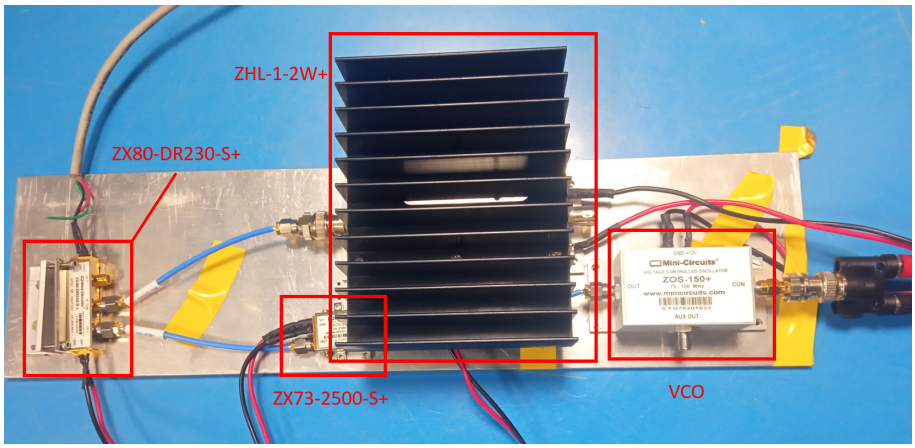


Figure 1.7: The image of the customize AOM driver circuit consisting of VCO, VVA, RF switch, RF amplifier.

Table- 1.2 lists the components have been used in the customized AOM circuit.

Component	supplier	Part number
Voltage control oscillator(VCO)	Mini circuits	ZOS-150+/ ZOS-300+
Voltage variable attenuator(VVA)	Mini circuits	ZX73-2500-S+
RF switch	Mini circuits	ZX80-DR230+
Amplifier	Mini circuits	ZHL-1-2W+

Table 1.2: Lists of the components used in the AOM driver.

The circuit consists of four components. The frequency of the RF signal controlled by applying an analog voltage to the voltage controlled oscillator(VCO). The voltage variable attenuator(VVA) regulates the power of the generated RF signal and the signal is fed into a RF switch. This allows fast switching of the RF signal. The RF signal is then fed into a fixed gain amplifier and the amplified signal ($\sim$ 1 Watt) is delivered to the AOMs via high bandwidth ($\sim$ 1 GHz) coaxial cables.

1.1.2 Electro-optic modulator

A laser cooling and trapping experiment requires a repumper beam in addition to the cooling beam (more details in Section-2.3). To generate a repumper transition for the sodium atom, which is 1771 MHz higher in frequency compared to the cooling transition, we have used electro-optic modulators (EOMs). We inject the cooling beam into an EOM which adds frequency sidebands (equal to the driving frequency of the EOM) on top of the cooling beam frequency.

A laser beam when injected into an AOM is diffracted into many orders: each order differs by an amount equal to the operating frequency from each other. Each order is spatially separated from each other (Eqn.1.5). On the other hand, an EOM adds frequency sidebands, different frequency sidebands are spatially overlapped on top of the incident beam but shifted in frequency. The principle of EOMs is based on the phase modulation of the incident light. The incident beam's phase modulation is obtained using

Pockel's effect [188]. The modification of the refractive index of a non-linear crystal by an applied electric field is proportional to the strength of the electric field.



Figure 1.8: The phase modulator EOM that we have employed in the experiment to generate the repumper frequency for the sodium atoms.

The refractive index of the non-linear crystal is modulated by applying a RF signal of frequency Ω to the crystal. The phase of the electric field of the incident beam (ω_L) is modulated when the light beam passes through the crystal. The electric field of the light beam becomes [189],

$$\begin{aligned} E &= E_0 e^{i(\omega_L t + \beta Sin(\Omega t))} \\ &\approx E_0 \times \left[J_0(\beta) e^{i\omega_L t} + J_1(\beta) e^{i(\omega_L + \Omega)t} - J_1(\beta) e^{i(\omega_L - \Omega)t} \right] \end{aligned} \tag{1.6}$$

Where, β is the depth of the modulation. The above form of the equation shows the modulated beam contains three frequency components. One component is the carrier, with a frequency same as the incident beam and two sidebands has frequencies $\omega_L \pm \Omega$. If the total power of the incident beam is P_0, then the power contained in the carrier is $J_0^2(\beta)P_0$ and power contained in each of the components of the first-order sidebands is $J_1^2(\beta)P_0$.

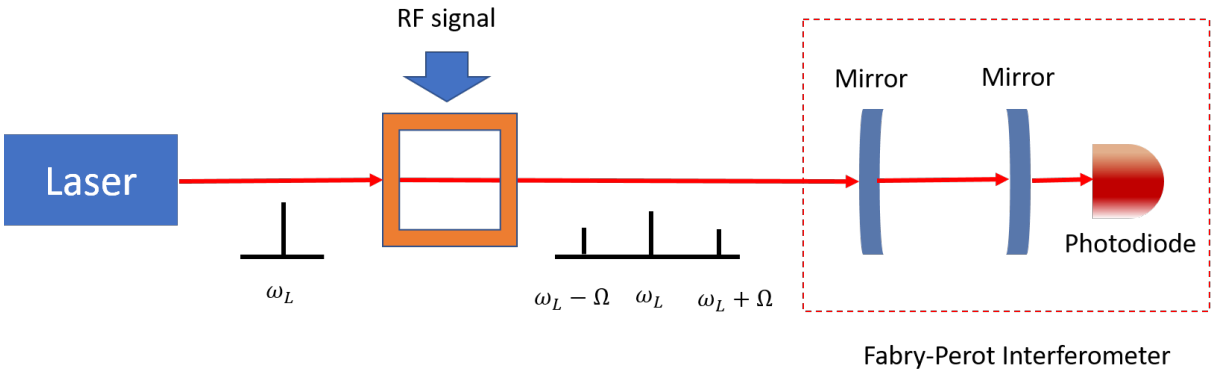


Figure 1.9: A schematic diagram of a phase modulation of incident light by an EOM. The phase-modulated beam from the EOM is injected into a Febry-Perot interferometer for characterization.

Figure-1.9 shows a laser beam of frequency ω_L incident on an EOM. A RF signal drives the EOM at a frequency Ω. The EOM generates two sidebands at frequencies $\omega_L + \Omega$ and $\omega_L - \Omega$ on top frequency ω_L of the incident beam.

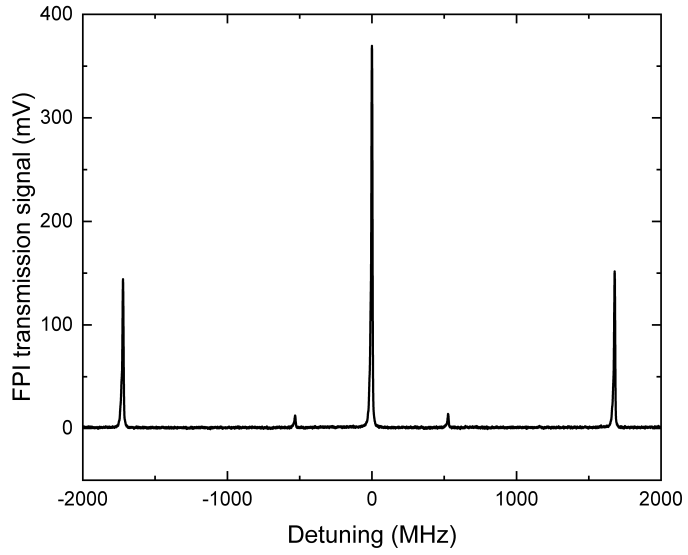


Figure 1.10: The transmission signal of FPI100. The Phase phase-modulated light from the EOM (PM-Na23-1.7-M3, QUBIG) is injected into the EOM. The carrier and the two sidebands are shown . The x-axis scaling has been done relative to the frequency of the incident beam and sidebands have been generated at ± 1725 MHz.

To characterize the modulated beam and determine the strength of the generated sidebands, we inject the EOM output beam into a Fabry- Perot cavity (FPI100, TOPTICA). We scan the separation between FPI100 cavity mirrors and monitor the transmitted signal on the photodiode. Figure-1.10 shows the transmission signal of FPI100 when the phase-modulated light of the EOM is injected into FPI100.

1.1.3 CMOS camera

We have used scientific CMOS camera for the quantitative measurements. A significant amount of measurements presented in this thesis have been performed by Quantalux CS2100M-USB (Thorlabs) by capturing the fluorescence of the 3DMOTs.



Figure 1.11: The CMOS CCD camera used in the measurements of the 3DMOTs.

It has 1920×1080 pixels with each pixel's size of $5\,\mu$m. It has a peak quantum efficiency of $\sim$61% at 600 nm.

1.2 Automation of the experiment

Laser cooling and trapping experiments require precise control over the experimental parameters and their timing sequence ($\sim \mu$sec). We control all the instruments employed in the experiment by LabVIEW from the control computer. The control computer is con-

nected to a PXIe chassis-1062Q, National Instruments (NI). The chassis contains analog (NI PXIe-6738) and digital cards (NI PXIe-6535). We generate all the analog and digital signals from these cards. The generated signals are connected to the respective ports of the instruments. The layout of the automation system is shown in Figure-1.12.

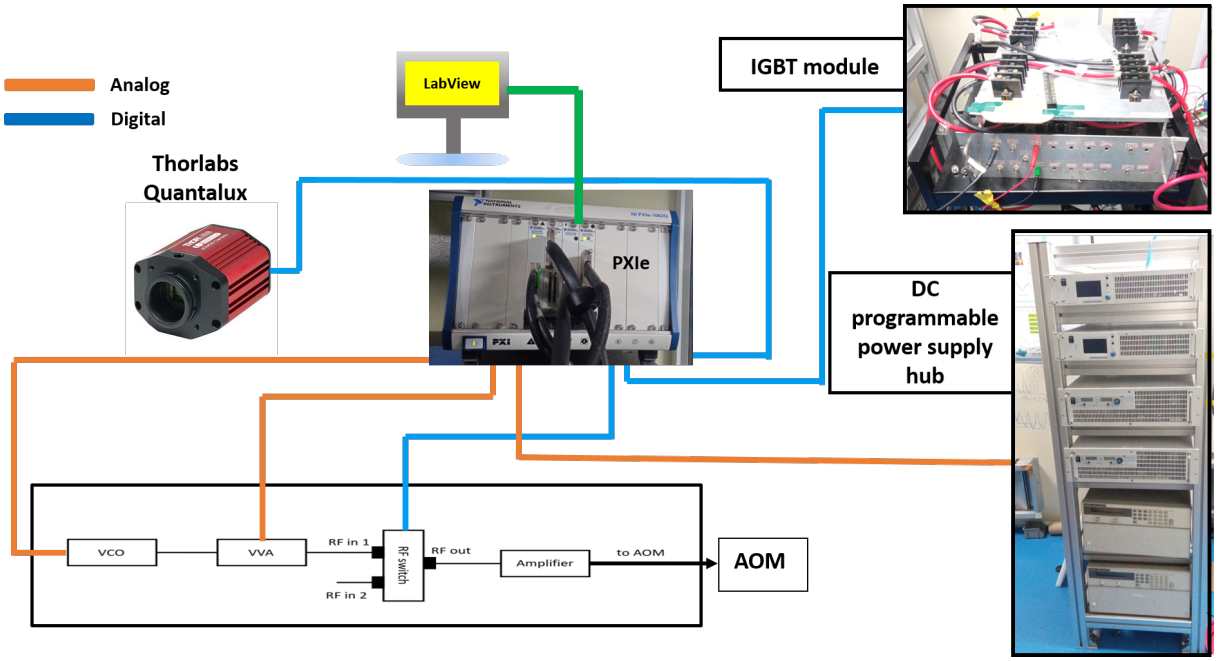


Figure 1.12: The automation layout of the experiment. We use the LabVIEW interfacing software from a host PC, which controls all the analog and digital cards installed in the PXIe chassis. The generated analog and digital voltages in turn controls the AOM's driver circuit, gate of the IGBT for switching the current in the MOT coils, the CCD camera and so on.

The precise timing of the switching on and off of the laser beams, such as the cooling, repumper, and imaging beams, and their frequencies and intensities, are obtained by controlling the respective AOM driver circuits. The frequency detuning and the power of the laser beams are dynamically controlled by applying the analog voltages generated from the PXIe to the VCOs and VVAs of the AOM circuits. The fast switching of the laser beams is obtained by driving the RF switch of the AOM driver with a digital signal generated from the PXIe.

The fast switching of current in the magnetic coils is obtained by using insulated gate

bipolar transistor (IGBT) based switching circuits. A digital signal from PXIe opens and closes the gate of the IGBT and provides fast switching of the current in the coils. We exploit the analog interfacing of the high-current programmable power supplies and control the magnitude of the current in the coils by feeding the analog voltages generated from the PXIe to the interfacing ports.

Figure-1.13 and Figure-1.14 show the the control panel of sodium and potassium 2DMOT and 3DMOT.

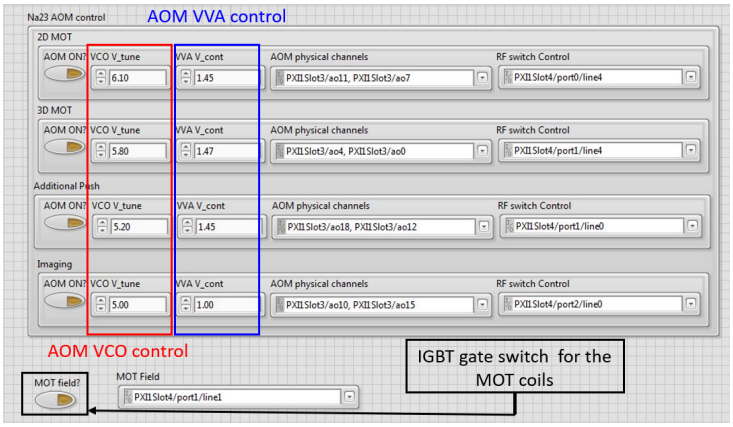


Figure 1.13: Control panel of the sodium MOT in the LabVIEW.

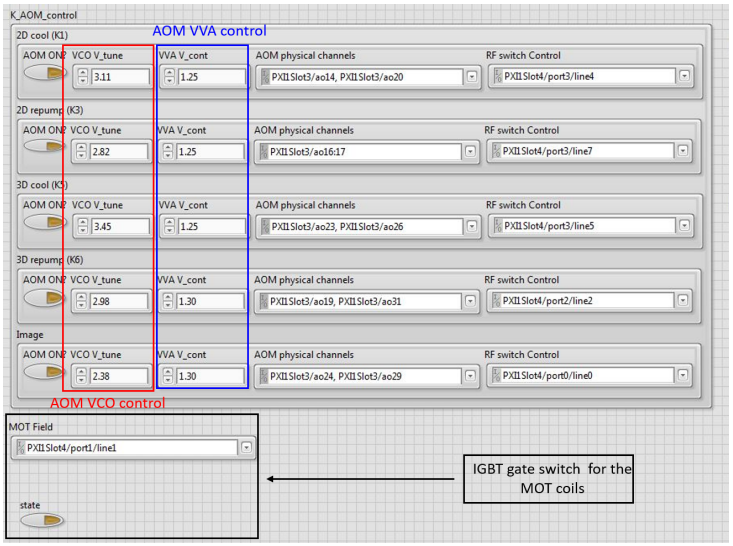


Figure 1.14: Control panel of the potassium MOT in the LabVIEW.

1.3 Aim of this thesis

This thesis reports the design, construction, characterization of a compact, versatile experimental setup to experimentally study a dual species ultracold gas mixture.

1. In Chapter-2, I shall give a through and comprehensive description of the state-of-the-art experimental system that I have built during the course of this thesis work. This includes the design and installation of the ultrahigh vacuum system, the description of the laser systems for laser cooling and trapping of neutral sodium (^{23}Na) and potassium (^{39}K) atoms.

2. In Chapter-3, I shall give a overview on the mechanism of the laser cooling and trapping of neutral atoms in a magneto-optical trap(MOT). I have given a detailed description of the numerical simulation we have performed to model the cold and collimated atomic beams sources: 2D^{+}MOTs for sodium and potassium atoms.

3. In Chapter-4, I shall describe the detection schemes I have implemented to observe the cold atoms of sodium and potassium atoms. In the following discussion, I have described our experimental observation of the characterization of the system. I have described the experimental study of the light-assisted interspecies collisional dynamics of cold and trapped sodium and potassium atoms.

4. In Chapter-5, I described in detailed the design, construction, and installation of a magnetic transport assembly. The magnetic transport scheme aims to transfer the cold and trapped cold atoms from our three dimensional MOT (3DMOT) ultra-high vacuum chamber to the “science cell” for the future experiments.

Chapter 2

Construction of the sodium-potassium cold atom experiment

This chapter describes the design and the implementation of a new state-of-the-art experimental apparatus that simultaneously cooling and trapping neutral sodium and potassium atoms in a two-species degenerate quantum gas experiment in our group, QuMix Laboratory, Raman Research Institute, Bangalore. The entire experiment facility has been conceived, designed, and constructed, starting with the work of this Ph.D. thesis. Therefore, this thesis documents the details of this experimental system.

This particular chapter is organized as follows, in section 2.1, I shall discuss the general philosophy behind the experimental system. In section 2.2, I shall discuss the design, construction, implementation, and characterization of the ultra-high vacuum (UHV) system. In section 2.3, I shall discuss two independent lasers system (each for sodium and potassium atoms). In section 2.4, I shall discuss laser frequency stabilization for both sodium and potassium lasers: it includes the implementation of saturation absorption spectroscopy, locking of laser frequency, and the laser beams preparation using acousto-optic modulators (AOMs) and electro-optic modulator (EOMs). In section 2.6, I shall review the literature on different available cold atomic sources and discuss the design and construction of the atomic sources I developed for this experiment.

2.1 Philosophy behind the system design

In a gas, quantum degeneracy is achieved when the de-Broglie wavelength becomes comparable to the inter-atomic spacing. In this respect, the atoms must be cooled and trapped at extremely low temperatures. Most cold atom experiments employ a magneto-optical trap (MOT) [24, 49] for the pre-cooling stage, and a subsequent evaporation cooling [120] brings the atoms into the quantum degeneracy. We have decided to employ MOT, and our initial consideration has been to determine how to load the MOT most efficiently. In general, a MOT can be loaded from the background vapor [190] or from a beam of slow atoms [24]. The loading from a background vapor is comparatively easy to implement, but it has a limited trap lifetime due to the degradation of the vacuum. The vapor pressure must be high for the efficient loading of atoms into a MOT: therefore, it causes more collisional losses with the background thermal atoms.

A MOT loading from alkali dispensers [191–194], an atomic beam, generated from alkali dispenser source [195], light-induced atomic desorption(LIAD) [196–199], and the vapor generated by applying polarized voltage on solid-state alkali metal source [200] have been demonstrated. The above-mentioned methods can improve the MOT loading but still can't compete with the trapped atom's lifetime, the loading rate, and the total number of trapped atoms achieved using a beam of slow atoms [53, 201–203]. In a dispenser MOT loading, a loading rate $\sim 10^7$ atoms sec^{-1} and the total number of trapped atoms $\sim 10^8$ could be achieved with a limited lifetime of a few tens of seconds. On the other hand, a LIAD MOT loading could produce a loading rate $\sim 10^9$ atoms sec^{-1} and the trapped atom number $\sim 10^9$. In contrast, the MOT loading schemes based on slow atomic beam, in general, could produce orders of magnitude higher loading rates and a higher number of trapped atoms with a larger trap lifetime (a few hundreds of seconds) [204]. The experimental techniques [53, 202, 203], produce a slow atomic beam from a background vapor with pressure in the range of 10^{-8} –10^{-7} mbar. These techniques generate an atomic beam in a separate part of the vacuum system, and the MOT is developed in another part

having a much better vacuum. Both the parts are connected by a differential pumping tube: this allows to keep the MOT part in UHV. This mechanism loads the MOT with a higher loading rate but without deteriorating the MOT chamber UHV environment, thus allowing a higher number of trapped atoms and a longer lifetime of the trap. Considering all the above technical pros and cons, we have opted to design and implement $2D^+$ MOT-based 3D MOT loading for both atomic species.

After obtaining the MOT, to reach the degeneracy, evaporation cooling needs to be performed, which is a time-consuming stage (typically, it takes $\sim$ 30 sec). The ambient pressure surrounding the MOT is limited since all the atomic beams are directed to the MOT chamber. The restricted background pressure in the MOT section leads to a significant loss of the degenerate atoms and limits the lifetime of the magnetic or optical traps. Also, optical access is limited in the MOT vacuum chamber because there already exist three pairs of MOT cooling and repumping laser beams along with the detection beam, the presence of quadrupole coils, and so on. So it is desirable to transfer the trapped atoms to another section of the system ("Science cell", in our system) having a much better vacuum and more optical access for manipulation and detection of the degenerate cloud.

The smaller dimension of the "science cell" (in our case, it is $30\,mm \times 30\,mm \times 80\,mm$) allows us to place the quadrupole magnetic coils very close to the atoms, this provides a tighter confinement to the atoms. At the same time the smaller dimension of the "science cell" would give enough access to the imaging optics to be placed very close to the atoms, this yields a very high spatial resolution, a pre-requisite to image of individual atoms [113].

As a result, atoms will have a much better lifetime in the trap. In addition, magnetic transport added one more advantage; when the atoms are transferred and subsequent experiments are being carried out in the Science cell, the atoms can be loaded in the 3DMOT chamber. Therefore, the system will have a much better repetition rate of the experimental sequence.

The cold atoms can be transferred either using a moving optical dipole trap or using

moving magnetic trap. For optical transport, many techniques have been demonstrated, moving an optical lattice to transport a single atom [205] and a cloud of atoms [206], moving the dipole trap center by a lens mounted on a translational stage [207], and a static lens configuration by employing variable focal length lenses [208,209]. On the other hand, in a moving magnetic trap scheme, two configurations have been implemented. The first one employs time-varying currents in a static ensemble of pairs of coils [210–213]. The other one is based on a physical displacement of the trap coils [214,215]. The optical trapping volume induced by the dipolar forces is small (typically, beam waist $100\,\mu$m) compared to the magnetic trap (trap radius $\sim 1\,$mm). An efficient atom transfer using an optical transport requires the atoms to be cooled and spatially compressed by pre-evaporative cooling before the optical transport, and this process causes a significant atom loss. On the other hand, the atomic transport using magnetic force makes it possible to transfer atoms immediately after the MOT stage to better the vacuum. Based on these considerations, we have decided to implement magnetic transport similar to the schemes discussed in [210, 211, 213].

After scrutinizing the aforementioned considerations, We have designed the vacuum system carefully. The ultra-high vacuum system consists of four chambers: two spatially separated $2D^+$ MOT sections (each for sodium and potassium), one spherical octagon chamber for dual-species 3D MOT, and a separate glass cell (science cell).

2.2 The ultra high vacuum system

A vacuum system is integral to any laser cooling and trapping experiment. The collision between the background thermal atoms with the cooled and trapped atoms is one of the major reasons for the limited lifetime of the trapped atoms. By reducing the background pressure, We can minimize these collisions, hence can, reduce the atom loss from the trap. A ultra-high vacuum environment is extremely important for degenerate quantum gas experiments. In order to create and maintain the UHV, the vacuum system must be

leak-tight, sturdy, and bakeable to high temperatures. The size and shape of the vacuum system must be designed with great care to accommodate the magnetic coils and optics surrounding it. We should design the vacuum system with special care, mainly keeping in mind that the conductance between the vacuum system and the vacuum pumps must be large enough to have sufficient pumping speed. we have a high-pressure region in the source part ($2D^+$ MOT, in our case), and the conductance of the differential pumping tube connecting the source and the UHV part must be small.

Vacuum requirements

The ultracold atoms must be thermally insulated from the surroundings, and this is accomplished by holding them in a trap inside a UHV environment, isolated from any room temperature walls. The collision of the thermal background atoms with the cold and trapped atoms imparts energy to the trapped atoms, which is large enough to knock out the trapped atoms. Therefore, it is of utmost necessity to know the permissible range of background pressure for ultracold atomic experiments. The rate of background collisions per trapped atom is given by [120]-

$$R_{bg} = n_{bg}\,\sigma_{bg}\,v_{bg} \tag{2.1}$$

Where n_{bg}, σ_{bg}, and v_{bg} denote the density, collisional cross-section, and average thermal velocity of the background atoms. Considering the parameters of potassium atoms [216, 217], We can show that, to obtain a lifetime $\sim 100\,\text{sec}$ for the trapped atoms, it is necessary to keep the background pressure $\sim 10^{-11}\,\text{mbar}$. The detailed calculation of conductance of the differential pumping tubes is described in Appendix-A.1. The value of conductance for the differential pumping tube of sodium $2D^+$MOT is $0.043\,l/s$, and for potassium $2D^+$MOT is $0.038\,l/s$.

Set up of the experimental system

A high-flux atomic source must be used to load the MOT quickly. We have carefully designed the vacuum system to reconcile the need for fast loading with the need for an ultra-high vacuum environment. The result is the vacuum system shown in Figure-2.1. The system is segmented into two parts. In the first one, We have two independent $2D^{+}$MOT sections, each one for sodium and potassium atomic species. The other is a UHV section, including a 3D MOT section, magnetic transport, and a science cell. The system has five ion pumps and one titanium sublimation (Ti-sub) pump.

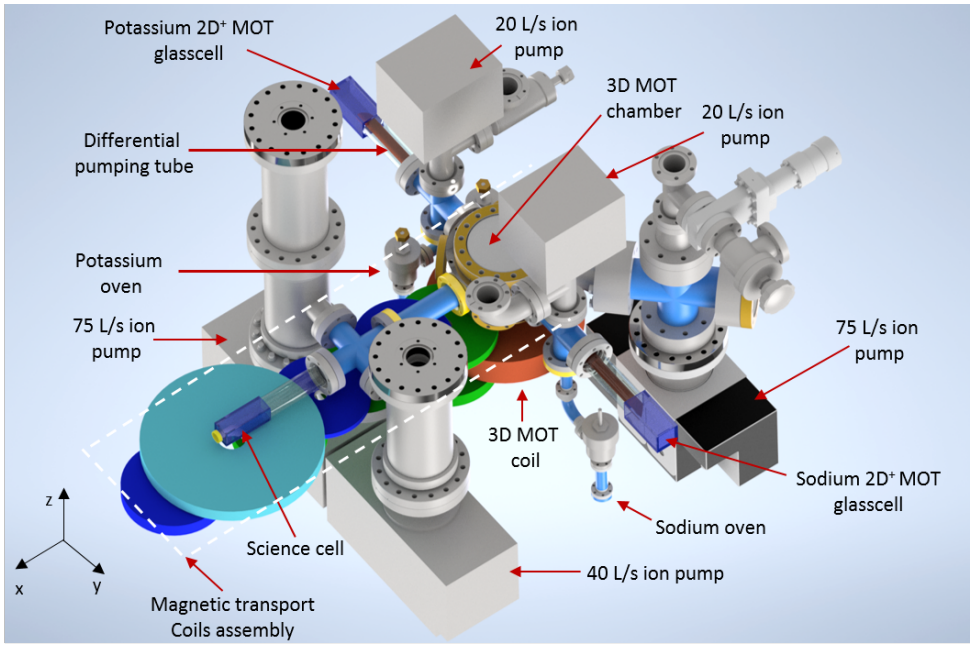


Figure 2.1: A 3D model of the vacuum setup. The dual-species 3D MOT is loaded from two counter-propagating $2D^{+}$ MOTs. A single-arm magnetic transport transfers the trapped atoms to the science cell.

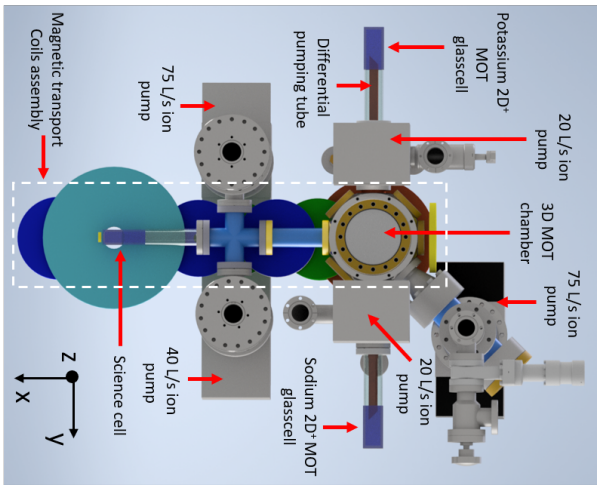


Figure 2.2: The top view of the 3D model of the vacuum setup. The dual-species 3D MOT is loaded from two counter-propagating $2D^+$ MOTs. A single-arm magnetic transport transfers the trapped atoms to the science cell.

$2D^+$MOT sections

The system has two independent $2D^+$MOT sections, each one for sodium and potassium atoms. The schematic of the setup is shown in Figure-2.3. It consists of an atomic sample part, a $2D^+$MOT glasscell, and a $20\,l/s$ ion pump. In the atomic sample part, we have a DN16CF (402000, MDC vacuum) full nipple, where We kept the atomic sample. One end of the full nipple is vacuum sealed by a DN16CF blank (110000, MDC vacuum), and another end is connected to a DN16CF angle valve (312015, MDC vacuum). The angle valve controls the flow of the atomic vapor into the $2D^+$MOT glasscell. It could also be used to isolate the atomic sample from the rest of the vacuum system during the replenishment of the atomic sample.

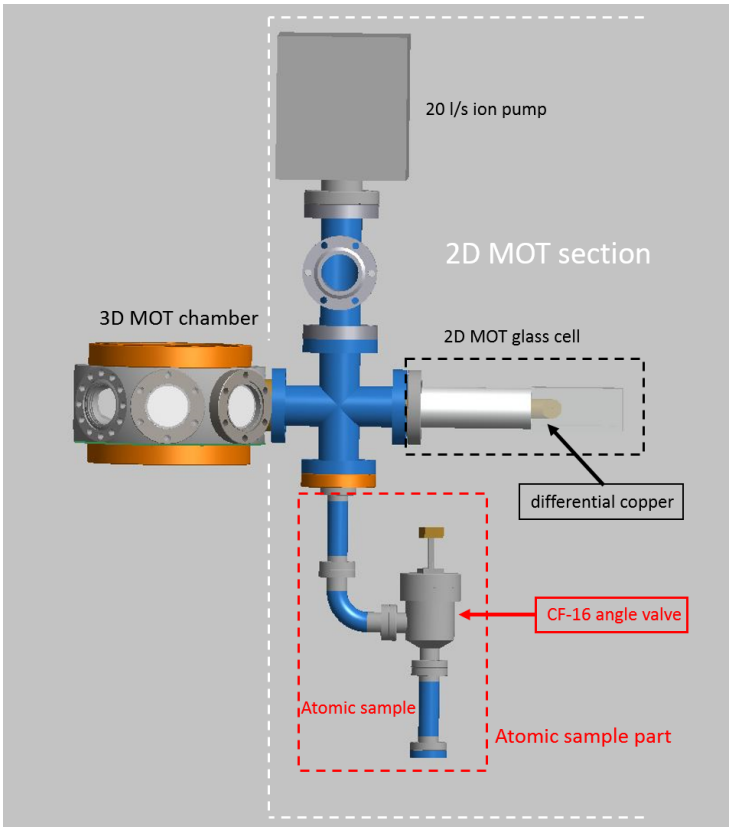


Figure 2.3: Schematic of the 2D$^+$MOT section. An atomic sample is kept inside the DN16CF I. The desired vapor pressure is obtained by heating the DN16CF I using heating tapes. The DN16CF gate valve controls the flow of the vapor into the 2D$^+$MOT glasscell, where an atomic beam is realized from the filled vapor.

The atomic sample part is connected to a DN40CF 4-way cross (405002, MDC vacuum). The vertical flange of the 4-way cross is connected to a $20\,l/s$ starcell ion pump (VacIon plus 20, Agilent) through a DN40CF Tee (404044, MDC vacuum). The 2D$^+$MOT glass is connected to one of the horizontal flanges of the 4-way cross. The entire 2D$^+$MOT section is connected to the 3D MOT chamber via the remaining horizontal flange of the 4-way cross. A differential pumping tube, manufactured from a block of oxygen-free high-conductive (OFHC) copper, with a hole at the center (that runs along the axis of the entire tube), is placed on the horizontal plane along the long axis of the glasscell. This differential pumping tube maintains $> 10^3$ pressure between the 2D$^+$MOT section and the 3D MOT chamber (UHV) and allows the cold atomic beam to pass through

from the 2D$^+$MOT side to the 3DMOT side. A turbo-molecular pumping station (ACT 600T, ALCATEL) is connected to the 2D$^+$MOT section through the horizontal flange of the DN40CF Tee. During the bakeout, the pumping station pumped out the 2D$^+$MOT section.

This vacuum setup consists of two spatially independent 2D$^+$MOT sections. One of the 2D$^+$MOT sections is dedicated to the natural abundance of sodium (262714-5G, Sigma Aldrich), and another one to the potassium atomic sources. The Potassium side has two independent atomic sample parts. Two atomic sample parts are connected together via a DN16CF Tee, and the combined part is connected to one of the flanges of the DN40CF 4-way cross of the 2D$^+$MOT section. One sample part contains a natural abundance of potassium (244856-5G, Sigma Aldrich), and the other one contains 10% enriched ^{40}K source (Precision Glass Blowing Incorporate, USA). The enriched source was delivered in a sealed glass ampoule, which needed to be broken inside the vacuum environment to avoid oxidation of the sample. So, we kept it inside a DN16CF full nipple with a stainless steel ball and crushed it under a vacuum by shaking the ball using a magnet from outside. All the DN16CF full nipples are wrapped with heating tapes to heat them sufficiently to generate operating vapor pressure inside the 2D$^+$MOT glass cells.

UHV section

This section is at the heart of the entire vacuum system and maintains a background pressure below 10^{-11} mbar. The UHV section can be divided into two parts. In the first part, a 3DMOT section combines a stainless steel spherical octagonal chamber (MCF600-SphOct-F2C8, Kimball physics), two DN100CF viewports (VPZL-600Q, Kurt J. Lesker), and five DN40CF viewports (VPZL-275Q, Kurt J. Lesker). This section is pumped out by a $75\,l/s$ ion pump (VacIon plus 75, Agilent), and the pressure is monitored by a nude Bayard-Alpert ion gauge (UHV-24P, Agilent).

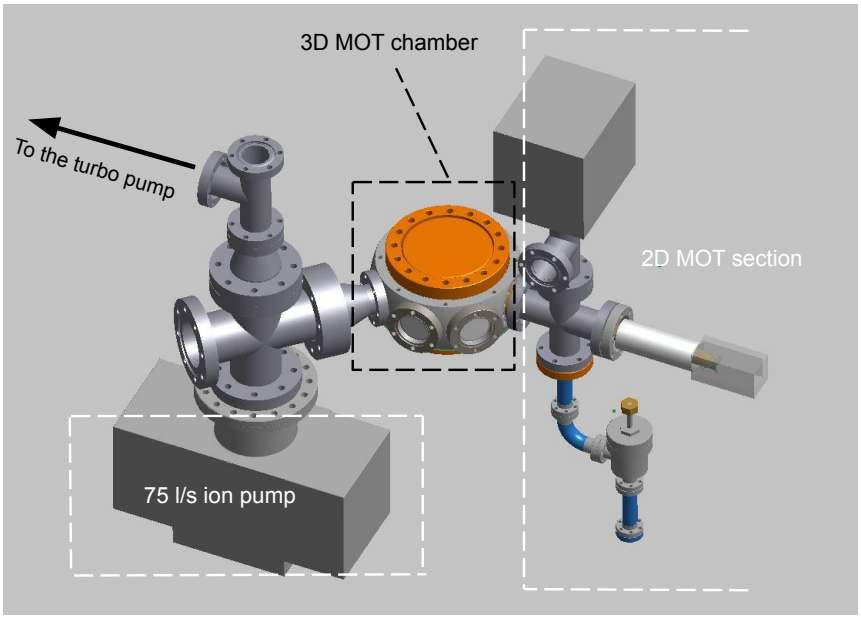


Figure 2.4: A schematic of 3DMOT section. A $75\,l/s$ ion pump and an ion gauge is connected to the 3DMOT chamber. Two $2D^+$ MOTs are connected to the chamber from two opposite DN40CF viewports.

The ion pump and the ion gauge are attached to a DN63CF four-way cross, and this combined part is connected to the 3D-MOT chamber through a DN63CF-DN40CF conical reducer. The reason behind using these vacuum parts is to obtain a high conductance between the ion pump and the 3DMOT chamber. Therefore, maintaining a high-pumping speed. Two $2D^+$MOTs are attached to the 3DMOT chamber from two opposite DN40CF viewports. The 3DMOT chamber is isolated from the turbo-molecular pump by a combination of a DN40CF gate valve (302012, manual, MDC vacuum) and a DN40CF all-metal angle valve (314003, MDC vacuum). The DN40CF angle valve is followed by a turbo molecular pumping station (ACT 600T, ALCATEL).

The second part extends the vacuum system from the 3D-MOT chamber and ends up in the science cell. The extension is realized by attaching a DN40CF full nipple to a DN40CF viewport of the 3D-MOT chamber in a direction normal to the $2D^+$MOT atomic beam axis. A DN40CF four-way cross follows the DN40CF nipple, and the opposite end

of the 4-way cross is connected to the DN40CF flange of the science cell. Two starcell ion pumps of capacities $75\,l/s$ (VacIon- 75) and $40\,l/s$ (VacIon- 40) are connected to the DN40CF four-way cross, aiming for a much better vacuum inside the science cell. A three-filament Ti-sub pump (9160050, Agilent) is placed inside a DN100CF full nipple to have a large surface area for the Titanium coating, providing more efficient pumping. We occasionally fired the Ti-Sub filaments. A residual gas analyzer(RGA) (Anglo Scientific Instruments, AX600-ECU) is attached to the section via a DN40CF-DN100CF reducer Tee. The RGA serves a crucial purpose during the UHV achievement; it yields the composition of the air inside the system by measuring the partial pressure of the different atomic masses.

The science cell is a UHV-compatible glasscell manufactured by Precision Glass blowing Incorporate, USA (refer to the engineering drawing in Appendix-A.2). The outer dimensions are: 28 mm x 28 mm x 80 mm, and the cell walls have a uniform thickness of 4 mm. The glass cell is attached to a DN40CF flange through a glass-to-metal junction. The smaller cell size provides larger optical access and good mechanical stability. It allows us to place the quadrupole-Ioffe-configuration (QUIC) trap magnetic coils very close to the atoms. The close placement of the magnetic coils provides steep magnetic confinement, which is desirable for efficient evaporative cooling [121]. Furthermore, it would allow the installation of an imaging system very close to the atomic cloud just outside the science cell, thus providing a high numerical aperture for the imaging system, which is a pre-requisite for high-resolution imaging [113].

2.2.1 Importance of the differential pumping tubes

The $2D^+$MOTs are an efficient source of high flux cold atomic beam of alkali atoms. This efficient cold atomic beams allow to capture a the large number ($\sim 10^{10}$) of cold atoms in the 3DMOT in the UHV chamber. As discussed in Section-2.2, the base pressure in the UHV chamber needs to be $\sim 10^{-11}$ mBar to achieve the quantum degeneracy. A $2D^+$MOT produces a cold atomic beam with large flux with a alkali vapor pressure

$\sim 10^{-7}$ mbar. The differential pumping tube bridged between the high pressure region of the 2D$^+$MOT chamber and the UHV chamber by maintaining orders of magnitude pressure difference. The conductance of the differential pumping tube is $0.043\,l/s$ for sodium and $0.038\,l/s$ potassium 2D$^+$MOTs respectively. The details of the calculation are described in Appendix-A.1. As we have discussed in detailed in Section-2.2, a $75\,l/s$ ion pump is connected to the 3DMOT chamber in addition to that we haveone more $75\,l/s$ ionpump and a $40\,l/s$ ionpump are connected near the science cell. With the the geometry of our vacuum system, We have a net $69\,l/s$ effective pumping speed in the 3DMOT chamber due the combined effect of all the ionpump (refer to Appendix-A.1 for detailed calculations). Let us denote the vapor pressure in the 2D$^+$MOT by P_{2D} and the pressure in the 3DMOT chamber by P_{3D}. We define the conductance of the differential pumping tube by C and the effective pumping speed at the 3DMOT chamber by S_{eff}. Therefore, using the mass conservation of mass flux [218],

$$(P_{2D} - P_{3D}) \times C = P_{3D} \times S_{eff} \tag{2.2}$$

The vapor pressure in the 2D$^+$MOT is orders of magnitude higher than the 3DMOT chamber (UHV), i.e. $P_{2D} \gg P_{3D}$. Therefore, Eqn.2.2 takes the form,

$$P_{2D} \times C \approx P_{3D} \times S_{eff} \tag{2.3}$$

With the calculated value of the conductance of the differential pumping tube of sodium and potassium 2D$^+$MOT and the effective speed of the ionpumps at the 3DMOT chamber, I obtain, $\frac{P_{3D}}{P_{2D}} \sim 6\times10^{-4}$ and $\frac{P_{3D}}{P_{2D}} \sim 5\times10^{-4}$, between the 3DMOT chamber and 2D$^+$MOTs of sodium and potassium respectively.

2.2.2 Achieving the ultra high vacuum

Achieving ultra-high vacuum is a challenging task: it requires carefully assembling the components and baking the system at high temperatures. Before installation, we made sure that all the components were cleaned. The dirty components are thoroughly cleaned in ultrasonic, especially the 2D$^+$MOT OFHC copper tubes, which Ire machined in the workshop. We assembled the components in parts, then integrated all of them on the proper and sturdy mounts manufactured from aluminum blocks, installed them on the optical table, and vacuum-tightened them using a digital torque wrench to the recommended values.

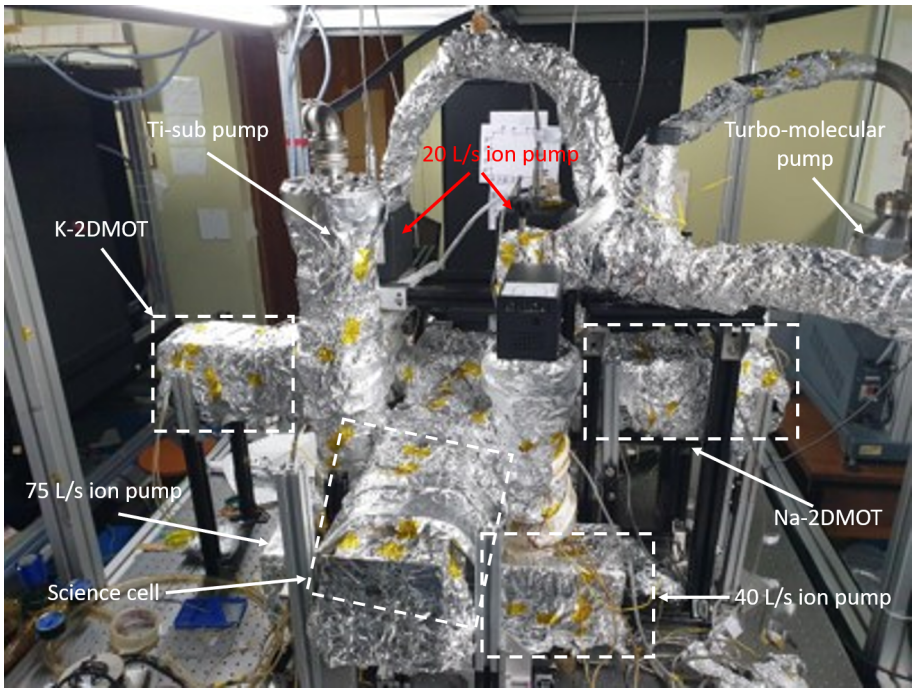


Figure 2.5: The UHV system during the baking process. We wrapped the all the components using heating as describe in the text.

When the system was sealed, we turned on the turbo-molecular pump and monitored the pressure using an ion gauge (which was operated by Agilent multi-channel controller XGS-600) and RGA. During this time, we injected acetone into all the junctions to figure out any major leaks. If any leak was founded, we tightened the screws to get it repaired.

we then blew helium to the junctions to find out for further leaks. After several days of pumping using the turbo-molecular pump, the pressure falls below 10^{-7}, and at this moment, we decided to bake the system. We first cover all the glass cells (two $2D^{+}$ MOTs and one science cell) with boxes made out of thin aluminum sheets for protection. Next, we placed thermocouples at all the critical junctions, such as viewports, the glass-to-metal junction of the glasscells, and all the valves. After that, we wrapped aluminum boxes with resistive heating tapes.

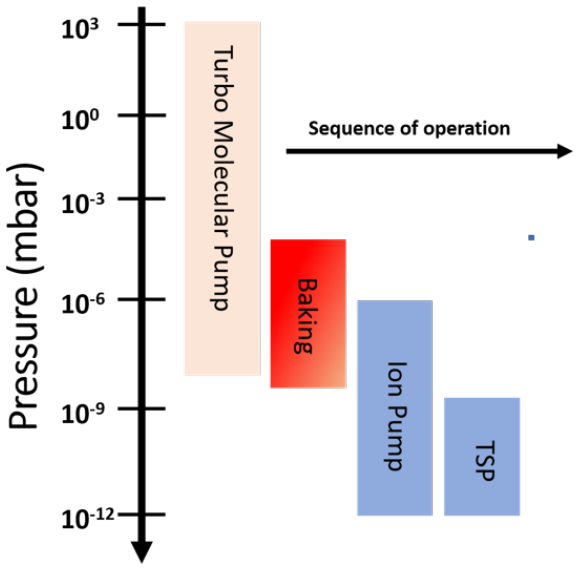


Figure 2.6: A schematic diagram showing the sequence of the pumps operation. The diagram outlined condition; the pressure range over which different vacuum pumps operate.

We directly wrapped the system's metal parts with the heating tapes, including ion pumps (keeping their magnets in place). Ac heating controllers powered the heating tapes. We wrapped the entire system with many layers of aluminum foils in order to obtain a uniform temperature around the system. A uniform temperature throughout the system is necessary; otherwise, during bakeout, the released "dirt" from the hot surfaces could be piled up on the colder surfaces. This could be lethal, as these surfaces would become potential sources of outgassing, which restricts the system's achievable low pressure. We

started to heat the entire system simultaneously and cautiously.

We increased the temperature of the entire system gradually, during this time we always made sure that the temperature change never exceeding 1^oC per min. During this warming up time, only turbo-molecular pumps were operational and we kept all the ion pumps off to minimize their contamination.

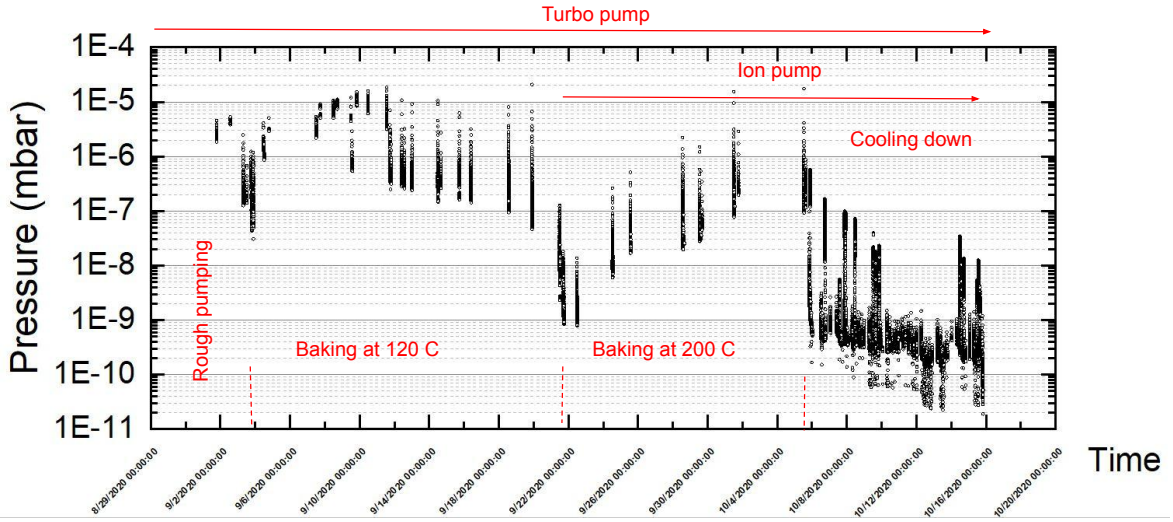


Figure 2.7: The variation of the pressure inside at the 3DMOT chamber measured by an ion-gauge during the bakeout procedure.

During the baking process, we always ensured that the temperature gradients, especially across the fragile components: glasscell, glass-to-metal junctions, and viewports, remained less. During this process, we constantly monitored temperature using the thermocouples and the pressure reading from the XGS-600 controller. Once we reached the desired temperature, we baked the system for two weeks keeping the turbo-molecular pumps on. During this time, we have fired multiple Ti-Sub shots. All the filaments of Ti-Sub should be fired sequentially. Otherwise, the dirt can sit on the colder filaments. Each filament shot lasts for a duration of 30 sec, and we have run them over the current range from 40 Amps to 45 Amps. After each Ti-sub shot, the pressure had increased to

a high value: we had to wait for the pressure to decrease for the next shot. After a few successive shots of Ti-Sub, most of the 'dirt' was out of the system, and at this point, we turned on all the ion pumps and baked the system for two more weeks. During this time, we constantly monitor the pressure using the ion gauge. We couldn't measure the partial pressure using RGA: at this high temperature of the baking, the RGA failed to operate. We decided to cool down the system when the pressure falls below 10^{-9}mBar. The system is cooled down slowly over 24 hours to avoid any thermal shock. When we reached room temperature, the ion pumps showed a pressure at the lower side of 10^{-10} mBar. After a few shots of Ti-Sub, the pressure has finally reached below 10^{-11} mBar.

2.3 The laser system

A single valence electron at the outer shell of the alkali atoms makes them a promising candidate for laser cooling and trapping experiments by providing strong optical transitions. A sketch of the energy level diagram of potassium and sodium atoms is shown in Figure-2.8.

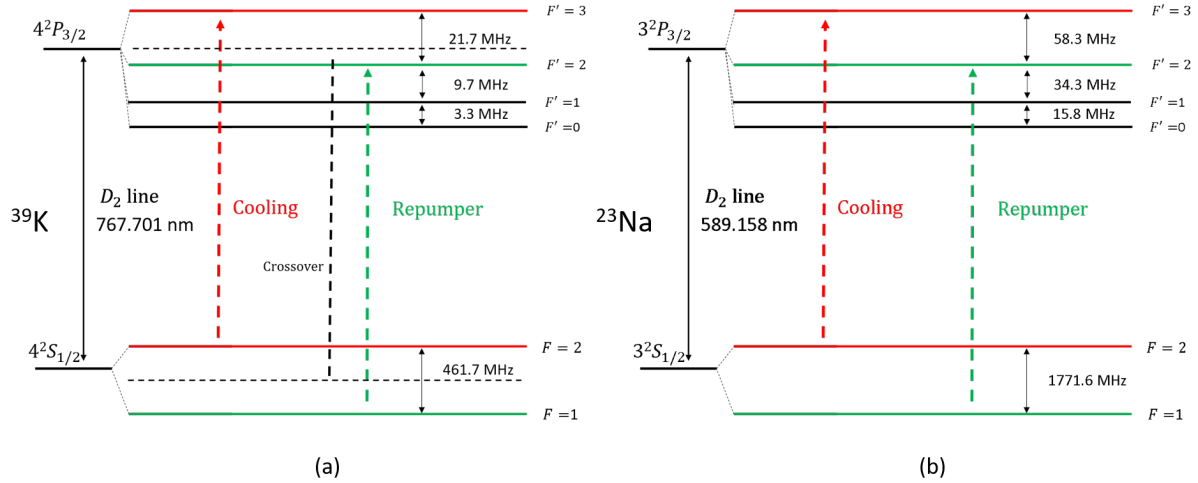


Figure 2.8: The hyperfine energy level structure for the $^2S_{1/2}$ ground state and the $^2P_{3/2}$ excited state of the D_2 transition line of (a) potassium and (b) sodium atoms. The hyperfine energy splittings are given in MHz.

We have used three independent diode lasers. We have used an all-solid-state laser (Ta SHG pro, TOPTICA) to generate cooling and repumper beams for the sodium atoms. We have generated cooling and repumper beams for the potassium atoms using two independent external cavity diode lasers (ECDLs) (DL pro and DL100, TOPTICA), whose output powers are separately amplified by two separate tapered amplifiers (TAs) (Boosta pro, TOPTICA) respectively. The prepared laser beams are transferred from the laser table to the main experimental table using polarization-maintaining (PM) optical fibers.

The ECDL lasers we have used are in Littrow configuration [219]. Figure-2.10 shows a schematic diagram of an ECDL in Littrow configuration. The laser diode emits a divergent beam. An aspheric lens collimates the emitted divergent beam. The collimated beam falls

on a reflective diffraction grating. The grating is placed at such an angle that the -1th order diffracted beam is coupled back to the diode while directly reflected beam forms the main output beam. The diode laser used in this configuration has an anti-reflection (AR) coating on the output facet, and the rear facet is highly reflective. An external cavity is formed between the rear facet of the laser diode and the grating face. Due to the AR coating on the laser diode's output facet, the stimulated emission is dominated by the photons from the external feedback by the grating. Hence, the oscillation lifetime of the photons is enhanced in the external cavity compared to the one in a bare laser diode. Therefore, the increase in the lifetime of the photons in the external cavity leads to the narrowing of the spectral linewidth [219].

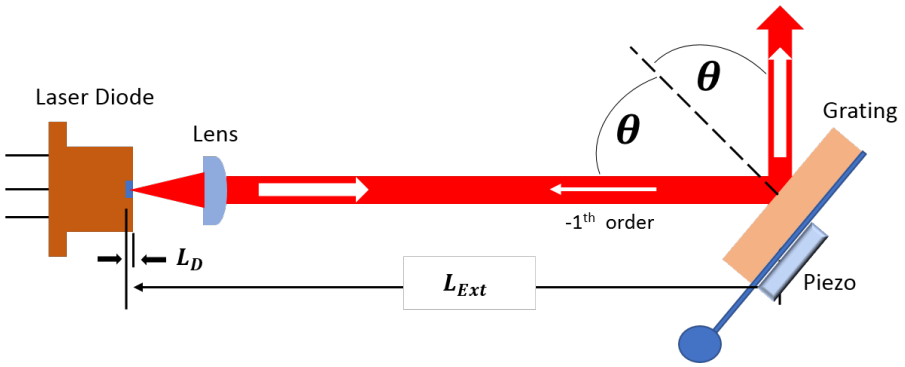


Figure 2.9: A schematic diagram of an external cavity diode laser. The schematic shows that a lens collimates a divergent beam from an AR-coated diode laser. The length of the diode laser is L_D. The collimated light is incident on the reflective grating. The piezo actuator attached behind the grating pushes the grating back and forth. This mechanism rotates the grating around the pivot point. The grating angle is kept so that the -1^{th} order is coupled back into the laser diode. Thus the rear facet of the laser diode and the grating surface forms an external cavity. The length of the cavity is given by L_{ext}.

In an ECDL configuration, the angle of diffraction depends on the wavelength of the incident light. The expression of $-1th$ order diffraction of the laser beam by the grating is given by the grating equation,

$$2\,d\,Sin\theta\, = \lambda, \tag{2.4}$$

Where d is the grating constant and θ is the incident angle of the collimated light from the laser diode with respect to the normal of the grating surface. A piezo actuator is attached behind the grating, and an applied external voltage can change the length of the piezo. When a voltage is applied to the piezo, it rotates the grating with respect to a pivot point; as a result, the incident angle of the incident beam and the grating surface is also changed. Therefore, $-1th$ order external feedback to the laser becomes angle dependent, in other words, wavelength dependent. Thus, the wavelength of the output light can be tuned precisely. The coarse tuning of the wavelength can also be done by controlling the current passing through the laser diode and the temperature of the laser diode.

2.3.1 Laser system for cooling and trapping of potassium atoms

We have two independent ECDLs for potassium cooling and repumper beams. Both the lasers are frequency stabilized (more details in 2.4) by locking to the ^{39}K D_2 cooling and crossover transitions, respectively, using frequency modulation (FM) spectroscopy [220]. The frequency of the laser beams is detuned using AOMs to derive cooling and repumper beams from their respective lasers.

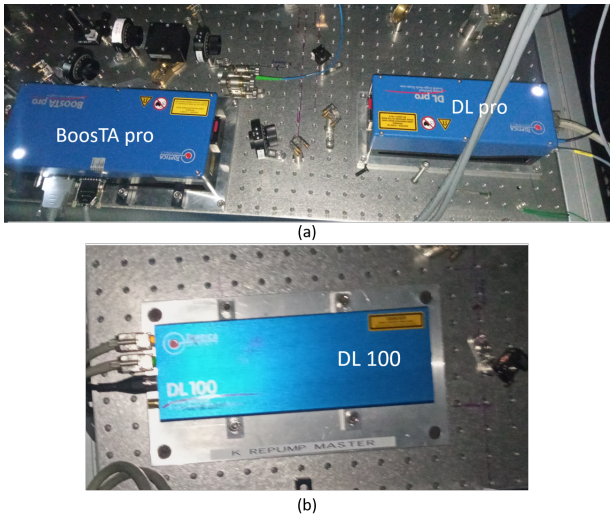


Figure 2.10: Laser system for cooling and trapping of potassium atoms. (a) cooling beam is derived from the DL pro and followed by the BoosTA pro and (b) the repumper beam is derived from DL 100 and subsequently amplified by another BoosTA pro.

2.3.2 Laser system for cooling and trapping of sodium atoms

Alkali species, such as rubidium, cesium, or potassium transition wavelengths, can easily be accessed by commercially available laser diodes [219]. The non-availability of diode lasers around the sodium transition line (589 nm) makes it a challenging atomic species to work with. Till recently, groups that have been working with sodium atoms have been using dye lasers [221], but advances in non-linear optics have changed the picture. Nowadays, commercial lasers at this wavelength are available. For our experiment, we used an all-solid-state TOPTICA TA SHG pro laser. Figure-2.11 shows a schematic diagram of a TA-SHG pro laser system.

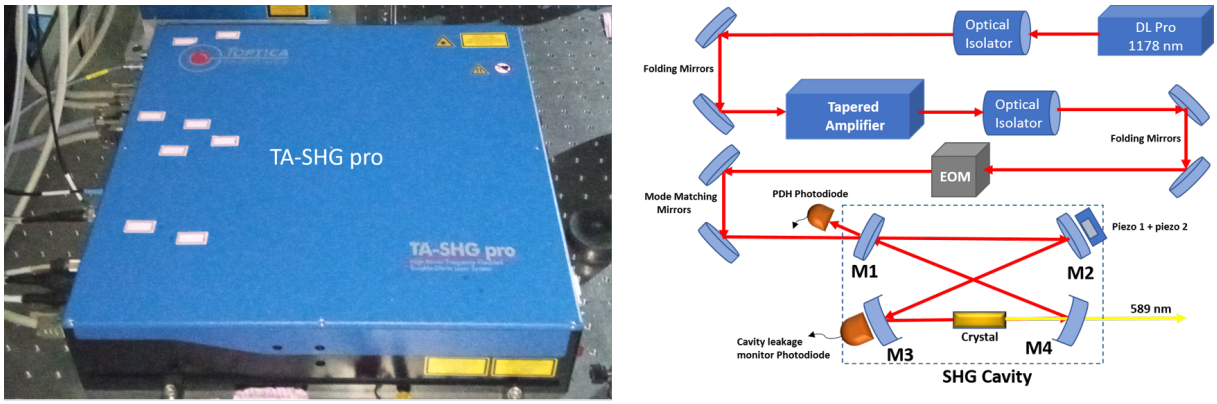


Figure 2.11: Laser system for cooling and trapping of sodium atoms. (a) TA-SHG pro laser system and (b) a schematic diagram of the TA SHG pro laser system. The master laser (DLpro) emits 1178 nm light beam, and the beam is injected into a Tapered amplifier. The amplified light beam is passed through an EOM and injected into a Bow-tie cavity. An intensity-stabilized continuous wave laser beam at 589 nm is out-coupled through the cavity mirror M4.

The system consists of a master DL pro diode laser in ECDL configuration, which emits a pump laser beam at 1178 nm wavelength at power $\sim$ 100 mW. The laser beam is passed through an optical isolator, ensuring that the reflected light back into the DL pro is negligible. The output beam is injected into a tapered amplifier using two folding

mirrors, and the power gets amplified to up to 2 Watts. Two folding mirrors guide the amplified laser beam through an electro-optic modulator (EOM). The EOM modulates the phase of the pump beam at 20 MHz frequency. Two more folding mirrors injected the pump beam into a Bow-tie cavity. A pair of piezo actuators stacked together and placed behind the cavity mirror M2 is being used to move the mirror back and forth by applying a voltage ramp. Therefore, this pair of piezos controls the length of the cavity. A photo-diode mounted behind the mirror M3 monitors the leakage of the intra-cavity power that builds up inside the cavity.

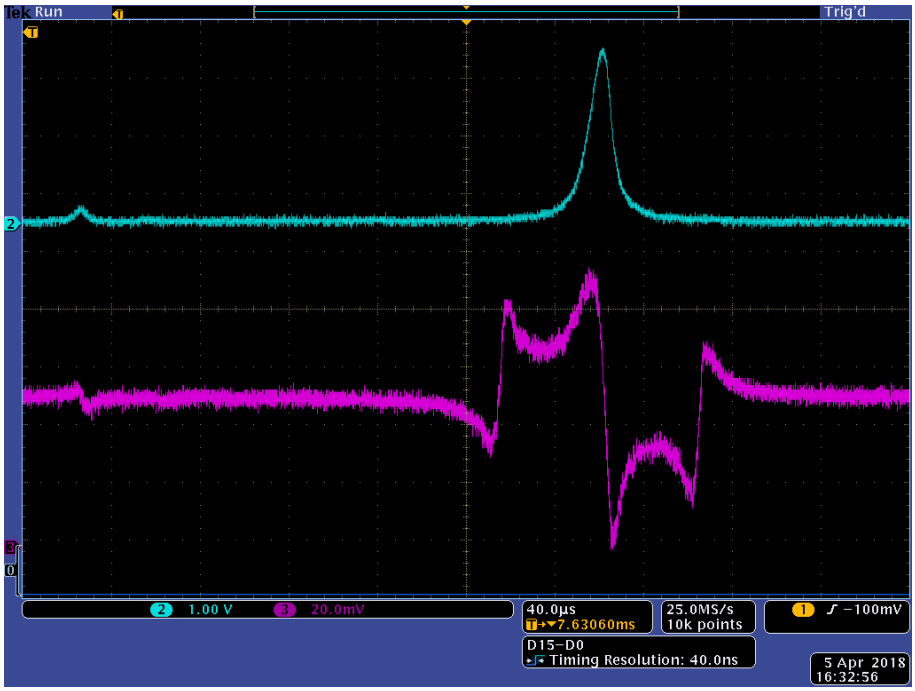


Figure 2.12: TA-SHG intra-cavity leakage (aqua) and the PDH error (pink) signals. A ramp voltage from PID110 module is applied to the piezos behind mirrors M2 in Figure-2.11 and changes the length of the SHG cavity. The intra-cavity power is measured by the detector behind the mirror M3, and the error signal is generated from the modulated reflected light that falls on the PDH photo-detector.

In the 'cavity scan' mode of the laser, a ramp voltage is applied to the piezos; as a result, the cavity length changes in synchronization with the applied ramp voltage. At the resonance condition i.e., when the cavity length is an integral multiple of the incident

wavelength, in this case, the pump beam (1178 nm). The pump beam gets transmitted through the cavity. The transmitted pump beam interacts with a temperature-stabilized crystal (ppKTP), typically kept at 47^{o}C. The crystal is placed at the waist of the cavity and generates the frequency doubled light at 589 nm. The cavity's resonance condition ensures a long oscillating time of the photons inside the cavity. Therefore, increasing the probability of second harmonic generation.

For a sufficient and continuous generation of the laser beam at 589 nm, the cavity length must be stabilized and always kept in resonance with respect to the pump beam wavelength. This is accomplished by using Pound-Drever-Hall (PDH) techniques [189]. The pump beam is phase modulated by the EOM and injected into the cavity. When the cavity drifts away from the resonance condition, some fraction of the pump beam gets reflected from the mirror M1 and falls on the PDH photodetector. The PDH photodetector signal is fed into the PDD 110/F module of the Toptica Sys DC110 controller to generate an error signal.

In Figure-2.12, the aqua color curve shows the intra-cavity leakage power measured by the photo-diode behind the mirror M3 and the pink curve represents the PDH error signal obtained from the PDD 110/F module. The signals mentioned above are obtained in the 'cavity scan' mode of the laser, where the cavity length periodically changes across the length corresponding to the resonance condition. The peak of the intra-cavity leakage corresponds to the resonance length of the cavity for the given pump beam wavelength. The PDH error signal is fed into the PID110 of the Toptica Sys DC110 controller, which is a Proportional-integral-derivative (PID) circuit, and generates a feedback voltage. The feedback voltage is fed back to the piezos behind mirror M2. Therefore, the cavity remains at length, corresponding to the resonance. Thus, the cavity generates an intensity stabilized continuous wave (CW) laser beam at 589 nm.

2.4 Laser frequency stabilization

The frequency of the emitted light from a diode laser is determined by the energy band gap of the semiconductor material being used. The bandgap depends on the temperature of the laser diode and the current passing through it [219]. Therefore, the drift in the temperature and fluctuation in the current could change the frequency of the laser light during the experiment.

The scattering rate of photons from an atom depends on the detuning of the laser light frequency from the atomic transition frequency. Therefore, the fluctuation in laser frequency causes inefficient laser cooling. To minimize the frequency fluctuation of the laser beam, we must stabilize the frequency of the laser light relative to the atomic transition frequencies. Therefore, measuring the atomic transition frequencies precisely is essential, and we determine the transition lines implementing the saturation absorption spectroscopy (SAS) [222]. Using standard frequency locking techniques to the atomic transition lines obtained in SAS, we could obtain frequency stability better than 10^{-10}.

2.4.1 Saturation Absorption Spectroscopy

The Doppler broadening mechanism caused by the thermal velocity of the atoms masks the hyperfine atomic transition lines in single-beam absorption spectroscopy. For sodium atoms at room temperature, the Doppler width is $\sim$ 1400 MHz, and for potassium atoms, it is $\sim$ 800 MHz. To overcome this problem, we have implemented the saturation absorption spectroscopy setup. A schematic diagram of a SAS setup is shown in Figure-2.13. In the setup, a part of the laser light is incident on a polarization beam splitter (PBS). The reflected light (low intensity, $\sim I_{sat}$, I_{sat} is the saturation intensity of the atomic transition in consideration) forms the probe beam, and the transmitted beam (high intensity, $> 10I_{sat}$) forms the pump beam. The probe and pump beams are aligned such that they are overlapped inside the glass cell containing the vapor of the atomic species. I monitor the transmission power of the probe beam using a photodiode while the frequency of the

laser is swept through the atomic transitions.

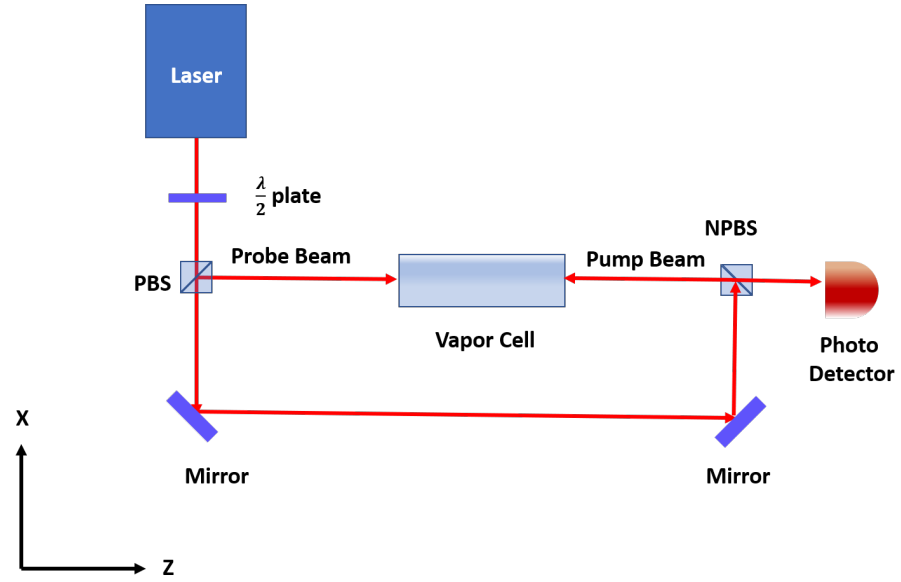
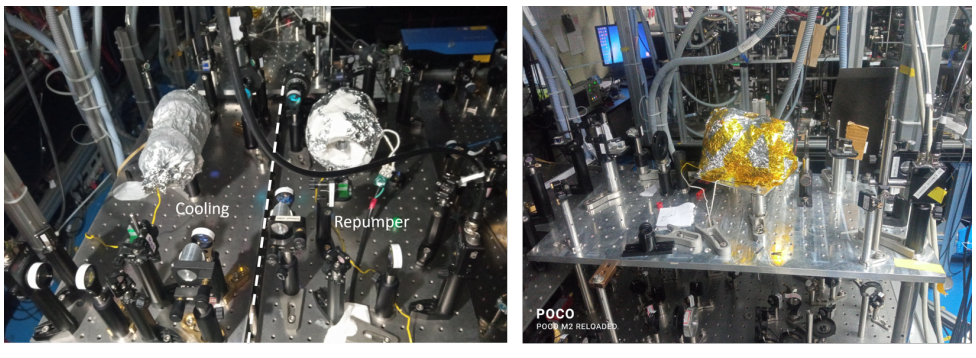


Figure 2.13: A schematic diagram of the saturation absorption spectroscopy setup. The laser beam is divided into probe and pump beams. The probe and pump beams are made to overlap inside the vapor cell. The vapor cell is heated at the required temperature using heating tapes. The transmitted power of the probe beam incident into the photodiode.

As mentioned earlier, we have used two separate diode lasers for the laser cooling of potassium atoms, one dedicated for the cooling transition and the other one for the repumper transition.

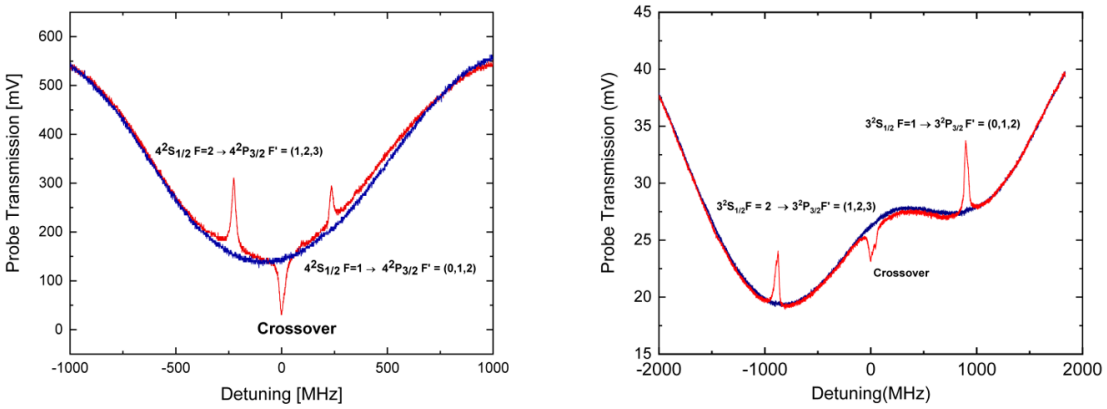


(a) (b)

Figure 2.14: Experimental arrangements to observe the saturation absorption spectroscopy signals of (a) potassium and (b) sodium atoms.

Therefore, we implemented two identical SAS setups for potassium atoms. One is used to stabilize the frequency of the cooling laser (DL pro), and the other is used to stabilize the frequency of the repumper laser (DL 100). Figure-2.14(a) and Figure-2.14(b) show the experimental arrangement of the SAS setup we have implemented for the potassium lasers and the sodium laser.

Figure-2.15(a) and Figure-2.15(b) show the SAS signals of potassium and sodium D_2 transitions, respectively. The blue and red plots represent the transmission of the probe beam through the vapor cells in the absence and the presence of the pump beam, respectively.



(a) (b)

Figure 2.15: Saturation absorption spectroscopy signal of (a) potassium and (b) sodium atoms. The blue plots show the transmission of the probe through the vapor cell in the absence of the pump beam, while the red plots show the same in the presence of the pump beam.

The peaks in the SAS signal are labeled by corresponding ground and excited hyperfine transitions. The cooling laser for the potassium atoms is locked w.r.t $\left|4^2S_{1/2}F=2\right\rangle \rightarrow \left|4^2P_{3/2}F=(1,2,3)\right\rangle$ transitions while the repumper laser is locked to the crossover transition. The sodium laser is locked to $\left|3^2S_{1/2}F=2\right\rangle \rightarrow \left|3^2P_{3/2}F=3\right\rangle$ transition.

As we introduce the intense counter-propagating pump beam at the same frequency

as the probe beam, narrow peaks appear around the transition frequencies. To see how they are originating, let's consider the laser frequency is tuned at ν_0, then the atoms with $v_z \sim 0$ along the beams will be in resonance simultaneously with both the probe and pump beams. The atoms will experience more scattering by an intense pump beam; this will deplete the ground state of the atoms to the excited state. Now, at the same time, the atoms are encountering the probe l ight beam; this, in turn, results in less absorption of photons from the probe beam over a narrow range of frequencies around the transition frequencies. Therefore, the probe beam shows a peak in the transmission signal around the transition frequency.

In Figure-2.15(a) and Figure-2.15(b), we have observed crossover transitions between the ground hyperfine states ($F = 1$ and $F = 2$) as well. These later crossover transitions are inverted, which signifies that, at that frequency of the probe and the pump beams, there is an additional increase of the probe beam.

We typically operate the vapor cells of the potassium and sodium atoms at $\sim 50^o\,C$ and $\sim 150^o\,C$, respectively to obtained the SAS signal. At these temperatures, we obtained the Doppler width $\sim 820\,\text{MHz}$ and $\sim$1600 MHz for potassium and sodium atoms respectively. In case of potassium atoms (^{39}K), the Doppler width is more than the ground state hyperfine splitting (461 MHz), while its is comparable to the ground state hyperfine splitting in the case of sodium atoms. As a result, when the frequency of the probe and the pump beams is tuned across the crossover transitions, the probe and pump beams interacts with the ground hyperfine states simultaneously. For example, if the atoms are moving counter-propagating to the probe beam, the probe beam would excite the $F = 1$ hyperfine states, while the pump beam would excite $F = 2$ hyperfine states. The scattering rate experienced by the atoms due to the pump beam is higher compared to the probe beam, as a result the atoms are optically pumped from the hyperfine F=2 states to F=1 states. This increased population of atoms in F=1 states, results in an enhanced absorption of the probe beam. This explains the observed inverted peaks in the SAS signal of potassium and sodium atoms.

Typically, the frequency swiping of the light of the diode laser is realized by applying a triangular voltage signal (the mechanism of the frequency tuning of an ECDL using piezo has been explained in Section-2.3) or by sinusoidal modulating the current flowing through the laser diode.

In the following subsections, we will describe the frequency stabilization techniques we have employed during our work.

2.4.2 Frequency stabilization using Pound-Drever-Hall (PDH) locking techniques

The stabilization of laser light frequency using the PDH technique relies on the phase modulation of the probe light [189]. A non-resonant electro-optic modulator (EO-PM-NR-C1, Thorlabs) is placed in the path of the probe beam as shown in Figure-2.16. A high bandwidth amplifier (ZHL-1-2W+, Mini-circuits) drives the EOM, and the phase of the probe beam gets modulated when it passes through the EOM. The phase modulated probe light interacts with the atoms inside the vapor cell in the presence of the pump beam and incident on the photodiode. The photodiode signal is fed into the digilock module (Digilock 110, Toptica). The PDH error signal is generated through the Digilock module from the SAS signal as shown in the in Figure-2.17. The PDH error signal is fed into the PIDs, and the resulting feedback signal is transferred to the laser diode via the operating current and the piezo's driving voltage. The flow chart of the process is shown in Figure-2.16.

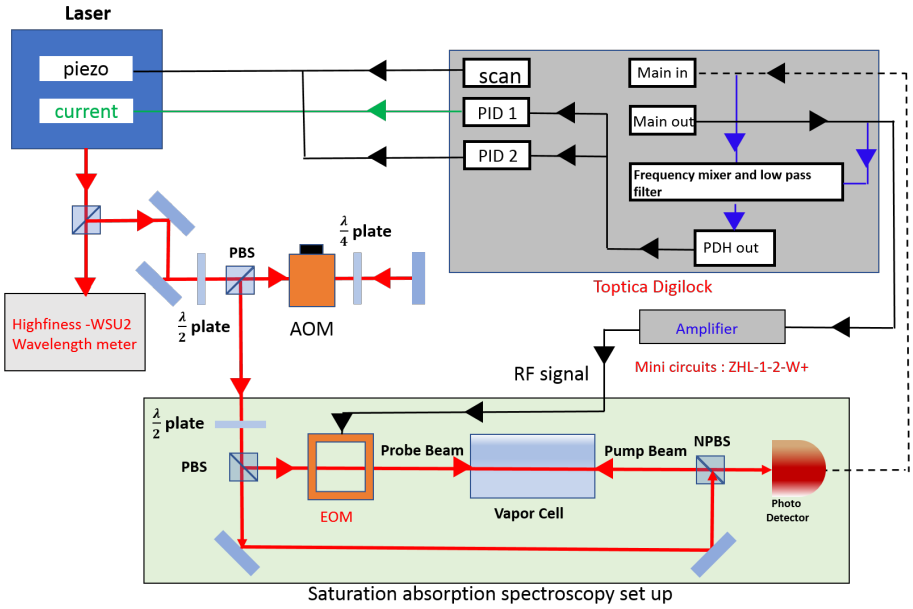


Figure 2.16: A schematic diagram of saturation absorption spectroscopy set up and the frequency stabilization scheme using the PDH technique. The spectroscopy signal from the photodiode is fed into the Digilock module. The feedback signals from the Digilock module are fed to the laser via the operating current and the piezo driving voltage. A wavelength meter (WSU2, Highfiness) monitors the laser's wavelength during the experiment.

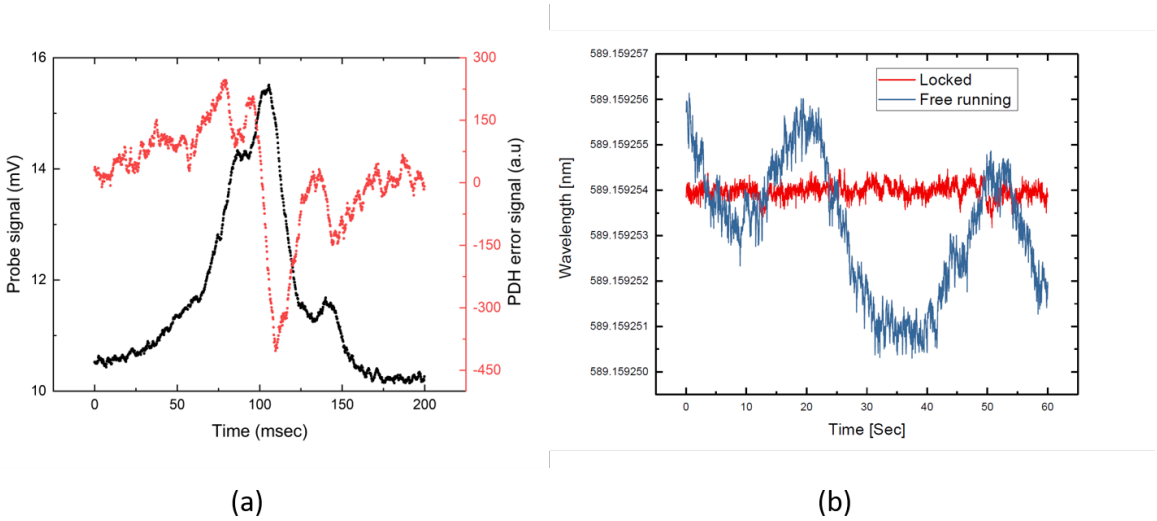


Figure 2.17: Sodium laser frequency locking technique. (a) Saturation absorption spectroscopy of sodium $D2$ transition. The black plot shows the SAS signal and the red plot shows corresponding PDH error signal. (b) The locking stability of the laser using the PDH locking technique. The red plot shows the wavelength of the laser while the laser is locked to the atomic transition line using PDH locking technique. The blue plot shows the wavelength variation of the laser light when free running.

Figure-2.17(a) shows the sodium D_2 transition SAS signal and corresponding PDH error signal. The locking stability the laser using PDH locking technique is shown in Figure-2.17(b).

2.4.3 Frequency stabilization using side-of-fringe technique

The layout of the side-of-the-fringe locking technique is depicted in Figure-2.18. In our system, we have implemented this locking technique to stabilize the frequency of the potassium cooling laser and the sodium laser. A part of the laser output is injected into an AOM (the detail of the layout is described in Section-2.5), and the double pass output of the AOM is sent to the spectroscopy setup. The Digilock module is controlled by the graphical user interface (GUI) software (Toptica) from the control computer. Using the 'scan' of the Digilock software, we modulated the piezo with a triangular ramp with an amplitude V_{pp} and frequency 5Hz (typically, we keep this value fixed) and swept the

laser frequency across the resonance transition frequency and corresponding SAS signal is captured by a photodiode. The voltage signal from the photodiode is sent to the 'main in' port of the Toptica Digilock module. We monitor the SAS signal in the control computer as shown in the Figure-2.18.

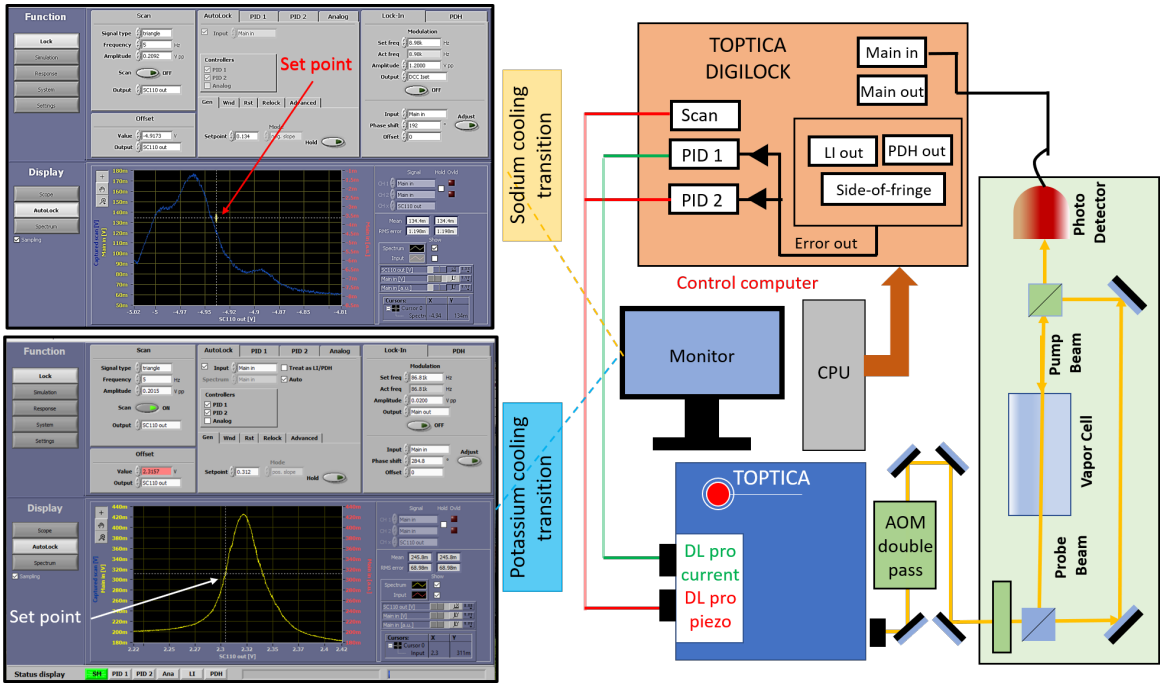


Figure 2.18: The schematic diagram is showing the frequency stabilization of the sodium and potassium lasers using the side-of-the-fringe locking technique. The SAS signal of the atomic species is sent to Toptica Digilock module and the frequency is stabilized by choosing a set point on the SAS signal (as described in the text).

In SAS spectroscopy, as the laser frequency is tuned, there is a change in the value of the signal level, and the side of the fringe locking scheme uses this corresponds between the frequency of the laser and the SAS signal level. The frequency locking is realized in the following way, we choose a set point (V^{set}) on the SAS signal (as highlighted in the figure), which corresponds to a specific frequency of the laser light and activate the locking from the Digilock software. Digilock module in real-time measures the photodiode

signal $V(t)$ and determines the error signal,

$$e(t) = V^{set} - V(t) \tag{2.5}$$

The error signal is fed into the Digilock PID1 and PID2. The generated feedback signal from the PID1 is fed into the current of the laser module, while the feedback signal from the PID2 module is fed into the piezo scan voltage of the laser module. As mentioned earlier, the frequency of the laser light on an ECDL could be tuned by tuning the voltage applied to the piezo and the current flowing through the diode laser. Once the frequency locking is activated from the Digilock software and if the frequency of the laser light drifts, there will be a change in the photodiode signal and the $e(t) \neq 0$. PID1 and PID2 generate the required feedback signals and change the laser frequency accordingly to maintain the error signal at minimum, i.e., $e(t) = 0$. In other words, the Digilock module stabilizes the frequency of the laser.

2.5 Optical layout

The experimental arrangement features two independent laser systems: one for potassium and one for sodium atoms. This section discusses the details of the laser beam preparation and frequency tuning to the desired atomic transitions.

Potassium optical layout

As described in 2.3.1, the laser system for the potassium atoms consists of two independent master lasers (Dl pro and DL100) and two BoosTA pro to amplify the laser output power. The DL pro laser (cooling laser) is tuned to the cooling transition. The output of the DL pro laser is injected into one of the BoosTa pro (cooling BoosTa). The DL100 laser (repumper laser) is tuned to the repumper transition. The output of the DL 100 laser is injected into the second Boosta pro (repumper BoosTa).

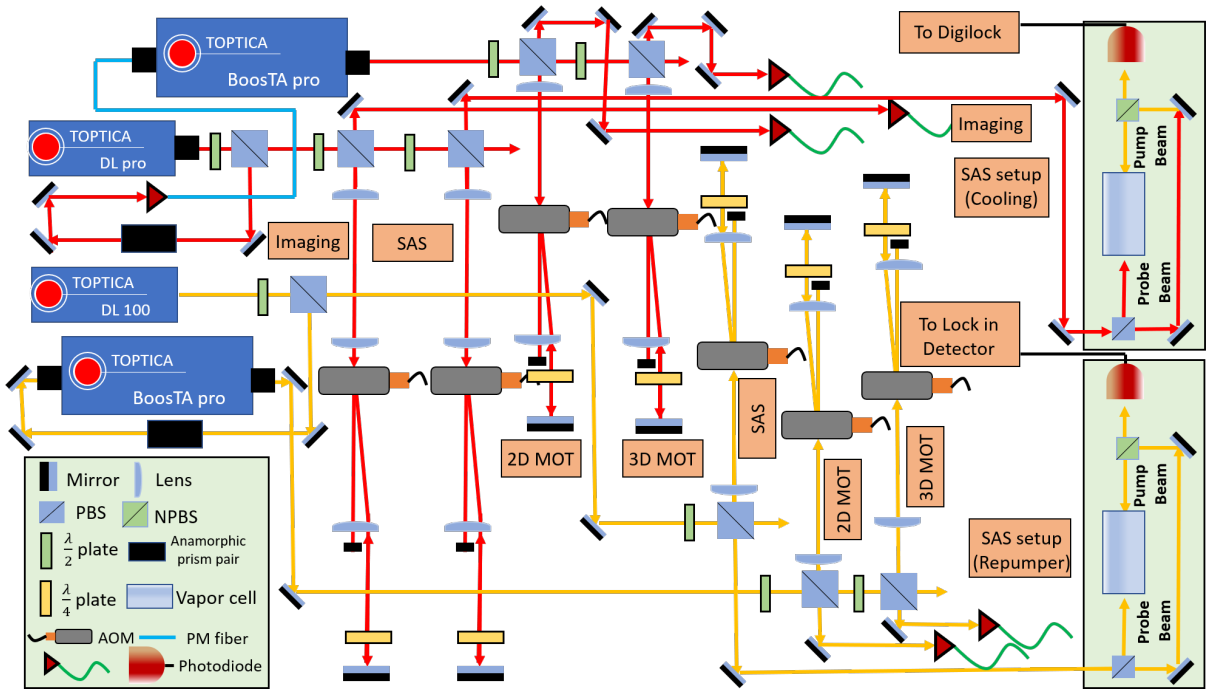


Figure 2.19: The layout of the potassium laser system. Each of the outputs of the Dl pro and DL 100 is split into two beams using the combination of half-waveplates and the PBSs. One of the beams is sent to respective tapered amplifiers. The amplified output beam from the respective tapered amplifiers is split into a series of beams, and each beam is sent to respective AOMs. The double pass output of the AOMs is injected into their individual PM fiber. The remaining beam of Dl100 is sent to an AOM, and the double pass output beam is sent to the SAS setup. In the case of DL pro, the remaining beam is split into two more beams; both beams are sent to AOMs. The double pass output of one of the AOMs is sent to the SAS setup, while the double pass output of the other AOM is tuned to imaging transition and injected into the respective PM fiber.

The output beam from the laser is elliptical. The beam is sent through a pair of anamorphic prisms to make the beam circular in shape. The circular shape improves the mode matching of the laser beam to the optical elements. Then it is sent through an optical isolator (not shown in the Figure-2.19) that prevents the reflected light back into the laser diode; this ensures the frequency stability of the laser. After the isolator, a PBS divides the beam into two parts. The half-waveplates placed before each PBSs control the power into the reflected and transmitted arms. The reflected beam of power $\sim$ 15 mW is injected into the BoosTA pro, and I obtained an amplified output of power $\sim$ 1.2 Watts.

Upto this stage, the optical assembly is similar for both the cooling and repumper lasers.

The transmitted beam of the first PBS is divided into two parts for the cooling laser. The reflected beams from the PBSs are injected into two independent AOMs. The double pass output beam of one of the AOMs is prepared for the imaging and is injected into a PM fiber to transfer to the experimental table. The double pass output beam of the other AOM is directed into the SAS setup.

The amplified output from the cooling BoosTa pro is divided into several beams using PBSs. Two of the reflected beams from the PBSs are injected into two AOMs. One of the double pass output beams of the AOMs is prepared for the $2D^+$MOT cooling transition, and the other one is for the 3DMOT cooling transition. The double pass output beams are injected into respective PM fibers and transferred to the experimental table.

The laser beams required for the repumper transitions in $2D^+$MOT and 3DMOT are derived from the amplified output beam from the repumper BoosTA. Optical arrangement for the repumper follows the similar optical arrangement implemented for the cooling beams. The reflected lights from two PBSs are injected into two AOMs, $2D^+$MOT repump and 3DMOT repump as shown in Figure-2.19, and the double pass outputs are injected into their respective PM fibers.

beam	detuning (Γ)	power (I_{sat})
2DMOT cooling	-6.5	11
2DMOT repumper	on resonance	8.25
3DMOT cooling	-6.8	20
3DMOT repumper	on resonance	15

Table 2.1: Typical value of the parameters of the potassium light beams prepared for the 2DMOT and 3DMOT. The detuning and the power delivered to the main experimental table. The power has been Measured after the respective fiber collimators.

Sodium optical layout

A schematic of the sodium laser system is shown in Figure-2.20. The output beam from the Ta SHG pro is circular (with $\frac{1}{e^2}$ diameter $\sim$ 2.2 mm). The output beam is split by a series PBSs into several beams. The fraction of the power is controlled by half waveplates in front of each of the PBSs.

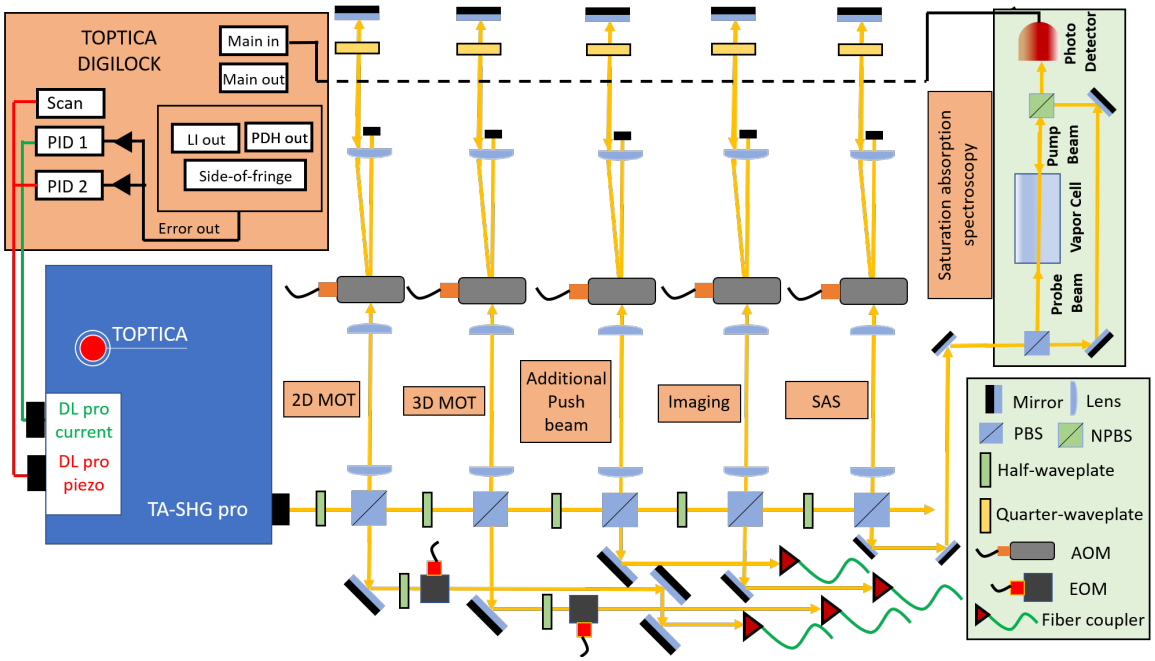


Figure 2.20: Sodium laser system. The output beam from TA SHG pro is split into a number of beams. A series of AOM double pass configurations tuned and controlled the frequencies and intensities of these beams. One of the double pass beam is directed to the saturation absorption spectroscopy (SAS) setup.

One arm of the beam is sent to an AOM, and the double pass output beam is sent to the SAS setup. The double pass output of $2D^{+}$MOT and 3D-MOT AOMs are sent through phase-modulating EOMs, and the output beams are injected into respective PM fibers. As mentioned in Section-1.1.2, the EOM adds a pair of sidebands symmetrically around the cooling laser in the frequency spectrum. The higher frequency ($\sim$ 1700 MHz higher relative to the cooling frequency) sideband is tuned to the repumper transition.

beam	detuning (Γ)	power (I_{sat})
2DMOT cooling	-1.5	1.9
2DMOT repumper	on resonance	0.35
Additional push	-2	10
3DMOT cooling	-1.4	10
3DMOT repumper	on resonance	0.22

Table 2.2: Typical value of the parameters of the sodium light beams prepared for the 2DMOT and 3DMOT. The detuning and the power delivered to the main experimental table. The power has been Measured after the respective fiber collimators.

2.6 Atomic beam source

A magneto-optical trap (MOT) has a finite trap depth (order of a few Kelvin). A MOT can only capture those atoms having a velocity less than the MOT's characteristic velocity, termed as the capture velocity of the MOT (typically ranging between 30 to 100 m/s). Furthermore, the collisions of the trapped cold atoms with the residual background atoms present inside the UHV system limit the lifetime and steady-state number of the trapped atoms in a MOT. Achieving a degenerate cloud of ultracold atoms involves an evaporation cooling stage, where the higher velocity atoms are forcefully removed from the trapped. Hence, to obtain a large number of atoms in the degenerate cloud, it is necessary to start with many atoms in the 3D MOT.

A brief description of the loading schemes of a MOT has been given in 2.1. A MOT, when loaded from an alkali metal dispenser [191, 193, 194], requires a high current ($\sim 10 Amps$) for their operation. The emitted atoms are hot as the dispenser reaches a temperature of 500^oC or more [223]. The fraction of the atoms trappable in a MOT using this scheme is relatively small ($\sim 10^{-5}$) due to the high temperatures of the dispenser.

Typically, the number of trapped atoms is limited to $\sim 10^7$ with a few tens of seconds lifetime. Increasing the vapor pressure increases the loading rate, but at the same time, due to high background pressure, the collisional losses of the trapped atoms have also increased. As a result, the steady-state number of the trapped atoms reaches a limit.

The requirements mentioned above demand a large number of atoms in a MOT in an ultra-high vacuum environment. The UHV environment ensures a long lifetime of the ultracold atoms in the trap. The severe drawbacks of MOT loading using conventional dispensers demand that the MOT should be loaded using an intense and reliable source of atoms. The atomic source should generate a collimated atomic beam with a mean velocity below the MOT's capture velocity by keeping intact the system's ultra-high vacuum (UHV) condition.

The deceleration of an atomic beam [224] using a counter-propagating laser beam in the presence of a spatially varying magnetic field paved the way to load a MOT [24] using a high-intense low velocity cold atomic beams. It is highly desirable to obtain the best possible signal-to-noise ratio in cold atoms experiments: atom laser [12], atomic interferometry [225, 226], atomic clocks [227, 228], precision measurements (fundamental constant measurements). The process of evaporative cooling [229] demands a high number of atoms as a starting point to reach quantum degeneracy.

Two classes of atomic sources are promising for the high fluxes of cold atoms in ultracold atom experiments. In the first kind, a Zeeman slower: a flux of atoms is slowed down by using a counter-propagating red-detuned laser beam in the presence of a spatially inhomogeneous magnetic field. The phenomenon of the Zeeman shift of the magnetic sublevels of the atoms in the presence of a magnetic field is exploited here. The spatially inhomogeneous magnetic field keeps the atoms in resonance with the laser beam while they are decelerating [224, 230].

The second kind of source is based on a two-chamber model, where the atomic beam is produced in one chamber directly from the vapor of the atom (typically, vapor pressure is maintained between 10^{-6}-10^{-8} mbar) and subsequently transferring them to the final

chamber(maintains UHV environment). Based on this principle, two different classes of sources are developed: low-velocity intense source (LVIS) [52] and two-dimensional magneto-optical trap(2DMOT) [231]. The later work demonstrated that the atomic flux is higher in 2DMOT than the atomic flux achieved in the LVIS, with an order of magnitude less power. The 2DMOT scheme was later successfully implemented by many groups over a wide range of atomic masses [202, 204, 232–236].

A Zeeman slower decelerates an intense thermal atomic beam along the propagation axis of the beam by a counter-propagating red-detune laser beam (termed as a slowing beam). The counter-propagating laser beam produces radiation pressure on the atoms and reduces their velocity. A Zeeman slower can produce an atomic flux up to 10^{11} atoms/ sec [237]. The spontaneous emission process associated with the photon absorptions from the slowing beam produces a transverse velocity to the atoms. The transverse velocity causes the cold atomic beam to diverge. This effect results in an inefficient loading of the cold atomic beam into the capture volume defined by the cooling beams, which is determined by the diameter of the cooling beams of the MOT. The efficiency of a directly loaded MOT from a Zeeman slower is typically limited to a few percent, and it requires additional transverse cooling technique [238] to improve the beam's collimation.

In addition, the Zeeman slowers can only reduce a part of the atomic velocity distribution; typically, the order of the average velocity of the distribution of the atoms emerges from the oven. The higher velocities of the distribution are unaffected by the Zeeman slowers. The atoms with higher velocities collide with the cold atoms trapped in the MOT and limit the performance of the MOT. In some cases, the slowing light might affect the performance of the MOT. The residual magnetic field at the slower end could alter the magnetic field gradient required for the MOT and must be compensated by additional coils. The Zeeman slowers oven requires higher vapor pressure for the operation. Therefore, the ovens are typically operated at higher temperatures which cause higher material consumption compared to the 2DMOT [236].

In a 2DMOT, two orthogonal pairs of counter-propagating laser beams are shone into

a vapor cell in combination with a two-dimensional magnetic quadrupole. This system creates a radial restoring force towards the line of zero magnetic fields (y-axis). The atoms entering into the cooling volume are slowed down in the radial direction and compressed onto the y-axis, but the velocity along the y-axis remains the same. Another beam, the push beam along the y-axis, pushes out the atoms from the 2DMOT cooling volume towards the 3DMOT through a differential tube that separates the 2DMOT section and the 3DMOT chamber.

In the case of sodium atoms, the most common source of slow atoms is Zeeman slower, which can generate an atomic flux up to 10^{11} atoms/sec [237,239,240]. First 2DMOT cold atoms source of sodium was developed by G.Lamporesi et al. [204], based on the work initially developed for lithium atoms [234]. With this pure 2DMOT source, the group has obtained a loading rate $\sim 4\times10^{9}$ atoms/sec of sodium atoms with an average velocity $\sim$ 20 m/s and a total number of trapped atoms of the order of 10^{10} atoms/sec.

The significance of such an atomic source is demonstrated by producing a large BEC of atoms number $> 10^{7}$, and background pressure limited lifetime $\sim$5 minutes. In their work, E Pedrozo-Penafiel et al. [236] developed a sodium 2DMOT inspired by the work [204] and a sodium spin-flip Zeeman slower [237,240] in the same vacuum system. This experiment compares the performance of these two atomic sources in similar 3D MOT experimental conditions. They have concluded that both sources could reach similar atomic fluxes.

A Zeeman slower is well known for its robustness and the high flux of trappable atoms; it requires comparatively less optical setup and less laser power. In contrast, it is technically challenging to construct a 2DMOT. The upside is that it is a more compact and clean system regarding background pressure in the 3DMOT chamber. Unlike Zeeman slower, in 2DMOT, the axial velocity of the atoms reaching the 3DMOT is lower, while Zeeman slower doesn't prevent hot atoms from reaching the 3DMOT region. These features of 2DMOT make it an ideal source of cold atomic beam for a BEC experiment, where a high flux atom number is required while maintaining an ultra-high vacuum in the final trapping region to reach the quantum degeneracy.

A cold atomic beam source: 2D$^+$MOT

A three-dimensional model of a 2D$^+$MOT is shown in Figure 2.22. In our design, we have a UHV-compatible glasscell (dimensions: 40 mm x 40 mm x 85 mm, refer to Appendix-A). A differential pumping tube, manufactured from OFHC, is inserted along the long-axis of the glasscell.

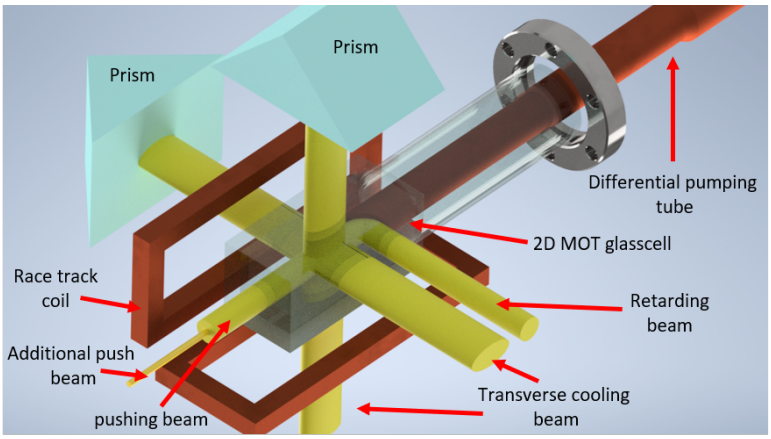


Figure 2.21: A schematic diagram of 2D+MOT configuration. It consists of a UHV-compatible glasscell, and one differential pumping tube is inserted inside the glasscell. The differential tube has a 45deg cut at the surface; this surface is placed inside the glass cell. A pair of racetrack coils (all of them are not shown for image clarity) generates a 2D quadrupole magnetic field configuration. The transverse cooling beams and the retro-reflected beam from the prisms form the transverse cooling and trapping volume. The pushing and the retarding beams overlapped in the cooling volume to form the longitudinal optical molasses. An additional push beam is aligned along the longitudinal direction, enhancing the atomic flux through the differential pumping hole to the 3DMOT chamber.

The differential pumping tube separates the 2D$^+$MOT side from the 3DMOT side and maintains $> 10^3$ pressure difference between both sides. Four racetrack coils generate the required two-dimensional(2D) quadrupole magnetic field. The 2D quadrupole magnetic field configuration has a line of zero magnetic field along the tube axis (y-axis). The racetrack coils are placed around the glasscell such that the line of zero magnetic field is aligned w.r.t the hole of the differential pumping tube. Two pairs of transverse cooling beams create a cooling volume in the presence of the 2D-quadrupole magnetic field, cre-

ating a restoring force along the radial direction. The restoring force confined the atoms onto the y-axis.

In a 2DMOT, the atoms with a transverse component of the initial velocity less than the transverse capture velocity only participate in forming the atomic beam. The atoms must spend enough time in the cooling volume so that the transverse velocity becomes sufficiently low. Once the atoms leave the cooling volume, their divergence in the transverse direction must be small enough to enter the differential tube.

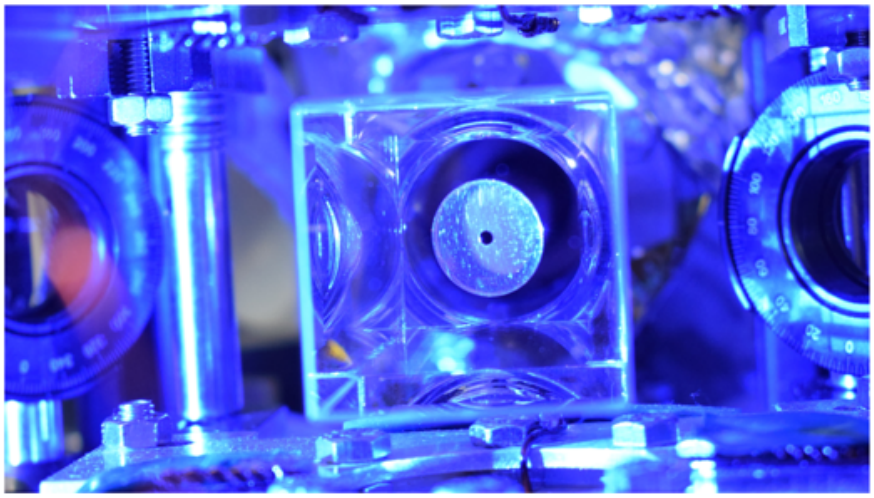


Figure 2.22: The image of UHV glasscell and the differential pumping tube of K-2D$^+$MOT.

During the flight of the atoms through the differential tube, the transverse divergence must be small compared to the inner diameter of the differential tube at any instant. The vapor pressure inside the glass cell is an important factor in determining the flux of the atomic beam. The vapor pressure inside the glass cell determines the mean free path of the atoms. The mean free path must be larger than or comparable to the trajectory of the atoms. At the higher pressure, the collisions among the atoms in the atomic beam with the surrounding atoms would be high enough that they would get knocked out of the atomic beam before entering into the differential tube. Therefore, the interplay of the interaction time of the atoms in the cooling volume and the dimension of the differential

pumping tube determined the flux of the atoms in the generated cold atomic beam.

The 2DMOT cooling beams and the quadrupole magnetic field reduce the component of the velocity in the transverse plane but do not change the velocity along the longitudinal direction (atomic beam direction). A $2D^+$ MOT further increases the atomic beam's flux. In this advanced scheme, one more beam is introduced in addition to the push beam: the retardation beam, which is counter-propagating to the push beam. The 2D quadrupole magnetic field configuration doesn't have any magnetic field component along the longitudinal direction (y-axis), so there will not be any trapping of the atoms along this direction. The pushing and the retardation beams produce optical molasses along the longitudinal direction, which reduces the longitudinal component of the velocity of the atoms. Therefore, the interaction time of the atoms in the cooling volume has further increased due to the reduction of the longitudinal velocity. As a result, the flux of the atomic beam has increased [233, 235].

Design of the $2D^+$ MOT

The $2D^+$MOT vacuum system consists of a UHV-grade glass cuboid (dimensions: 40 mm x 40 mm x 85 mm) connected to a standard DN40CF flange through a metal-to-glass connector. A differential pumping tube is inserted along the long axis of the glass cell. A Oxygen free high conductive (OFHC) copper with a centered hole is inserted into the glass cell along its long axis and separates the $2D^+$MOT chamber from the rest of the vacuum system. The copper tubes (for two independent $2D^+$MOT for sodium and potassium) have a diameter of 2mm over 20mm distance and stepwise widen up to 14 mm and 12mm over a total length of 270mm for ^{23}Na and ^{39}K respectively (refer to A.1). These tubes have a conductance of $0.043\,l/s$ and $0.038\,l/s$ for ^{23}Na and ^{39}K, respectively. The differential pumping tubes maintain a pressure difference better than 10^3 between the $2D^+$MOTs and the 3DMOT chamber.

One of the end faces of the copper tube, which is inside the glass cell, has a 45^o angle cut with respect to the axis of the tube and is hand polished with great care to get a

reflectivity of more than 90% and a smooth surface quality. This allows the overlapping of pushing and retarding beams inside the glass cell along the atomic beam direction. Since the 45^o surface has a centered hole, the retardation beam creates a central dark region upon reflection from this surface. Therefore, there is an imbalance of radiation force on the overlapped area of the pushing beam and the retardation beams around the line of zero magnetic field.

Four rectangular shape magnetic coils (refer to Appendix-A) are placed around the glass cell to produce a 2D quadrupole magnetic field with cylindrical symmetry and a line of zero magnetic field along the y-axis. The currents in the coils are arranged such that the line of zero field can be controlled.

To produce a collimated atomic beam, the glass cell is filled with the atomic vapor at a pressure typically in the range 10^{-8}-10^{-6} mbar. Two pairs of transverse cooling beams confine the atoms towards the line of zero magnetic field, and the longitudinal overlapped beams (pushing and retardation) create optical molasses. The atoms get cooled and confined towards the line of zero magnetic field. In the presence of longitudinal molasses, their longitudinal velocity is also reduced. Once they enter the dark cylindrical region in the overlapped area, they are accelerated and pushed towards the 3DMOT chamber, thus producing a cold and collimated atomic beam.

A schematic diagram of the experimental arrangement of $2D^+$MOT is shown in Figure-2.23. The arrangement consists of the $2D^+$MOT glasscell containing the vapor of the atomic species, four racetrack coils, which produce a 2D quadrupole magnetic field configuration, and the layout of the transverse cooling beams.

Two pairs of racetrack coils in anti-Helmholtz configuration are placed around the glasscell. The white arrows show the corresponding direction of the current flow in the coils and produce a 2D quadrupole magnetic field.

The optical layout for the $2D^+$MOT is designed carefully. The collimated output beam (of $\frac{1}{e^2}$ diameter of 12 mm) from the fiber collimator is divided into two parts, typically in a power ratio of 6:1 between the reflected and transmitted beams. The high power beam

has been employed for the transverse cooling beams, and the low power beam is used to derive the push and retardation beams.

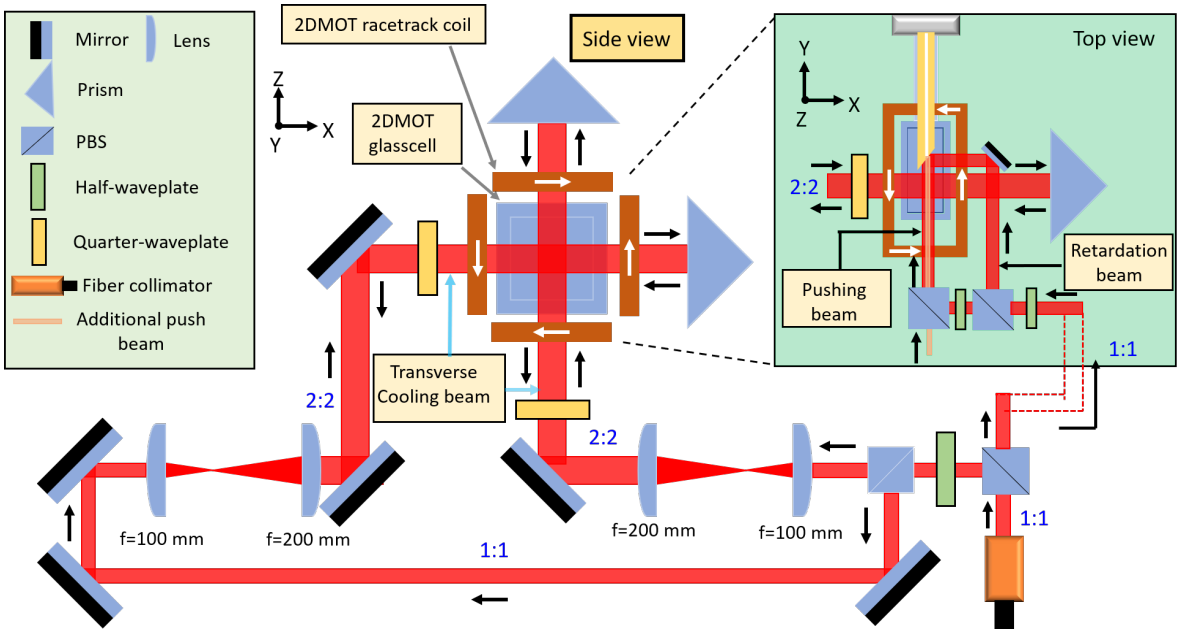


Figure 2.23: The schematic diagram of sodium 2D$^+$MOT experimental arrangement. The collimated output from the fiber collimator of diameter 12 mm is divided by several half-waveplate and PBS combinations. I indicate the ratio of the $\frac{1}{e^2}$ diameter of the beam on the XZ plane to the $\frac{1}{e^2}$ diameter of the beam on the XY plane at a given position. For example, quantity 1:1 corresponds to a laser beam of a circular cross-section diameter of 12 mm. In comparison, quantity 2:2 corresponds to a laser beam circular cross-section of diameter 24 mm. The white arrows indicate the direction of the current flow in the 2D$^+$MOT magnetic coils.

The reflected beam from the PBS is sent through a half-waveplate followed by another PBS and divided into two more beams, transmitted and reflected. The transmitted beam is used as one of the transverse cooling beams along the vertical direction (Z-axis), and the reflected beam is employed as another transverse cooling beam along the horizontal direction (X-axis). A number of mirrors are used to direct the transverse beams to the 2D$^+$MOT glasscell. Two independent telescopes of magnification 2×, each of them has consisted of two plano-convex lenses of focal lengths 100 mm and 200 mm respectively, are employed on the transverse cooling beam paths (as shown in Figure-2.23) and the

corresponding beam diameter becomes 24 mm. The magnified output beams are directed towards the glasscell; just in front of the glasscell, both beams are sent through quarter waveplates. The waveplates convert the polarization of the beams into a circular one. I obtained more than 95% purity in the circular polarization for both the transverse cooling beams. The transmitted beams through the glasscell are retro-reflected using uncoated prisms. The light beam upon two total internal reflections from the two inner surfaces of the prism retains the sense of the orientation of the circular polarization w.r.t the direction of propagation ($\vec{k}$) as shown in Figure-**??**.

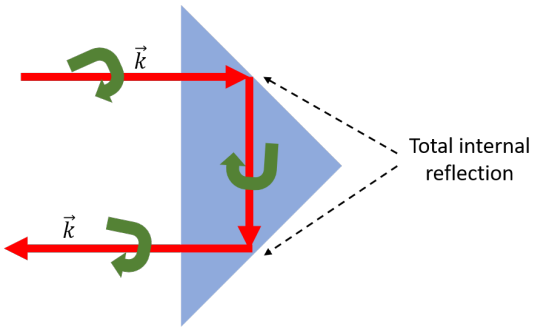


Figure 2.24: The schematic diagram shows a laser beam retro-reflected from a prism. The laser beam preserves the helicity of the circular polarization experiencing two total internal reflections.

The inset diagram shows the optical layout of the pushing, retardation, and additional push beams. The transmitted beam of the first PBS is transferred to an optical breadboard at the height of 450 mm using a periscope. The beam is sent through a half-waveplate followed by a PBS and gets divided into two beams. The transmitted beam is incident on another PBS; using the reflecting surface of the PBS, the beam is injected into the glasscell and incident on the 45^o angle surface of the differential pumping tubes such that it is centered w.r.t the tube axis. The reflected beam of the PBS is used as the retardation beam; upon reflection from another mirror, the beam is incident on the 45^o angle surface of the differential pumping tubes. The retardation beam is reflected from the polished 45^o surface and overlapped with the pushing beam in the cooling volume.

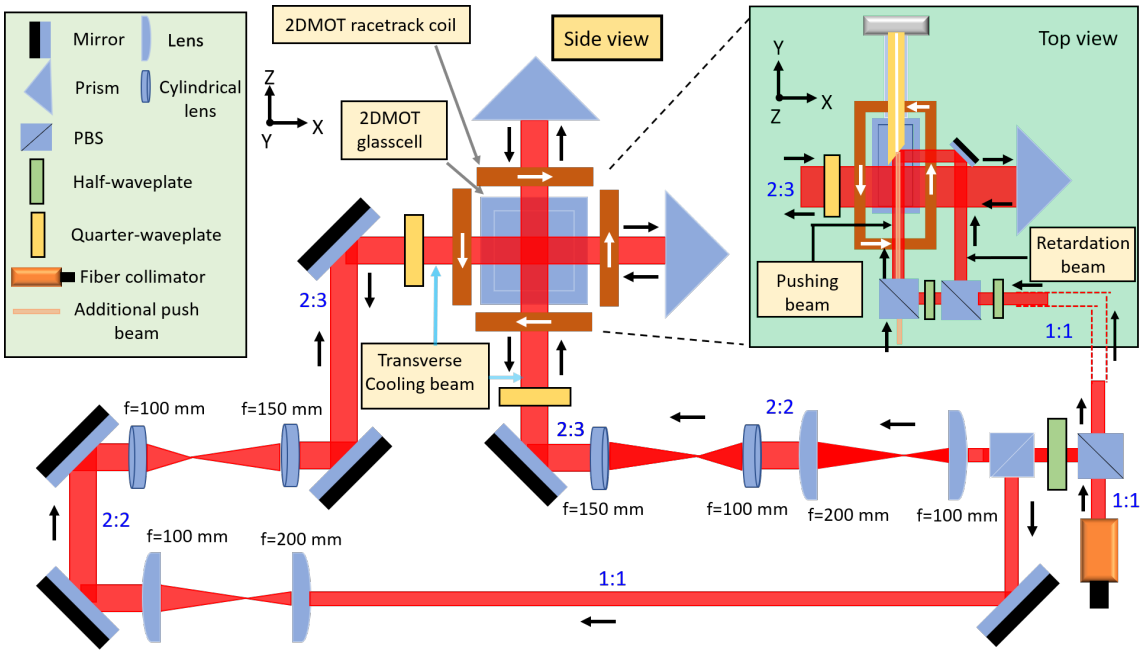


Figure 2.25: The schematic diagram of potassium 2D$^+$MOT experimental arrangement. The collimated output from the fiber collimator of diameter 12 mm is divided by a number of half-waveplate and PBS combinations. I indicate the ratio of the $\frac{1}{e^2}$ diameter of the beam on the XZ plane to the $\frac{1}{e^2}$ diameter of the beam on the XY plane at a given position. For example, quantity 1:1 corresponds to a laser beam circular cross-section of diameter 12 mm. In comparison, the quantity 2:3 corresponds to a laser beam with an elliptical cross-section of minor and major axes diameter of 24 mm and 36 mm, respectively. The white arrows indicate the direction of the current flow in the 2D$^+$MOT magnetic coils.

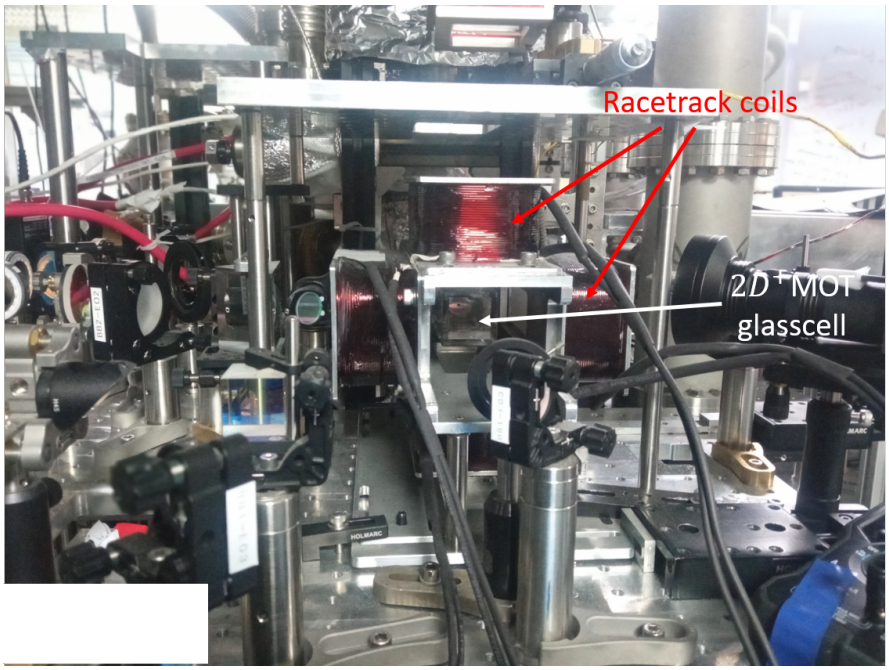


Figure 2.26: The image of the 2D$^+$MOT of potassium atoms. The glasscell and the racetrack coils to generate 2D quadrupole magnetic field configuration is indicted.

2.7 Magnetic field coils

An ultracold atom experiment requires a large number of magnetic coils. Specifically, in our 2D$^+$MOT loaded 3DMOT experiment and the subsequent transfer of cold and trapped atomic towards science, we require different sorts of magnetic coils. In particular, for 2D$^+$MOT operation, we need a 2D quadrupole magnetic field configuration. In this regard, we have designed and manufactured two pairs of racetrack coils in an anti-Helmholtz configuration. The detail of this specific type of magnetic coils and the experimental characterization of the generated magnetic fields is discussed in Appendix-A.3.

We need a spherical quadrupole magnetic field configuration for the 3DMOT and the magnetic trap operation. We generated this magnetic field configuration using two circular coils placed in an anti-Helmholtz configuration. Each coil's design, construction, and experimental characterization are described in detail in Appendix-E.

2.8 Fast switching of the current in the magnetic coils

The faster switching of magnetic coils has important consequences in ultracold atomic experiments. The absorption images of cold atoms are performed without any magnetic field to improve the signal-to-noise ratio. For absorption imaging, obtaining a high-speed switching of time ($\sim 100\,\mu$s) of the magnetic field is desirable. As mentioned, we would like to transfer ultracold sodium and potassium atoms from the 3DMOT chamber to the science cell using a moving magnetic trapping potential produced by dynamically varying currents in a series of static magnetic coils. A pair of magnetic coils in an anti-Helmholtz configuration creates magnetic potential with minimum potential at the center of the coils. Turning on and off the currents in the consecutive magnetic pairs adiabatically will transfer the trapping potential gradually toward the science cell. Thus it is crucial to get precise control over the magnetic field switching of all the magnetic transport coils. Fast and accurate switching is necessary for the efficiency of the process.

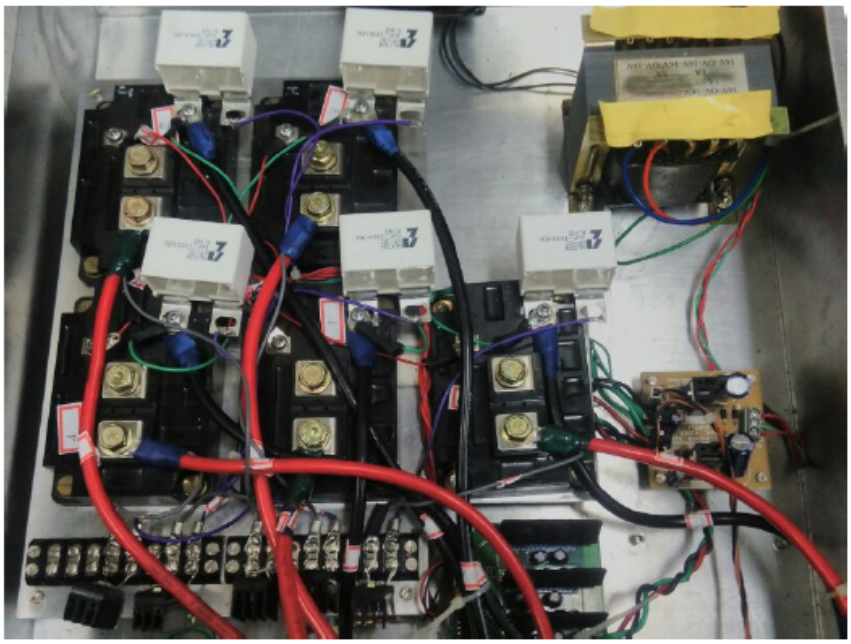


Figure 2.27: Schematic of IGBT based fast switching circuit for magnetic coils

The detail of the switching mechanism of current in the coils using the IGBT switch-

ing circuit and the circuit diagram is described in Appendix-B. The current switching dynamics of the MOT coils using the IGBT switching circuit are shown in Figure-2.28.

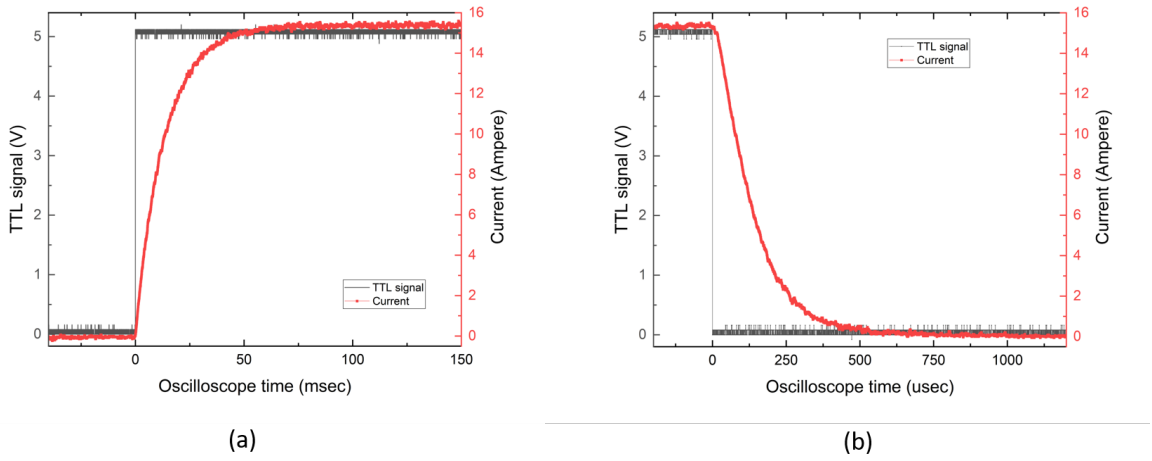


Figure 2.28: The switching characteristics of current in the MOT coil using the IGBT based switching circuit. (a) Rise and (b) fall dynamics of the current.

By using the IGBT switching circuit with the 3DMOT coils we have observed the exponential rise time of the current $\sim$ 13ms and fall time $\sim$ 150 μs.

Chapter 3

Laser cooling and trapping of neutral alkali atoms

The trapping and cooling of atoms in a magneto-optical trap (MOT) have proven to be a powerful tool for preparing an ensemble of ultracold atoms at temperatures down to several hundreds of micro-Kelvin from room-temperature atoms. Laser cooling and trapping of neutral atoms paved the way for tremendous research progress in atomic physics. Laser cooling is based on the radiative scattering force that uses the transfer of the momentum of photons of a near-resonant laser beam to the atoms. By carefully choosing the frequency of the laser in the presence of an anti-Helmholtz magnetic field configuration, we can exploit the Doppler shift to make the radiative force-velocity and position-dependent. The velocity and position-dependent optical force cools the atoms and traps them around the zero magnetic field in the anti-Helmholtz configuration.

In Section-3.1, I have given a brief overview on the concept of laser cooling of neutral atoms. This section describes the optical forces experience by the atoms in a radiation field, followed by the mechanism of the Doppler cooling, which results in the reduction of the kinetic energy of the atoms and hence cooling of the atoms. In Section-**??**, I have described the mechanism of the cooling and the trapping of atoms in a standard magneto-optical trap (MOT) [24]. In Section-3.3, I have given a description of the numerical

simulation we have performed in order to model the cold and collimated atomic beam flux in 2D$^+$MOT, we have implemented in our system.

3.1 Laser cooling of neutral atoms

Let us start with a two-level atom at rest, interacting with a well-directed laser beam of frequency ω_L, nearly resonant with the atomic transition frequency ω_0. The atom is initially in the ground state, and it absorbs a photon from a well-directed laser beam to make a transition to the excited state. As a result, it gets a momentum kick from the absorbed photon by an amount $\hbar k$, where, k is the wavevector of the light, in the direction of the laser beam, as shown in Figure-3.1(a).

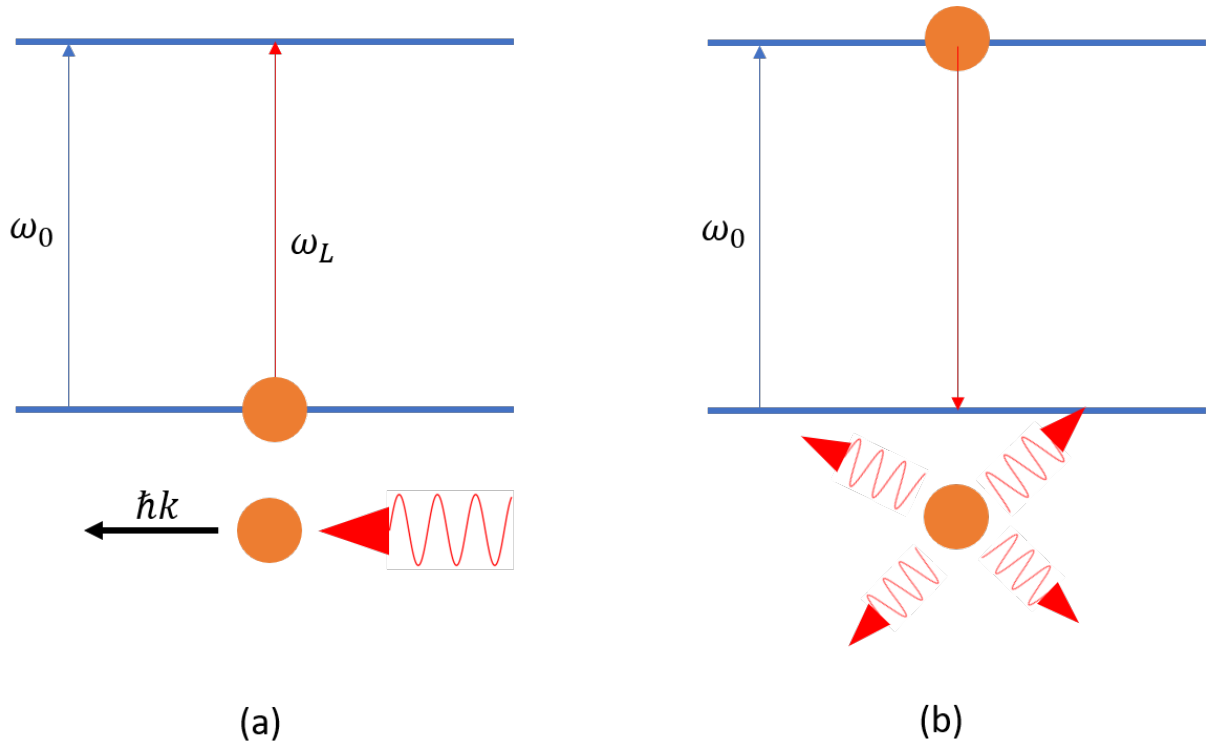


Figure 3.1: A resonant laser beam interacts with a two-level atomic system. The atom absorbs a photon from the laser beam and gets a momentum kick by an amount $\hbar k$ towards the direction of the laser beam. (b) The excited atom emits a photon via spontaneous emission. The direction of the spontaneously emitted photon is random and could be directed in any direction.

The excited atom makes a transition to the ground state by spontaneously emitting a photon in a time scale ($\sim \tau$) determined by the linewidth (Γ) of the transition, where $\tau = \frac{1}{\Gamma}$. The spontaneously emitted photon can be released randomly in any direction Figure-3.1(b). Therefore, after many cycles of absorption of photons from the well-directed laser beam and subsequent spontaneous emissions, the net momentum change due to spontaneously emitted photons averages out to be zero. The atom experiences only a net change of momentum along the direction of the laser beam.

Optical forces on the atoms

The radiation field of the laser beam imparted momentum when an atom absorbs photons from the well directed laser beam and results in a radiative force [50],

$$\vec{F} = \hbar\vec{k}\, R_s \tag{3.1}$$

Where $\hbar\vec{k}$ is the momentum carried by each photon and R_s is the scattering rate of the photons by the atom. The scattering rate determines the number of photons absorbed by the atoms per second from the light field.

The value of R_s depends on the detuning between the frequency (ω_L) of the laser and the atomic transition frequency (ω_a), i.e., $\delta_0 = \omega_L - \omega_a$ which is measured in the rest frame of the atom, and on the intensity of the laser beam. Here we are considering the case, $\omega_L < \omega_0$, therefore, $\delta_0 < 0$. For two-level atoms the value of R_s is given by the Lorentzian [50],

$$R_s = \frac{\Gamma}{2}\frac{s}{1 + s + (\frac{2\delta_0}{\Gamma})^2} \tag{3.2}$$

Where, $s = \frac{I}{I_s}$ is the saturation parameter. The quantity s is the ratio of the intensity of the laser beam to the saturation intensity of the atomic transition (I_s) under consideration. The saturation intensity of the atomic transition is expressed by, $I_s = \frac{\pi hc}{3\lambda^3\tau}$. The value of I_s is of the order of few mW/cm^2 for the atomic transitions of the alkali atoms.

Doppler cooling

So far we have been considering an atom at rest and interacting with a single laser beam. Let us assume that, the atom is at rest and interacting with two counter-propagating laser beams. Let us also consider the laser frequency is tuned below the atomic transition frequency i.e. red-detuned ($\delta_0 < 0$). One of the laser beam is propagating along $+\hat{z}$ axis while the other one is propagating along $-\hat{z}$ axis as shown in Figure-**??**(a). The atoms will experience same scattering rate of the photons from both the laser beams.

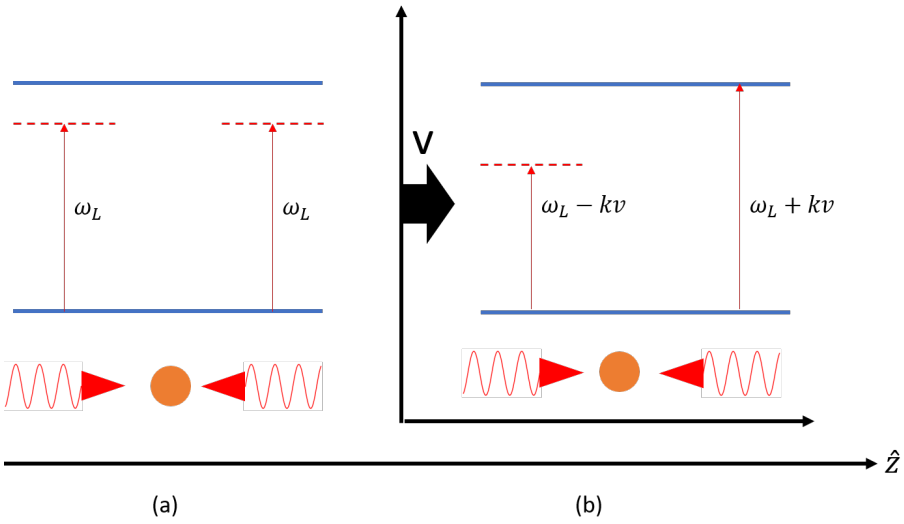


Figure 3.2: (a) Two counter-propagating red detune laser beams interacting with a two-level atom at rest. The atom absorbs a photon from the laser beam and gets a momentum kick by an amount $\hbar k$ towards the direction of the laser beam. (b) The atom is moving with a velocity v along $\hat{z}$ direction. Due to Doppler shift the atom encounter more scattering from the laser beam moving counter-propagating compared to the laser beam co-propagating with the atom.

Now consider the atom is moving with a velocity v along $\hat{z}$ direction. Therefore, the laser beam moving towards $\hat{z}$ direction is co-propagation with the atoms while the laser beam propagating towards $-\hat{z}$ direction is counter-propagating to the atoms. Due to the Doppler shift, the atoms will experience the laser beam moving along $\hat{z}$ direction as red-detuned while the laser beam moving along $-\hat{z}$ direction as blue-detuned in its rest frame. Therefore, in the rest frame of the atom, the detuning appears to be $\delta_+ = \delta_0 - |\vec{k}.\vec{v}|$

and $\delta_- = \delta_0 + |\vec{k}.\vec{v}|$ for the beam propagating along $+\hat{z}$ and $-\hat{z}$ direction respectively.

The optical force experienced by the atom from the co-propagating beam is given by [50],

$$\vec{F_+} = \hat{z}\ \hbar\vec{k}\,\frac{\Gamma}{2}\frac{s}{1+s+(\frac{2\delta_+}{\Gamma})^2} \tag{3.3}$$

and the optical force experienced by the atom from the counter-propagating beam is,

$$\vec{F_-} = -\hat{z}\ \hbar\vec{k}\,\frac{\Gamma}{2}\frac{s}{1+s+(\frac{2\delta_-}{\Gamma})^2} \tag{3.4}$$

The optical force acting on the atoms due to the two counter-propagating laser beams is shown in Figure-3.3.

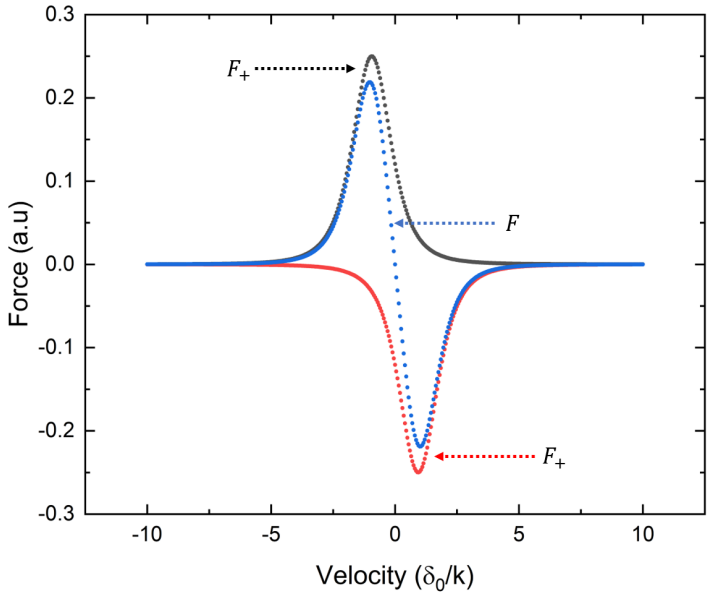


Figure 3.3: The force on an atom in optical molasses. The force experienced by the atom from the co-propagating laser beam is denoted by F_+, while the force acting on the atom by the counter-propagating laser beam is indicated by F_-. The damping of the atomic motion is governed by the slope of the resultant force (F) at $v = 0$.

Therefore, the resultant force acting on the atoms is given by,

$$\begin{aligned}\vec{F} &= \vec{F_+} + \vec{F_-} \\ &= \frac{4\hbar\, k^2\, \delta_0}{\Gamma^2} \frac{s}{(1+s+(\frac{2\delta_0}{\Gamma})^2)^2}\, \vec{v} \\ &= -\beta\, \vec{v} \end{aligned} \tag{3.5}$$

in the limit $|\vec{k}.\vec{v}| << \Gamma$. Therefore, the force on the atom is proportional to the velocity with the damping coefficient β.

The optical force dampens the atomic motion, reducing the atom's velocity. In other words, the optical forces cool the atoms. This arrangement of optical force on the atoms is called optical molasses since it acts like a viscous fluid on the atomic motion.

3.2 The cooling and trapping atoms in a MOT

The basic principle of a MOT can be illustrated by considering a simple two-level atomic system with hyperfine quantum numbers, $F = 0$ in the ground state and $F = 1$ in the excited state as shown in Figure-3.4.

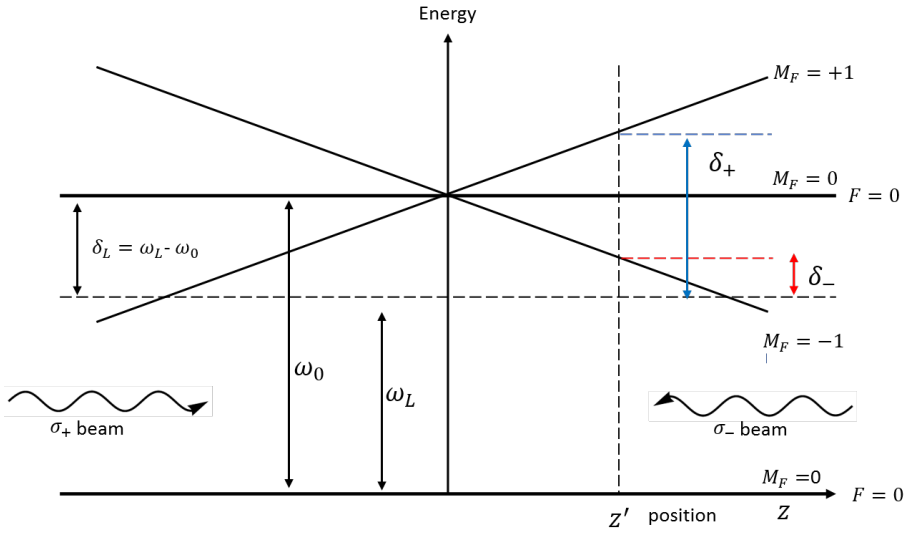


Figure 3.4: The arrangement of a MOT in 1D. The horizontal dashed line(black) represents the laser frequency seen by an atom at rest in the trap's center. The Zeeman shifts of the atomic transition frequencies in the inhomogeneous magnetic field $B(z) = bz$. Therefore, atoms at $z = z'$ are closer to resonance with the σ^- laser beam than with the σ^+ beam and are therefore driven toward the center of the trap.

In a weak inhomogeneous magnetic field, $B(z) = b\,z$, b is the gradient of the magnetic field, the magnetic hyperfine quantum states (M_F) are split by the Zeeman effect. The energy levels are shifted by an amount $\Delta E(z) = g_F m_F \mu_B B(z)$, where g_F is the hyperfine Lande-g factor, μ_B is the Bohr magneton. We assume the quantization axis is along $\hat{z}$. Now illuminate the atom with weak collimated laser beams: one is σ^- polarized and propagating along $-\hat{z}$ direction. The other one is σ^+ polarized and propagating along $+\hat{z}$ direction. The frequency (ω_L) of both the laser beams is tuned below the atomic resonance frequency (ω_0). We are considering the the value of ω_0 is at zero magnetic field. The detuning of the laser beam is defined as $\delta_L = \omega_L - \omega_0$ (as indicated by the horizontal

black dotted line in Figure-3.4.

Let us consider an atom at the ground hyperfine state, $F = 0$, and at the position $z'(> 0)$. The atoms is exposed to both the laser beams: σ^- polarized beam propagating along $-\hat{z}$ direction and σ^+ polarized beam propagating along $+\hat{z}$ direction. The Zeeman shift at the position z' makes the frequency (ω_L) of the laser beam less detuned to the excited state energy level $|F = 1, M_F = -1\rangle$ compared to the energy level of the state $|F = 1, M_F = +1\rangle$. As a result, the atom will scatter more photons from the σ^- polarized laser beam than σ^+ polarized laser. Hence, the atom will feel a net radiative force towards the center ($z = 0$). For an atom at a position $z < 0$, the Zeeman shifts are reversed, and the atom will absorb more photons from the σ^+ polarized. As a result, the atoms will experience a radiative force toward the center.

Therefore, the arrangement of a magneto-optical trap cools the atoms by using the viscous force of the optical field: at the same time, the position-dependent radiation pressure imbalanced will push the atoms toward the center (the position of the zero magnetic field), and trapped them around the center. Therefore, in a MOT, the effective detuning becomes position and velocity dependent,

$$\delta_{\pm}^{M}(\vec{v}, \vec{r}) = \delta_L \pm \vec{k}.\vec{v} \mp \frac{\mu_B B(r)}{\hbar} \tag{3.6}$$

Where $|\frac{\mu_B B(r)}{\hbar}|$ represents detuning due to the Zeeman shifts of the energy level in the magnetic field at the position z.

The resultant force on an atom in a MOT can be written as,

$$\vec{F_M} = \vec{F_+^M} + \vec{F_-^M} \tag{3.7}$$

Where the force on the atom along $+\hat{z}$ direction is given by the expression,

$$\vec{F_+^M} = \hat{z}\hbar\vec{k}\,\frac{\Gamma}{2}\frac{s}{1 + s + (\frac{2\delta_+^M}{\Gamma})^2} \tag{3.8}$$

While the force on the atoms along $-\hat{z}$ is,

$$F_{-}^{\vec{M}} = -\hat{z}\hbar\vec{k}\frac{\Gamma}{2}\frac{s}{1+s+(\frac{2\delta_{-}^{M}}{\Gamma})^2} \tag{3.9}$$

An arrangement of a three dimensional magneto-optical trap (3DMOT) is shown in Figure-3.5. A 3DMOT consists of three pairs of counter-propagating laser beams in the presence of a three dimensional quadrupole magnetic field.

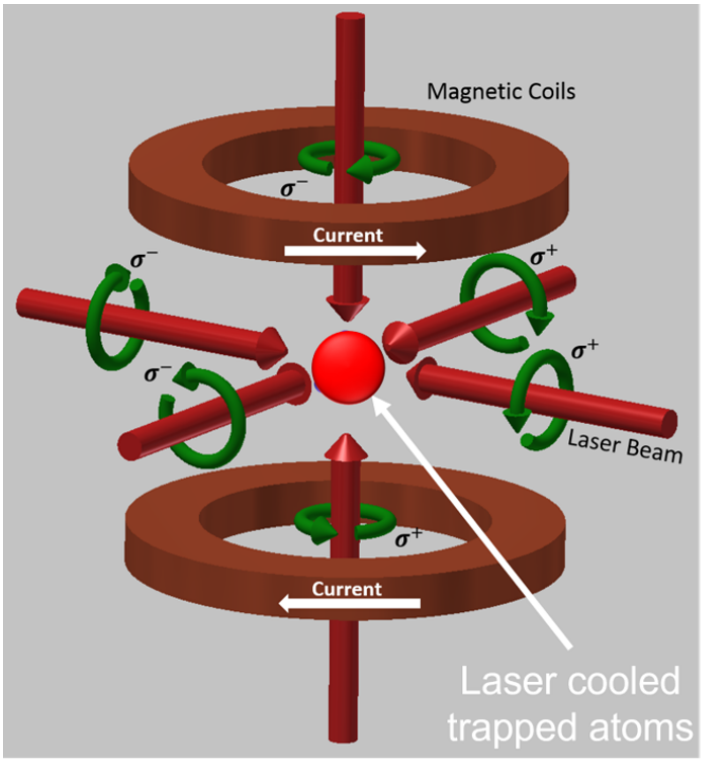


Figure 3.5: A schematic diagram of a 3DMOT. Three pairs of circularly polarized counter-propagating lasers beam are directed towards the position of zero magnetic field of a three dimensional quadrupole magnetic configuration.

3.3 Modelling of the cold atomic beam flux of the 2D$^+$MOT

Equipped with the concepts of the laser cooling and trapping of atoms in a MOT, now we will model the cold and collimated atomic beam that we have generated in the 2D$^+$MOTs of ^{23}Na and ^{39}K atoms.

In the simulation, we have consider a two-level atomic system and calculate the position and the velocity of the atoms in the cooling volume using the optical force as given Eqn.3.7 acting on the atoms. As discussed in Section-2.3.2, let us recall that, the 2D$^+$MOT consists of two pairs of transverse cooling beams in the presence of 2D quadrupole magnetic field configuration, and two counter-propagating laser beams: pushing and retardation beams. The pushing beam is directed along the atomic beam direction towards the 3DMOT.

Let us consider Figure-3.6, a schematic diagram of the longitudinal view of the 2D$^+$MOT, generating cold and collimated atomic beam and loading the 3DMOT.

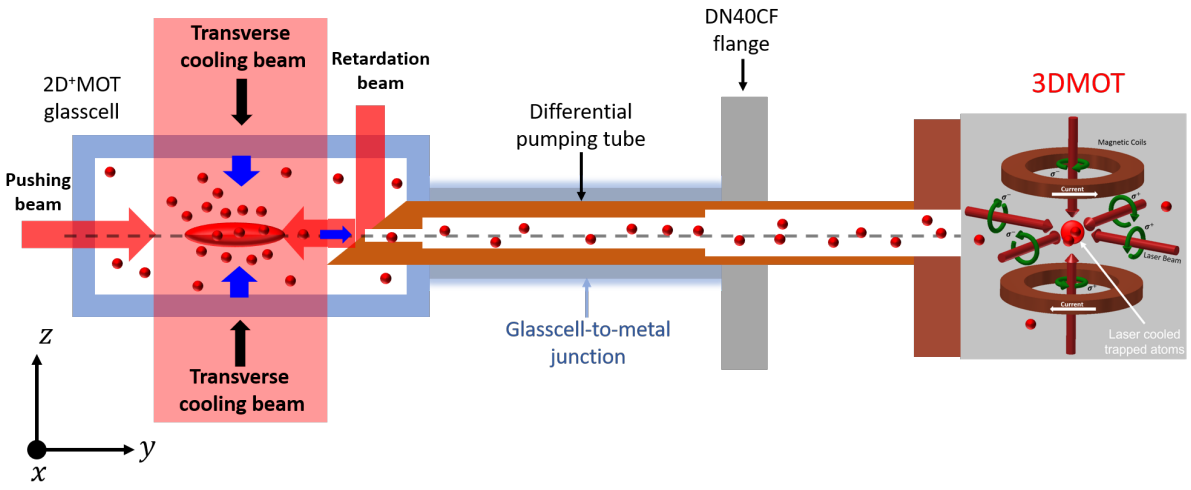


Figure 3.6: A schematic diagram of a 3DMOT loaded by the cold and collimated atomic beam produced by the 2D$^+$MOT.

To assign the initial position and the velocity to the atoms, we have assumed that, the glasscell is uniformly filled with the alkali atoms at temperature T_{vapor}. Therefore, we have chosen the initial position of the atoms randomly within the 2D$^+$MOT glass cell.

For this purpose, we have discarded the portion of the glasscell where the front face of the differential pumping tube protrudes out into the glass cell. We have assigned the initial velocity to the atoms according to Maxwell-Boltzmann (MB) velocity distribution at temperature T_{vapor} using the Monte Carlo method.

In the simulation, we consider the trajectories of the atoms having velocities less than the capture velocity (v_c) of the 2D$^+$MOT. We have determined the capture velocity using the equation of motion, $v_f^2 = v_{int}^2 - 2as$, where, s is the distance. We assume the final velocity, $v_f \sim 0$, we obtained,

$$v_{int} = \sqrt{2a\, D_{MOT}} \tag{3.10}$$

Where, v_{int} is the initial velocity of atoms in the glasscell, D_{MOT} is the diameter of the transverse cooling MOT beams, and a is the deceleration on the atoms.

Therefore, the capture velocity of the MOT corresponds to $v_c \approx v_{int}$. The deceleration is calculated using the formula Eqn.3.1 as $a = \frac{|\vec{F}|}{m}$, where m is the mass of the atoms. Using the experimental parameters of 2D$^+$MOT: the intensity, detuning, and diameter of the cooling beam, we have calculated the value of v_c. For example, with the experimental parameters used in our system, we obtained $v_c \approx 150$m/s for ^{23}Na and $v_c \approx 50$m/s for ^{39}K.

Optical force imparted on the atoms

As mentioned earlier, in order to calculate the force on each of the atoms we have numerically solved the equation Eqn.3.7. To model the optical force on ^{23}Na and ^{39}K atoms, we are considering a two-level atomic system and assuming the transverse cooling beams are exciting $|F = 2, M_F = 2\rangle \rightarrow \left|F' = 3, M_F^{'} = 3\right\rangle$ transition in both the 2D$^+$MOTs. Therefore, we have employed the following form of the expression of the effective detuning in the optical force equations Eqn.3.7, Eqn.3.8, and Eqn.3.9 rather than using Eqn.3.6,

$$\delta_{\pm}^{M}(\vec{v}, \vec{r}) = \delta_L \pm \vec{k}.\vec{v} \mp \frac{\mu_{eg} B(r)}{\hbar} \tag{3.11}$$

Where, $\mu_{eg} = (g_e\, M_{Fe} - g_g\, M_{Fg}) \times \mu_B$, is the difference of the magnetic dipole moment between the excited and the ground states. We obtained, $(g_e\, M_{Fe} - g_g\, M_{Fg}) = 1$ for the D_2 optical transition for both the atomic species.

We first assign an initial position and an initial velocity to each of the atoms. Thereafter, we solve the optical force equation Eqn.3.7 on each of the atoms by employing the Runge-Kutta 4th order ($RK4$) method to find the position and velocity of the atoms with time. The mapping of the resultant positions with time yields the trajectories of each of the atoms. The atoms experience a velocity and position-dependent force around the zero magnetic field line on the transverse plane ($x - z$ plane) due to two pairs of transverse cooling beams in the presence of the 2D quadrupole magnetic field. On the other hand, there is no magnetic field along the longitudinal direction, which is the resultant cold atomic beam direction. Therefore, the force along the longitudinal direction (y-axis) is purely optical, which arises due to the overlapping of the pushing and retardation beams. We have taken into consideration the contributions of all the resultant forces in the model and solved the equation of motion of the atoms.

Results of the numerical simulation

We have performed the numerical simulation on 10^5 atoms. The resultant trajectories of the atoms from the 2D$^+$MOT is shown in Figure-3.7.

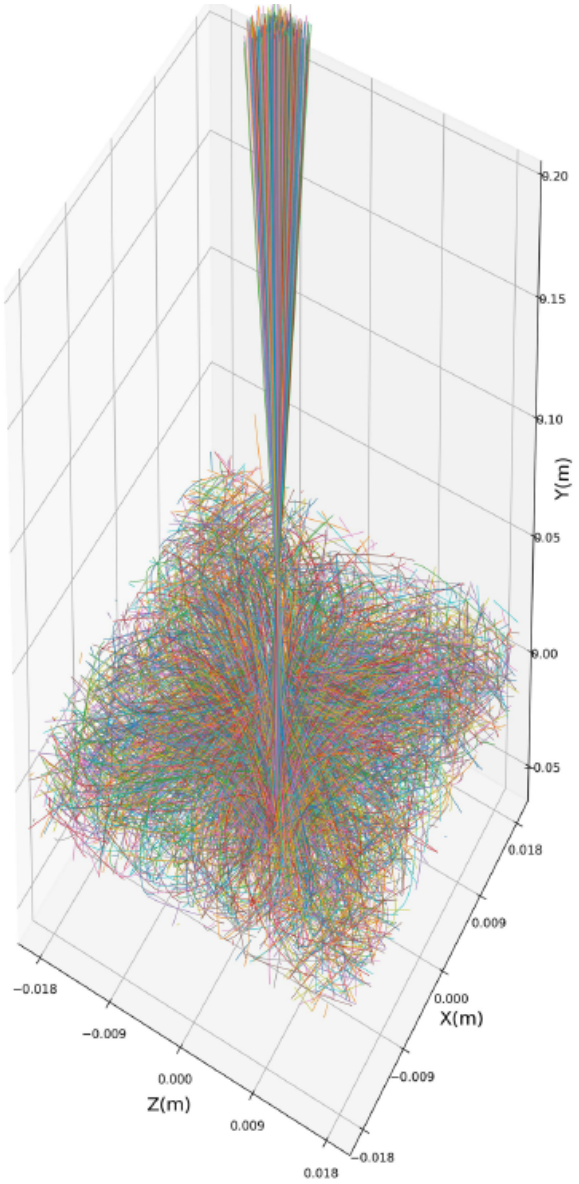


Figure 3.7: The trajectories of the atoms emerging from the 2D$^+$MOT.

The dynamics of the atoms in the 2D$^+$MOT is nicely captured by the numerical simulation. As can be seen, the initial spatial distribution of the atoms is widely spaced in the smaller values of y-axis, i.e., at the beginning of the transverse cooling beams. As

the atom is moving forward, i.e. towards higher value of y, we have observed a gradual reduction of the orbit of the atoms on the transverse plane around the line of zero magnetic field. The reduction of size of the orbit demonstrates the reduction of the velocity of the atoms on the transverse plane. From the numerical simulation, we have also observed a gradual reduction of the longitudinal velocity of the atoms as the atoms are moving in the longitudinal optical molasses towards the hole of the differential pumping tube.

Figure-3.8 shows the distribution of the atoms' position on the transverse plane $(x-z)$ at the position of the 3DMOT.

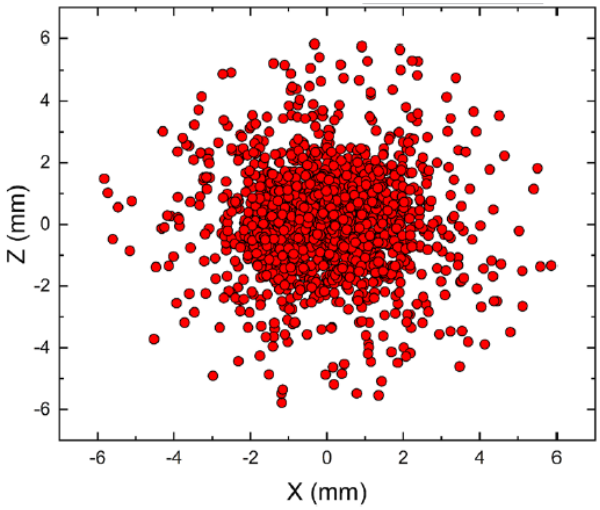


Figure 3.8: The distribution of the atoms emerging from the $2D^{+}$MOT on the transverse plane at the position of the 3DMOT.

The smaller spatial extension of the distribution demonstrates the collimation nature of our cold atomic beams emerging from the $2D^{+}$MOT.

Therefore, the numerical simulation nicely model the formation of the cold and collimated atomic beam in a $2D^{+}$MOT from a uniform distribution of the alkali atoms.

Chapter 4

Experimental realization of a dual-species magneto-optical trap

In this chapter, I will describe the experimental arrangement of the single species 3DMOT of the sodium and potassium atoms. After that, I will describe the underlying dynamics of a dual-species 3DMOT of sodium and potassium atoms. We have studied intra and inter-species collisional dynamics of the cold and trapped sodium and potassium atoms in dual-species 3DMOT in great detail.

I have organized the description of the characterization of this machine as follows: Section-4.2 describes the measurement techniques we have implemented to determine the number of trapped atoms in the individual 3DMOTs. In Section-4.3, I have described all the relevant experimental parameters of the $2D^{+}$MOT and systematic variation of the parameters to obtain the best possible loading rate and a large number of the trapped atoms in the 3DMOT. I have discussed the loading dynamics and the underlying collisional mechanisms present in the single species 3DMOT of sodium and potassium in detail in Section-4.4 and determined the intraspecies collisional rate from the experimental data. In Section-4.5, I have described the interspecies collisional dynamics of sodium and potassium in the dual-species 3DMOT. We observed the loss of trapped sodium in the presence of the potassium atoms in the dual-species 3DMOT. We determined the interspecies collisional

cross-section from the dynamics of the dual-species 3DMOT.

4.1 The description of the experimental arrangement of the magneto-optical trap

The experimental arrangement of the 3DMOT of sodium and potassium atoms is depicted in Figure-4.1 and Figure-4.2. We employed retro-reflection configurations for both the 3DMOTs. One of the advantages of this configuration is that it requires less total power compared to the six independent MOT beams configuration. Still, it may restrict the power balance.

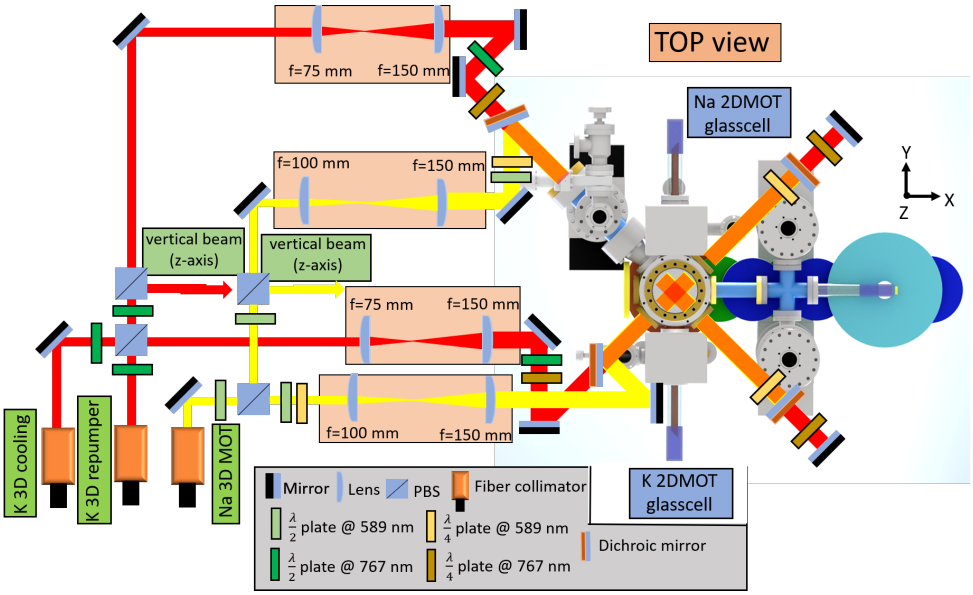


Figure 4.1: The top view of the layout of the experimental arrangement of sodium and potassium 3DMOTs. The laser beams required for the 3DMOT are out-coupled from the PM fibers. In the case of potassium, we merged the cooling and the repumper beams using PBS, while for sodium, we have a single fiber. The output beam of respective fiber collimators is divided into three beams using half-waveplates. Each of the beams is sent through a telescopic expansion and directed along three orthogonal directions. The sodium and potassium beams are made to overlap using a dichroic before injecting into the 3DMOT chamber along three orthogonal directions.

The MOT beams are derived from the collimators of individual PM optical fibers. We have an optical table dedicated to the laser systems as described in detail in Section-2.5. The prepared laser beams from the respective AOMs are transferred to the main experimental table using respective PM optical fibers. The laser beams are out-coupled from the fibers using fiber collimators. We obtained collimated laser beams from the fiber collimators of $\frac{1}{e^2}$ diameter of 12 mm for both species.

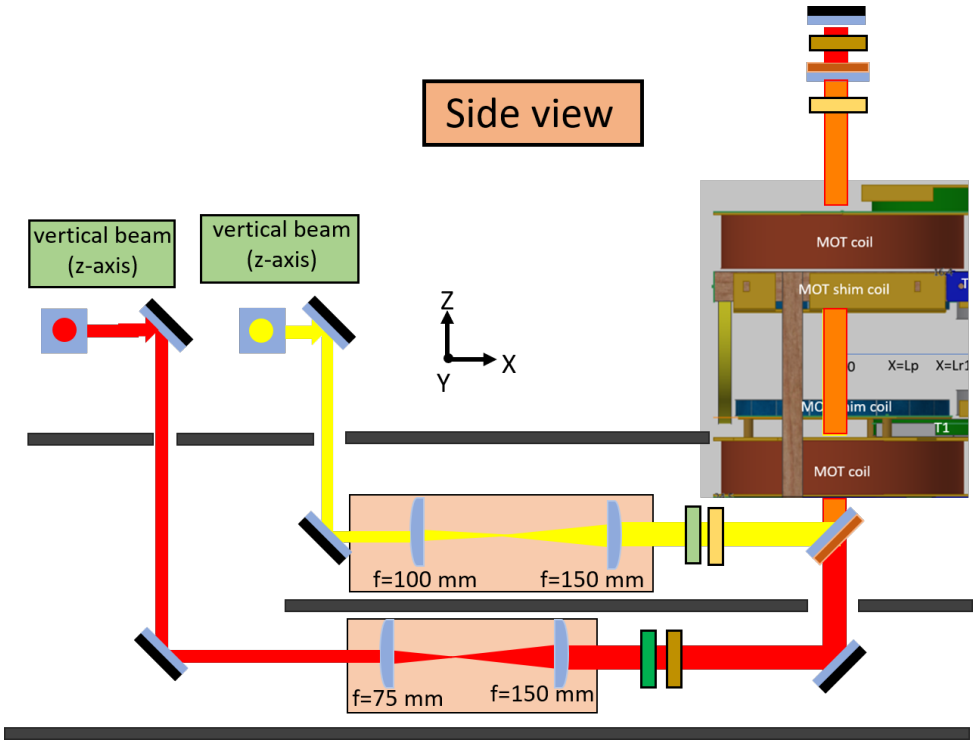


Figure 4.2: The side view of the layout of the experimental arrangement of sodium and potassium 3DMOTs. This projection shows the configuration and path of the 3DMOT beams along the vertical direction. The prepared vertical beams of sodium and potassium 3DMOTs are made to overlap using a dichroic mirror before injecting into the vacuum chamber.

As describe in Section-2.5, we prepared the repumper transition for the Na-3DMOT (and 2D$^+$MOT) by sending the cooling beam (the double-pass output of the AOM dedicated to tuning the frequency to the cooling transition), through a 1.7 GHz EOM. The output laser beam from the EOM contains both transition frequencies: cooling and re-

pumper. We inject the laser beam for the 3DMOT cooling and repumper into a PM fiber. In contrast, for the potassium, we have prepared the 3DMOT cooling and repumper laser beams from two separate lasers Section-2.5. The 3DMOT cooling and repumper beams are injected into respective PM fibers. Two independent fiber collimators out-coupled the laser beams from the respective PM fibers on the experimental table. We overlap the 3DMOT cooling and repumper beam using a polarizing beam splitter (PBS).

A series of half-waveplates($\frac{\lambda}{2}$-plates) and PBSs are used to divide the main beam of sodium and potassium into three beams, corresponding to three orthogonal directions of the sodium and potassium MOTs. The $\frac{\lambda}{2}$-plates distribute power among the three beams. We measure the power of all three beams in front of the viewports of the 3DMOT chamber and, typically, maintain equal power in all of the beams. We expand each of beam (for both sodium and potassium) by employing a telescope on each of the paths of the 3DMOTs. For sodium 3DMOT(Na-3DMOT), for each of the telescopes, we have used two anti-reflection coated spherical plano-convex lenses of focal lengths 100 mm, followed by a 150 mm lens, which yields 1.5× magnification. Therefore, the size of each of the Na-3DMOT beams becomes 18 mm ($\frac{1}{e^2}$ diameter). On the other hand, for potassium 3DMOT(K-3DMOT) beams, we have used two anti-reflection coated spherical plano-convex lenses of focal lengths 75 mm, followed by a 150 mm lens for each of the telescopes. Therefore, we obtain 2× magnification, and the size of each of the K-3DMOT beams becomes 24 mm ($\frac{1}{e^2}$) diameter as shown in Figure-4.1 and Figure-4.2. As mentioned earlier, one of our major goal is to obtain a dual-species 3DMOT of sodium and potassium atoms and study the inter-species collisional dynamics. Therefore, getting a perfect overlapping of both 3DMOTs is the utmost requirement. To fulfill the purpose, we must have a perfect overlap of all the three 3DMOT beams of both species along the three orthogonal directions of the 3DMOTs. We placed a dichroic mirror (DMLP650, Thorlabs) before each viewport. This specific mirror has a cutoff at 650 nm: it reflects the lights below the given wavelength and transmits them above the specified wavelength.

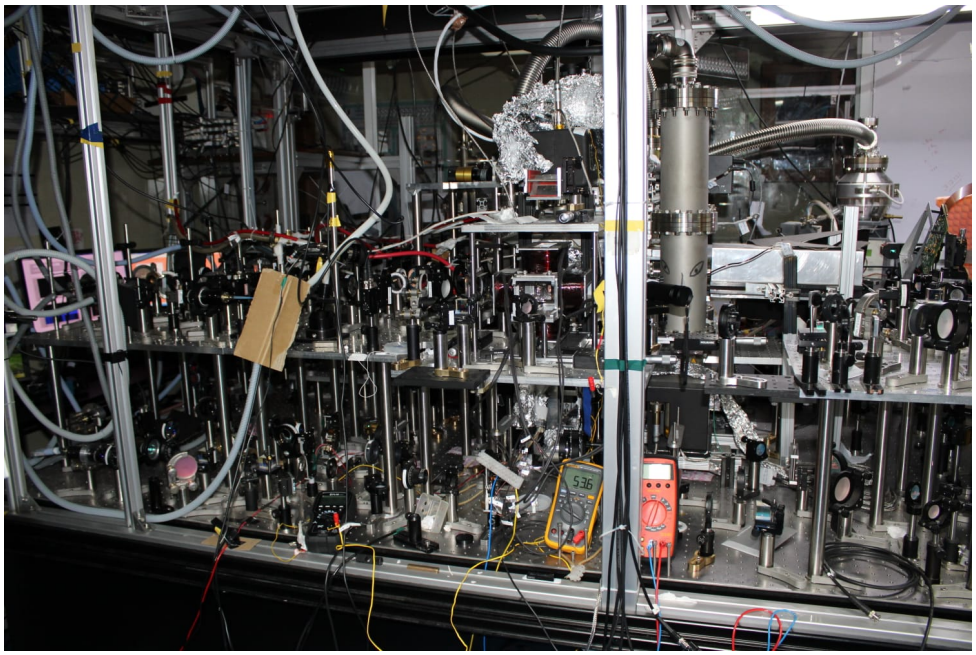
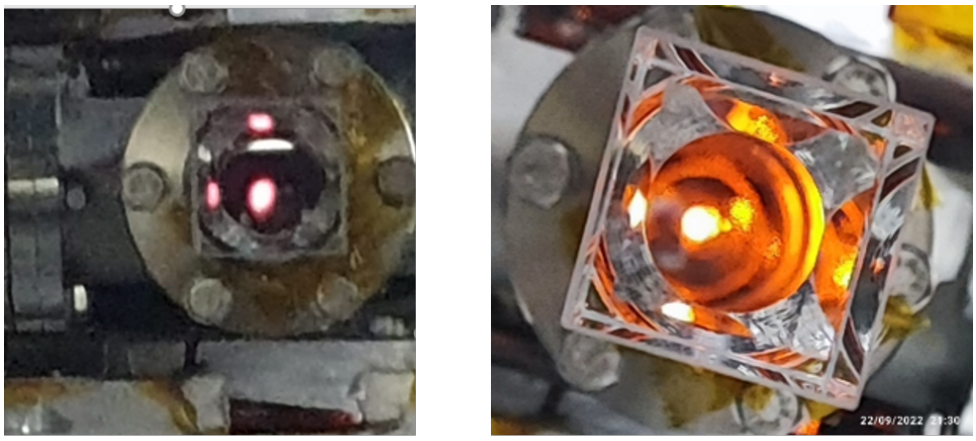


Figure 4.3: The arrangement of the 3DMOT on the experimental table for both the species: sodium and potassium.

Therefore, for our experimental conditions, this mirror reflects the laser beams used for Na-3DMOT (589 nm) and transmits the laser beams used for K-3DMOT (767 nm). We have carefully designed our optical layout. As shown in Figure-4.1 and Figure-4.2, we have aligned all the Na-3DMOT beams such that they get reflected from the dichroic mirrors and injected into the vacuum chamber through the viewports. All the K-3DMOT beams are aligned so that they are incident on the dichroic mirrors, transmitted through the dichroic mirrors, and overlapped with the laser beams of the Na-3DMOT. We employed several mirrors for both species for each of the 3DMOT beams, which helped us obtain a good overlapping of the 3DMOT beams downstream of the dichroic mirrors.



(a) (b)

Figure 4.4: Images of (a) potassium and (b) Na-3DMOT in the 3DMOT chamber. The images were capture through the 'science cell' by a smartphone.

To obtain a stable 3DMOT, it is required to get an excellent circular polarization for all the MOT beams. With a combination of a $\frac{\lambda}{2}$-plate and a $\frac{\lambda}{4}$-plate of respective wavelengths on each of the incoming beams of the 3DMOT, we obtain a high degree of circular polarization for both the atomic species. The position of the waveplates is shown in Figure-4.1 and Figure-4.2. We measured the degree of circular polarization using a polarizer, and we obtained better than 90% purity for all the MOT beams. In the downstream, for each of the 3DMOT beams, we placed a $\frac{\lambda}{4}$ at 589 nm followed by a dichroic mirror, which retro-reflect the Na-3DMOT beams and tuning the tuning knobs of the mirror mounts, we made sure they are overlapped with the incoming laser beam throughout the vacuum chamber. The laser beams for the K-3DMOT transmitted through all the dichroic mirrors: just behind the dichroic mirrors, we placed $\frac{\lambda}{4}$ at 767 nm, followed by a dielectric mirror. The dielectric mirrors are aligned carefully to ensure a good overlap with the incoming K-3DMOT beams.

4.2 Experimental arrangement to determine number of atoms trapped in the 3DMOT

In this section, I will describe our procedure to detect and determine the total number of atoms trapped in the 3DMOT. We have determined the number of trapped cold atoms in the 3DMOT by capturing the fluorescence photons emitting from the trapped cold cloud. Typically, with the imaging system, we could only capture a fraction of the total number of photons emitted by the trapped atoms in the 3DMOT. The fraction of the photons captured by the imaging system depends on the solid angle subtended by first collection lens (of the imaging system) onto the 3DMOT's position. Figure-4.5 represents the schematic diagram of the detection system we have implemented for the fluorescence measurements. In our detection system, we have two detectors: one charge-coupled-device (CCD) camera (CS2100M-USB Quantalux 2.1 MP, Thorlabs) and a Femtowatt photo-detector (FWPD) (2151, Newport). The photons emitted from the cold atoms are collected by the first lens of the imaging system and followed by a PBS, which divides the power of the fluorescence into two parts. The transmitted part is focused on the CCD camera by using a lens, while the reflected part is focused on the FWPD.

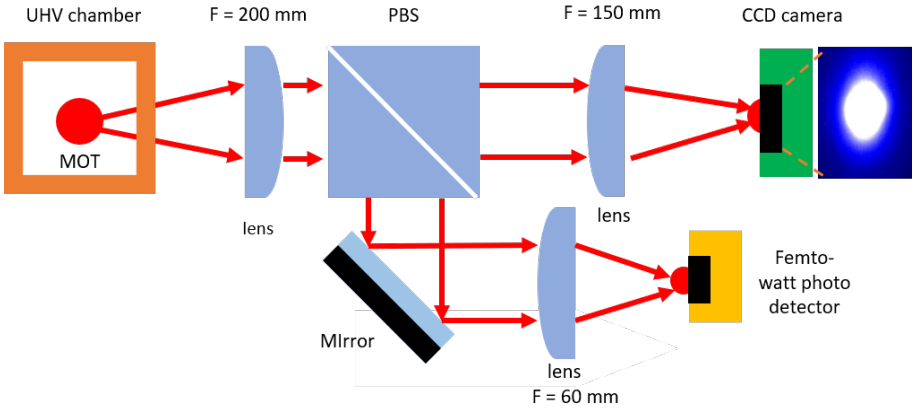


Figure 4.5: Schematic diagram of fluorescence imaging setup. The first lens captures the fluorescence emitted by the cloud of atoms. The first lens is placed such that the MOT is located at its focal length. The collimated output of the fluorescence is divided into two arms by a polarization beam splitter. The transmitted arm, followed by a lens, falls on the CCD camera. The reflected component, followed by one mirror reflection and a lens incident on a Femtowatt detector.

Eqn.3.2 represents the scattering rate of photons from an atom when the atoms are interacting with a laser beam with detuning δ_0 and saturation parameter s (already defined). In a 3DMOT, a cold atom interacts with three pairs of counter-propagating laser beams. Therefore, the scattering rate is modified as,

$$R_s = \frac{\Gamma}{2}\frac{6\,s}{1+6\,s+(\frac{2\delta_0}{\Gamma})^2} \tag{4.1}$$

In a 3DMOT, an atom absorbs a well-directed photon and subsequently emits a photon of energy $h\nu$ by spontaneous emission. The amount of energy emitted by an atom per second (or the power) is given by $R_s \times h\nu$.

If there are N^{at} number of cold atoms trapped in the 3DMOT, then the total number of photons emitted by the MOT fluorescence per second is given by,

$$N^{ph}_{tot} = N^{at} \times R_s \tag{4.2}$$

The spontaneous emission from an atom is isotropically distributed in 4π solid angle. Therefore, the total number of photons, N_{tot}^{ph}, emitted from the 3DMOT isotropically, while the amount of photon captured by the detection system is determined by the solid angle subtended by the first lens of the detection system as shown in Figure-4.5.

The solid angle subtended by the first lens onto the 3DMOT is given by,

$$\Omega_s = \frac{\pi r^2}{f^2} \tag{4.3}$$

Where r is the radius of the lens and f is the focal length of the lens.

Therefore, the number of photons collected by the first lens is given by,

$$N_{det}^{ph} = \frac{\Omega_s}{4\pi} N_{tot}^{ph} \tag{4.4}$$

Replacing the expression of N_{tot}^{ph} from Eqn.4.2 into Eqn.4.4, we arrived at the equation,

$$N_{det}^{ph} = \frac{\Omega_s}{4\pi} N^{at}\, R_s \tag{4.5}$$

Therefore, the amount of fluorescence power captured by the detection system is given by,

$$P_{det} = N_{det}^{ph} \times h\nu \tag{4.6}$$

Rearranging Eqn.4.5, we arrived at the expression of the total number of trapped atoms in the 3DMOT becomes,

$$N^{at} = \frac{4\pi}{\Omega_s} \frac{N_{det}^{ph}}{R_s} \tag{4.7}$$

The second lens of the imaging system focuses the captured fluorescence on the Charge Coupled Device (CCD) camera (and the photo-detector). In the following subsections, I will describe the procedure to determine the number of atoms trapped in the 3DMOT from the captured images obtained using the CCD camera and the voltage signal generated using FWPD.

4.2.1 Determination of atoms number using CCD camera

A CCD camera consists of an array of pixels. When photons incident on these pixels, each pixel generates electron counts depending on the number of photons incident on the pixel over exposure time of the camera and the camera's quantum efficiency.

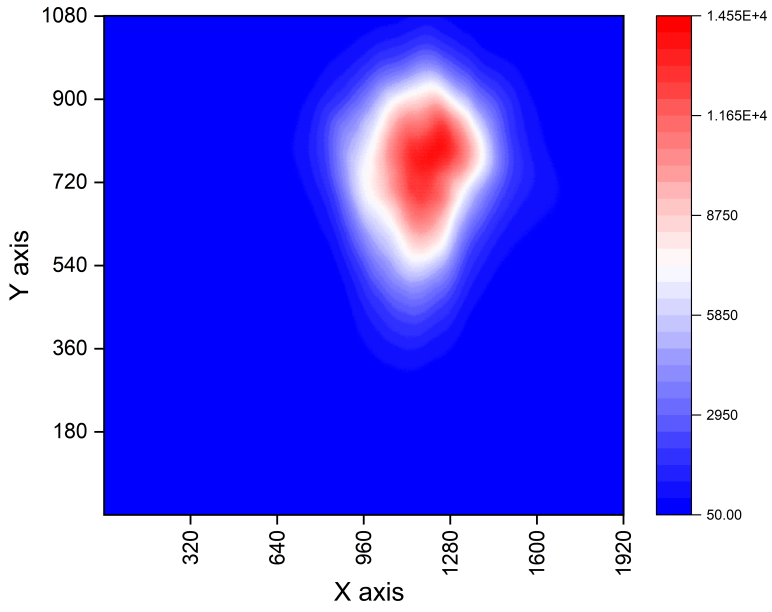


Figure 4.6: The captured fluorescence image of the 3DMOT in the CCD camera. The CCD camera has 1920 pixels along the X-axis and 1080 pixels along the Y-axis. The heat map shows the generated counts in each pixel.

Therefore, the sum of the counts (N_c^{det}) generated by all the pixels of the CCD camera is a measure of the number of the photons capture by the imaging system, N_{det}^{ph}, of Eqn.4.7. We can write,

$$N_c^{det} = \sum_{1 \leq i,j \leq (1920,1080)} n_{i,j} \tag{4.8}$$

Where, $n_{i,j}$ is the electron count generated in the (i, j) pixel of the CCD camera. The sum is over 1920×1080 number of pixels.

The captured image on the CCD camera yields the spatial distribution of a 3DMOT, and we could determine the size of the 3DMOT. Each pixel size is $5.08\,\mu m \times 5.08\,\mu m$ in

the CCD camera. Thus by knowing the extension of the image of the atomic cloud on the CCD camera and the magnification of the imaging system, we determine the size of the atomic cloud in the 3DMOT.

Therefore, to determine the number of atoms trapped in the 3DMOT, we need to calculate the total number of photons (N_{det}^{ph}) incident on the CCD camera. The CCD camera yields the total number of counts (N_c^{det}) produced by all pixels due to N_{det}^{ph} numbers of fluorescence photons incident on the CCD camera over the given exposure time. Thus we need a calibration between the total number of counts generated by the CCD camera for a given number of incident photons (or power). After knowing the calibration factor, we can determine the number of photons incident on the camera due to MOT fluorescence. Afterward, we use Eqn. 4.7 to determine the number of trapped atoms in the 3DMOT.

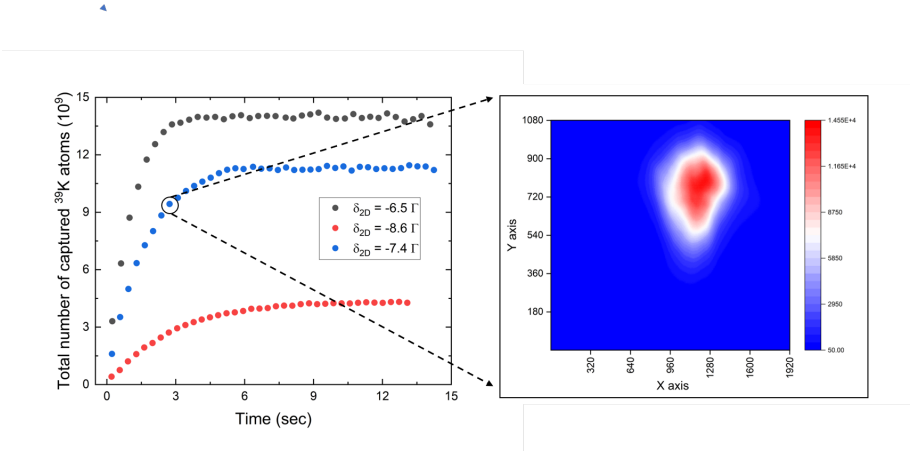


Figure 4.7: A typical loading curve of K-3DMOT. The atom number is calculated from the counts of the CCD camera for the given exposure time. Each point on the curve corresponds to a captured fluorescence image in the CCD camera.

Thus, before proceeding further, we need to calibrate the CCD camera. For this purpose, we send a probe beam of known power (P_{cal}) to the CCD camera over a given exposure time (τ_{CCD}) and determine the total number of counts (N_c^{cal}) generated by the pixels of the CCD camera. The process has been described in Appendix-D.

If we consider N_{ph}^{τ} is the number of photons of the probe beam incident on the CCD camera over the exposure time (τ_{CCD}).

Then, the measurement for the calibration holds the relation,

$$N_c^{cal} = \alpha_{CCD} \times N_{ph}^{\tau} \tag{4.9}$$

Where α_{CCD} is calibration factor of the CCD camera for the given exposure time.

We use this calibration factor to convert the total count (N_c^{det}) generated by the CCD camera to the total number of photons (N_{det}^{ph}) incident on the CCD camera for the given exposure time. Therefore, we obtained the following relation,

$$N_c^{det} = \alpha_{CCD} \times N_{det}^{ph} \tag{4.10}$$

Using Eqn. 4.7 we obtain,

$$N^{at} = \frac{4\pi}{\Omega_s}.\frac{1}{R_s}.\frac{N_c^{det}}{\alpha_{CCD}} \tag{4.11}$$

We determine solid angle (Ω_s), and the scattering rate (${R_s}^{MOT}$) from the experimental parameters. Therefore, by using Eqn.4.11, we obtain the number of trapped atoms in the 3DMOT directly by determining the total generated counts generated in the CCD camera. The details of the calculation is represented in Appendix-D.

4.2.2 Determination of atoms number from Femtowatt detector signal

In Figure-4.5, the second lens focused the captured fluorescence onto the photo-detector. The incident fluorescence photons on the photo-detector, produces a photo-current, which in turn generates a voltage signal on a load resistance (oscilloscope coupling port).

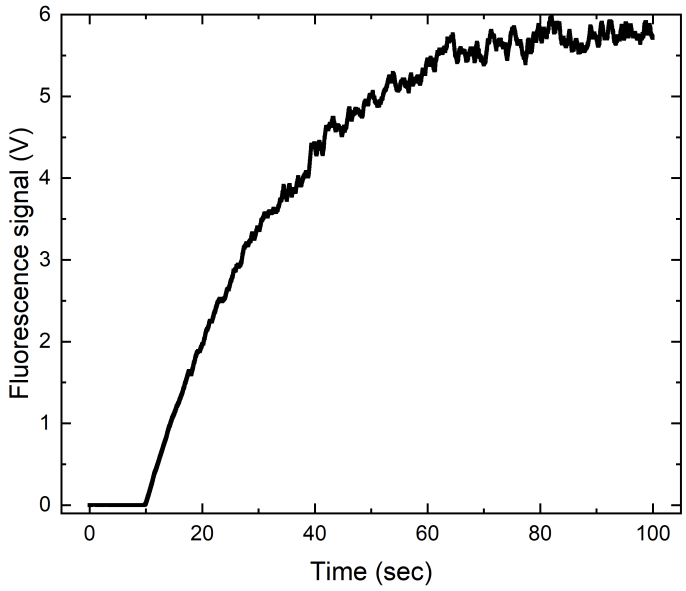


Figure 4.8: A typical 3DMOT loading signal is obtained from the Femtowatt photo-detector. The incident photons from fluorescence of the 3DMOT, generates a photo-current, which in turn produces a voltage signal across the load resistance of the oscilloscope. Using the calibration factor, we determine the loading rate and number of atoms trapped in the the steady state of the 3DMOT.

The voltage (V_{det}) generated by the photo-detector for an incident fluorescence power (P_{det}) is related by the equation, $V_{det} = \kappa P_{det}$, where κ is the proportionality factor having the unit of $\frac{V}{W}$. κ is obtained by calibrating the photo-detector (needs to be determined experimentally). In our case, the fluorescence power incident on the photo-detector is determined by the solid angle of the first lens, as given by the Eqn.4.3. After that, subsequent use of Eqn.4.6 and Eqn.4.7 yields the expression of the total number of

trapped atoms in the MOT,

$$N^{at} = \frac{4\pi}{\Omega} \frac{1}{h\nu\, R_s} \frac{V_{det}}{\kappa} \tag{4.12}$$

In the above equation, once we provide all the experimental parameters, we obtain the number of atoms trapped in the MOT.

To find out the number of atoms in the MOT from the voltage generated by FWPD, we have calibrated the FWPD voltage signal in the following way. At very first, we imaged the florescence of the 3DMOT on the CCD camera and determined the number of atoms trapped in the 3DMOT individually for both the species using the procedure describe in Section-4.2.1. Thereafter, We introduced the PBS in the imaging system as shown in Figure-4.5. The captured fluorescence power gets divided into the ratio 50:50 into the transmitted and reflected arms of the PBS. The reflected part of the fluorescence is focused on the FWPD. We load the 3DMOT and capture the fluorescence signal simultaneously on both the CCD camera and the FWPD. Then, we map the FWPD voltage signal on the number of atoms measured by the CCD camera, the proportionality constant corresponds to the number of atoms trapped in the 3DMOT for the unit volt signal of the FWPD.

4.3 Optimization of 2D$^+$MOT of potassium and sodium

In the following sections, I will describe the performance of the system and its dependence on the experimental parameters. In each of the measurements, we determine the number of atoms trapped in the 3DMOT, obtained by using either of the two methods Section-4.2.1 or Section-4.2.2.

In the following sections, I will describe the performance of the system and its dependence on the experimental parameters. In each of the measurements, we determine the number of atoms trapped in the 3DMOT, obtained by using either of the two methods Section-4.2.1 or Section-4.2.2.

We have designed the 2D$^+$MOT to obtain a higher loading rate of the atoms in the

3DMOT and to obtain higher numbers of atoms at the steady state. As mentioned in Section-2.1, the large number of atoms in the 3DMOT is a pre-requisite to obtain a large number of atoms in the quantum degenerate cloud, at the same time, the higher loading rate of the atoms facilitates to obtain a large number of experimental run. The state-of-the-art design of our $2D^+$MOTs produce cold and highly collimated beams of sodium and potassium atoms. The cold beams are directed toward the respective 3DMOTs. Therefore, the efficiency of the $2D^+$MOTs could be quantified by the loading rate of atoms and steady-state atoms number in the 3DMOT. In other words, we have used the 3DMOT as a detector, during the characterization of the $2D^+$MOTs of the sodium and potassium atoms, we kept the respective 3DMOTs parameters fixed. Therefore, the variation of the fluorescence of the 3DMOT while tuning the experimental parameters of the $2D^+$MOTs is a direct measure of the variation of the number of atoms in the 3DMOT.

In the following, I will describe the systematic tuning of all the experimental parameters of the $2D^+$MOT, to obtain an optimum operating condition for the 3DMOT of sodium and potassium atoms.

4.3.1 3DMOT capture rate vs $2D^+$MOTs' cooling beam detuning

During this measurement, we first make the intensity of the $2D^+$MOT cooling beams to the maximum possible values for both species. We kept the repumper to cooling beam intensity ratio to the highest possible value. The cooling and repumping transitions involved for the laser cooling purpose are indicated in Figure-2.8. We gradually vary the detuning of the $2D^+$MOT cooling beam and at each step determine the loading rate using the procedure mentioned in Section-4.2. The characteristic loading of potassium and sodium atoms in the respective 3DMOTs for three different detunings of respective 2DMOT cooling beams are shown in Figure-4.9.

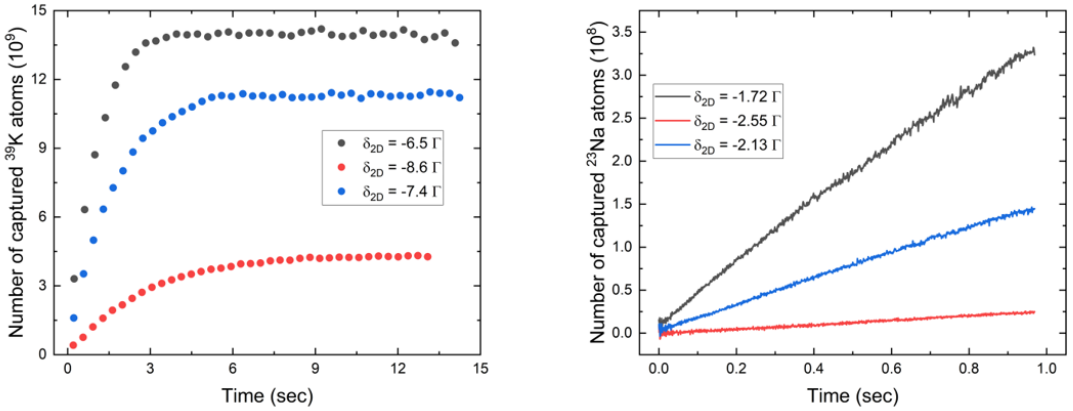


Figure 4.9: The loading dynamics of (a) potassium and (b) sodium atoms in respective 3DMOT. The loading dynamics are represented at different detuning of the 2D$^+$MOT cooling beam detuning.

Figure-4.10 (a) and Figure-4.10 (b) show the dependence of the capture rate in the 3DMOT on the detuning of the 2D$^+$MOT cooling beams for ^{39}K and ^{23}Na atoms, respectively.

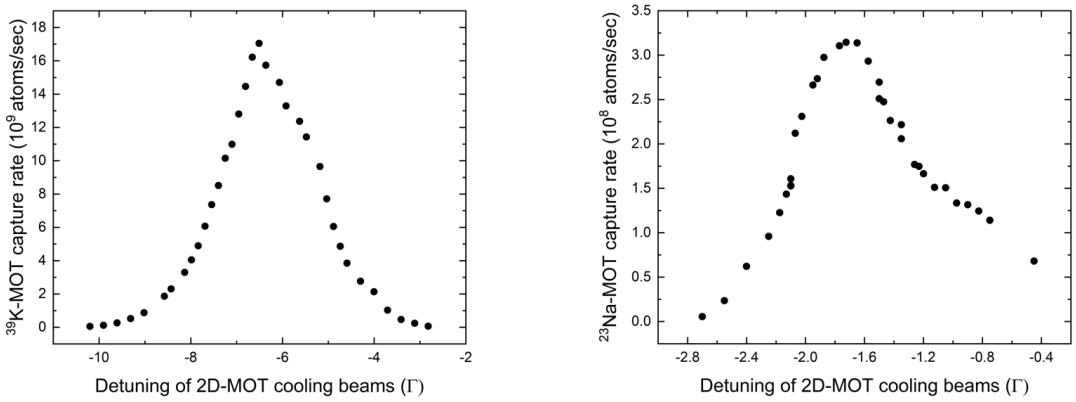


Figure 4.10: The variation of the capture rate of (a) potassium and (b) sodium 3DMOTs at different 2D$^+$MOT cooling beam detunings. We obtained a maximum capture rate at detunings of -6.5Γ and -1.8Γ of the potassium and sodium 2D$^+$MOT cooling beams.

The characteristic feature of the plots in Figure-4.10 can be understood as follows: at

smaller detunings, the scattering rate is high (Eqn.4.1), which results in efficient transverse cooling of the atoms but the capture velocity of the $2D^+$MOT is very small, because, the capture velocity is proportional to the detuning of the cooling beams. As a result, less number of potassium and sodium atoms could be captured from the vapor of their respective $2D^+$MOTs. In the opposite limit, at large detunings, the capture velocity is significantly large. Therefore, a higher velocity class of the atoms in the $2D^+$MOT glass cell can be captured. But, at the same time, the scattering rate decreases drastically. This results in inefficient transverse cooling of the atoms in the $2D^+$MOTs. Therefore, the dependence of the capture rate in the 3DMOT w.r.t cooling beam detuning is an interplay of two opposite effects. As a result, we have seen the capture rate is maximum at some intermediate value of the detuning of the cooling beams of the $2D^+$MOTs.

We obtained the maximum capture rate of the 3DMOT at -6.5Γ and -1.8Γ detuning of the cooling beams of the $2D^+$MOT of potassium and sodium atoms, respectively. The value of the detuning at which the maximum capture rate in the 3DMOT is obtained corresponds to the most efficient transverse cooling of the atoms in the $2D^+$MOT. This value of the detuning results in a cold atomic beam with high flux and narrow velocity distribution. Therefore, the atoms pass through the hole of the differential pumping tube with minimum divergence.

4.3.2 3DMOT capture rate vs $2D^+$MOTs' cooling beam intensity

The experimental measurements and the comparison with numerical simulation of the dependence of the capture rate in the 3DMOT on the the $2D^+$MOT cooling beam intensity is shown in Figure-4.11. During these measurements we kept the detuning of $2D^+$MOT cooling beams at the optimum values as obtained in Section-4.3.1 for both the species. We observed almost a linear increase in the capture rate at low and intermediate intensities. At higher intensities the rate has reduced for both the atomic species, but we haven't observed any saturation effects.

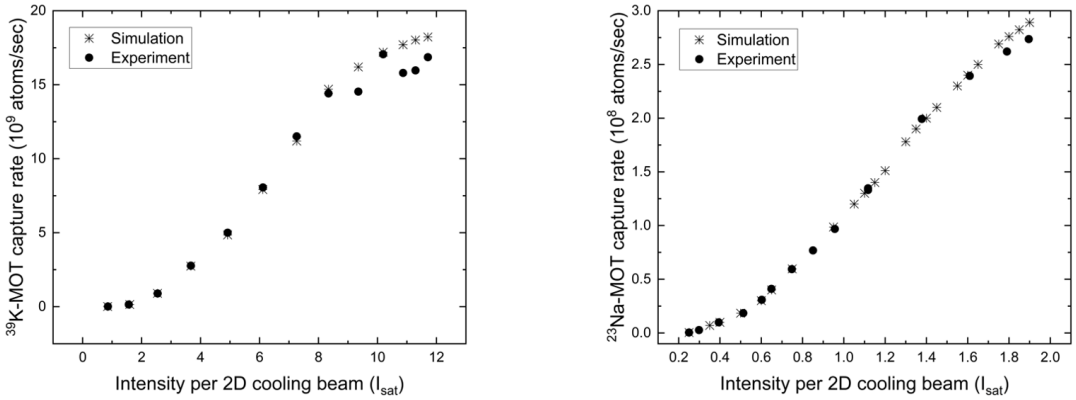


Figure 4.11: The experimental observations and the comparison with the numerical simulation of the variation of the capture rate of (a) potassium and (b) sodium atoms in their respective 3DMOTs with the intensity of the 2D$^+$MOT cooling beams. As we increased the intensity of the cooling beam we observed an increase of the the capture rate. At higher intensities the rate of increase of capture rate slows down. At much higher intensities the capture rate expected to saturate as described in the text.

The observed behavior can be attributed to the fact that, as the cooling beam intensity increases, it provides tighter transverse confinement to the atoms in the 2D$^+$MOT. This results in an easy passage of the atoms through the differential pumping tube towards the 3DMOT, which in turn increases the capture rate. In addition, the higher cooling beam intensity power broadened the excited linewidth of the interacting atoms: as a result, it has increased the scattering rate of the photons from the cooling beam and provides an increased scattering force. The curves show no sign of saturation yet but are expected to show saturation effects at higher intensities. The saturation would arise due to two underlying effects. First, the scattering rate of the atomic transitions involved in the cooling will saturate. The second reason is that, the temperature of the cooled atoms and the light-assisted collisions [241, 242] increase with the cooling beam's intensity. The latter effect is much less severe in 2D$^+$MOT than in 3DMOT: because the density in 2D$^+$MOT is two-three orders of magnitude less than the 3DMOT due to the absence of the three-dimensional confinement. We have seen a very good agreement between the

numerical simulation of the capture rate in the respective 3DMOTs with the experimental data.

4.3.3 Capture rate of 3DMOT vs 2D$^+$MOTs repumper and cooling beam intensity ratio

The dependence of the 3DMOT capture rate on the ratio of the repumper and cooling beams intensity of 2D$^+$MOT is shown in Figure-4.12. For potassium atoms, we have used two independent laser systems for cooling and repumper beams so we could independently control cooling and repumper beams.

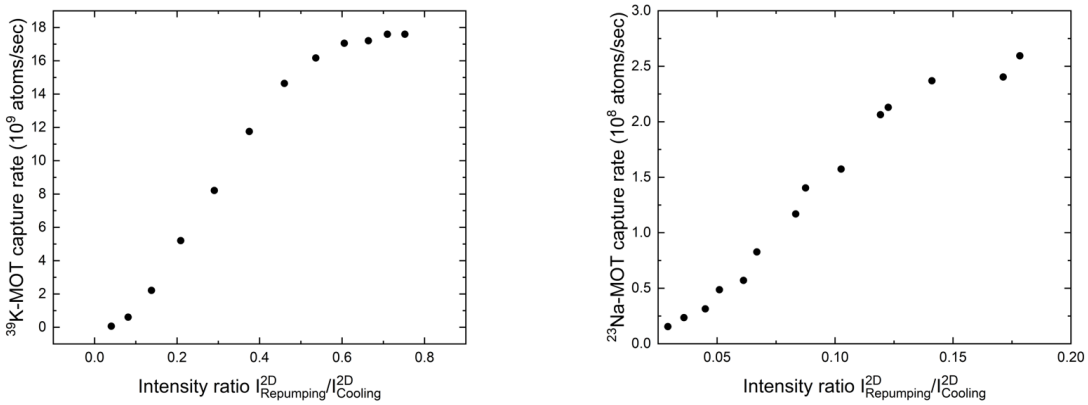


Figure 4.12: The variation of the capture rate in the 3DMOT of (a) potassium and (b) sodium atoms with the intensity ratio of repumper and cooling beams of respective 2D$^+$MOTs. As we increase the ratio, we observed a rapid increment in the capture rate in both the 3DMOTs. At higher values of the ratio, the capture rate is saturated. We can see a stark difference between the values at which the saturation of the capture rate occurs in potassium and sodium. The higher value of the ratio in the case of potassium atoms is attributed to the fact that the energy splitting of the excited state is less(factor $\sim$3) compared to the same of the sodium atoms. As a result, the atoms are more likely to get transferred into the dark hyperfine state $|F = 1\rangle$. Therefore, it required more repumper power in comparison to the sodium atoms to get the saturation in the capture rate.

To increase the ratio mentioned above, in the case of potassium atoms, we fixed the cooling beam intensity to the maximum possible value and gradually increases the

repumper beam intensity.

In the case of sodium atoms, we have changed the given ratio in the following way: to generate a frequency of the repumper transition, we have used EOMs. We kept the input laser power to the EOM fixed, and during the measurement, we gradually changed the RF power to the EOM. Changing the RF power to the EOM changes the ratio of the repumper to the cooling beam component. A typical repumper and cooing beam component generated using EOM are shown in Figure-1.10.

The graphs show that the capture rate in the 3DMOT is almost linearly increasing with the intensity of the repumper beam. This is evident from the fact that as the repumper beam intensity has increased, it results in an increse of the strength of the repumper transition. The increased strength of the repumper transition increases the optical pumping of the atoms from the ground hyperfine state $|F = 1\rangle$ to the hyperfine state $|F = 2\rangle$. This results in efficient cooling of the atoms in the $2D^{+}$MOT, which in turn increase the flux of the atoms in the atomic beam. As a result, we obtained an increased capture rate in the 3DMOT. As the repumper intensity has increased further, we have observed the capture rate reaches saturation. This saturation effect is attributed to the fact that the repumper transition has also saturated at higher repumper intensity.

An important point to note is that we have observed a stark difference between the values of the repumper to cooling beams intensity ratio at which the loading rate reaches the saturation in the capture rate in the 3DMOT for both species. We attributed this effect to the difference in the energy splittings of excited state hyperfine levels of ^{39}K and ^{23}Na atoms. As shown in Figure-2.8, the excited state hyperfine levels are closely spaced in ^{39}K atoms compared to ^{23}Na atoms. As a result, when the potassium atoms encounter a cooling photon, they are more likely to de-excited to the $|F = 1\rangle$ hyperfine ground state than sodium atoms. Therefore, it requires more repumper intensity for the potassium atoms to obtain high repumping transition strength to optically pump the atoms back to the $|F = 2\rangle$ hyperfine state.

4.3.4 3DMOT capture rate vs 2D$^+$MOTs intensity ratio of push and retardation beam

The dependence of the 3DMOT capture rate on the intensity ratio of the pushing and retardation beams of the 2D$^+$MOT is shown in Figure-4.13.

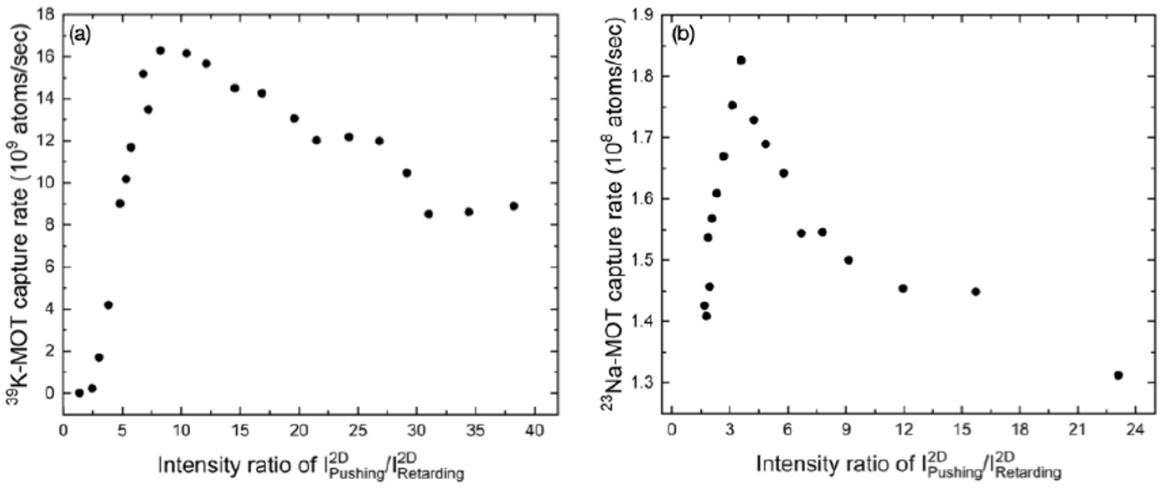


Figure 4.13: The variation of the capture rate in the 3DMOT of (a) potassium and (b) sodium atoms with the intensity ratio of the pushing and retardation beams of 2D$^+$MOTs.

As we increase the ratio, we have seen a sharp increase in the capture rate in the 3DMOT. This is because the longitudinal optical molasses is forming very efficiently. The capture rate is maximized at some intermediate values, in the case of potassium the value is ~ 8, while for sodium the corresponding value is ~ 3.5. At these values, the longitudinal optical molasses is working the most efficiently. When the atoms are moving through the cooling volume, the longitudinal velocity is reduced by a significant amount so that they are interacting with the transverse cooling beams for a longer duration. As a result, the atoms are much more confined on the transverse plane and very efficiently pass through the hole of the differential pumping tube. This results in the increase of the capture rate in the 3DMOT.

As we increase the value of the ratio further, we have observed a decrease in the capture rate in the 3DMOT. At a higher value of the ratio, the effect of the longitudinal molasses

has decreased significantly. Therefore, we have seen a gradual decrease in the capture rate in the 3DMOT. At a very high value of the ratio, the system practically becomes a 2DMOT, where the pushing beam is only effective. Therefore, our observations explain the superiority of the performance of the $2D^+$MOT over 2DMOT in terms of the higher capture rate in the 3DMOT.

An important point to note is that, the value of the ratio at which the capture rate is optimized: as mentioned earlier, in the case of ^{39}K atoms, the value is ~ 8 and for ^{23}Na atoms the value is ~ 3.5. The value of the optimized value of the ratio demonstrates that, in the case of $2D^+$MOT, ^{23}Na atoms need a more delicate balance between the pushing and the retardation beams compared to ^{39}K atoms. ^{23}Na atoms are lighter compared to ^{39}K atoms, in addition to that, the scattering rate of ^{23}Na atoms are larger than the scattering rate ^{39}K atoms. As a result, the sodium atoms tend to diffuse out from the cooling volume of the $2D^+$MOT more compared to potassium atoms. Therefore, sodium atoms require efficient cooling along the longitudinal direction, so that the transverse cooling on them will be significant.

4.3.5 the capture rate in the 3DMOT vs the magnetic field gradient of $2D^+$MOTs

Figure-4.14 represents the dependence of the capture rate in the 3DMOT on the $2D^+$MOTs' magnetic field gradient. As the field gradient increases, we have observed a steep increase in the capture rate in the 3DMOT for both atomic species.

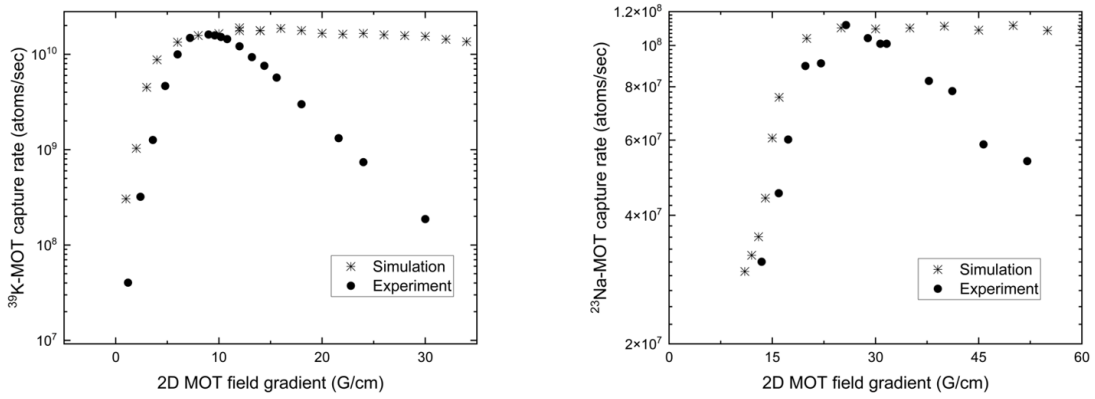


Figure 4.14: The experimental observations and the comparison with numerical simulation of the capture rate in the 3DMOT of (a) potassium and (b) sodium atoms with the magnetic field gradient of 2D^{+}MOTs.

At a higher magnetic field gradient, the atoms are more compressed around the zero magnetic field line. Therefore, when they are pushed out from the cooling volume, they have an easy passage through the hole of the differential tube. As a result, it increases the capture rate in the 3DMOT. Further, increase in the gradient, the atoms are heavily compressed in the cooling volume, and when they are pushed out from the cooling volume, the potential energy is converted to kinetic energy. Therefore, the atoms acquire a high transverse velocity. As a result, when the atoms are pushed out of the cooling volume, they acquire high enough velocity that during their flight toward the hole of the differential pumping tube, the atoms diverge a lot such that they couldn't enter the hole of the differential pumping tube. This behavior is evident from decreased capture rate in the 3DMOT as we increased the 2D^{+}MOT magnetic field.

We have seen a good agreement between the measured capture rate in the 3DMOT and numerical simulation results at the lower values of the field gradient for both species. But, at the higher values, there is a deviation between the measured and the simulation results. In the case of ^{39}K atoms, the deviation is more compared to ^{23}Na atoms. As mentioned in Section-3.3, we have performed the simulation on a two-level atomic system, and at

higher magnetic field gradients this approximation breaks down. In case of ^{39}K atoms, the excited state manifold (spacing between $|F' = 1\rangle$ and $|F' = 3\rangle$ states) is relatively small (∼31 MHz) in comparison to the excited state manifold of ^{23}Na atoms (∼93 MHz). Therefore, away from the center of the 2D$^+$MOT, ^{39}K atoms experience a significantly higher trapping force compared to that determined by the two-level model. The above-mentioned effect, results in an increased divergence of the ^{39}K atomic beam, which in turn limits the capture rate in the 3DMOT.

4.3.6 The capture rate in the 3DMOT vs the vapor pressure of the 2D$^+$MOTs

Figure-4.15 shows the dependence of the capture rate in the 3DMOT on the vapor pressure of the 2D$^+$MOT of potassium and sodium atoms.

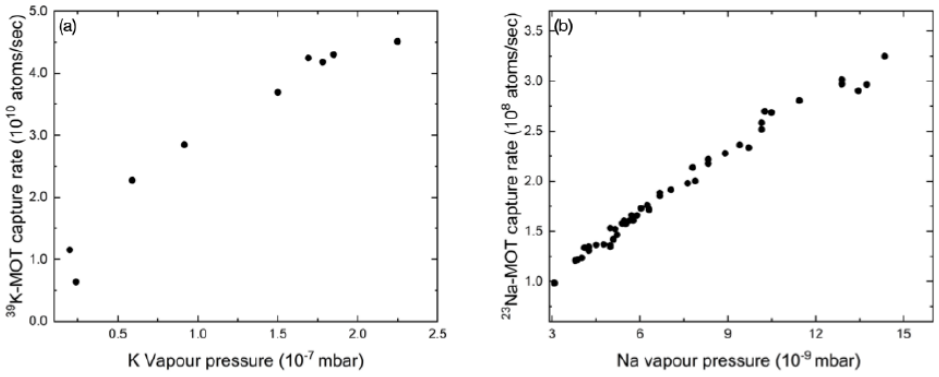


Figure 4.15: The variation of the capture rate in the 3DMOT of (a) potassium and (b) sodium atoms with the vapor pressure of 2D$^+$MOTs.

As we have increased the vapor pressure in the 2D$^+$MOT, we have observed a monotonic increase in the capture rate in the 3DMOT for both species. In the case of 2D$^+$MOT of ^{39}K atoms (K-2D$^+$MOT), we have seen a saturation behaviour in the capture rate above 2×10^{-7} mbar partial pressure. On the other hand, 2D$^+$MOT of ^{23}Na atoms (Na-2D$^+$MOT), the capture rate in the 3DMOT is limited by the available partial vapor pressure in the 2D$^+$MOT.

We have varied the vapor pressure in the K-2D$^+$MOT by heating the oven between the temperatures 50^o-130^o. We maintain a temperature gradient from the oven to the glasscell, which facilitate atomic vapor of ^{39}K atoms in coming into the glass cell.

To vary the vapor pressure in the Na-2D$^+$MOT, we heat the oven to high temperatures up to 300^{o}C. We maintain the temperature of the metal parts near the glass cell to 100^{o}C. This prevents the coating of the ^{23}Na atoms around this region. We have placed heating rods around the glasscell and wrapped the region around Na-2D$^+$MOT using a heat-insulation blanket and layers of aluminum foils. This special arrangement maintains the temperature of the air surrounding the 2D$^+$MOT between 60^o-75^o.

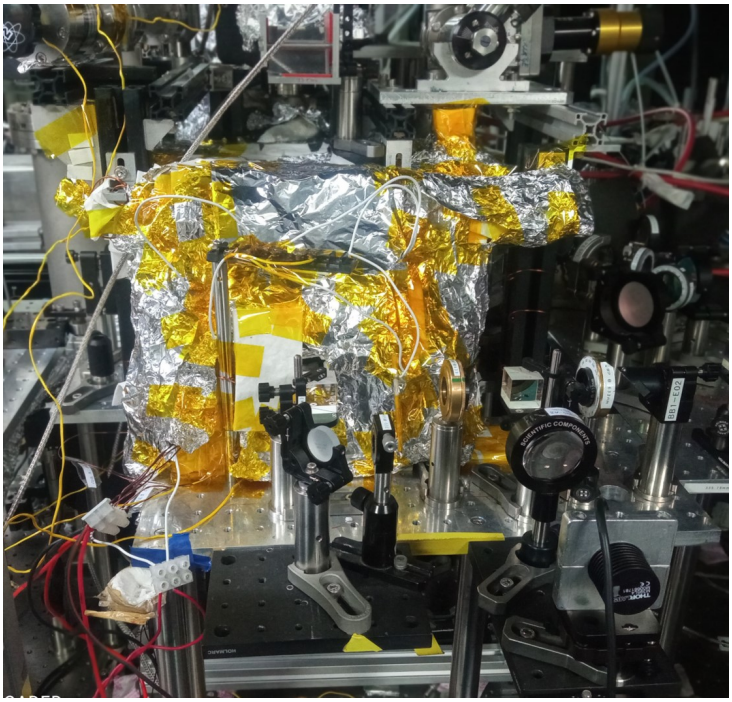


Figure 4.16: The Na-2D$^+$MOT is wrapped by the heat-insulation blanket and the layers of aluminium foils.

We have devised this specialized technique for Na-2D$^+$MOT because ^{23}Na atoms have more tendency to stick to the glass surfaces than the ^{39}K atoms. In addition to that, the melting point of ^{23}Na atoms is also relatively high (∼98^o). We have avoided direct heating of the glass cell to a high-temperatures rather we keep the temperature of the air

surrounding the glasscell to the above-mentioned values.

To determine the pressure inside the 2D$^+$MOT glasscell, we have sent a near-resonant probe beam through the glasscell. We measured the absorption of the probe beam as we varied the pressure inside the glasscell. As the pressure is increased in the glasscell, this results in an increase in the probe beam absorption, from this information we have determined the pressure inside the glasscell.

parameters	K-MOT	Na-MOT
Cooling detuning (Γ)	-6.5	-1.8
Cooling intensity (I_{sat})	10	7
$\frac{I_{rep}}{I_{cool}}$	0.75	0.18
$\frac{I_{pushing}}{I_{retarding}}$	8.1	3.6
∂_xB, ∂_yB	9	26
$I_{additional-push}$ (I_{sat})	5.3	7.7
Vapor pressure (mbar)	2.7×10^{-7}	1.4×10^{-8}
3DMOT capture rate (atoms/sec)	5×10^{10}	3.5×10^{8}

Table 4.1: The optimized parameters of the 2D$^+$MOT for maximum capture rate of potassium and sodium atoms in the respective 3DMOTs.

parameters	K-MOT	Na-MOT
Cooling detuning (Γ)	-6.8	-1.4
Total Cooling intensity (I_{sat})	22.7	10
$\frac{I_{rep}}{I_{cool}}$	0.75	.22
Magnetic field gradient (Gauss/cm)	18.5	17.6
Total number of atoms	3×10^{10}	5.8×10^{8}

Table 4.2: The experimental values of the parameters of employed for potassium and sodium 3DMOTs.

4.4 Collisional dynamics of cold atoms in a MOT

In Section-4.3, I have given a detailed description of the performance of the 2D$^+$MOT for both species. During the optimization, we have maximized the capture rate of the atoms in the respective single-species 3DMOTs by tuning the parameters of 2D$^+$MOTs (refer to Table-4.1) and 3DMOTs (refer to Table-4.2). We have built efficient cold atomic beam sources of potassium and sodium with a large capture rate and a large number of atoms in the single species 3DMOTs in a very short time. We have obtained a capture rate of $\sim 5 \times 10^{10}$ atoms/sec and total $\sim 3 \times 10^{10}$ atoms in 800 msec for ^{39}K and a capture rate of $\sim 3 \times 10^{8}$ atoms/sec and total $\sim 5 \times 10^{8}$ atoms in 3 sec for ^{23}Na. The value of the parameters used for the respective 3DMOTs of potassium and sodium is listed in Table-4.2.

A MOT is a novel system to study the collisional dynamics of the trapped atoms in a low-energy regime. The temperature of the trapped atoms in a MOT is around a few hundreds of μK, and a 3DMOT has a typical density of atoms $\sim 10^{10}/cm^3$. Using dimensional analysis, using the relation, $h\nu = k_B T$, we could show 50 nK$\sim$1 kHz. Therefore, at the typical temperature of $\sim$500 μK of the 3DMOT, the trapped cold atoms have 10 MHz of kinetic energy. The ground state hyperfine splittings of the alkali atoms are much larger

than the collisional energy of the cold atoms. For example, the energy splitting of $F = 1$ and $F = 2$ hyperfine ground state of ^{39}K and ^{23}Na atoms is 471 MHz and 1771 MHz, respectively. Thus, the collisional dynamics of the cold atoms in a 3DMOT depend on the specific quantum state of the atoms and are governed by the interatomic potential of the specific quantum states involved during the collisions.

The detailed study of collisions between ultracold atoms is of both fundamental and practical importance. The collisional dynamics provides vital information regarding the molecular potential energy curves [242], identification of Feshbach resonances [179, 243], and creating molecules using photo-association [179, 244]. Detailed knowledge of the mechanism present in cold collisions is essential to optimize the number of trapped atoms, the temperature, and the density of the trapped cold atomic cloud.

Exploring the collisional dynamics involving two different atomic species is of tremendous importance. This has opened up the possibility of sympathetic cooling of the neutral atoms. In sympathetic cooling, one atomic species is cooled by another atomic species using hetero-nuclear collisional dynamics. For example, the sympathetic cooling strategy has been employed for the fermionic species by using evaporative cooling of the bosonic species, which led to the observation of the celebrated phenomenon of Fermi degeneracy [245,246]. The direct evaporative cooling of fermionic species is impossible due to the absence of the s-wave collisions at ultracold temperatures.

In a MOT, inelastic collisions between the trapped atoms could occur, resulting in exoergic collisions. An exoergic collision converts the internal energy of the colliding atoms (atomic species A and B) to their kinetic energy. The atoms share the kinetic energy equally in the case of the same atomic species (A=B). In contrast, in the case of hetero-nuclear atomic species, the energy is divided between the colliding atoms according to their mass ratio, $\frac{m_A}{m_B}$. If the release of the energy is sufficiently high, then the atoms could escape their respective MOTs, and this process causes a significant loss of atoms from the trap. The underlying mechanism of the collisions could be classified into three categories according to the change in the internal states of the colliding atoms. The

hyperfine-changing collision (HCC) [242, 247, 248] occurs when both the colliding atoms are in their ground states. In the presence of trapping laser beams, there is a possibility of excitation of the colliding atoms to the excited state during the collisions, which leads to light-assisted collisions [249, 250]. The radiative escape (RE) and fine-structure changing (FSC) collision occur when one of the atoms is in the ground state and the other one is in the excited state [242, 248].

In a MOT, at any given instant, the cold atoms could be in the ground state or in the excited state, where the state's population depends on the parameters of the trapping laser beams, detuning, and intensity. During the collision, if both the atoms are in their ground hyperfine state (electronic ground state), only elastic collisions and hyperfine-changing collisions (HCC) could occur. Elastic collisions do not change the internal states: therefore, they are not exoergic. Elastic collisions are of fundamental importance in the production of BEC, which requires a favorable ratio of the elastic collisional rate to the inelastic collisional rate [120]. During the collisions, the HCC transfers the colliding atom pair from the higher hyperfine energy state to the lower one. The HCC causes a release of energy, which is equal to the difference in the energy of the higher and the lower hyperfine energy states (E_{HFS}). This amount of energy is converted to the kinetic energy of the colliding atom pair. In sodium MOT, the HCC from $\left|3^2S_{1/2}F=2\right\rangle \rightarrow \left|3^2S_{1/2}F=1\right\rangle$ hyperfine state corresponding to a release of 1771 MHz of energy, which equally shared between the two sodium atoms and would cause an increase of velocity by 5.5 m/s [247]. In the case of ^{39}K MOT, due to smaller hyperfine splitting of 471 MHz between $\left|4^2S_{1/2}F=2\right\rangle$ and $\left|4^2S_{1/2}F=1\right\rangle$ states and having larger atomic mass, HCC result in an increase of velocity by 2 m/s. This collisional process leads to a significant loss of trapped atoms when the trap depth (or the capture velocity) of the MOT is small.

During the collisions, if one of the atoms is excited by the trapping laser beams, then the collisional channel involves an excited-ground state collision: this class of collisions is categorized as light-assisted collisions between the cold atoms. The collisions are governed by the interatomic potential, which is $\sim \frac{1}{R^3}$ for the homo-nuclear case, while it is $\sim \frac{1}{R^6}$

for the hetero-nuclear collisions.

With a typical density(n) of atoms $\sim 10^{10}/cm^3$ in a 3DMOT, the average distance ($d_{avg} \sim \frac{1}{n^3}$) between the atoms $\sim 4\,\mu$m (80000a_0, a_0 is the Bohr radius). During the collision, the average distance between the atoms is large, and the atoms feel the interatomic potential in the asymptotic limit. We consider the colliding atoms are of atomic species 'A' and 'B', and the colliding pair $A(S_{1/2})$-$B(S_{1/2})$ absorbs a photon and excited to an attractive potential during the collision. The repulsive or attractive nature of the excited state depends on the quantum states involved during the collisional process [251].

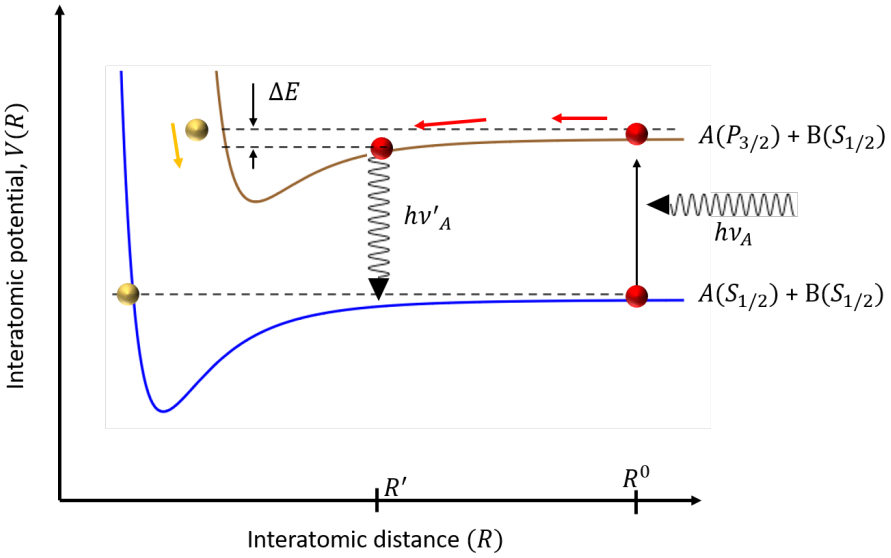


Figure 4.17: A schematic of excite state -ground state collision between two atoms of species 'A' and 'B'in a dual-species MOT. An atom of the species 'A' adsorbs a photon of energy $h\nu_A$ and makes a transition to the excited state $A(P_{3/2})$ at the interatomic distance R_0. The atoms in the excited state $A(P_{3/2})$ and ground state $B(S_{1/2})$ approach each other in the attractive potential. Over the duration of the lifetime of the excited state (τ) atoms approach an interatomic distance R' and the atom 'A' is de-excited to the ground state by emitting a photon of energy $h\nu'_A$ ($< h\nu_A$). The difference of the energy, $\Delta E = h\nu_A - h\nu'_A$, converted to the kinetic energy of the atoms 'A' and 'B'.

In this discussion, we are considering the attractive nature of the excited state. During the collisional process, any one of the two atoms or both atoms may be excited by absorbing photons of resonant frequency ν_A and ν_B. We are considering the scenario where only

atomic species A is excited. The atoms of the atomic species A are excited by absorbing photons of energy $h\nu_A$ from the trapping light as shown in Figure-4.17.

The collisional channels involve during the process are $A(S_{1/2})-B(S_{1/2})$ and $A(P_{3/2})-B(S_{1/2})$, here we are considering the D_2 transition of the atomic species A. During the collision in the attractive potential of the excited state, the colliding atoms approach each other. During this time, the atom pair may decay to the ground state by emitting a photon of energy $h\nu'_A$, red-detune to the atomic transition. The lifetime of the excited state of the colliding atom pair is determined by the excited state lifetime (τ)of the atomic species A: for example, for ^{39}K atoms, the excited state lifetime is 27 ns and while for ^{23}Na the excited state, lifetime is 16 ns. During this collisional process, the colliding pair emits a red-detune photon to the atomic transition. The difference in the energy $\Delta E = h\nu_A - h\nu'_A$ is converted into the kinetic energy of the colliding atom pair and shared between the colliding atoms according to their mass ratio $\frac{m_A}{m_B}$. If the release of the energy is sufficiently high, then both the atoms and (or) the lighter atom will escape the trap. This collisional loss process is known as the radiative escape (RE). The loss of the atoms from the trap depends on the release of the energy during the collisional process and the trap depth of the individual MOTs, which is determined by the detuning, intensity, and size of the trapping beams.

Another loss mechanism exits for a collision involving the excited-ground state of trapped cold atoms. The alkali atoms have fine-structure doublet ($P_{1/2}$ and $P_{3/2}$) in theie excited state. During the collisions, the colliding pair of excited-ground state atoms transfer to the lower fine-structure ($P_{1/2}$) doublet. This collisional mechanism is termed as fine-structure change (FSC) collision. This collisional process is followed by a release of energy of amount E_{FS}, where E_{FS} is the energy difference between the fine-structure doublet ($P_{1/2}$, $P_{3/2}$). The colliding partners share the released energy according to their mass ratio. For ^{39}K atoms, the FSC collisions release 83 K of energy [216], while for ^{23}Na atoms, corresponding value is 25 K [252]. This amount of energy is large enough that the atom pair escape from the trap.

4.4.1 Collisional dynamics of cold atoms in a single species 3DMOT

A typical loading curve of atoms in a single-species 3DMOT is shown in Figure-4.7. First, we study the loading dynamics of the single species 3DMOT of potassium and sodium atoms separately. We experimentally measured the loading of atoms in a 3DMOT using fluorescence imaging and studied the collisional dynamics in a single species 3DMOT. I have discussed the underlying process of the collisional loss mechanism in a 3DMOT in detail already (Section-4.4). The loss mechanism in a single-species 3DMOT is quantified by the intra-species collisional loss rate β_{ii} ($i \in \{K, Na\}$).

In a dilute ultracold gas, the loading of atoms in a single-species 3DMOT is modeled as [248],

$$\frac{dN}{dt} = L - \gamma N - \beta \int n^2 d^3r \tag{4.13}$$

Where N is the number of trapped atoms in the 3DMOT, the first term on the left-hand side, L is the loading rate, determines the rate of capturing the cold atoms in the trapping volume of the 3DMOT. The second term describes the collisional rate caused by the collisions of the trapped and cold atoms in the 3DMOT with the thermal background atoms, and γ is the corresponding collisional loss rate defined per trapped atom per second. The quantity γ is the inverse of the lifetime (τ) of the the atoms in the 3DMOT and defined as $\gamma = \frac{1}{\tau}$. The third term describes the two-body collisional rate resulting from the collisions between the trapped and cold atoms in the MOT. The quantity β is the two-body decay rate constant. The integration is performed over the volume of the 3DMOT.

Eqn.4.13 can be expressed in terms of the loading dynamics of the density as [253],

$$\frac{dn}{dt} = L_n - \gamma n - \beta n^2 \tag{4.14}$$

Where L_n is the loading rate of the atoms per unit volume. The solution of the above

equation can be expressed as,

$$n = n_{ss}\frac{1 - e^{-\Gamma t}}{1 + \zeta e^{-\Gamma t}} \tag{4.15}$$

Where, n_{ss} is the steady state density.

The quantities Γ and ζ can be expressed as,

$$\Gamma = \gamma + 2\beta n_{ss} \tag{4.16}$$

and

$$\zeta = \frac{\beta n_{ss}}{\beta n_{ss} + \gamma} \tag{4.17}$$

A typical density evolution of K-3DMOT and Na-3DMOT are shown in Figure-4.18. The steady state density is given by,

$$n_{ss} = \frac{N_{ss}}{(\sqrt{2}a)^3} \tag{4.18}$$

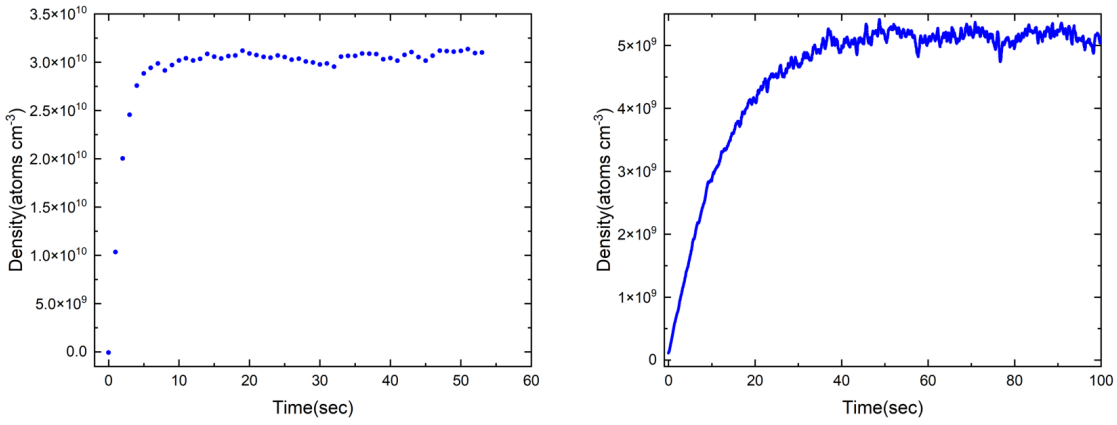


Figure 4.18: The density evolution of the 3DMOT of (a) potassium and (b) sodium atoms. During the initial part of the loading, the density gradually increases. In the case of potassium 3DMOT, the density saturates after t ∼10 sec, while for Na-3DMOT, it happens after ∼40 sec. The loading of 3DMOT in this regime is termed 'constant density limit'.

The density of the 3DMOT can be expressed as,

$$n(r) = n_0\, e^{-(r/a)^2} \tag{4.19}$$

where n_0 is the peak density and a is the $\frac{1}{e}$ radius of the Gaussian distribution.

Fitting Eqn.4.15 to the experimentally obtain density evolution of the K-3DMOT, Figure-4.18(a) and Na-3DMOT, Figure-4.18(b), we obtain Γ and ζ parameters respectively. The experimentally obtained values of Γ and ζ yield the intraspecies collisional loss-rate β_{KK} and β_{NaNa}. The details of the procedure of the fitting of Eqn.4.14 to the experimental data and the details of the calculations are described in Appendix-D.

We determine the value of the loss rate γ from the decay curve of the 3DMOT. For this purpose, we blocked the cold atomic beam from the $2D^+$MOT and observed the decay of the number of atoms in the 3DMOTs of ^{39}K and ^{23}Na atoms. An exponential fit to the data of the loss of the trapped atoms at a longer decay time, yields the value of γ. For our experimental system, we obtained, $\gamma \approx 0.03 s^{-1}$.

4.5 Interspecies collisional dynamics of spatially overlapped ^{39}K and ^{23}Na MOTs

In this section, I have describe the interspecies collisional dynamics of cold and trapped sodium and potassium atoms in a spatially overlapped 3DMOTs. During the measurement, we simultaneously load sodium and potassium MOTs. In our experimental setup, the geometry and the experimental configuration are such that we obtain spatially overlapped sodium and potassium MOTs (although we have experimentally verified the fact by observing the sodium and potassium 3DMOTs simultaneously in the CCD camera). We determine the dependence of the collisional dynamics on the number of trapped sodium and potassium atoms in the 3DMOT and on the excited state fraction of the potassium atomic species.

In a dual-species 3DMOT, the inelastic collisions between the trapped atoms of two-different atomic species result in a significant loss of atoms [247, 254]. For heteronuclear atomic species cold collisions, the underlying mechanism of the loss of the atoms is the same as described in Section-4.4. As described earlier, in the case of single species 3DMOT of sodium atoms, the HCC causes an increment of the velocity of each atom by 5.5 m/s. Whereas, in the case of spatially overlapped 3DMOT of sodium-potassium heteronuclear collisions, HCC causes an increment of the velocity of the sodium atoms by 6.3 m/s [247] due to the smaller mass of the sodium atoms. Therefore, HCC causes a significant loss of sodium atoms in a shallower trap.

Light-assisted collisions govern one of the loss mechanisms between the hetero-nuclear atomic species. The principal contribution comes from the collisional channels where one species is in the ground state and the other in the excited state. The atom pairs can undergo radiative escape (RE) and the fine structure-changing (FSC) collisions [242, 255]. As described earlier, ground-excited state collisions could occur in the presence of the trapping beams of the 3DMOT. In the case of hetero-nuclear collisions of the atoms, the ground-excited state interaction potential depends on $\sim \frac{1}{R^6}$, in contrast to the homo-nuclear case, while it depends on $\sim \frac{1}{R^3}$. Therefore, in hetero-nuclear collisions, the colliding atoms need to come closer for the RE or FSC processes to occur. For example, if we consider sodium atoms in a 3DMOT of trap depth $\sim$2K, the RE process could take place and acquire enough energy when the colliding atoms approach $\sim 50\,\mathrm{A}^o$ distance. In contrast, in the case of the collisions of sodium and potassium atoms, the colliding pairs need to get much closer, and the equivalent distance is $\sim$20A^o [247]. Therefore, light-assisted collisions in hetero-nuclear collisions occur at shorter distances. In A 3DMOT, the number of colliding atoms decreases once the inter-nuclear distance is reduced: this explains that the collisional loss rate is less in hetero-nuclear collisions compared to the homo-nuclear case.

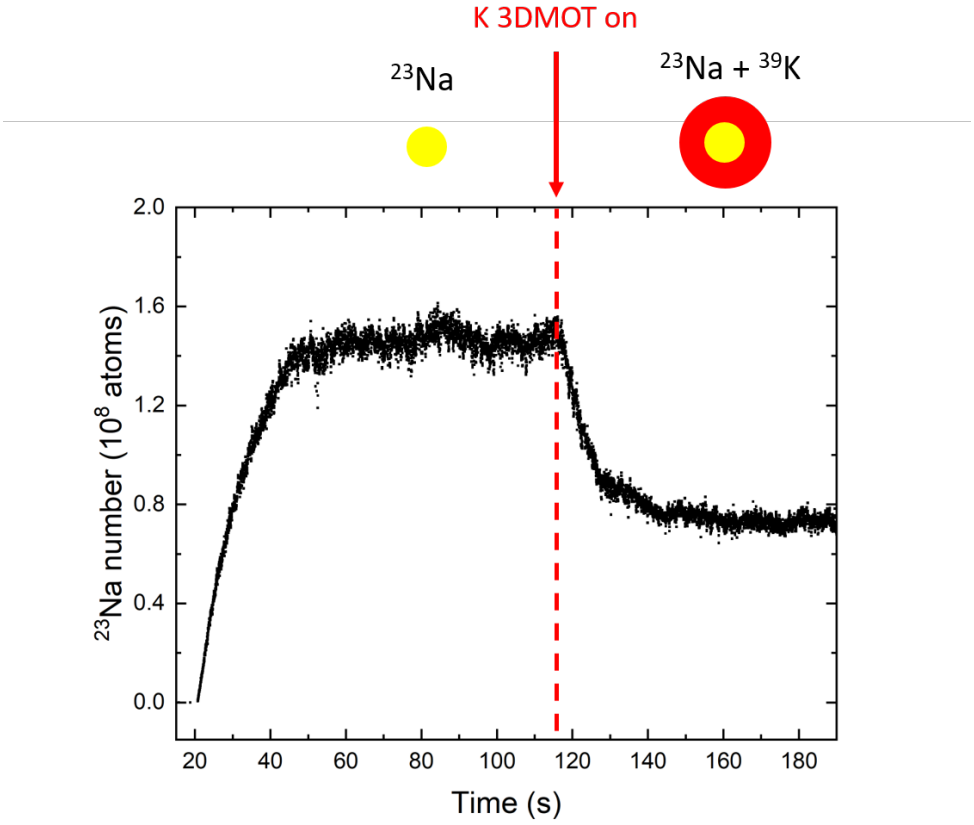


Figure 4.19: The loading dynamics of sodium atoms in the 3DMOT in the absence and the presence of potassium 3DMOT. We obtain a steady state atoms number in the Na-3DMOT, and after that, allow the loading of the potassium 3DMOT. We observed a significant loss of sodium atoms as large as 50%.

In the experiment, we observed the loading dynamics of sodium atoms in the presence of the potassium 3DMOT (K-3DMOT), and we observed a significant loss of the sodium atoms. To determine the interspecies collisional rate (β_{NaK}), we follow the procedure described in the ref [255]. The loading dynamics of the sodium atoms in the presence of the potassium atoms can be expressed as,

$$\frac{dN_{Na}}{dt} = L_{Na} - \gamma N_{Na} - \beta_{NaNa}\int_V n_{Na}^2 d^3r - \beta_{NaK}\int_V n_{Na}n_K d^3r \tag{4.20}$$

Typically, alkali 3DMOTs operate in the constant density limit when the number of

the trapped atoms is 10^5 or more [256, 257].

We consider, a Gaussian spatial density distribution of the trapped atoms in the sodium and potassium 3DMOTs.

$$n^{Na}(t) = n_0^{Na}(t)e^{-2\left(\frac{r}{w_{Na}}\right)^2} \tag{4.21}$$

and,

$$n^{K}(t) = n_0^{K}(t)e^{-2\left(\frac{r}{w_{K}}\right)^2} \tag{4.22}$$

The Eqn.4.20 becomes,

$$\frac{dN_{Na}}{dt} = L_{Na} - \left(\gamma + \beta_{NaNa} N_K \left[\frac{2}{\pi(w_{Na}^2 + w_K^2)}\right]^{3/2}\right) \times N_{Na} - \beta_{NaNa}\left(\frac{1}{\pi w_{Na}^2}\right)^{3/2} \times N_{Na}^2 \tag{4.23}$$

The size of the MOTs grows with the time in the constant density limit of the MOTs. Therefore, the quantities w_{Na} and w_K in the above equation are the function of time.

We calculate the value of the interspecies collisional loss rate (β_{NaK}) in the following way, we determine the number of sodium atoms trapped in the 3DMOT in the steady state in the absence and presence of the K-3DMOT. Using loading dynamics of the sodium atoms in the absence of K-3DMOT, We have determined the intraspecies collisional loss rate (β_{NaNa}), as described in Appendix-D.4. We define N'_{Na} and N_{Na} as the number of sodium atoms trapped in the Na-3DMOT (Na-3DMOT) in the presence and absence of K-3DMOT. We denote w'_{Na} and w_{Na} as the width of the Na-3DMOT in the presence and absence of K-3DMOT. In the absence of K-MOT, the Eqn.4.23 takes the following form,

$$\frac{dN_{Na}}{dt} = L_{Na} - \left[\gamma + \beta_{NaNa}\left(\frac{1}{\pi w_{Na}^2}\right)^{3/2} N_{Na}\right] \times N_{Na} \tag{4.24}$$

In the presence of K-MOT, the Eqn.4.23 takes the following form,

$$\frac{dN'_{Na}}{dt} = L_{Na} - \left(\gamma + \beta_{NaK} N_K \left[\frac{2}{\pi(w'^2_{Na} + w_K^2)}\right]^{3/2}\right) \times N'_{Na} - \beta_{NaNa}\left(\frac{1}{\pi w'^2_{Na}}\right)^{3/2} \times N'^2_{Na} \tag{4.25}$$

The steady state solutions of Eqn.4.24 and Eqn.4.25 leads to the following relation,

$$\beta_{NaK} = \Big[\frac{\pi(w'^2_{Na} + w^2_K)}{2}\Big]^{3/2} \times \frac{1}{N_K N'_{Na}} \Big\{\gamma(N_{Na} - N'_{Na}) + \beta_{NaNa}\Big[\Big(\frac{1}{\pi w^2_{Na}}\Big)^{3/2} N_{Na} - \Big(\frac{1}{\pi w'^2_{Na}}\Big)^{3/2} N'_{Na}\Big]\Big\} \tag{4.26}$$

In the experiment, we determine the sodium atom numbers N_{Na} and N'_{Na} in the steady state of the Na-3DMOT. The captured fluorescence images of the Na-3DMOT in the presence and absence of the K-3DMOT yield w'_{Na} and w_{Na}. We load the K-3DMOT in the absence of the Na-3DMOT and determine the number of trapped potassium atoms (N_K) and the width (w_K) in the steady state of the K-3DMOT.

As shown in Figure-4.19, we observe a significant loss of the trapped sodium atoms in the presence of the K-3DMOT. For the typical loading parameters of the sodium and potassium 3DMOTs, using the procedure outlined above and calculated in Appendix-D.4, we obtained $\beta_{NaK} \approx 2 \times 10^{-12}$ cm^3/sec.

We experimentally measured the dependence of the loss of the trapped sodium atoms on the number of trapped potassium atoms. In this experiment, we tuned the loading rate of the potassium atoms and controlled the number of trapped potassium atoms in the 3DMOT. We have tuned the potassium loading rate by varying the K-2D$^+$MOT parameters, the 2D$^+$MOT repumper beam intensity, and the 2D$^+$MOT magnetic field gradient. Thus, we have controlled the number of trapped potassium atoms in the 3DMOT. During the experiment, every time we load the Na-3DMOT at a fixed experimental conditions.

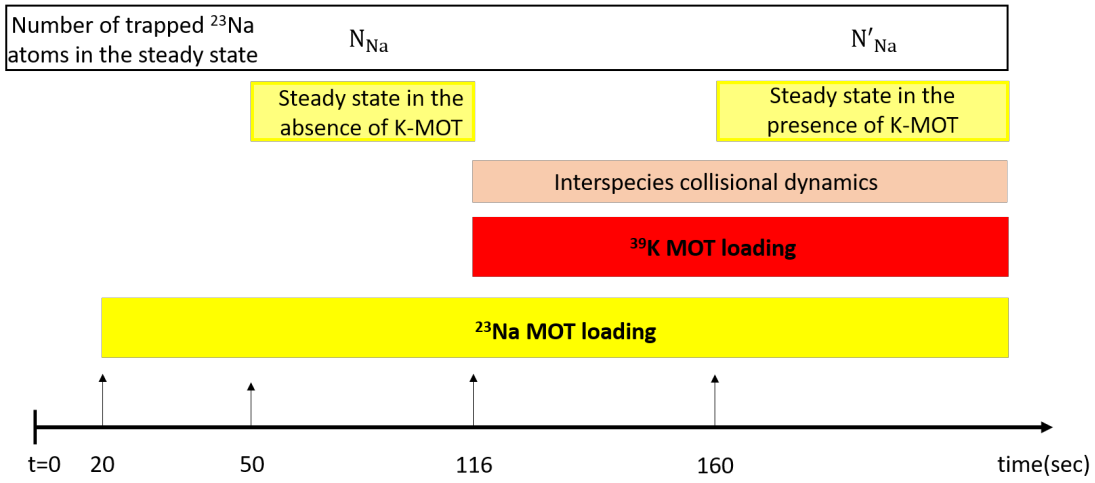


Figure 4.20: The schematic diagram of the sequence of the measurement of the number of trapped sodium atoms in the absence and the presence of the trapped potassium atoms in the 3DMOT. During the entire sequence, we observe the fluorescence of the Na-3DMOT by placing the band pass filter (FB590-10, Thorlabs) before the Femto Watt detector.

In the experiment, we capture the fluorescence of the Na-3DMOT on the Femtowatt detector. The sequence of the measurement is outlined in Figure-4.20. Initially, we blocked both sodium and potassium cold atomic beams from the respective 2D$^+$MOTs. In order to block the cold atomic beams, we use mechanical shutters (in-house design and manufactured using a hard disk driver) and place at the focus of the 2D$^+$MOT telescopic expansions. Then, we have allowed the cold atomic beam of sodium atoms to load the Na-3DMOT (at $\sim$ 20sec), and it reaches a steady state ($\sim$ 50sec) with a number of trapped atoms N_{Na}. Then we allow the potassium cold atomic beam (at $\sim$ 115sec) to load K-3DMOT. The interspecies collisions between trapped potassium and trapped sodium atoms set in, and this mechanism introduces the interspecies collisional loss rate (the last term) in Eqn.4.20. In the dual-species 3DMOT configuration, the Na-3DMOT again reaches a steady state ($\sim$ 160sec) with a number of trapped atoms N'_{Na}.

We define the quantity, $\frac{N'_{Na}}{N_{Na}}$ as the 'survival probability' of the trapped sodium atoms in the steady state in Na-3DMOT in the presence of K-3DMOT. We plot ^{23}Na survival probability' w.r.t the 'Mixture ratio'. We define the 'Mixture ratio' as the ratio of the

steady state number of the potassium atoms (N_K) in the K-3DMOT to the steady state number of sodium atoms (N_{Na}) in the Na-3DMOT in the absence of K-3DMOT.

Figure-4.21 shows the experimentally observed variation of the ^{23}Na survival probability' w.r.t to the 'Mixture ratio'.

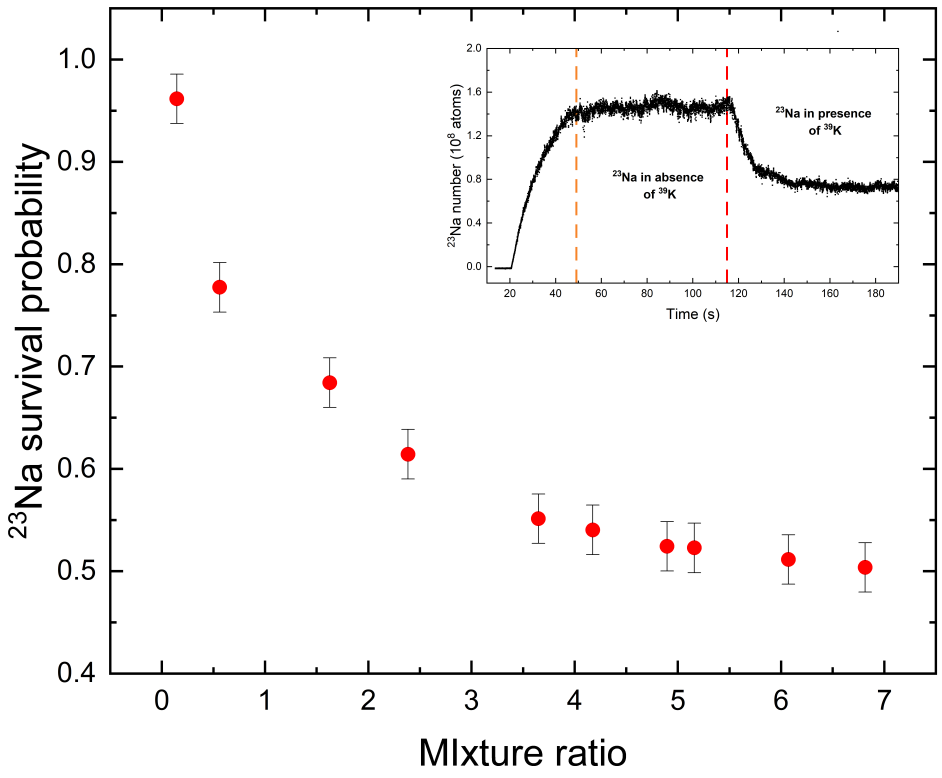


Figure 4.21: The variation of the 'survival probability ^{23}Na' with the 'Mixture ratio'. The survival probability decreases as the 'Mixture ratio' increases. As more potassium atoms are trapped in the dual-species 3DMOT, the collisional rate has also increased. The 'survival probability' saturates beyond the 'Mixture ratio' value of 5.

In a dual-species 3DMOT of sodium and potassium atoms, many collisional channels are involved in the process. The homo-nuclear collisional channels are $Na-Na$, Na^*-Na, $Na-Na^*$, and Na^*-Na^* for the sodium atoms, while for potassium atoms corresponding channels are $K-K$, $K-K^*$, K^*-K, and K^*-K^*. In the case of hetero-nuclear collisions,

the involved collisional channels are $Na - K$, $Na^* - K$, $Na - K^*$, and $Na^* - K^*$.

Figure-4.21 indicates that the survival probability gradually decreases as the 'Mixture ratio' is increased. As the loading rate of potassium atoms increases, the number of atoms and the density of the K-3DMOT increases. The increment of the density of the potassium atoms leads to an increment of the interspecies collisional losses. Therefore, the 'survival probability' of the sodium atoms in the 3DMOT has also decreased. We have observed that the survival probability saturates beyond the 'Mixture ratio' value of 5. At a higher loading rate of the potassium atoms, the number of the trapped atoms in the K-3DMOT has also increased, and the 3DMOT operates in the 'constant density limit.' In the 'constant density limit,' the density of the 3DMOT saturates to a value and doesn't increase further. As the number of potassium atoms in the K-3DMOT is increased by increasing the loading rate, the density doesn't increase, and the 3DMOT grows in size. As the density of the K-3DMOT remains the same, the trapped sodium atoms, on average, interact with the a fixed number of potassium atoms beyond the 'Mixture ratio' value of 5. Therefore, the interspecies collisional rate between the trapped sodium and the potassium atoms remains unchanged.

Figure-4.22 shows the variation of the '^{23}Na survival probability' w.r.t the excited state population of the ^{39}K trapped atoms in the 3DMOT.

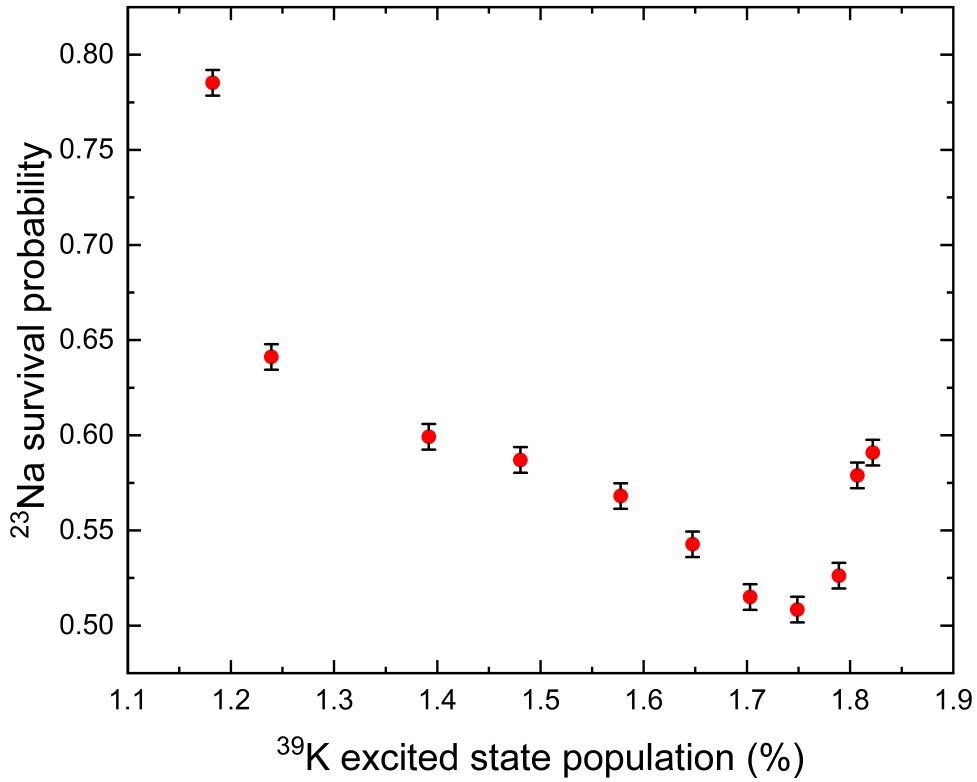


Figure 4.22: The variation of the 'survival probability of ^{23}Na' w.r.t the excited state population of the potassium atoms in the 3DMOT. As we increase the excited state population, there is a decrease in the survival probability. At higher values of the excited state population beyond 1.75%, the survival probability increases.

We have observed that the survival probability of the sodium atoms decreases with the increase of the excited state of the potassium atoms in the K-3DMOT. As the number of potassium atoms in the excited states increases, this results in an increase in the hetero-nuclear collisions between sodium and potassium atoms. As mentioned earlier, in hetero-nuclear collisions' significant contributions come from the collisional channels, where one of the atoms is in the excited state while the other atom of the different species is in the

ground state. To simplify the discussion of sodium-potassium hetero-nuclear collisions, let us consider the following loss channels Na*-K and Na-K* are only involved in the collisions. For sodium-potassium atoms, the interatomic potential energy involves in the excited-ground state collisions, all the potential energy curves are attractive for the collisional channel Na(3s)-K*(4p), while most of the potential energy curves are repulsive for the collisional channel Na*(3p)-K(4s) [251]. As discussed earlier, when the colliding atoms interact via an interatomic attractive potential energy in an excited-ground state collision, RE and FSC mechanisms result in a significant loss of atoms from the trap. An increment of the excited state population of the potassium atoms leads to an increment of Na-K* loss channels (attractive potential energy) in the hetero-nuclear collisional dynamics. Therefore, an increment of the excited state population of the potassium atoms decreases the '^{23}Na survival probability'.

As shown in Figure-4.22, the survival probability of ^{23}Na atoms gradually decreases as we increase the excited state population of ^{39}K atoms till the value of 1.75 %. As we increase the excited state population of ^{39}K further, we have observed an increment of '^{23}Na survival probability'.

An increase in the excited state population increases the collisional rate of the channels $K - K^*$ and $Na - K^*$. As mentioned earlier, the homo-nuclear collision is governed by the interatomic potential $\sim \frac{1}{R^3}$, while the hetero-nuclear collision is determined by the interatomic potential $\sim \frac{1}{R^6}$. As a result, once we increase the excited state population beyond 1.75%, the collisional rate of the channel $K - K^*$ dominates. Therefore, the repulsion between the cold potassium atoms depleted the density of the potassium atoms in K-3DMOT. Thus, the sodium atoms, on an average, interacting with fewer numbers of potassium atoms as we increased the excited state population of the potassium atoms. Therefore, the collisional loss rate of the sodium and potassium atoms has also decreased. This explains that, as we increased the excited state population beyond 1.75%, the survival probability of ^{23}Na has also increased.

In the experiment, we varied the repumper intensity of the K-3DMOT to tune the excited state population of the trapped potassium atoms. For a given repumper intensity, we determine the excited state population of the trapped potassium atoms in the K-3DMOT by measuring the absorption of a probe beam, resonant with the transition $\left|3^2S_{1/2}F=2\right\rangle \rightarrow \left|3^2P_{3/2}F=3'\right\rangle$, signal when sent through the atomic cloud. The measurement sequence is depicted Figure-4.23.

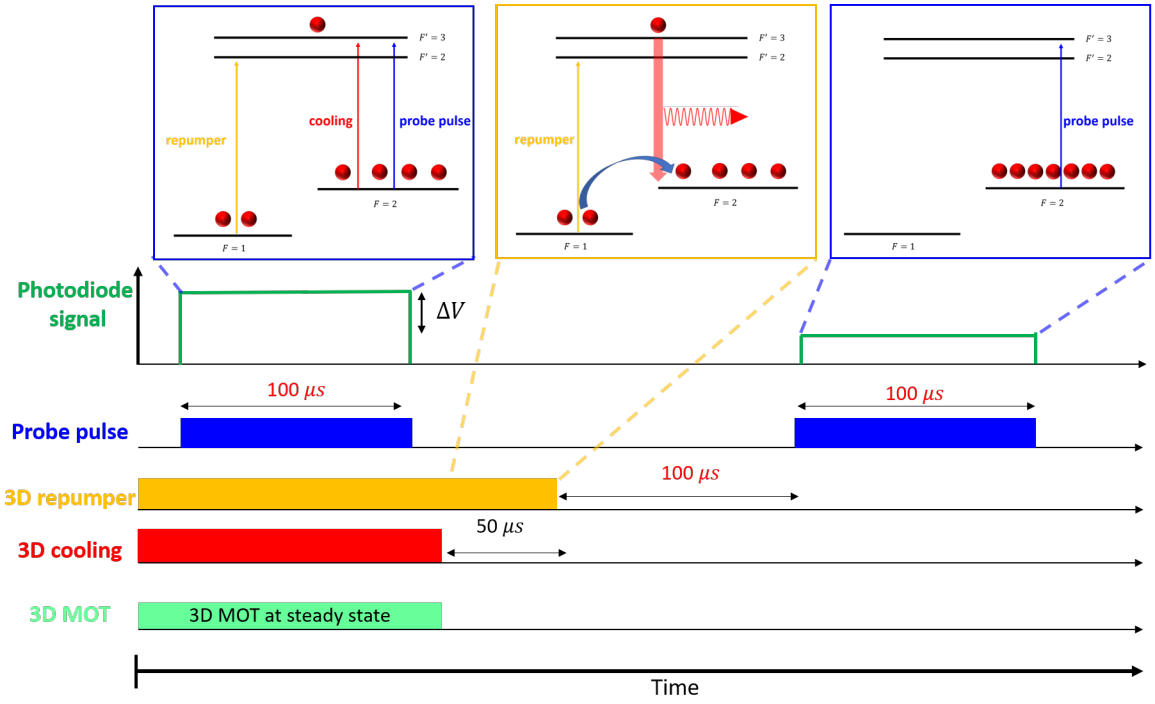


Figure 4.23: The schematic diagram shows the measurement scheme of the excited state population of the potassium atoms in the 3DMOT. We send the first pulse, 'probe 1' in the steady state of the 3DMOT. The transmission of the probe is shown by the photodiode signal(green). The distribution of the atoms in different hyperfine states is shown in the inset. Afterward, we turned off the cooling beam of the 3DMOT, and after 50 μs, we turned off the repumper beam of the 3DMOT. This scheme optically transfers the atoms in the hyperfine state $|F=1\rangle$ to $|F=2\rangle$. After 100 μs, we sent another pulse, 'probe 2', through the atomic cloud. The transmission of the probe is shown by the photodiode signal(green). The difference(ΔV) between the two consecutive signals is a measure of the optically pumped atoms to $|F=2\rangle$.

We sent a pulse ('pulse 1') of the probe beam through K-3DMOT and measured

the probe beam transmission on a fast photo-diode (PDA100A, Thorlabs). Then we perform an optical pumping to shelve the atoms from $\left|3^2S_{1/2}F=1\right\rangle$ hyperfine state to $\left|3^2S_{1/2}F=2\right\rangle$.

To perform the optical pumping, we turned off the 3DMOT cooling beam and exposed the atomic cloud to the 3DMOT repumper beam for another $\sim 50\,\mu$s and turned it off. As a result, the atoms are shelved to $\left|3^2S_{1/2}F=2\right\rangle$ as shown in Figure-4.23. During the experiment, we varied the time delay between the switching off time of the 3DMOT cooling beam followed by the 3DMOT repumper beam and found that $\sim 50\,\mu$s is optimized.

We have sent another pulse ('pulse 2') of the probe beam of duration$\sim 100\,\mu$s after a delay of $\sim 100\,\mu$s from switching off the 3DMOT repumper. We measured the transmission of the probe beam pulse on the photodiode. During the process, we registered the transmission signal of the two consecutive probe beam pulses on the oscilloscope. The optical pumping process shelves the atoms on $\left|3^2S_{1/2}F=2\right\rangle$ hyperfine states. As a result, there is an increment in the absorption of the probe beam, and it is obvious from the reduction of the transmission signal of the 'pulse 2'. The additional absorption of the probe beam (ΔV) (as shown in Figure-4.23) is a measure of the number of atoms that have been pumped optically from $\left|3^2S_{1/2}F=1\right\rangle$ state.

Chapter 5

Magnetic trap and magnetic transport

In this chapter, I will describe the detailed description of the magnetic transport scheme that I have designed, constructed, and installed to the main experimental facility in order to transfer cold and trapped sodium and potassium atoms from the 3DMOT chamber to the "science cell".

In Section-5.1, I have given an overview on the concept of a quadrupole magnetic trap. In Section-5.2, I have described the principle, algorithm, design, and the underlying considerations in order to perform an efficient transport of cold atoms magnetically. In Section-5.3 , I have described the construction of the magnetic transport assembly, which includes the manufacturing and the experimental characterization of each of the coils in the magnetic transport assembly. In Section-5.4, I have given an overview on the loss of atoms due Majorana spin-flip associated in a linear quadrupole trap. In Section-5.5, I have given a thorough description of the design and the realization of the Quadrupole-Ioffe quadrupole (QUIC) magnetic trap, which will be employed to trap the transported cold atoms in the "science cell". The QUIC trap aides in preventing the Majorana loss of cold atoms and in performing the evaporative cooling for longer duration to reach quantum degeneracy.

5.1 Magnetic trap

The coupling Hamiltonian of an atom with a total magnetic moment operator $\hat{\mu}$ in a given magnetic field $\vec{B}$ is given by [258],

$$H = -\hat{\mu}.\vec{B} \tag{5.1}$$

In the presence of the external magnetic field, the Zeeman energy of an atom in the basis $|I, J, F, M_F\rangle$ is given by [50],

$$E = g_F M_F \mu_B B \tag{5.2}$$

Where, B is the magnitude of the magnetic field, μ_B is the Bohr magneton, g_F is the hyperfine Lande-g factor, and M_F is the hyperfine magnetic quantum number.

The energy of an atom in the magnetic field depends on the quantity $g_F\, M_F$. For example, when $g_F\, M_F > 0$, $E > 0$, these states are called low-field seeking states, on the other hand, when $g_F\, M_F < 0$, $E < 0$, these states are called high-field seeking states.

Figure-5.1(a) shows the variation of the magnetic field in a quadrupole configuration. The field is zero at the center and the magnitude of the field is increasing linearly from the center. Figure-5.1(b) shows the Zeeman energy of an atom in the magnetic field in the low-field seeking states. The atoms could be trapped in the magnetic field, when the energy, $K_B T$ is well within the potential depth (V_{trap}) of the magnetic trap, where, T is the temperature of the atomic cloud and K_B is the Boltzmann constant. The underlying assumption is that the magnetic dipole moment of the atoms always precess around the local magnetic field.

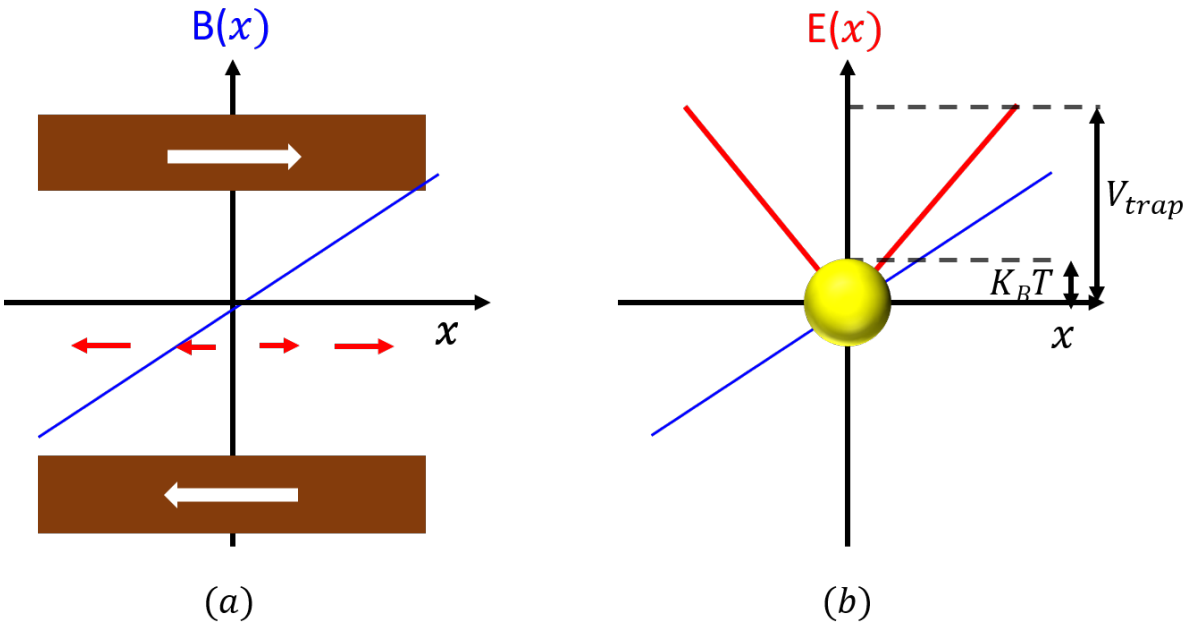


Figure 5.1: Trapping of an atom in a quadrupole magnetic field. (a) The magnetic field generated by a pair of coils in anti-Helmholtz configuration, the white arrows show the direction of the current flow and the blue line shows the variation of the field with the distance from the center and red arrows indicate the direction of the local magnetic field. (b) The potential energy of the atoms in the quadrupole magnetic field. The atoms could be trapped when, $\sim K_B\,T < V_{trap}$.

One could generate this sort of magnetic field configuration by applying current in anti-Helmholtz configuration in a pair of coaxial coils as shown in Figure-5.1(a). Using the Taylor series expansion, we can write the expression of the magnetic field near the center of the trap,

$$B(r) \approx B(0) + (r.\Delta)_{r=0} = b_x x + b_y y + b_z z \tag{5.3}$$

Where, $b_i = \frac{\partial B}{\partial r_i}$, where, $i \in (x, y, z)$, is the gradient of the magnetic field and (x, y) are radial co-ordinates, and z is the axial co-ordinate. Using cylindrical symmetry of the magnetic field configuration w.r.t z-axis, we can write $b_x = b_y = -b$, where b is the magnitude of the magnetic field gradient on $(x - y)$ plane. According to Maxwell's equation $\widehat{\nabla}.\widehat{B} = 0$, which allow us to write, $-2b_x = -2b_y = b_z$. Therefore, we can write $B(r) = (-x, -y, 2z)\,b$. Therefore, the Zeeman energy of an atom in a quadrupole

magnetic trap is given by,

$$E = g_F M_F \mu_B b \sqrt{x^2 + y^2 + 4z^2} \tag{5.4}$$

In practice, in a quadrupole magnetic trap, the magnetic field varies linearly with distance near the center of the trap as long as the distance is the smaller than the radius of the coils. The magnetic coils we have designed for the magnetic transport typically have an average radius $\sim$ 4.5 cm (inner radius $\sim$ 1 cm and outer radius $\sim$ 8 cm). The average radius of an atomic cloud is typically between 0.1-0.2 cm. We have explicitly checked that, the cloud is well within the linear region of the magnetic field variation, i.e. the atoms are experiencing a constant gradient b. As a result, a zero potential energy has been created at the center and linearly increases from the center for the low-field seeking Zeeman states. As a result, it is possible to trap spin-polarised atoms, i.e., the atoms in a given M_F state, in this magnetic trap. The expression of the magnetic field of a single coil along the radial and axial directions has been described in Appendix-E.

5.2 Realization of a magnetic transport

The design of the vacuum manifold has been describe in sufficient detail in Chapter-2. As describe in Section-2.1, we would like to transfer the cold and trapped atoms from the 3DMOT chamber to the "science cell". The smaller dimension of the "science cell" allows us to place the quadrupole coils very close to the atoms, this provides a tighter confinement to the atoms. At the same time the smaller dimension of the "science cell" would give enough access to the imaging optics to be placed very close to the atoms, this yields a very high spatial resolution, a pre-requisite to image of individual atoms [113].

We have decided to transfer the atoms to the "science cell" by transferring the atoms to a magnetic trap at the 3DMOT chamber, then subsequently moving the magnetic trap center towards the "science cell".

As discussed earlier, in a moving magnetic trap scheme, two configurations have been implemented. The first one relies on the varying current in the static ensemble of magnetic coils in anti-Helmholtz configuration [210–213]. The other one is based on a physical displacement of the magnetic trap coils [214,215]. We have taken the former approach. In this respect, I have designed and constructed a magnetic transport assembly and installed it around the vacuum system as shown in Figure-5.2.

I have written a Mathmematica script to obtained the optimized parameters of the magnetic coils require in order to perform an efficient magnetic transport of the atoms.

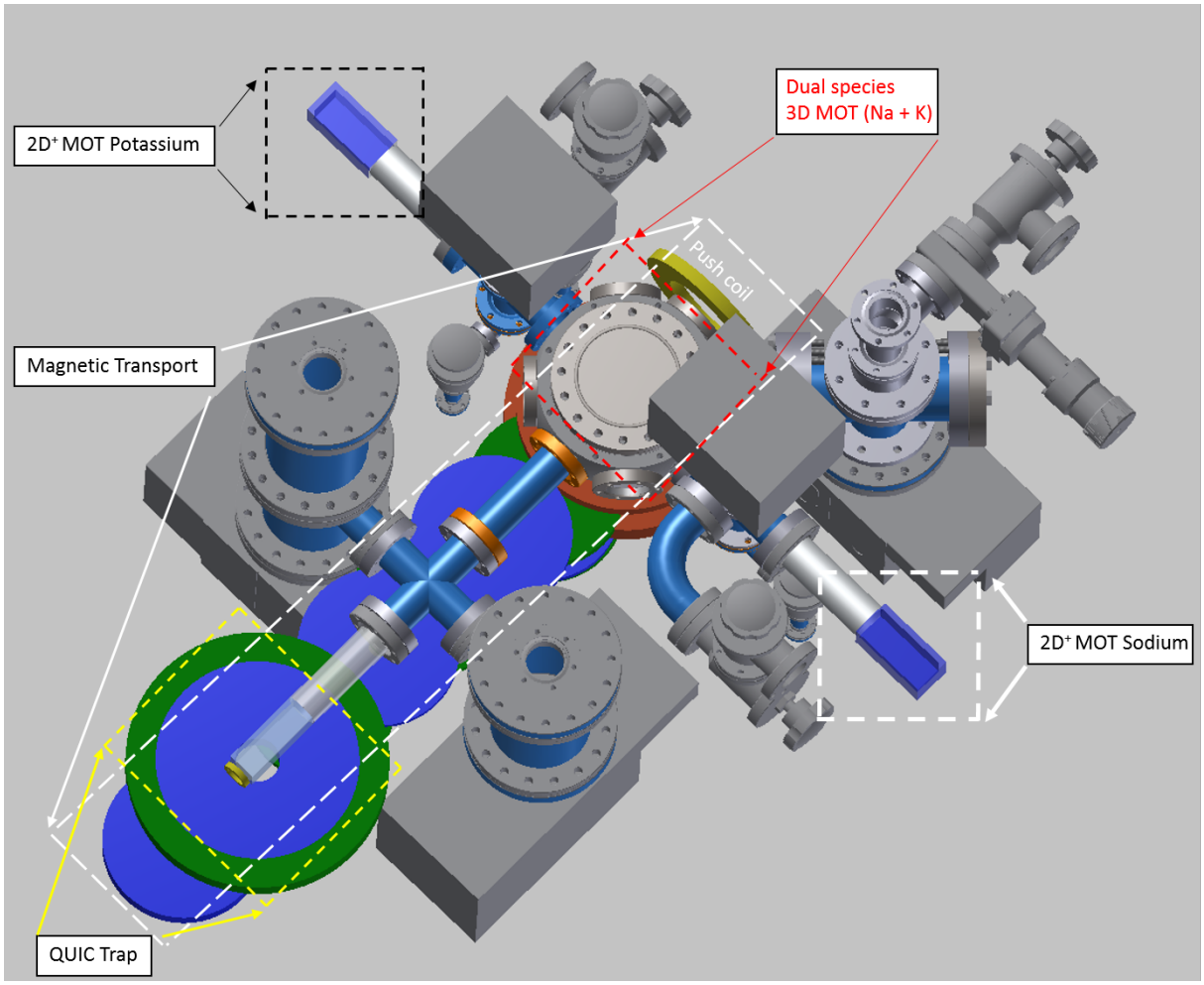


Figure 5.2: The magnetic transport assembly around the UHV chamber. A large number of coils are placed from the 3DMOT chamber towards the "science cell".

Figure-5.3 shows the side view of our vacuum system and the magnetic coils. In this

figure, we are showing only lower coils of the transport assembly. The parameters of each of the coils are listed in Table-E.1.

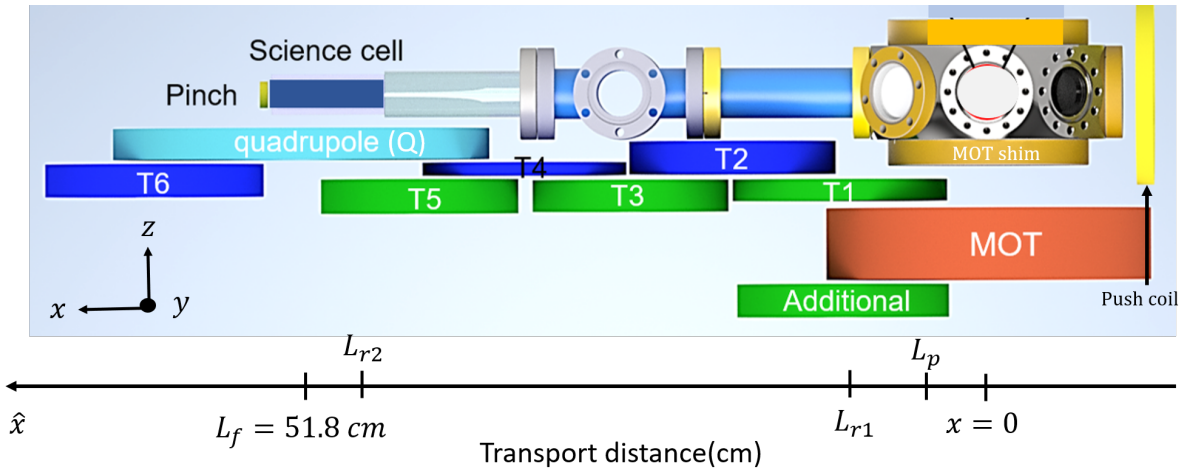


Figure 5.3: A side view of the magnetic transport assembly. A series of static coils are shown. After obtaining the atoms in the 3DMOT, the atoms would be trapped in the quadrupole magnetic trap of MOT coils by increasing the current in the MOT coils. Thereafter, dynamically varying the currents in the subsequent coils T_1, T_2, T_3 and so on, the magnetic trap would be dynamically moved towards the quadrupole coil(Q). The atoms would adiabatically follow the magnetic trap and would be transferred to the final quadrupole coil (Q) at a distance $x = 51.8$ cm in the "science cell".

5.2.1 Principle

In this section, we present the principle of the magnetic transport and the algorithm that calculates the current in each of the coils in order to perform the transfer of the atoms. let us consider the co-ordinate along the transport direction as $\hat{x}$, while $\hat{y}$, and $\hat{z}$ are along transverse directions. To perform the transport, we would like to transfer the atoms after the MOT phase to the magnetic trap generated by the MOT coils then will initiate the transport by employing the dynamical variation of the current in the subsequent transport coils. In the following discussion, we consider the atoms in $|F = 2, M_F = 2\rangle$ state for both the atoms ^{39}K and ^{23}Na atoms. For the atomic state under consideration, $g_F = 1/2$ and $M_F = 2$, therefore, we have $g_F\, M_F = 1$. As a result, we have the the dipole moment of

the atoms as, $\mu = \mu_B$.

Algorithm

We want to impose and control the shape and the position of the magnetic trap. Thus we need to control four parameters, position of the center of the trap (x^*) and the gradients of the trap along x, y, and z directions, which determine the shape of the cloud in the trap. But the gradients (b_x, b_y, b_z) along x, y, and z directions are not independent, they are linked through the Maxwell's equation as follows,

$$\begin{cases} \widehat{\nabla}.\widehat{B} = 0 \\ \\ b_x + b_y + b_z = 0 \end{cases} \tag{5.5}$$

Therefore, in order to control the magnetic transport during the transport, we consider the following parameters,

1. position of the trap center, x^*

2. b_y, gradient along $\hat{y}$ axis

3. Aspect ratio, $A = \frac{b_x}{b_z}$

The aspect ratio, 'A' varies as the trap changes from the quadrupole configuration to the transport one. For example, if we consider $\hat{z}$ along the axial direction of the magnetic coils, then using cylindrical symmetry of the quadrupole magnetic, we can write the value of 'A' as $-\frac{1}{2}$. This is the case for the quadrupole magnetic field generated by the MOT coils. In a magnetic transport scheme, the magnetic field configuration breaks the cylindrical symmetry because several coils are operating simultaneously. Therefore, during transport, the aspect ratio acquires a different value than -$\frac{1}{2}$.

The algorithm calculates the currents in all the coils as a function of the position of the centre of the trap (x^*). Then we assign a temporal dynamics by assigning a time at each position of the centre of the trap.

A priori, we defined two functions, the y-gradient, $b_{y0}(x)$, and aspect ratio $A_0(x)$ at each position x over the transport length as shown in Figure-5.4.

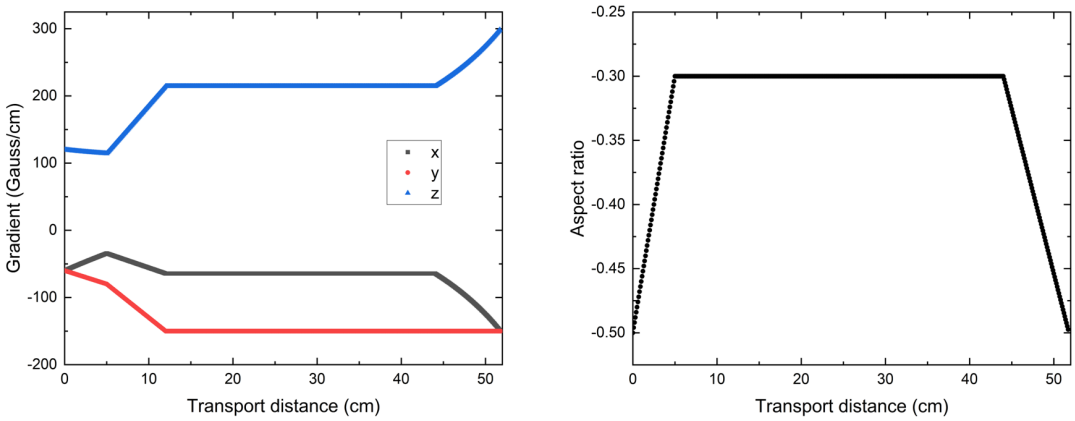


Figure 5.4: We have defined (a) the magnetic field gradient along y-axis and (b) the aspect ratio over the transport length. The numerical simulation determines the required current in each of the magnetic coils in order to obtained these defined y-gradient and aspect ratio over the transport length.

As mentioned earlier, our magnetic transport scheme has static ensemble of coils. Therefore, each of the coils has a distribution of magnetic field components along x, y,and z axes (the measurement and the simulation has been shown in Appendix-E). In other words each coils have corresponding field gradients $b_x(x), b_y(x)$, and $b_z(x)$ at a given position x, along the transport axis $\hat{x}$.

As we have described, we have three independent control parameters of the trap, therefore, in practice that we have control using currents in three consecutive coils of the magnetic transport assembly.

Therefore, at any given position x^*, we determine the resultant magnetic field, $B(x^*)$, the field gradient along y-axis, $b_y(x^*)$, and the aspect ratio, $A(x^*)$, due to three consecutive coils. Let us consider three consecutive coils with indices $i = 1, 2, 3$, with currents I_1, I_2, and I_3. Let us define the associated field of the coils as $\tilde{B}_i$ and y-gradient as $\tilde{b}_i$ by unit current flowing in the coils. Therefore, we can write,

$$\begin{cases} B(x^*) = \tilde{B_1}(x^*)\, I_1 + \tilde{B_2}(x^*)\, I_2 + \tilde{B_3}(x^*)\, I_3 = \sum_{i=1}^{3} \tilde{B_i}(x^*)\, I_i \\ b_y(x^*) = -\sum_{i=1}^{3} (\tilde{b}_{i,x}(x^*) + \tilde{b}_{i,z}(x^*))\, I_i \\ A(x^*) = \frac{\sum_{i=1}^{3} \tilde{b}_{i,x}(x^*)\, I_i}{\sum_{i=1}^{3} \tilde{b}_{i,z}(x^*)\, I_i} \end{cases} \tag{5.6}$$

If we consider, x^* as the center of the magnetic trap, then our algorithm solves the following set of equations,

$$\begin{cases} B(x^*) = 0 \\ b_y(x^*) = b_{y0}(x^*) \\ A(x^*) = A_0(x^*) \end{cases} \tag{5.7}$$

I have devised a numerical method (Appendix-E) in Wolfram Mathematica, which determines the current required in each of coils at any given position (r^*) of the transport to obtained the defined y-gradient, $b_{y0}(r^*)$ and the aspect ratio, $A_0(r^*)$. The numerical simulation yields required value of the current in each of the coils as shown in Figure-5.5.

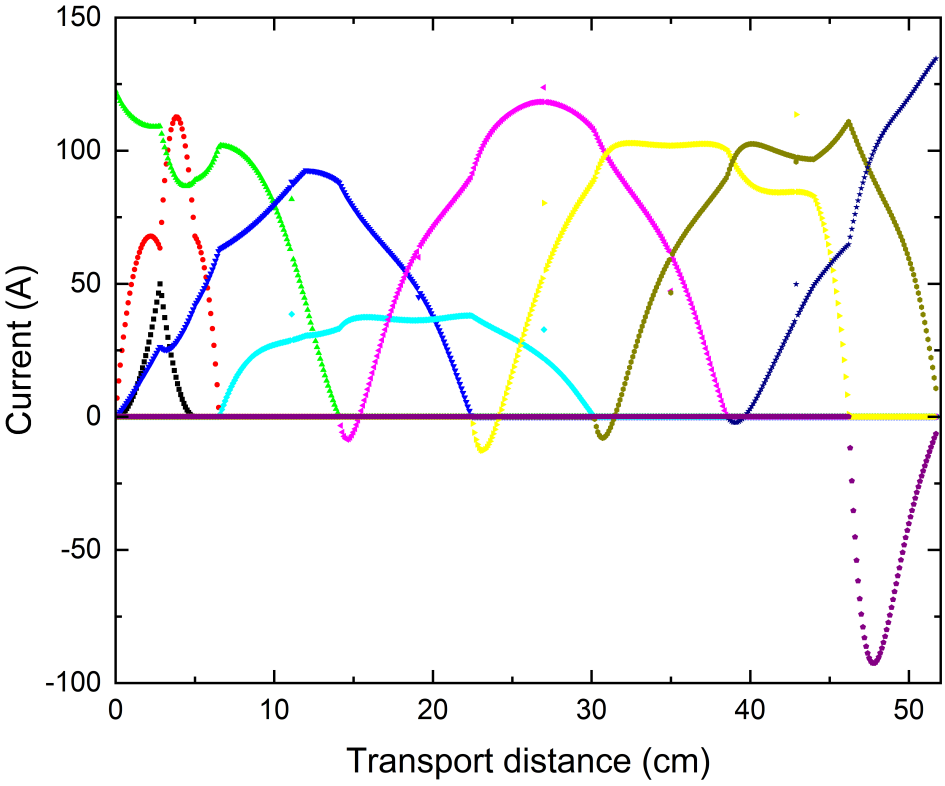


Figure 5.5: The solution of the numerical simulation. The current in each of the coils required in order obtained the defined y-gradient and the aspect ration as shown in Figure-5.4. The different coloured graphs indicate currents through different sets of coils: green - MOT coils, black - push coil, red - additional coils, blue - T_1, cyan - T_2, magenta - T_3, yellow - T_4, dark green - T_5, dark blue - quadrupole, and violet - T_6. The coil definition is given in Appendix-E.

We have segmented the entire transport sequence into three parts: "Initialization", "Transport", and "Out coupling".

Initialization

The transport is initialized by transferring the atomic cloud in the magnetic trapping potential of the MOT coils. For this purpose, the current in the MOT coils (defined as "M") is ramped to higher values from the operating value, required for the 3DMOT.

Due to the cylindrical symmetry of the MOT coils, the aspect ratio (A) is -0.5. At this high current, the y-gradient of the MOT coils becomes, $\sim$ 60 Gauss/cm as shown in Figure-5.4(a) at $x = 0$. Then we would like to transfer the atoms to the science cell by turning the current in the consecutive coils. As a result, the defined gradient and aspect ratio have to experience some ramps from their initial value (at position $x^* = 0$) to their specified transport values. To initiate the transport, the variation of the y-gradient and the aspect ratio is shown in Figure-5.4(a) and Figure-5.4(b), respectively. To obtain the defined y-gradient and the aspect ratio, we need the following set of coils: MOT coils (M), the coils (T_i, $i \in (1, 6)$), and the final quadrupole coils (Q) as shown in Figure-5.3. To ensure the good spatial overlap of the magnetic fields of the MOT coils, and the first transport coils, we placed two more coils: "MOT shim" and "Additional coil" (T_{ad}). We can divide the "Initialization" stage into two steps: the "Pushing" step and the "Ramp" step.

We have placed another coil "Push coil", behind the MOT coils as shown in Figure-5.3. This coil is operational during the "Pushing" step. During this step, the push coil, additional coils and MOT shim coils, and T_1 coils are turned on along with the MOT coils. This step continues till the pushing length, $x = L_p$, where the current in the push coil reaches the value zero as shown in Figure-5.5. At the end of this step, y-gradient (b_y) and aspect ratio (A) acquire values -80 Gauss/cm and -0.3, respectively, these values are not the fixed ones. We play around with these values to obtain an optimized situation. This step is followed by the "Ramp" step between the positions, $x = L_p$ and $x = L_{r1}$. Typically, L_p = 5 cm and L_{r1} = 12 cm. After this step, the y-gradient (b_y) and the aspect ratio (A) acquire the values specified for the transport sequence, for example, -150 Gauss/cm and -0.3, respectively. From, $x = L_{r1}$, the transport continues with a constant y-gradient (b_y) and aspect ratio(A). The current in the push coil is not a parameter like in other coils. In our transport scheme, we defined the current in the push coil to obtain reasonable current requirements in other coils during the "Pushing" step. Note that, L_p and L_{r1} are the parameters, we varied their value to get a optimized working condition.

Transport

Once the atoms arrived at $x = L_{r1}$, from that point onwards the gradient, and aspect ratio remain constant, till $x = L_{r2}$. Typically, $L_{r2} = 44\,\text{cm}$. Over this distance, the shape of the atomic cloud remains the same. During this sequence, The following coils are operational: MOT, T_1, T_2, T_3, T_4, and T_5 as shown in Figure-5.5.

Out coupling

At the end of the transport sequence, we want to transfer the atoms to the magnetic trapping potential of the "Quadrupole coil (Q)", where the aspect ratio again becomes $-\frac{1}{2}$. Therefore, we need to change the gradient and the aspect ratio from the transport sequence to the final quadrupole one. For this purpose, we ramp the gradient and the aspect ratio from $x = L_{r2}$ to $x = L_f$. The required currents in the coils are shown in Figure-5.5.

Step	Characteristic lengths
Pushing	$x = 0 \rightarrow x = L_p$
Ramp	$x = L_p \rightarrow x = L_{r1}$
Transport	$x = L_{r1} \rightarrow x = L_{r2}$
Out coupling	$x = L_{r2} \rightarrow x = L_f$

Table 5.1: Summarizing the sequence and the characteristic lengths involve in magnetic transport.

5.2.2 Dynamics

In the previous discussion we have been considering the properties of the atoms during the transport in the static conditions. In order to move the trap added the dynamics to the sequence. For this purpose, we define the position (x) as a function of the transport time. During the transport the trap will change its shape, due to the change in the value of the gradients and the aspect ratio. As a result, the magnetic trap no longer remains a

conservative one during the transport. It could cause a transfer of energy to the atomic cloud. Therefore, the transfer of atoms needs to be done carefully. We should be careful to decide the overall time required to transfer from $x = 0$ to $x = L_f$. A very fast transport would cause a high acceleration, which could cause the atoms to leak out from the trap, on the other hand, a too long transport would cause the Majorana loses (ref to Section-5.4) to become significant.

In the following, I will discuss some of the significant considerations required in order to perform an optimized magnetic transport of the atoms.

Inertia

If we perform the transport very fast, the atoms will experience a high acceleration. This could lead to the loss of atoms from the trap. When the center of the trap is accelerated too fast, the atoms are pushed away from the center. A magnetic trap has finite trap depth, if the acceleration is very fast this causes a separation between the center of the atomic cloud and the center of the trap, which would cause a significant loss of atoms from the trap. This phenomenon limits the maximum acceleration with which we could transfer magnetic trap.

Using dimensional analysis, the typical acceleration that we can associate to a magnetic trap with a gradient of magnetic field b as,

$$a_{max} = \frac{\mu_B b}{m} \tag{5.8}$$

Where, μ_B is Bohr magneton and m is the mass of the trapped atoms.

With the defined gradient values, we have minimum gradient $(b_x) \sim 35$ Gauss/cm along x direction at the position $x = L_P = 5$ cm as shown in Figure-5.4(a). At this position, if we consider ^{39}K, the heaviest atoms in our dual-species experiment, we obtained $a_{max} \sim 50m/s^2$.

The equation of motion of a single atom on the transport axis (x) can be written as,

$$\frac{d^2x'}{dt^2} = -a - \frac{\mu_B b_x}{m} sign[x'] \tag{5.9}$$

where x' is the distance from the center of the trap at the position $x = L_p$ on the transport axis and a is the acceleration of the trap during the transport. From the above equation, we can see that, the acceleration found in Eqn.5.8 corresponds to vanishing trapping force on the atoms i.e., if the trap center is accelerated with such a value, the trapping potential at position $x = L_P$ is tilted so much that the trapping potential become constant for $x' < 0$.

In practice, a magnetic trap is not a perfect quadrupole, non-linearities appear beyond the average radius of the coil.

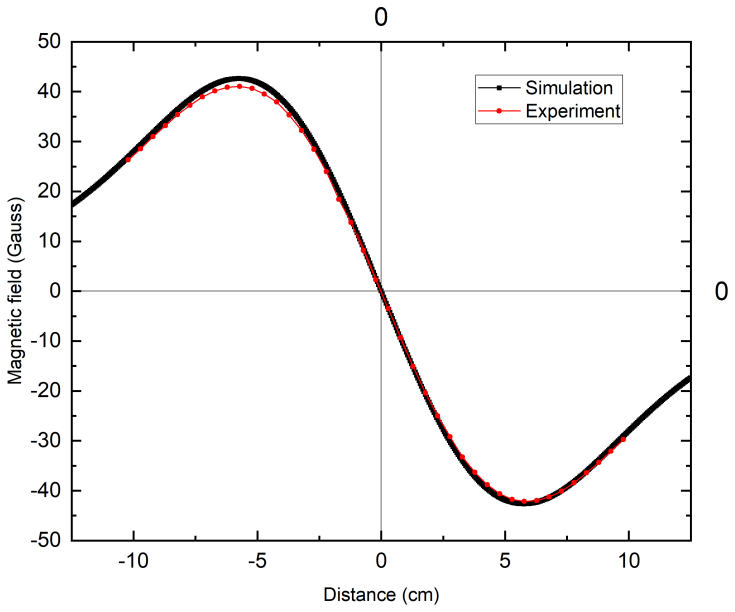


Figure 5.6: Magnetic field component along transport direction of T_1 coil. The magnetic field varies linearly over a distance $\sim$ 5 cm, beyond this point the non-linearity starts to appear.

Therefore, this length defines the effective spatial extension of the trap (R_{trap}). As a result of the non-linearities, the atoms could leave the trap at an acceleration smaller than

a_{max}, when the atomic cloud shifted by a distance $\sim R_{trap}$. Figure-5.6 shows the magnetic field component of T_1 coil along the transport direction. The magnetic field remains linear up to 5 cm, beyond that distance non-linearities arise. Typically, the region of the linear magnetic field defines the characteristic length (R_{trap}) of the magnetic trap.

We could write the expression of the energy of an atom in 1D potential by taking into consideration of the inertial tilt due to the acceleration of the center of the magnetic trap,

$$E = m(ax' + a_{max}\,|x'|) \tag{5.10}$$

For the region $x' < 0$, corresponding energy will be,

$$E = m(-a + a_{max})\,|x'| \tag{5.11}$$

Now, we will consider the effect of the temperature of the atomic cloud on the maximum allowed acceleration of transport. We assume that, the atoms will leave the trap when the thermal energy (K_BT) becomes equal to the depth of trap. If we consider an atomic cloud of temperature T, in a magnetic trap of trap length R_{trap}, then using dimensional analysis, we define a characteristic acceleration as, $\frac{K_BT}{m\,R_{trap}}$. Therefore, the allowed maximum acceleration of the transport reduces to,

$$a^*_{max} = a_{max} - \frac{K_BT}{mR_{trap}} \tag{5.12}$$

For an cloud of ^{39}K atoms at temperature (T) $\sim 1mK$, and with typically trap radius of $R_{trap} \approx 5$ cm, we obtained, $\frac{K_BT}{m\,R_{trap}} \approx 5\,m/s^2$. Therefore, we obtained, $a^*_{max} \sim 45m/s^2$.

As a result, the quantity a_{max} in Eqn.5.10 and Eqn.5.11 will be replaced by a^*_{max}. The corresponding equations become,

$$E = m(a\,x^{'} + a^*_{max}\,|x'|) \tag{5.13}$$

, and

$$E = m(-a + a^*_{max}) \left| x^{'} \right| \tag{5.14}$$

Thus, we can see that the non-linearities result in an even smaller value of the allowed maximum acceleration (a^*_{max}) at which the trap could be moved. For example, Figure-5.7(a) showing the potential energy of the magnetic trap in the units of mK at the position $x = L_P$ in static condition and comparing the temperature ($T \sim 1mK$) of the atomic cloud w.r.t to the depth of the potential.

An asymmetry can be seen in the potential of the trap between the region $x' < 0$ and $x' > 0$. This arises due to the variation of the $y-$gradient and the aspect ratio around the position $x = L_p$.

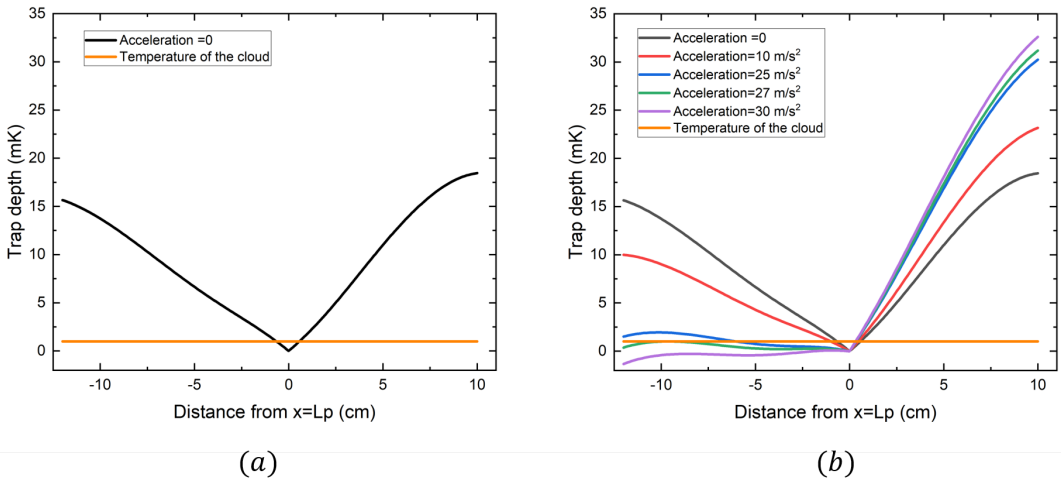


Figure 5.7: The potential of the magnetic trap at the position $x = L_P$ on the transport axis (a) at static condition, and (b) with different acceleration at which the trap is moved. At higher acceleration, the trap range of the trap is significantly reduced on $x' < 0$ region.

Figure-5.7(b) shows the dynamical profiles of the potential of the trap at the position $x = L_P$, taking into consideration the inertial til due to different values of the acceleration of the trap. As we increase the acceleration, the trap depth is continuously decreasing on $x' < 0$ side. At an acceleration $27\, m/s^2$, the trap depth becomes equal to the temperature of the cloud at temperature $\sim 1\, mK$ at position $x' = -10$ cm from the center of the

trap. From this position onwards the atoms will leave the trap. Therefore, if the trap is accelerated with a value $27\,m/s^2$ or higher, this could result in a significant loss of the atoms from the trap at the position $x = L_p$ on the transport axis.

Our above discussion sets the maximum value of the acceleration to $a^*_{max} \sim 27m/s^2$. At the acceleration $\sim 27m/s^2$.

We can calculate the minimum duration over which we can perform the transport by using the free fall formula,

$$\tau_{min} = 2\sqrt{\frac{2\,L_H}{a^*_{max}}} \tag{5.15}$$

where L_H is the half of the total transport length L_T, i.e, $L_T = 2 \times L_H$. In our design, $L_T = 51.7$ cm. Therefore, with the $a^*_{max} = 27\,m/s^2$, we obtain, $\tau_{min} \approx 280$ ms.

During the transport, we accelerated the trap over the distance L_H. Then subsequently, decelerated the trap over the rest of the distance, L_H in a total duration τ_T.

In practice, we set the total duration, τ_T, of the transport much longer than τ_{min}, such that, $\tau_T >> \tau_{min}$.

Adiabaticity

In our above discussion, we have set the maximum acceleration at which we could perform the transport of an atomic cloud at a temperature $\sim$ 1 mK. Our transport scheme involves a few ramp phases in the defined $y-$gradient and the aspect ratio. The ramp phases cause the change in the shape of the atomic cloud during transport. We need to be careful during the ramp phases, a very fast ramp could heat the atoms.

To prevent the heating of the atomic cloud during the ramp phases, the duration of the ramp phases (τ_{ramp}) must be longer than the characteristic evolution time of the atoms in the trap, T^{add}_{Na} and T^{add}_{K} respectively for ^{23}Na and ^{39}K. In other words, $\tau_{ramp} >> T^{add}_{Na}$ and T^{add}_{K}. This condition on the duration of the ramp phases is known as the adiabaticity criteria for magnetic transport.

A magnetic quadrupole trap is a linear trap, in a linear trap we cannot uniquely define a time period for the trapped atoms as it is usually defined in a harmonic trap. Nevertheless, we can define a characteristic time scale for an atomic cloud of size D_c trapped in a linear trap with a field gradient b as,

$$T = \sqrt{\frac{2\,m\,D_c}{\mu_B\,b}} \tag{5.16}$$

Where m is the mass of the atoms.

This time scale defines the typical time an atom takes to travel across the atomic cloud of size D_c. In the case of ^{39}K and ^{23}Na atomic clouds of size $D_c \approx 3$ mm, the corresponding time at the position $x = L_p$ will be $T_K^{add} \approx 14$ ms and $T_{Na}^{add} \approx 10$ ms, respectively. We have considered the position $x = L_p$ on the transport axis because this position corresponds to the lowest magnetic field gradient (along $x-$axis) compared to the entire transport distance. In terms of adiabaticity, this position will be worst, having a longer characteristic time period of the atoms. Therefore, the duration of the ramp phases should last more than T_K^{add} and T_{Na}^{add} in case of ^{39}K and ^{23}Na atoms.

From the above consideration, we can set a limit on the maximum velocity at which we can perform the transport of the atoms. To deduce the maximum velocity we state that, the atoms should not travel a distance equal to the size of the atomic cloud in a time scale faster than T_K^{add} and T_{Na}^{add} in the case of ^{39}K and ^{23}Na atoms. For a typical cloud size of $D_c \approx 3mm$, we obtain, $v_{max} \sim 0.21\,m/s$ and $v_{max} \sim 0.3\,m/s$ for ^{39}K and ^{23}Na atomic cloud.

Trap Trajectory

In Section-5.4, I have discussed the loss of the atoms from quadrupole trap due to Majorana spin flip. Therein, I have estimated the time required for the Majorana loss for both species and found that, $\tau_M^K \approx 130$ sec and $\tau_M^{Na} \approx 80$ sec receptively for ^{39}K and ^{23}Na atoms, for an atomic cloud of radius $R_c \sim 1$ mm. As a consequence, total transport

duration τ_{total} must follow the following condition,

$$T_K^{add}, T_{Na}^{add} << \tau_{min} << \tau_T << \tau_M^K, \tau_M^{Na} \tag{5.17}$$

Table-5.2, summarizes the characteristic time scales involve during the magnetic transport of the atoms.

Characteristic time	defined by	Value
Ramp	T_K^{add}, T_{Na}^{add}	14 ms, 10 ms
Minimum duration of transport	τ_{min}	280 ms
Majorana spinflip	τ_M^K, τ_M^{Na}	130 sec, 80 sec

Table 5.2: Summarizing the characteristic timescale involve in the Magnetic transport scheme.

A total transport duration (τ_T) of few seconds seems reasonable. A detailed consideration of all the above listed numbers allow us to define a position-to-velocity correspondence. The position of the center of the trap is shown in Figure-5.8.

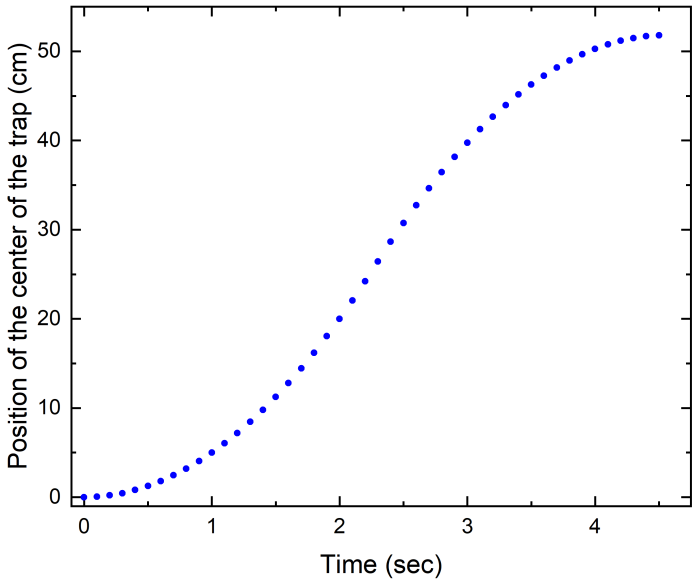


Figure 5.8: Position of the centre of trap during the transport.

We have used second order polynomial in position to ensure a constant acceleration for the center of the trap during the transport. The total duration of the transport has been decided 4.5s, with a acceleration $\sim$ $10cm/s^2$ $(0.1\ m/s^2)$, which is 270 times smaller than a^*_{max}.

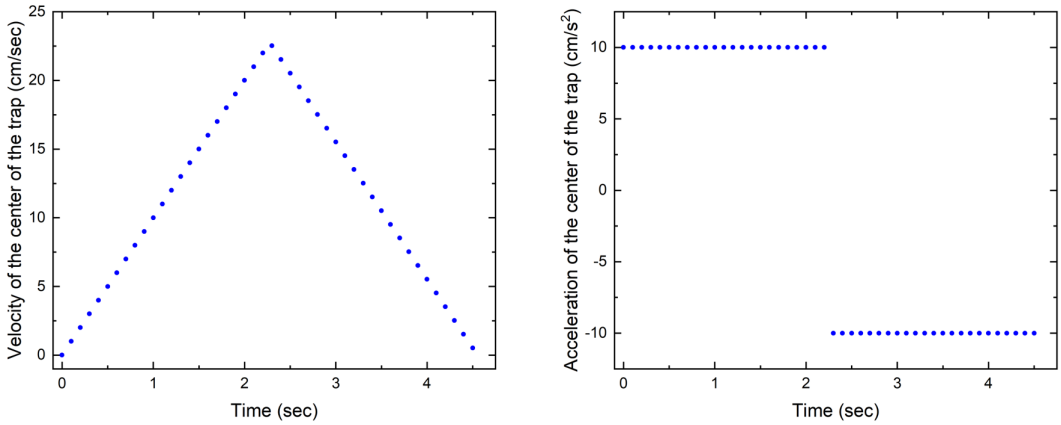


Figure 5.9: (a) The velocity and (b) acceleration of the centre of the trap during the transport.

Figure-5.9(a) and Figure-5.9(b) show the velocity and the acceleration of the center of the trap during the transport.

5.3 Construction of the magnetic transport assembly

Taking into all the considerations, we have started to make the coils. We numerically optimized the transport scheme by optimizing the current in each of the coils. To optimize, we have varied the parameters of the magnetic coils, for example, the inner radius of the coils, the number of turns in the coils, the position of the coils along transport direction, etc. For each given set of parameters of the coils, we perform the numerical simulation to obtain the optimized value of the currents in the coils. Our numerical simulations provide the parameters of the coils required for magnetic transport in optimized condition, as shown in Table-E.1.

On the basis of the numerical simulation, we have started to manufacture all the coils. shows the winding of the MOT coil in RRI workshop.



Figure 5.10: Winding of the MOT coil. We wrapped the capillary tube with a Nomex tape, then we wound the tube on a aluminium structure.

We made the MOT coils using copper capillary tubes. The tube has outer diameter ∼4.2 mm and a wall thickness of ∼ 0.6 mm. We wrap the tube with a electrical insulator tape (Nomex adhesive), which can withstand high temperature ∼ 200^{o}C. After making the MOT coils, we placed them in aluminium frames with proper cuts, which would prevent the eddy current during then switching of the MOT coils during the experiments. Figure-5.11 shows the image of one of the prepared MOT coils placed in its respective aluminium frame before the installation.

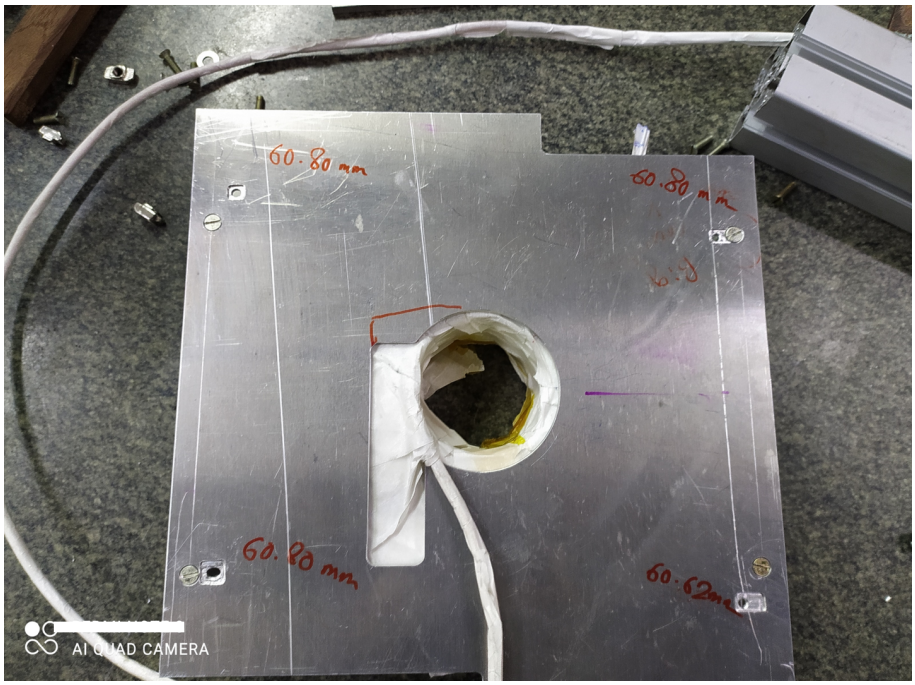


Figure 5.11: One of the prepared MOT coil is mounted in the aluminium frame just before the installation to the transport assembly.

Our transport coils are disk shaped, so we designed those coils with a proper care. We have used ribbon type enamelled copper wires of dimension, typically 1 mm × 5 mm and 1 mm × 3.2 mm respectively. To make the transport coils we have manufactured a special arrangement in our workshop, as shown in Figure-5.12.

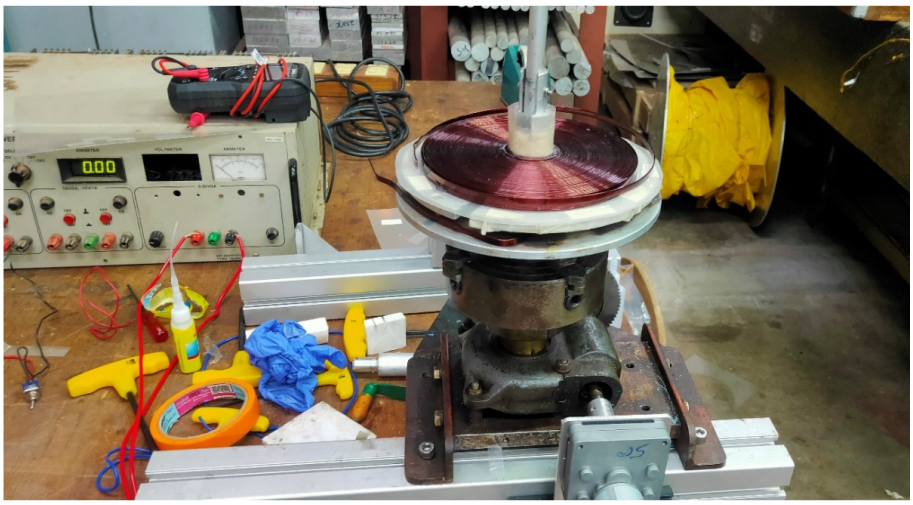


Figure 5.12: We have wound all of our magnetic transport coils in this specialized arrangement made by the RRI workshop.

Figure-5.13 shows one of the manufactured transport coil and respective aluminium frame.

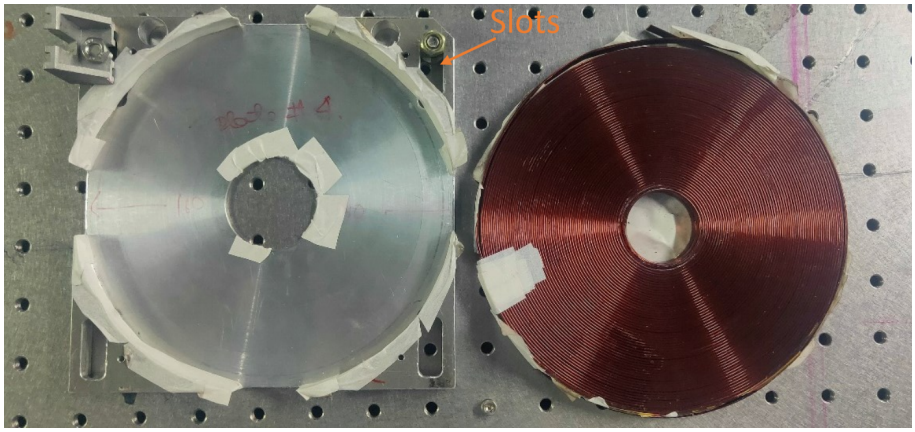


Figure 5.13: One of the transport coil and its mounting frame.

We have constructed the magnetic transport assembly into two stages. In stage-1 , we have constructed and assembled the coils upto transport coils T_2. Once all the coils and their respective aluminium mounting frames of the stage-1 were ready, we have install them in a rigid and stable mounting system made out of aluminium. Figure-5.14 shows the magnetic transport assembly in stage-1 before installation.

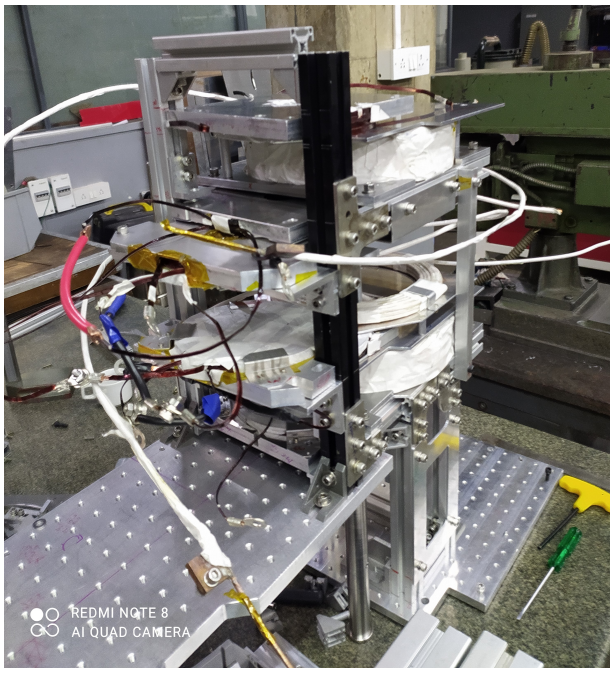


Figure 5.14: The stage-1 of magnetic transport assembly before installation.

In stage-2, we have manufactured and install rest of the transport coils till T_6. The assembly of the magnetic transport coil assembly in stage-2 are shown in Figure-5.15 and Figure-5.16.

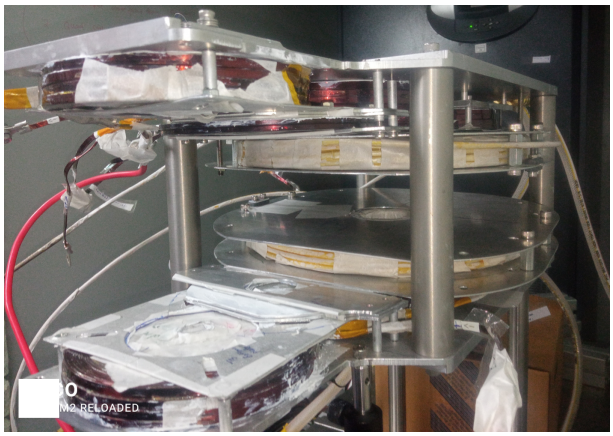


Figure 5.15: Stage-2 of the magnetic transport assembly.

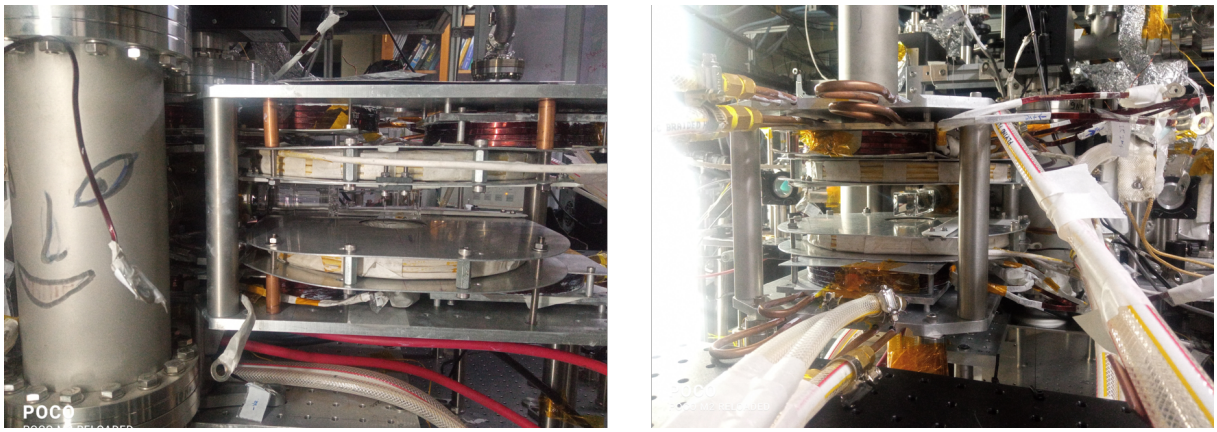


Figure 5.16: The installation of the magnetic transport stage-2 to the experiment.

5.4 Majorana losses from the quadrupole traps

A quadrupole magnetic field configuration could confine and trap the atoms in their low-field seeking states ($g_F M_F > 0$). As discussed earlier, in a quadrupole magnetic trap, the magnetic field is zero at the center and linearly increases from the center. As a result the energy of the low-field seeking states also increases as it moves from the center. Therefore, the atoms are trapped around the zero magnetic field region.

An atom with an internal magnetic dipole moment μ precess around the external magnetic field at the Larmor frequency,

$$\Omega_L = \frac{e\,B}{2m_e} = \frac{\mu_B B}{\hbar} \tag{5.18}$$

as shown in Figure-5.17. Where e is the electronic charge, B is the magnitude of the magnetic field, and m_e is the mass of the electron. $\mu_B = \frac{e\,\hbar}{2m_e}$ is the Bohr magneton.

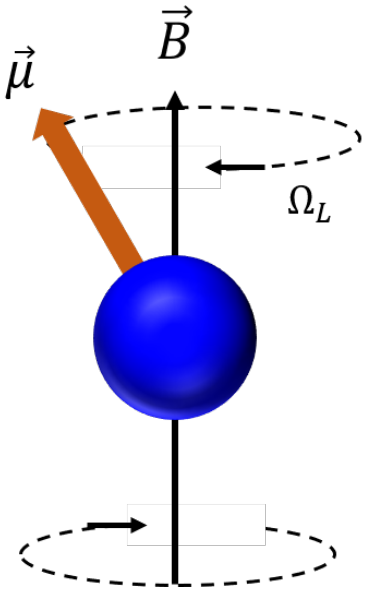


Figure 5.17: An atom with magnetic dipole moment μ is precessing around the external magnetic field with the Larmor frequency Ω_L.

To maintain the angular momentum projection, the atom must follow the external magnetic field adiabatically. This condition demands that the Larmor frequency must be larger than the rate of change of the angular orientation between the magnetic dipole moment and the magnetic field seen by the atom. This ensures the atom maintains its angular momentum projection the same relative to the instantaneous magnetic field direction.

But this condition breaks down near the zero magnetic field point. When an atom traversing through the very low magnetic field in the magnetic trap as shown in Figure-5.18, the Larmor frequency becomes very small and the atom experiences a change in the direction of the magnetic field. Therefore, the atom could not follow the direction of the local magnetic field and the atom may undergo a transition into untrapped states ($g_F M_F < 0$). This transition make the atoms to escape from the bottom of the magnetic trap, known as Majorana spin loss. As the atomic cloud becomes colder, the spatial extension of the orbit that atoms are exhibiting becomes gradually smaller around the zero magnetic field at the center. Therefore loss of the atoms becomes significant.

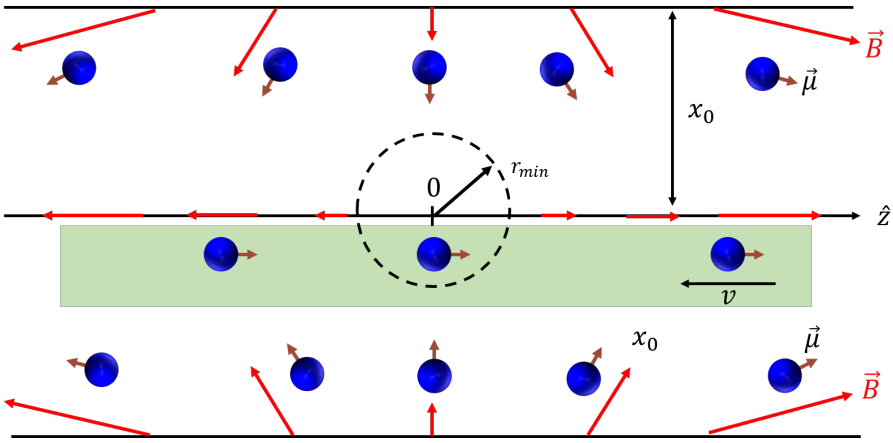


Figure 5.18: The schematic showing the Majorana spin flip. An atom which is exhibiting an orbit of spatial extension $x0$, follows the magnetic field orientation adiabatically. When the atoms is directly crossing the center of the quadrupole trap, the magnetic moment could not follow the direction of the local magnetic field direction. As a result, the atom transfer to the anti-trapping states on $z < 0$ region and the atom escape from the trap.

We can estimate the rate of loss of the atoms undergoing Majorana spin flips. An atom will remain in the trap as long as its dipole moment follows the magnetic field adiabatically. Let us consider an atom in a linear magnetic trap with field gradient b at a distance r from the center, the Zeemann energy at this position is μbr. Therefore, using Eqn.5.18 we can write the time period of the Larmor precession as $T_L = \frac{2\pi}{\Omega_L} = \frac{h}{\mu_B B}$, where $B = b\,r$. If the atom is moving towards the center of the trap, the time remaining for the flipping of the dipole moment is, $\tau_{flip} \sim \frac{r}{v}$. Thus, the condition of the trapping of the atoms would be, the time period of the Larmor precession must be faster than the flipping time of the dipole moment at any given position of the trap. As a result, there exists a minimum distance (r_{min}) for each class of velocity of the atoms. Whenever an atom reaches the center in a distance less than r_{min}, the atom couldn't maintain its spin state. Therefore, the orientation of the dipole moment of the atom would be anti-trapping w.r.t the local magnetic field direction, as a consequence the atom would be lost from the trap.

We could estimate the value of the minimum distance as, by equating the time period of the Larmor presession (T_L) and the time required for flipping (τ_{flip}) of the spin at the

position r_{min} as,

$$\frac{h}{\mu_B\, b\, r_{min}} = \frac{r_{min}}{v} \tag{5.19}$$

Therefore, we have,

$$r_{min} = \sqrt{\frac{vh}{\mu_B\, b}} \tag{5.20}$$

To estimate the loss rate of Majorana spin-flip, we consider the RMS velocity (v_R) of the velocity distribution rather than each class of the velocities. The average volume of the cloud occupied the spin-flip region in an infinitesimal time dt is given by,

$$dV = 4\pi r_{min}^2(v_R)\, v_R\, dt \tag{5.21}$$

The rate, $\frac{dN}{dt}$, of atoms entering the spin-flip region is given by the volume of the spin-flip region and the typical density ($\frac{N_T}{\frac{4\pi}{3}R^3}$) of the atomic cloud in the trap,

$$\begin{aligned} \frac{dN}{dt} &= 4\pi r_{min}^2(v_R)\, v_R \times \frac{N_T}{\frac{4\pi}{3}R^3} \\ &= \frac{3r_{min}^2(v_R)\, v_R}{R^3} \times N_T \\ \frac{dN}{dt} &= \frac{N_T}{\tau_M} \end{aligned} \tag{5.22}$$

Where N_T is the total number of atoms in the trap and R is the average radius of the atomic cloud. τ_M is the characteristic time scale for the Majorana spin flip. Therefore, the loss rate is given by,

$$\frac{1}{\tau_M} = \frac{3r_{min}^2(v_R)v_R}{R^3} \tag{5.23}$$

We can express the loss rate in terms of the experimentally measurable quantities, such as the average radius of the atomci cloud. For this purpose, we connect the average radius of the atomic cloud, R to the RMS velocity of the atomic cloud. We employ the Virial theorem to the atoms trapped in a linear trap as follows,

$$m\,v_R^2 = \mu_B\,b\,R \tag{5.24}$$

We can re-write Eqn.5.20 in terms of the RMS velocity v_R as,

$$r_{min}^2(v_R) = \frac{v_R\,h}{m\,b} \tag{5.25}$$

Now replacing the quantity $r_{min}^2(v_R)$ and subsequently, the value of v_R from Eqn.5.24 in to Eqn.5.23, we obtain the following expression of the rate of loss of atoms due to Majorana spin flip,

$$\frac{1}{\tau_M} = \frac{3\,h}{mR^2} \tag{5.26}$$

In other word, the characteristic time for the loss of atoms due to Majorana spin-flip,

$$\tau_M = \frac{mR^2}{3\,h} \tag{5.27}$$

For example, a ^{23}Na atomic cloud with an average radius of 2 mm, τ_M^{Na} corresponds to 80 sec, while for a ^{39}K atomic cloud the corresponding time is $\tau_M^K \sim 130$ sec.

The above discussion demonstrates that the Majorna spin flip could cause a significant loss of atoms in a linear quadrupole magnetic trap. To reduce the temperature of an atomic cloud, forced evaporative cooling technique [120] is employed which lasts typically over 50 sec. Therefore, performing evaporation cooling in linear quadrupole results in an undesirable loss of atoms from the trap. The situation is much more severe when the temperature of the atomic cloud reaches the critical temperature for quantum degeneracy, which results in a smaller radius of the atomic cloud. Therefore, it is important to perform further evaporation cooling of the atomic cloud in modified magnetic traps.

To circumvent the described limitation of the quadrupole traps, several trap configurations have been adopted. For example, the first BEC experiment [1] was carried out in a time-averaged orbiting potential (TOP) trap, where a rapidly rotating uniform bias magnetic field is superimposed onto the quadrupole magnetic field. The time average of

the resulting instantaneous potential yielded a harmonic-type potential. In MIT BEC experiment [3], a repulsive potential has been superimposed at the center of a quadrupole magnetic trap, so that the atoms are repelled from the center. This trap configuration has been realized by focusing a blue-detuned laser beam through the center of the quadrupole trap.

Several groups employed different configurations of the modified magnetic traps for the degenerate experiments, namely Ioffe-Pritchard trap [186], Quadrupole -Ioffe configuration (QUIC) trap [121, 187, 259].

In our case, we have decided to employ a QUIC trap for future experiments. In the following section, I will give a detailed description of the design, construction, and installation of the QUIC trap in the experimental system.

5.5 Quadrupole-Ioffe configuration (QUIC) trap

A QUIC trap consists of two quadrupole coils and one Ioffe coil as shown in Figure-5.19. This modified magnetic field configuration was first employed by Hansch's group [121] for the production of BEC of ^{87}Rb. In our setup, the final quadrupole coils (Q) of the magnetic transport assembly near the science cell will be converted into a QUIC trap after the magnetic transport sequence. The Magnetic transport scheme transfers an atomic cloud from the 3DMOT chamber over a distance $\sim$ 52 cm to the quadrupole magnetic trap produced by the final quadrupole coils(Q). To obtain the QUIC trap, we have placed another coils: Ioffe coils, with the axis of the coil along the transport axis, as shown in Figure-5.22.

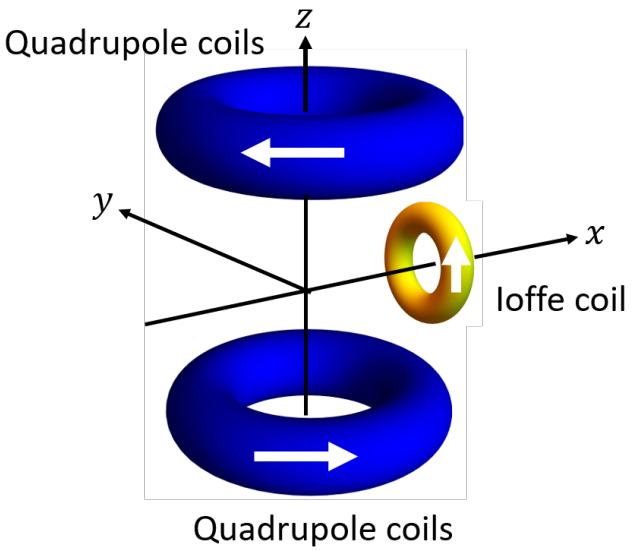


Figure 5.19: A QUIC trap set up. Two pair of coils with symmetry axis along z -axis produces a quadrupole trap in anti-Helmholtz configuration. The Ioffe coil is placed, with its axis of symmetry along the transport direction. The current in the Ioffe coil produces a curvature and offset magnetic field along x-axis.Turning on the current in the Ioffe coil converts the quadrupole trap into a QUIC trap with the trap center moving towards the Ioffe coil along the x-axis.

After transferring the atoms to the magnetic trap created by the quadrupole coils (Q), the current in the Ioffe coil will be switched on and ramped to the higher values.

As a result, the quadrupole magnetic field configuration will be converted into a QUIC trap field configuration, the evolution of a quadrupole trap to a QUIC trap is shown in Figure-5.22.

A schematic diagram of a QUIC trap arrangement is shown in Figure-5.20. The quadrupole coils (Q) are center around $X = L_f$ on transport axis ($\hat{X}$). The Ioffe coil is placed with symmetry axis on the transport axis. The positions and the dimensions of the quadrupole coils and the Ioffe coil are shown in the diagram. For purpose of the following discussions, I have shifted the origin ($x = 0$) to the center of the quadrupole coils(Q) at $X = L_f$. Therefore, from now onwards, $x = 0$ position corresponds to the center of the quadrupole coils (Q).

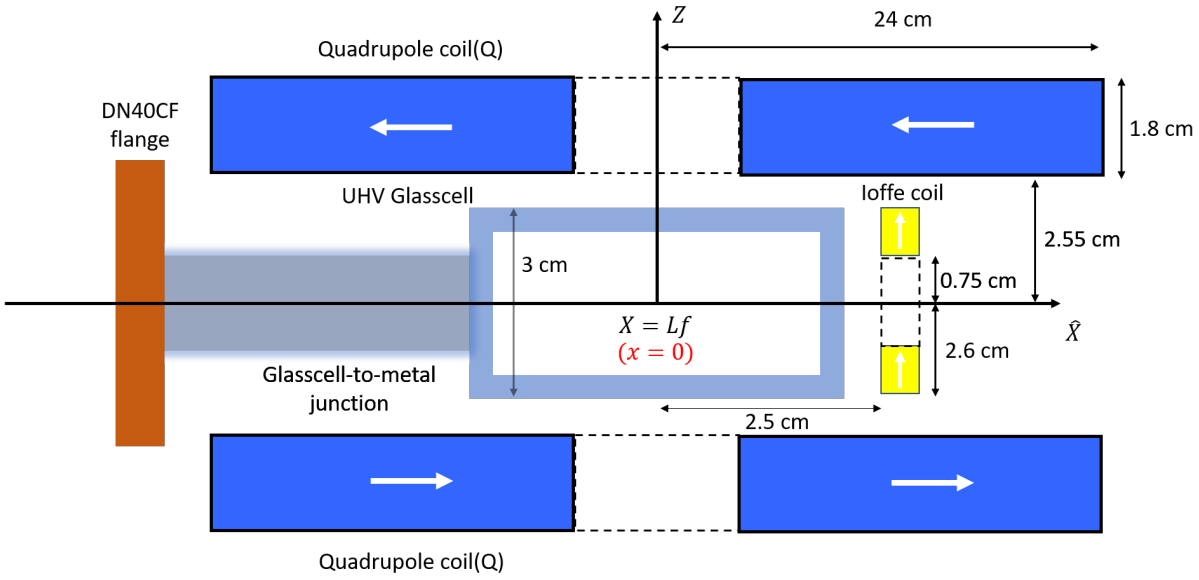


Figure 5.20: Schematic of the QUIC trap coils assembly. x=0 position corresponds to the center of the quadrupole trap. The Ioffe coil is placed with its symmetry axis along the x direction.

The direction of the current in the quadrupole coils and Ioffe coil is chosen in such a way that the radial field of the quadrupole field and axial field of the Ioffe coil are in the opposite sense for the positions ($x > 0$). The direction and the magnitude of the magnetic field component of the quadrupole coil(radial field) and Ioffe coil(axial field)

along the transport axis are shown Figure-5.21.

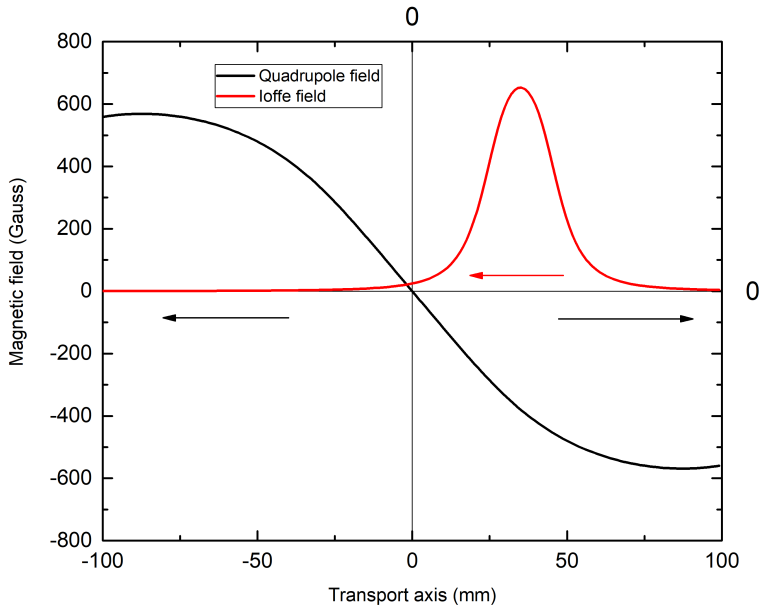


Figure 5.21: The radial magnetic field of the quadrupole trap and the axial magnetic field of Ioffe coil along the transport axis(x-axis).The black arrows represent the magnetic field direction of the quadrupole field and the red arrow is that of the axial field of the Ioffe coil.

As we send the current through the Ioffe coil, it produces an offset magnetic field that suppresses Majorana losses, which occurs near the zero magnetic field region. A non-uniform axial magnetic field along the symmetry axis (in our case, this is the transport axis) of the Ioffe coil provides axial confinement. The axial field of the Ioffe coil and the radial field of the quadrupole pair are applied in opposite directions along the x-axis as shown in Figure-5.21 so that they almost cancel each other. At higher currents, the Ioffe coil generates a higher magnetic field compared to the magnetic field generated by the quadrupole coil over the region $x > 0$ along the transport axis(x-axis). As a result, this coil geometry results in a harmonic single well with a small offset magnetic field (∼few Gauss). In the opposite limit, if the magnetic field produced by the Ioffe coil is less than that of the quadrupole coil, a double well potential is generated along the x-axis. The

atoms could be lost from these zero magnetic field points.

An evolution of a quadrupole trap into a QUIC trap along the x-axis is shown in Figure-5.22. The absolute magnitude of the magnetic field along the transport axis (x-axis) has been shown. We turned on the current in the quadrupole coils to 95 Amps and the current in the Ioffe coils ramped up from 0 to 95 Amps gradually. As the process continued, the center point of the trap gradually moved towards the Ioffe coil along x-axis Figure-5.22(b). As the Ioffe current increased, a second zero point appears and the trap magnetic field forms a double well Figure-5.22(c). As we increased the current in the Ioffe coil further, the position of the zero magnetic field points approaches each other Figure-5.22(d). With increasing the current, the position of the zero field points gradually approaches each other. Eventually, above a threshold current two zero points merged together Figure-5.22(e), in our design it happened at around $\sim$ 90 Amps. The combined field of the quadrupole coils and the Ioffe coils produces a non-zero magnetic field on the x-axis Figure-5.22(f). As we gradually increase the current in the Ioffe coil the resultant magnetic field turns into a QUIC trap and the trapping potential becomes a harmonic one near the minimum.

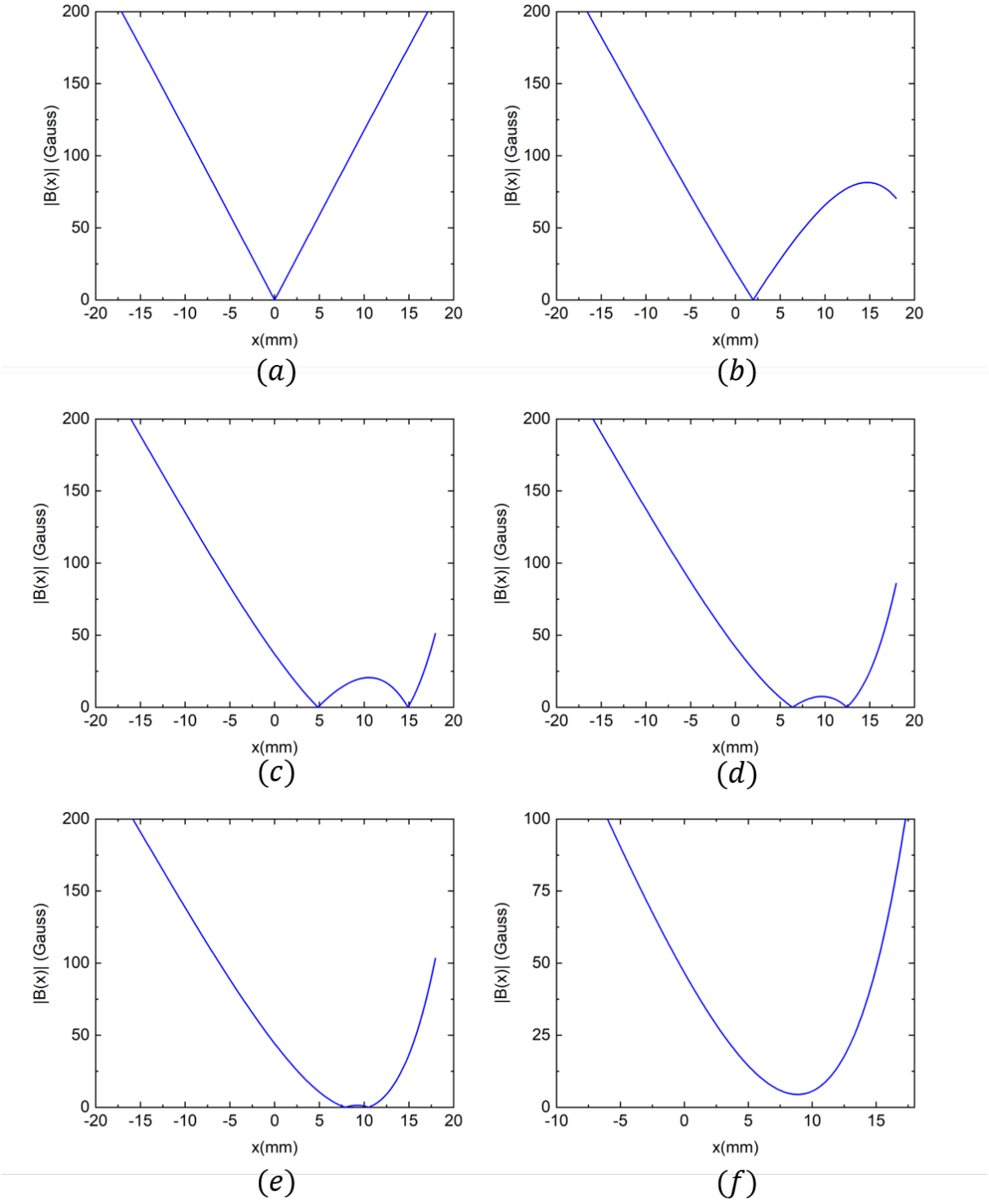


Figure 5.22: The evolution of a quadrupole trap into a QUIC one. The graphs are showing the absolute value of the magnetic field along the x-axis with 95 amps of current in the quadrupole coils and (a) 0 amps, (b) 40 Amps, (c) 75 Amps, (d) 85 Amps, (e) 90 Amps, and (f) 95 Amps of current in the Ioffe coil.

The magnetic field near the bottom of the QUIC trap generated by all the coils can be approximated as,

$$B(x,r) \approx B_0 + B_x^{''} x^2 + B_r(r) \tag{5.28}$$

where, B_0 is the offset of the magnetic field and $B_x^{''}$ is the curvature of the the axial direction and $B_r(r)$ is the magnetic field component on the transverse plane.

The potential energy of an trapped atom in this magnetic field is,

$$\begin{aligned} U(x,r) &= g_F M_F \mu_B \, B(x,r) \\ &= g_F M_F \mu_B \, B_0 + g_F M_F \, \mu_B \, B_x'' \, x^2 + g_F M_F \, \mu_B \, B_r(r) \\ &= U_0 + \frac{m}{2}\omega_a^2 x^2 + g_F M_F \mu_B \, B_r(r) \end{aligned} \tag{5.29}$$

Where, m is the mass of the trapped atom. We have, the offset of the potential energy,

$$U_0 = g_F M_F \mu_B B_0 \tag{5.30}$$

and the frequency of the trap along the transport direction,

$$\omega_a = \sqrt{\frac{2 g_F M_F \mu_B B_a''}{m}} \tag{5.31}$$

The third term is the energy contribution due to the component of the magnetic field on the transverse plane.

Determination the offset and the curvature of the magnetic field along transport axis

Figure-5.23 represents the magnitude of magnetic field of the QUIC trap along the x-axis. Near bottom of the trap, we assume potential is harmonic, therefore, we fit the absolute magnetic field with a second order polynomial. The fitting yields the offset magnetic field (B_0) and the magnitude of the curvature($B_x^{''}$) generated by the QUIC trap along x-axis.

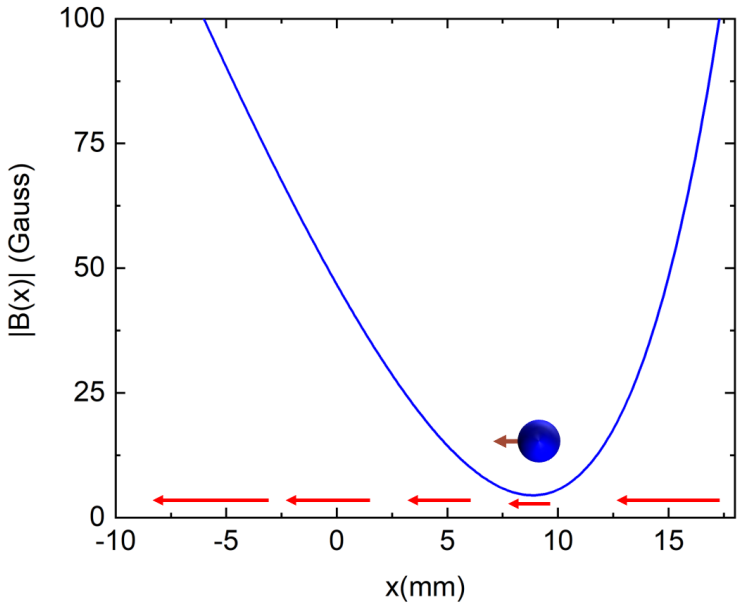


Figure 5.23: The magnitude of the magnetic field of the QUIC trap along the transport direction . The arrows represent the magnetic field direction of axial field along the transport axis.

Applying the Virial theorem to a thermal atom trapped in a magnetic trap, we can write,

$$K_B T = \mu_B B \tag{5.32}$$

Where, K_B is the Boltzmann constant, T is the temperature of the atomic cloud, μ_B is the Bohr magneton, and B is the magnetic field at the classical turning point of the particle's orbit.

From the energy scaling Eqn.5.32, we obtained, $1mK \equiv 14.8$ Gauss. Near the minimum field position in Figure-5.23, we have fitted the magnetic field using a harmonic function,

$$B(x) = b_0 + b_2(x - x_0)^2 \tag{5.33}$$

Where, b_0 is the offset of the magnetic field in Gauss and b_2 represents the curvature, $\frac{d^2B(x)}{dx^2}$, of the magnetic field in $Gauss/cm^2$.

In Figure-5.26, the bottom of the magnetic field corresponds to 4.5 Gauss. Using the above consideration of the scaling factor, the trap positions corresponding to 12 Gauss (6 Gauss) of the magnetic field will be the classical turning point for the atoms in an atomic cloud at temperature $\sim 500\,\mu K$ ($\sim 100\,\mu K$).

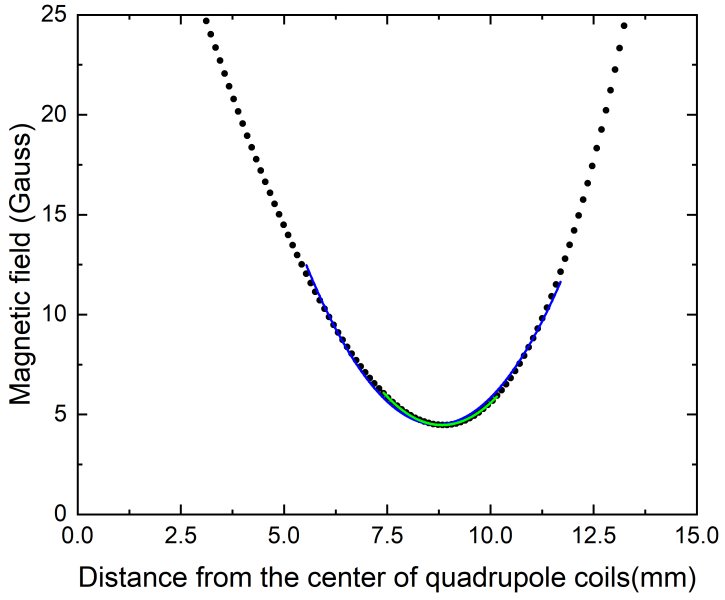


Figure 5.24: A close view of Figure-5.23 around the minimum field position. We have fitted the curve over two different spatial extensions. The blue curve represent the fitting over range below 12 Gauss ($500\,\mu K$) magnetic field while the green curve represents the fitting over the extension below 6 Gauss ($100\,\mu K$) magnetic field.

We have fitted the graph over two different extensions. At first, we have fitted over

the range corresponding to the magnetic fields below 12 Gauss. Next, we have fitted over the range corresponding to the magnetic fields below 6 Gauss.

A very well fitting of the above curve by Eqn.5.33 demonstrates the validity of our approximation of the harmonic nature of the trap near the bottom of the magnetic field. The fitting yields, $b_0 \approx 4.5$ Gauss and $b_2 \approx 80\ \frac{Gauss}{cm^2}$. Therefore, we obtained the offset magnetic field, $B_0 \sim 4.5$ Gauss, and the curvature of the field, $B_x'' \sim 80\,\frac{Gauss}{cm^2}$ for the QUIC trap.

As discussed earlier, $g_F = -\frac{1}{2}$ in the hyperfine state $F = 1$ for both ^{23}Na and ^{39}K atoms. Therefore, we can trap the atoms in $M_F = -1$ Zeeman level. Using Eqn.5.31, we obtained the trap frequency around $22\,Hz$ and $17\,Hz$ for ^{23}Na and ^{39}K atoms, respectively along the transport direction.

Magnetic field components of the QUIC trap at the bottom of the potential along the transverse directions: y and z axes at the bottom of the potential when both the quadrupole coils and the Ioffe coil are operating at 95 Amps of current.

Figure-5.25 (a) and Figure-5.25 (b) show the offset and the curvature of the magnetic field along the transport axis for a range of current in the Ioffe coil for 90 Amps and 95 Amps of current in the quadrupole coils.

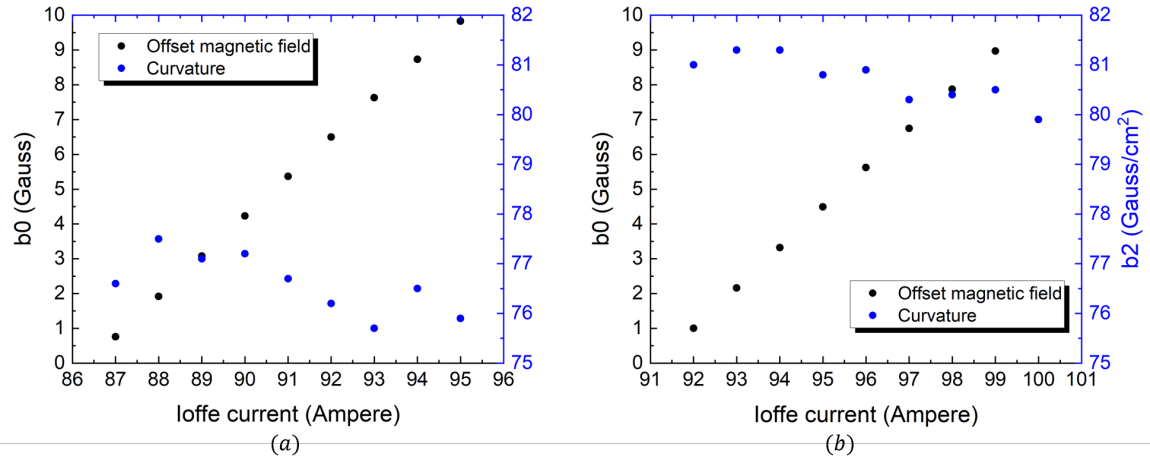


Figure 5.25: The fitting parameters $b0$ and $b2$ at different Ioffe coils current with (a) 90 Amperes and (b) 95 Amperes of current in the quadrupole coil.

The magnetic field gradients along y and z axes are listed in Table-5.3 for the Ioffe current in 0 Amps and 95 Amps.

Current in Ioffe coil	**y-gradient**	**z-gradient**
Ampere	Gauss/cm	Gauss/cm
0	-117	235
95	-172	179

Table 5.3: The field gradients along y and z axes. For 95 Amps of current in the quadrupole coils and different currents in the Ioffe coil.

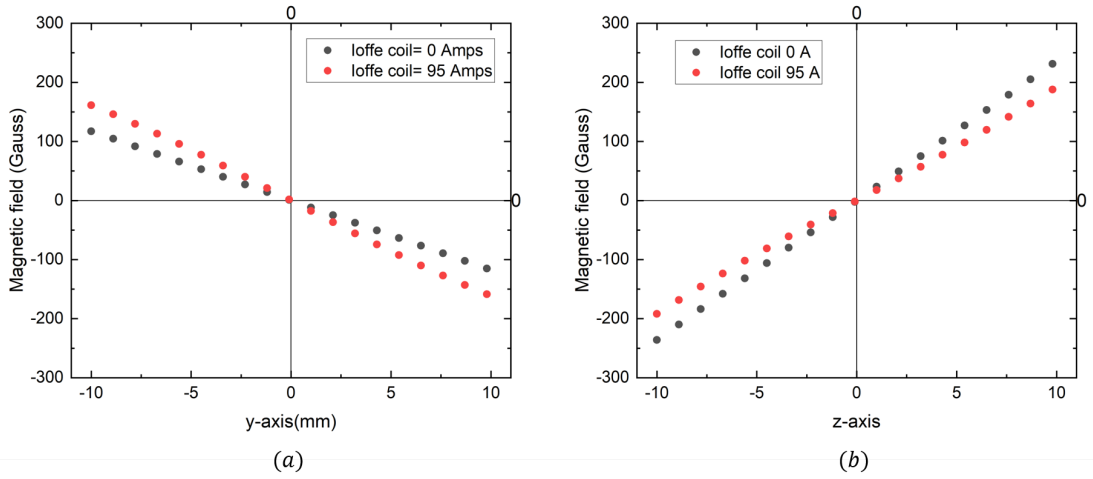


Figure 5.26: The magnetic field components along (a) y-axis and (b) z-axis of the QUIC trap.

These optimized parameters for magnetic transport, and trapping are ideal starting point for evaporative cooling to multi-species BEC in our experiment. The next set of experiments in the laboratory I built and described in this thesis will start from this point and demonstrate two species mass imbalanced BEC with inter-species tunable interactions.

Conclusion and outlook

A unique experimental system of cold atomic mixture has been built in the course of this thesis work. One of the salient features of this experimental system is the realization of two independent $2D^{+}$MOTs as atomic sources. The atomic sources produce intense, cold atomic beams of ^{23}Na and ^{39}K atoms loading their respective 3DMOTs. In the optimized condition, we trap 5.8×10^{8} ^{23}Na and 3×10^{10} ^{39}K atoms in the 3DMOT with loading rates of 3.5×10^{8} atoms/sec and 5×10^{10} atoms/sec respectively.

This experimental facility is designed and realized to study the dynamics of quantum degenerate mixtures of sodium and potassium atoms. The achievement of the scientific goals relies on the high signal-to-noise ratio of the experiments: therefore, it is an utmost priority to obtain a large number of atoms in the degenerate cloud of both the atomic species with a long lifetime ($\sim$ min). The system features a magnetic transport stage which will be employed to transfer the atoms to the science cell. The section containing the science cell is designed to maintain a much better vacuum as well as greater optical access compared to the 3D MOT chamber: this ensures a large lifetime of the degenerate clouds as well as it offers provisions to include optical lattice laser beams and high-resolution imaging systems. At the science cell, the atoms will be transferred to the quadrupole-Ioffe-configuration (QUIC) trap, and by employing radio frequency (RF) evaporative cooling quantum degenerate clouds of ^{23}Na and ^{39}K atoms will be achieved. The experimental system is carefully designed to accommodate optical potentials for the degenerate clouds using additional laser beams which enables us to study the quantum degenerate mixture in arbitrary optical potentials, such as the physics of quantum degenerate mixture in lower

dimensions (1D, 2D) and the bilayer systems. The science cell's small size allows for installing high-resolution microscopes very close to the degenerate clouds. This opens the possibility of studying the dynamics of exotic quantum phases using degenerate quantum mixtures.

The hereto-nuclear molecules in their ro-vibrational ground state have long-range ($\propto \frac{1}{R^3}$) and anisotropic interactions, in contrast to the atoms, which has isotropic and short-ranged ($\propto \frac{1}{R^6}$) interactions, where R is the inter-particle distance. The electric dipole strength of the hetero-nuclear molecules can be controlled using an external electric field. These characteristic features make them a suitable candidate to explore the many-body quantum system in optical potentials. NaK molecules at their ground state have an electric dipole moment of 2.72 Debye, and it is chemically stable. In an optical lattice, the characteristic length of the dipole-dipole interaction is ~ 3 times the lattice spacing (typically 532 nm). Therefore, NaK ground state molecule is an ideal choice to explore many-body dynamics. Thus, one of the near future goals is to employ Feshbach resonance in the quantum degenerate mixture of Na and K. This process associates Na and K atoms into weakly bound molecules in their electronic ground state. Thereafter, using a two-photon transition, Stimulated Raman adiabatic passage (STIRAP), the weakly bound NaK molecules will be transferred into the ro-vibrational ground state.

The experimental system described in this thesis can set a benchmark in the domain of ultracold atom mixture studies and show its capabilities to explore the plethora of experimental possibilities in the quantum degenerate mixture.

Bibliography

[1] M. H. Anderson, J. R. Ensher, M. R. Matthews, C. E. Wieman, and E. A. Cornell. Observation of bose-einstein condensation in a dilute atomic vapor. *Science*, 269(5221):198–201, 1995.

[2] C. C. Bradley, C. A. Sackett, J. J. Tollett, and R. G. Hulet. Evidence of bose-einstein condensation in an atomic gas with attractive interactions. *Phys. Rev. Lett.*, 75:1687–1690, Aug 1995.

[3] K. B. Davis, M. O. Mewes, M. R. Andrews, N. J. van Druten, D. S. Durfee, D. M. Kurn, and W. Ketterle. Bose-einstein condensation in a gas of sodium atoms. *Phys. Rev. Lett.*, 75:3969–3973, Nov 1995.

[4] B. DeMarco and D. S. Jin. Onset of fermi degeneracy in a trapped atomic gas. *Science*, 285(5434):1703–1706, 1999.

[5] Andrew G. Truscott, Kevin E. Strecker, William I. McAlexander, Guthrie B. Partridge, and Randall G. Hulet. Observation of fermi pressure in a gas of trapped atoms. *Science*, 291(5513):2570–2572, 2001.

[6] Observation of interference between two bose condensates. *Science*, 275(5300):637–641, 1997.

[7] M. R. Matthews, B. P. Anderson, P. C. Haljan, D. S. Hall, C. E. Wieman, and E. A. Cornell. Vortices in a bose-einstein condensate. *Phys. Rev. Lett.*, 83:2498–2501, Sep 1999.

[8] K. W. Madison, F. Chevy, W. Wohlleben, and J. Dalibard. Vortex formation in a stirred bose-einstein condensate. *Phys. Rev. Lett.*, 84:806–809, Jan 2000.

[9] J. R. Abo-Shaeer, C. Raman, J. M. Vogels, and W. Ketterle. Observation of vortex lattices in bose-einstein condensates. *Science*, 292(5516):476–479, 2001.

[10] I. Bloch, T. W. Hänsch, and T. Esslinger. Measurement of the spatial coherence of a trapped bose gas at the phase transition. *Nature*, 403(6766):166–170, Jan 2000.

[11] H.-J. Miesner, D. M. Stamper-Kurn, M. R. Andrews, D. S. Durfee, S. Inouye, and W. Ketterle. Bosonic stimulation in the formation of a bose-einstein condensate. *Science*, 279(5353):1005–1007, 1998.

[12] Immanuel Bloch, Theodor W. Hänsch, and Tilman Esslinger. Atom laser with a cw output coupler. *Phys. Rev. Lett.*, 82:3008–3011, Apr 1999.

[13] D. S. Jin, J. R. Ensher, M. R. Matthews, C. E. Wieman, and E. A. Cornell. Collective excitations of a bose-einstein condensate in a dilute gas. *Phys. Rev. Lett.*, 77:420–423, Jul 1996.

[14] M. R. Andrews, D. M. Kurn, H.-J. Miesner, D. S. Durfee, C. G. Townsend, S. Inouye, and W. Ketterle. Propagation of sound in a bose-einstein condensate. *Phys. Rev. Lett.*, 79:553–556, Jul 1997.

[15] D. Jaksch, C. Bruder, J. I. Cirac, C. W. Gardiner, and P. Zoller. Cold bosonic atoms in optical lattices. *Phys. Rev. Lett.*, 81:3108–3111, Oct 1998.

[16] Markus Greiner, Olaf Mandel, Tilman Esslinger, Theodor W. Hänsch, and Immanuel Bloch. Quantum phase transition from a superfluid to a mott insulator in a gas of ultracold atoms. *Nature*, 415(6867):39–44, Jan 2002.

[17] M Baranov, M Dalmonte, G Pupillo, and P Zoller. Condensed matter theory of dipolar quantum gases. *Chemical reviews*, 112:5012–61, 08 2012.

[18] C. A. Regal, M. Greiner, and D. S. Jin. Observation of resonance condensation of fermionic atom pairs. *Phys. Rev. Lett.*, 92:040403, Jan 2004.

[19] M Zwierlein, J Abo-Shaeer, A Schirotzek, Christian Schunck, and W Ketterle. Vortices and superfluidity in a strongly interacting fermi gas. *Nature*, 435:1047–51, 07 2005.

[20] Immanuel Bloch, Jean Dalibard, and Wilhelm Zwerger. Many-body physics with ultracold gases. *Rev. Mod. Phys.*, 80:885–964, Jul 2008.

[21] T Lahaye, C Menotti, L Santos, M Lewenstein, and T Pfau. The physics of dipolar bosonic quantum gases. *Reports on Progress in Physics*, 72(12):126401, nov 2009.

[22] Lincoln Carr, David DeMille, Roman Krems, and Jun Ye. Cold and ultracold molecules: Science, technology, and applications. *New Journal of Physics*, 11, 05 2009.

[23] I. M. Georgescu, S. Ashhab, and Franco Nori. Quantum simulation. *Rev. Mod. Phys.*, 86:153–185, Mar 2014.

[24] E. L. Raab, M. Prentiss, Alex Cable, Steven Chu, and D. E. Pritchard. Trapping of neutral sodium atoms with radiation pressure. *Phys. Rev. Lett.*, 59:2631–2634, Dec 1987.

[25] J. Dalibard and C. Cohen-Tannoudji. Laser cooling below the doppler limit by polarization gradients: simple theoretical models. *J. Opt. Soc. Am. B*, 6(11):2023–2045, Nov 1989.

[26] Paul D. Lett, Richard N. Watts, Christoph I. Westbrook, William D. Phillips, Phillip L. Gould, and Harold J. Metcalf. Observation of atoms laser cooled below the doppler limit. *Phys. Rev. Lett.*, 61:169–172, Jul 1988.

[27] J. Lawall, F. Bardou, B. Saubamea, K. Shimizu, M. Leduc, A. Aspect, and C. Cohen-Tannoudji. Two-dimensional subrecoil laser cooling. *Phys. Rev. Lett.*, 73:1915–1918, Oct 1994.

[28] Nir Davidson, Heun Jin Lee, Mark Kasevich, and Steven Chu. Raman cooling of atoms in two and three dimensions. *Phys. Rev. Lett.*, 72:3158–3161, May 1994.

[29] Wolfgang Ketterle, Kendall B. Davis, Michael A. Joffe, Alex Martin, and David E. Pritchard. High densities of cold atoms in a dark spontaneous-force optical trap. *Phys. Rev. Lett.*, 70:2253–2256, Apr 1993.

[30] Harald F. Hess. Evaporative cooling of magnetically trapped and compressed spin-polarized hydrogen. *Phys. Rev. B*, 34:3476–3479, Sep 1986.

[31] Naoto Masuhara, John M. Doyle, Jon C. Sandberg, Daniel Kleppner, Thomas J. Greytak, Harald F. Hess, and Greg P. Kochanski. Evaporative cooling of spin-polarized atomic hydrogen. *Phys. Rev. Lett.*, 61:935–938, Aug 1988.

[32] Wolfgang Petrich, Michael H. Anderson, Jason R. Ensher, and Eric A. Cornell. Stable, tightly confining magnetic trap for evaporative cooling of neutral atoms. *Phys. Rev. Lett.*, 74:3352–3355, Apr 1995.

[33] Giacomo Roati, Francesco Riboli, Giovanni Modugno, and M Inguscio. Fermi-bose quantum degenerate ^{40}k-^{87}rb mixture with attractive interaction. *Physical review letters*, 89:150403, 11 2002.

[34] J. Catani, L. De Sarlo, G. Barontini, F. Minardi, and M. Inguscio. Degenerate bose-bose mixture in a three-dimensional optical lattice. *Phys. Rev. A*, 77:011603, Jan 2008.

[35] M. Taglieber, A.-C. Voigt, T. Aoki, T. W. Hänsch, and K. Dieckmann. Quantum degenerate two-species fermi-fermi mixture coexisting with a bose-einstein condensate. *Phys. Rev. Lett.*, 100:010401, Jan 2008.

[36] L. Viverit, C. J. Pethick, and H. Smith. Zero-temperature phase diagram of binary boson-fermion mixtures. *Phys. Rev. A*, 61:053605, Apr 2000.

[37] Eddy Timmermans, Kyoko Furuya, Peter W. Milonni, and Arthur K. Kerman. Prospect of creating a composite fermi–bose superfluid. *Physics Letters A*, 285(3):228 – 233, 2001.

[38] Michael Brown-Hayes and Roberto Onofrio. Optimal cooling strategies for magnetically trapped atomic fermi-bose mixtures. *Phys. Rev. A*, 70:063614, Dec 2004.

[39] I. Ferrier-Barbut, M. Delehaye, S. Laurent, A. T. Grier, M. Pierce, B. S. Rem, F. Chevy, and C. Salomon. A mixture of bose and fermi superfluids. *Science*, 345(6200):1035–1038, 2014.

[40] B. DeSalvo, Krutik Patel, Geyue Cai, and Cheng Chin. Fermion-mediated interactions between bosonic atoms. 08 2018.

[41] M. Tinkham. *Introduction to Superconductivity.* Dover Books on Physics Series. Dover Publications, 2004.

[42] Marko Cetina, Michael Jag, Rianne S. Lous, Isabella Fritsche, Jook T. M. Walraven, Rudolf Grimm, Jesper Levinsen, Meera M. Parish, Richard Schmidt, Michael Knap, and Eugene Demler. Ultrafast many-body interferometry of impurities coupled to a fermi sea. *Science*, 354(6308):96–99, 2016.

[43] D.-W. Wang, M. D. Lukin, and E. Demler. Engineering superfluidity in bose-fermi mixtures of ultracold atoms. *Phys. Rev. A*, 72:051604, Nov 2005.

[44] Subhadeep De and Ian Spielman. Fermion-mediated long-range interactions between bosons stored in an optical lattice. *Applied Physics B*, 114, 02 2014.

[45] H. P. Büchler and G. Blatter. Supersolid versus phase separation in atomic bose-fermi mixtures. *Phys. Rev. Lett.*, 91:130404, Sep 2003.

[46] S. Ospelkaus, K.-K. Ni, G. Quéméner, B. Neyenhuis, D. Wang, M. H. G. de Miranda, J. L. Bohn, J. Ye, and D. S. Jin. Controlling the hyperfine state of rovibronic ground-state polar molecules. *Phys. Rev. Lett.*, 104:030402, Jan 2010.

[47] A. Gerdes, O. Dulieu, H. Knöckel, and E. Tiemann. Stark effect measurements on the nak molecule. *The European Physical Journal D*, 65(1):105–111, Nov 2011.

[48] M. A. Baranov, A. Micheli, S. Ronen, and P. Zoller. Bilayer superfluidity of fermionic polar molecules: Many-body effects. *Phys. Rev. A*, 83:043602, Apr 2011.

[49] William D. Phillips. Nobel lecture: Laser cooling and trapping of neutral atoms. *Rev. Mod. Phys.*, 70:721–741, Jul 1998.

[50] CJ Foot. Atomic physics. 2005.

[51] K. M. R. van der Stam, E. D. van Ooijen, R. Meppelink, J. M. Vogels, and P. van der Straten. Large atom number bose-einstein condensate of sodium. *Review of Scientific Instruments*, 78(1):013102, 2007.

[52] Z. T. Lu, K. L. Corwin, M. J. Renn, M. H. Anderson, E. A. Cornell, and C. E. Wieman. Low-velocity intense source of atoms from a magneto-optical trap. *Phys. Rev. Lett.*, 77:3331–3334, Oct 1996.

[53] E Pedrozo-Peñafiel, F Vivanco, P Castilho, R R Paiva, K M Farias, and V S Bagnato. Direct comparison between a two-dimensional magneto-optical trap and a zeeman slower as sources of cold sodium atoms. *Laser Physics Letters*, 13(6):065501, may 2016.

[54] K. Goral, L. Santos, and M. Lewenstein. Quantum phases of dipolar bosons in optical lattices. *Phys. Rev. Lett.*, 88:170406, Apr 2002.

[55] Immanuel Bloch, Jean Dalibard, and Sylvain. Quantum simulations with ultracold quantum gases. *Nature Physics*, 8:267–276, 04 2012.

[56] Nathan Goldman, Jan Budich, and P. Zoller. Topological quantum matter with ultracold gases in optical lattices. *Nature Physics*, 12:639–645, 06 2016.

[57] Christian Gross and Immanuel Bloch. Quantum simulations with ultracold atoms in optical lattices. *Science*, 357(6355):995–1001, 2017.

[58] Florian Schäfer, Takeshi Fukuhara, Seiji Sugawa, Yosuke Takasu, and Yoshiro Takahashi. Tools for quantum simulation with ultracold atoms in optical lattices. *Nature Reviews Physics*, 2(8):411–425, Aug 2020.

[59] Cheng Chin, Rudolf Grimm, Paul Julienne, and Eite Tiesinga. Feshbach resonances in ultracold gases. *Rev. Mod. Phys.*, 82:1225–1286, Apr 2010.

[60] S. Inouye, M. R. Andrews, J. Stenger, H. J. Miesner, D. M. Stamper-Kurn, and W. Ketterle. Observation of Feshbach resonances in a Bose-Einstein condensate. *nature*, 392(6672):151–154, March 1998.

[61] Chiara D'Errico, Matteo Zaccanti, Marco Fattori, Giacomo Roati, Massimo Inguscio, Giovanni Modugno, and Andrea Simoni. Feshbach resonances in ultracold 39k. *New Journal of Physics*, 9:223, 07 2007.

[62] Francesca Ferlaino, Chiara D'Errico, Giacomo Roati, Matteo Zaccanti, Massimo Inguscio, Giovanni Modugno, and Andrea Simoni. Feshbach spectroscopy of a K−Rb atomic mixture. *Phys. Rev. A*, 73:040702, Apr 2006.

[63] J. J. Zirbel, K.-K. Ni, S. Ospelkaus, J. P. D'Incao, C. E. Wieman, J. Ye, and D. S. Jin. Collisional stability of fermionic feshbach molecules. *Phys. Rev. Lett.*, 100:143201, Apr 2008.

[64] Cheng-Hsun Wu, Jee Woo Park, Peyman Ahmadi, Sebastian Will, and Martin W. Zwierlein. Ultracold fermionic feshbach molecules of ^{23}Na^{40}**K**. *Phys. Rev. Lett.*, 109:085301, Aug 2012.

[65] Torben A. Schulze, Torsten Hartmann, Kai K. Voges, Matthias W. Gempel, Eberhard Tiemann, Alessandro Zenesini, and Silke Ospelkaus. Feshbach spectroscopy and dual-species bose-einstein condensation of ^{23}Na$-^{39}$K mixtures. *Phys. Rev. A*, 97:023623, Feb 2018.

[66] Huan Yang, De-Chao Zhang, Lan Liu, Yaxiong Liu, Nan Jue, Bo Zhao, and Jian-Wei Pan. Observation of magnetically tunable feshbach resonances in ultracold 23 na 40 k + 40 k collisions. *Science*, 363:261–264, 01 2019.

[67] Giacomo Roati, Chiara D'Errico, Leonardo Fallani, Marco Fattori, Chiara Fort, Matteo Zaccanti, Giovanni Modugno, Michele Modugno, and Massimo Inguscio. Anderson localization of a non-interacting bose–einstein condensate. *Nature*, 453(7197):895–898, Jun 2008.

[68] Juliette Billy, Vincent Josse, Zhanchun Zuo, Alain Bernard, Ben Hambrecht, Pierre Lugan, David Clément, Laurent Sanchez-Palencia, Philippe Bouyer, and Alain Aspect. Direct observation of anderson localization of matter waves in a controlled disorder. *Nature*, 453(7197):891–894, Jun 2008.

[69] P. W. Anderson. Absence of diffusion in certain random lattices. *Phys. Rev.*, 109:1492–1505, Mar 1958.

[70] Wolfgang Ketterle and Martin Zwierlein. Making, probing and understanding ultracold fermi gases. *Rivista del Nuovo Cimento*, 164, 01 2008.

[71] Stefano Giorgini, Lev P. Pitaevskii, and Sandro Stringari. Theory of ultracold atomic fermi gases. *Rev. Mod. Phys.*, 80:1215–1274, Oct 2008.

[72] Mohit Randeria and Edward Taylor. Crossover from bardeen-cooper-schrieffer to bose-einstein condensation and the unitary fermi gas. *Annual Review of Condensed Matter Physics*, 5(1):209–232, 2014.

[73] André Schirotzek, Cheng-Hsun Wu, Ariel Sommer, and Martin W. Zwierlein. Observation of fermi polarons in a tunable fermi liquid of ultracold atoms. *Phys. Rev. Lett.*, 102:230402, Jun 2009.

[74] Complete list of l d landau's works. *Physics-Uspekhi*, 41(6):621, jun 1998.

[75] Patrick A. Lee, Naoto Nagaosa, and Xiao-Gang Wen. Doping a mott insulator: Physics of high-temperature superconductivity. *Rev. Mod. Phys.*, 78:17–85, Jan 2006.

[76] K.-K. Ni, S. Ospelkaus, M. H. G. de Miranda, A. Pe'er, B. Neyenhuis, J. J. Zirbel, S. Kotochigova, P. S. Julienne, D. S. Jin, and J. Ye. A high phase-space-density gas of polar molecules. *Science*, 322(5899):231–235, 2008.

[77] Tetsu Takekoshi, Lukas Reichsöllner, Andreas Schindewolf, Jeremy M. Hutson, C. Ruth Le Sueur, Olivier Dulieu, Francesca Ferlaino, Rudolf Grimm, and Hanns-Christoph Nägerl. Ultracold dense samples of dipolar rbcs molecules in the rovibrational and hyperfine ground state. *Phys. Rev. Lett.*, 113:205301, Nov 2014.

[78] Jee Woo Park, Sebastian A. Will, and Martin W. Zwierlein. Ultracold dipolar gas of fermionic $^{23}Na^{40}K$ molecules in their absolute ground state. *Phys. Rev. Lett.*, 114:205302, May 2015.

[79] Kai K. Voges, Philipp Gersema, Mara Meyer zum Alten Borgloh, Torben A. Schulze, Torsten Hartmann, Alessandro Zenesini, and Silke Ospelkaus. Ultracold gas of bosonic $^{23}Na^{39}K$ ground-state molecules. *Phys. Rev. Lett.*, 125:083401, Aug 2020.

[80] Roman Bause, Akira Kamijo, Xing-Yan Chen, Marcel Duda, Andreas Schindewolf, Immanuel Bloch, and Xin-Yu Luo. Efficient conversion of closed-channel-dominated feshbach molecules of $^{23}Na^{40}K$ to their absolute ground state. *Phys. Rev. A*, 104:043321, Oct 2021.

[81] Bryce Gadway and Bo Yan. Strongly interacting ultracold polar molecules. *Journal of Physics B: Atomic, Molecular and Optical Physics*, 49(15):152002, jun 2016.

[82] W Hofstetter and T Qin. Quantum simulation of strongly correlated condensed matter systems. *Journal of Physics B: Atomic, Molecular and Optical Physics*, 51(8):082001, mar 2018.

[83] B. Capogrosso-Sansone, C. Trefzger, M. Lewenstein, P. Zoller, and G. Pupillo. Quantum phases of cold polar molecules in 2d optical lattices. *Phys. Rev. Lett.*, 104:125301, Mar 2010.

[84] Salvatore R. Manmana, E. M. Stoudenmire, Kaden R. A. Hazzard, Ana Maria Rey, and Alexey V. Gorshkov. Topological phases in ultracold polar-molecule quantum magnets. *Phys. Rev. B*, 87:081106, Feb 2013.

[85] Andreas Kruckenhauser, Lukas M. Sieberer, Luigi De Marco, Jun-Ru Li, Kyle Matsuda, William G. Tobias, Giacomo Valtolina, Jun Ye, Ana Maria Rey, Mikhail A. Baranov, and Peter Zoller. Quantum many-body physics with ultracold polar molecules: Nanostructured potential barriers and interactions. *Phys. Rev. A*, 102:023320, Aug 2020.

[86] G. Pupillo, A. Micheli, H.-P Büchler, and P. Zoller. *Condensed matter physics with cold polar molecules*, pages 421–470. 01 2009.

[87] Maciej Lewenstein, Anna Sanpera, Veronica Ahufinger, Bogdan Damski, Aditi Sen(De), and Ujjwal Sen. Ultracold atomic gases in optical lattices: mimicking condensed matter physics and beyond. *Advances in Physics*, 56(2):243–379, 2007.

[88] W. Hofstetter, J. I. Cirac, P. Zoller, E. Demler, and M. D. Lukin. High-temperature superfluidity of fermionic atoms in optical lattices. *Phys. Rev. Lett.*, 89:220407, Nov 2002.

[89] A. Pikovski, M. Klawunn, G. V. Shlyapnikov, and L. Santos. Interlayer superfluidity in bilayer systems of fermionic polar molecules. *Phys. Rev. Lett.*, 105:215302, Nov 2010.

[90] Thierry Lahaye, Tobias Koch, Bernd Fröhlich, Marco Fattori, Jonas Metz, Axel Griesmaier, Stefano Giovanazzi, and Tilman Pfau. Strong dipolar effects in a quantum ferrofluid. *Nature*, 448(7154):672–675, Aug 2007.

[91] Alexey V. Gorshkov, Salvatore R. Manmana, Gang Chen, Eugene Demler, Mikhail D. Lukin, and Ana Maria Rey. Quantum magnetism with polar alkali-metal dimers. *Phys. Rev. A*, 84:033619, Sep 2011.

[92] Alexey V. Gorshkov, Salvatore R. Manmana, Gang Chen, Jun Ye, Eugene Demler, Mikhail D. Lukin, and Ana Maria Rey. Tunable superfluidity and quantum magnetism with ultracold polar molecules. *Phys. Rev. Lett.*, 107:115301, Sep 2011.

[93] Sebastian A. Will, Jee Woo Park, Zoe Z. Yan, Huanqian Loh, and Martin W. Zwierlein. Coherent microwave control of ultracold ^{23}Na^{40}K molecules. *Phys. Rev. Lett.*, 116:225306, Jun 2016.

[94] R. V. Krems. Cold controlled chemistry. *Phys. Chem. Chem. Phys.*, 10:4079–4092, 2008.

[95] S. Ospelkaus, K.-K. Ni, D. Wang, M. H. G. de Miranda, B. Neyenhuis, G. Quéméner, P. S. Julienne, J. L. Bohn, D. S. Jin, and J. Ye. Quantum-state controlled chemical reactions of ultracold potassium-rubidium molecules. *Science*, 327(5967):853–857, 2010.

[96] Simon L. Cornish and Jeremy M. Hutson. Toward a coherent ultracold chemistry. *Science*, 375(6584):975–976, 2022.

[97] Philip D. Gregory, Jacob A. Blackmore, Sarah L. Bromley, Jeremy M. Hutson, and Simon L. Cornish. Robust storage qubits in ultracold polar molecules. *Nature Physics*, 17(10):1149–1153, Oct 2021.

[98] Jacob A Blackmore, Luke Caldwell, Philip D Gregory, Elizabeth M Bridge, Rahul Sawant, Jesús Aldegunde, Jordi Mur-Petit, Dieter Jaksch, Jeremy M Hutson, B E Sauer, M R Tarbutt, and Simon L Cornish. Ultracold molecules for quantum simulation: rotational coherences in caf and rbcs. *Quantum Science and Technology*, 4(1):014010, dec 2018.

[99] Yu Liu, Ming-Guang Hu, Matthew A. Nichols, Dongzheng Yang, Daiqian Xie, Hua Guo, and Kang-Kuen Ni. Precision test of statistical dynamics with state-to-state ultracold chemistry. *Nature*, 593:379 – 384, 2020.

[100]

[101] Steven A. Moses, Jacob P. Covey, Matthew T. Miecnikowski, Bo Yan, Bryce Gadway, Jun Ye, and Deborah S. Jin. Creation of a low-entropy quantum gas of polar molecules in an optical lattice. *Science*, 350(6261):659–662, November 2015.

[102] William G. Tobias, Kyle Matsuda, Jun-Ru Li, Calder Miller, Annette N. Carroll, Thomas Bilitewski, Ana Maria Rey, and Jun Ye. Reactions between layer-resolved molecules mediated by dipolar spin exchange. *Science*, 375(6586):1299–1303, 2022.

[103] D. DeMille. Quantum computation with trapped polar molecules. *Phys. Rev. Lett.*, 88:067901, Jan 2002.

[104] S. F. Yelin, K. Kirby, and Robin Côté. Schemes for robust quantum computation with polar molecules. *Phys. Rev. A*, 74:050301, Nov 2006.

[105] Kang-Kuen Ni, Till Rosenband, and David D. Grimes. Dipolar exchange quantum logic gate with polar molecules. *Chem. Sci.*, 9:6830–6838, 2018.

[106] Michael Hughes, Matthew D. Frye, Rahul Sawant, Gaurav Bhole, Jonathan A. Jones, Simon L. Cornish, M. R. Tarbutt, Jeremy M. Hutson, Dieter Jaksch, and Jordi Mur-Petit. Robust entangling gate for polar molecules using magnetic and microwave fields. *Phys. Rev. A*, 101:062308, Jun 2020.

[107] Philip D. Gregory, Jesus Aldegunde, Jeremy M. Hutson, and Simon L. Cornish. Controlling the rotational and hyperfine state of ultracold $^{87}Rb^{133}Cs$ molecules. *Phys. Rev. A*, 94:041403, Oct 2016.

[108] Andreas Schindewolf, Roman Bause, Xing-Yan Chen, Marcel Duda, Tijs Karman, Immanuel Bloch, and Xin-Yu Luo. Evaporation of microwave-shielded polar molecules to quantum degeneracy. *Nature*, 607(7920):677–681, Jul 2022.

[109] Jessie T Zhang, Lewis R B Picard, William B Cairncross, Kenneth Wang, Yichao Yu, Fang Fang, and Kang-Kuen Ni. An optical tweezer array of ground-state polar molecules. *Quantum Science and Technology*, 7(3):035006, may 2022.

[110] Jee Woo Park, Zoe Z. Yan, Huanqian Loh, Sebastian A. Will, and Martin W. Zwierlein. Second-scale nuclear spin coherence time of ultracold ²³na⁴⁰k molecules. *Science*, 357(6349):372–375, 2017.

[111] Jacob A Blackmore, Luke Caldwell, Philip D Gregory, Elizabeth M Bridge, Rahul Sawant, Jesús Aldegunde, Jordi Mur-Petit, Dieter Jaksch, Jeremy M Hutson, B E Sauer, M R Tarbutt, and Simon L Cornish. Ultracold molecules for quantum simulation: rotational coherences in caf and rbcs. *Quantum Science and Technology*, 4(1):014010, dec 2018.

[112] Ian Stevenson, Aden Z. Lam, Niccolò Bigagli, Claire Warner, Weijun Yuan, Siwei Zhang, and Sebastian Will. Ultracold gas of dipolar nacs ground state molecules. *Phys. Rev. Lett.*, 130:113002, Mar 2023.

[113] Waseem S. Bakr, Jonathon I. Gillen, Amy Peng, Simon Fölling, and Markus Greiner. A quantum gas microscope for detecting single atoms in a hubbard-regime optical lattice. *Nature*, 462(7269):74–77, Nov 2009.

[114] Jacob F. Sherson, Christof Weitenberg, Manuel Endres, Marc Cheneau, Immanuel Bloch, and Stefan Kuhr. Single-atom-resolved fluorescence imaging of an atomic mott insulator. *Nature*, 467(7311):68–72, Sep 2010.

[115] Elmar Haller, James Hudson, Andrew Kelly, Dylan A. Cotta, Bruno Peaudecerf, Graham D. Bruce, and Stefan Kuhr. Single-atom imaging of fermions in a quantum-gas microscope. *Nature Physics*, 11(9):738–742, Sep 2015.

[116] Lawrence W. Cheuk, Matthew A. Nichols, Melih Okan, Thomas Gersdorf, Vinay V. Ramasesh, Waseem S. Bakr, Thomas Lompe, and Martin W. Zwierlein. Quantum-gas microscope for fermionic atoms. *Phys. Rev. Lett.*, 114:193001, May 2015.

[117] G. J. A. Edge, R. Anderson, D. Jervis, D. C. McKay, R. Day, S. Trotzky, and J. H. Thywissen. Imaging and addressing of individual fermionic atoms in an optical lattice. *Phys. Rev. A*, 92:063406, Dec 2015.

[118] Jason S. Rosenberg, Lysander Christakis, Elmer Guardado-Sanchez, Zoe Z. Yan, and Waseem S. Bakr. Observation of the hanbury brown and twiss effect with ultracold molecules. 2021.

[119] Harold Metcalf and Peter van der Straten. Cooling and trapping of neutral atoms. *Physics Reports*, 244(4):203–286, 1994.

[120] Wolfgang Ketterle and N.J. Van Druten. Evaporative cooling of trapped atoms. volume 37 of *Advances In Atomic, Molecular, and Optical Physics*, pages 181–236. Academic Press, 1996.

[121] Tilman Esslinger, Immanuel Bloch, and Theodor W. Hänsch. Bose-einstein condensation in a quadrupole-ioffe-configuration trap. *Phys. Rev. A*, 58:R2664–R2667, Oct 1998.

[122] Rudolf Grimm, Matthias Weidemüller, and Yurii B. Ovchinnikov. Optical dipole traps for neutral atoms. volume 42 of *Advances In Atomic, Molecular, and Optical Physics*, pages 95–170. Academic Press, 2000.

[123] M. D. Barrett, J. A. Sauer, and M. S. Chapman. All-optical formation of an atomic bose-einstein condensate. *Phys. Rev. Lett.*, 87:010404, Jun 2001.

[124] Saptarishi Chaudhuri, Sanjukta Roy, and C.s Unnikrishnan. Bose-einstein condensation in optical traps and in a 1d optical lattice. *Current Science*, 95, 10 2008.

[125] Bose. Plancks gesetz und lichtquantenhypothese. *Zeitschrift für Physik*, 26(1):178–181, Dec 1924.

[126] F. London. On the bose-einstein condensation. *Phys. Rev.*, 54:947–954, Dec 1938.

[127] Paul D. Lett, Richard N. Watts, Christoph I. Westbrook, William D. Phillips, Phillip L. Gould, and Harold J. Metcalf. Observation of atoms laser cooled below the doppler limit. *Phys. Rev. Lett.*, 61:169–172, Jul 1988.

[128] Kendall B. Davis, Marc-Oliver Mewes, Michael A. Joffe, Michael R. Andrews, and Wolfgang Ketterle. Evaporative cooling of sodium atoms. *Phys. Rev. Lett.*, 74:5202–5205, Jun 1995.

[129] Jee Woo Park, Cheng-Hsun Wu, Ibon Santiago, Tobias G. Tiecke, Sebastian Will, Peyman Ahmadi, and Martin W. Zwierlein. Quantum degenerate bose-fermi mixture of chemically different atomic species with widely tunable interactions. *Phys. Rev. A*, 85:051602, May 2012.

[130] M. Gröbner, P. Weinmann, F. Meinert, K. Lauber, E. Kirilov, and H.-C. Nägerl. A new quantum gas apparatus for ultracold mixtures of k and cs and kcs ground-state molecules. *Journal of Modern Optics*, 63(18):1829–1839, 2016.

[131] M. Lewenstein, L. Santos, M. A. Baranov, and H. Fehrmann. Atomic bose-fermi mixtures in an optical lattice. *Phys. Rev. Lett.*, 92:050401, Feb 2004.

[132] M. J. Bijlsma, B. A. Heringa, and H. T. C. Stoof. Phonon exchange in dilute fermi-bose mixtures: Tailoring the fermi-fermi interaction. *Phys. Rev. A*, 61:053601, Apr 2000.

[133] H. Heiselberg, C. J. Pethick, H. Smith, and L. Viverit. Influence of induced interactions on the superfluid transition in dilute fermi gases. *Phys. Rev. Lett.*, 85:2418–2421, Sep 2000.

[134] F. Matera. Fermion pairing in bose-fermi mixtures. *Phys. Rev. A*, 68:043624, Oct 2003.

[135] A. Storozhenko, P. Schuck, T. Suzuki, H. Yabu, and J. Dukelsky. Boson-fermion pairing in a boson-fermion environment. *Phys. Rev. A*, 71:063617, Jun 2005.

[136] M. Zaccanti, C. D'Errico, F. Ferlaino, G. Roati, M. Inguscio, and G. Modugno. Control of the interaction in a fermi-bose mixture. *Phys. Rev. A*, 74:041605, Oct 2006.

[137] S. Ospelkaus, C. Ospelkaus, L. Humbert, K. Sengstock, and K. Bongs. Tuning of heteronuclear interactions in a degenerate fermi-bose mixture. *Phys. Rev. Lett.*, 97:120403, Sep 2006.

[138] Debraj Rakshit, Tomasz Karpiuk, Mirosław Brewczyk, and Mariusz Gajda. Quantum Bose-Fermi droplets. *SciPost Phys.*, 6:079, 2019.

[139] D. S. Petrov. Quantum mechanical stabilization of a collapsing bose-bose mixture. *Phys. Rev. Lett.*, 115:155302, Oct 2015.

[140] T. D. Lee, Kerson Huang, and C. N. Yang. Eigenvalues and eigenfunctions of a bose system of hard spheres and its low-temperature properties. *Phys. Rev.*, 106:1135–1145, Jun 1957.

[141] C. R. Cabrera, L. Tanzi, J. Sanz, B. Naylor, P. Thomas, P. Cheiney, and L. Tarruell. Quantum liquid droplets in a mixture of bose-einstein condensates. *Science*, 359(6373):301–304, 2018.

[142] G. Semeghini, G. Ferioli, L. Masi, C. Mazzinghi, L. Wolswijk, F. Minardi, M. Modugno, G. Modugno, M. Inguscio, and M. Fattori. Self-bound quantum droplets of atomic mixtures in free space. *Phys. Rev. Lett.*, 120:235301, Jun 2018.

[143] Jing-Bo Wang, Jian-Song Pan, Xiaoling Cui, and Wei Yi. Quantum droplets in a mixture of bose–fermi superfluids. *Chinese Physics Letters*, 37(7):076701, jul 2020.

[144] Zhichao Guo, Fan Jia, Lintao Li, Yinfeng Ma, Jeremy M. Hutson, Xiaoling Cui, and Dajun Wang. Lee-huang-yang effects in the ultracold mixture of ^{23}Na and ^{87}Rb with attractive interspecies interactions. *Phys. Rev. Res.*, 3:033247, Sep 2021.

[145] Eric Vernier, David Pekker, Martin W. Zwierlein, and Eugene Demler. Bound states of a localized magnetic impurity in a superfluid of paired ultracold fermions. *Phys. Rev. A*, 83:033619, Mar 2011.

[146] C Ospelkaus, S Ospelkaus, K Sengstock, and Kai Bongs. Interaction-driven dynamics of k 40 rb 87 fermion-boson gas mixtures in the large-particle-number limit. *Physical review letters*, 96:020401, 02 2006.

[147] L. Mathey, D.-W. Wang, W. Hofstetter, M. D. Lukin, and Eugene Demler. Luttinger liquid of polarons in one-dimensional boson-fermion mixtures. *Phys. Rev. Lett.*, 93:120404, Sep 2004.

[148] Thomas Kohlert, Sebastian Scherg, Xiao Li, Henrik P. Lüschen, Sankar Das Sarma, Immanuel Bloch, and Monika Aidelsburger. Observation of many-body localization

in a one-dimensional system with a single-particle mobility edge. *Phys. Rev. Lett.*, 122:170403, May 2019.

[149] H. P. Zahn, V. P. Singh, M. N. Kosch, L. Asteria, L. Freystatzky, K. Sengstock, L. Mathey, and C. Weitenberg. Formation of spontaneous density-wave patterns in dc driven lattices. *Phys. Rev. X*, 12:021014, Apr 2022.

[150] H. P. Büchler and G. Blatter. Supersolid versus phase separation in atomic bose-fermi mixtures. *Phys. Rev. Lett.*, 91:130404, Sep 2003.

[151] B. Bazak and D. S. Petrov. Stable p-wave resonant two-dimensional fermi-bose dimers. *Phys. Rev. Lett.*, 121:263001, Dec 2018.

[152] C. Trefzger, C. Menotti, and M. Lewenstein. Pair-supersolid phase in a bilayer system of dipolar lattice bosons. *Phys. Rev. Lett.*, 103:035304, Jul 2009.

[153] Jee Park. *An ultracold gas of dipolar fermionic ^{23}NaK molecules.* PhD thesis, 01 2016.

[154] Paul S. Julienne, Thomas M. Hanna, and Zbigniew Idziaszek. Universal ultracold collision rates for polar molecules of two alkali-metal atoms. *Phys. Chem. Chem. Phys.*, 13:19114–19124, 2011.

[155] Axel Griesmaier, Jörg Werner, Sven Hensler, Jürgen Stuhler, and Tilman Pfau. Bose-einstein condensation of chromium. *Phys. Rev. Lett.*, 94:160401, Apr 2005.

[156] Mingwu Lu, Nathaniel Q. Burdick, Seo Ho Youn, and Benjamin L. Lev. Strongly dipolar bose-einstein condensate of dysprosium. *Phys. Rev. Lett.*, 107:190401, Oct 2011.

[157] K. Aikawa, A. Frisch, M. Mark, S. Baier, A. Rietzler, R. Grimm, and F. Ferlaino. Bose-einstein condensation of erbium. *Phys. Rev. Lett.*, 108:210401, May 2012.

[158] A. de Paz, A. Sharma, A. Chotia, E. Maréchal, J. H. Huckans, P. Pedri, L. Santos, O. Gorceix, L. Vernac, and B. Laburthe-Tolra. Nonequilibrium quantum magnetism in a dipolar lattice gas. *Phys. Rev. Lett.*, 111:185305, Oct 2013.

[159] Lauriane Chomaz, Igor Ferrier-Barbut, Francesca Ferlaino, Bruno Laburthe-Tolra, Benjamin L Lev, and Tilman Pfau. Dipolar physics: a review of experiments with magnetic quantum gases. *Reports on Progress in Physics*, 86(2):026401, dec 2022.

[160] Holger Kadau, Matthias Schmitt, Matthias Wenzel, Clarissa Wink, Thomas Maier, Igor Ferrier-Barbut, and Tilman Pfau. Observing the rosensweig instability of a quantum ferrofluid. *Nature*, 530(7589):194–197, Feb 2016.

[161] Loïc Anderegg, Benjamin L. Augenbraun, Eunmi Chae, Boerge Hemmerling, Nicholas R. Hutzler, Aakash Ravi, Alejandra Collopy, Jun Ye, Wolfgang Ketterle, and John M. Doyle. Radio frequency magneto-optical trapping of caf with high density. *Phys. Rev. Lett.*, 119:103201, Sep 2017.

[162] J. F. Barry, D. J. McCarron, E. B. Norrgard, M. H. Steinecker, and D. DeMille. Magneto-optical trapping of a diatomic molecule. *Nature*, 512(7514):286–289, Aug 2014.

[163] Nicholas R. Hutzler, Hsin-I Lu, and John M. Doyle. The buffer gas beam: An intense, cold, and slow source for atoms and molecules. *Chemical Reviews*, 112(9):4803–4827, Sep 2012.

[164] Hendrick L. Bethlem, Giel Berden, and Gerard Meijer. Decelerating neutral dipolar molecules. *Phys. Rev. Lett.*, 83:1558–1561, Aug 1999.

[165] M Petzold, P Kaebert, P Gersema, M Siercke, and S Ospelkaus. A zeeman slower for diatomic molecules. *New Journal of Physics*, 20(4):042001, apr 2018.

[166] Matthew T. Hummon, Mark Yeo, Benjamin K. Stuhl, Alejandra L. Collopy, Yong Xia, and Jun Ye. 2d magneto-optical trapping of diatomic molecules. *Phys. Rev. Lett.*, 110:143001, Apr 2013.

[167] Jonathan D. Weinstein, Robert deCarvalho, Thierry Guillet, Bretislav Friedrich, and John M. Doyle. Magnetic trapping of calcium monohydride molecules at millikelvin temperatures. *Nature*, 395(6698):148–150, Sep 1998.

[168] Loïc Anderegg, Benjamin L. Augenbraun, Yicheng Bao, Sean Burchesky, Lawrence W. Cheuk, Wolfgang Ketterle, and John M. Doyle. Laser cooling of optically trapped molecules. *Nature Physics*, 14(9):890–893, Sep 2018.

[169] Benjamin K. Stuhl, Matthew T. Hummon, Mark Yeo, Goulven Quéméner, John L. Bohn, and Jun Ye. Evaporative cooling of the dipolar hydroxyl radical. *Nature*, 492(7429):396–400, Dec 2012.

[170] S. Ospelkaus, A. Pe'er, K.-K. Ni, J. J. Zirbel, B. Neyenhuis, S. Kotochigova, P. S. Julienne, J. Ye, and D. S. Jin. Efficient state transfer in an ultracold dense gas of heteronuclear molecules. *Nature Physics*, 4(8):622–626, Aug 2008.

[171] J. Deiglmayr, A. Grochola, M. Repp, K. Mörtlbauer, C. Glück, J. Lange, O. Dulieu, R. Wester, and M. Weidemüller. Formation of ultracold polar molecules in the rovibrational ground state. *Phys. Rev. Lett.*, 101:133004, Sep 2008.

[172] Peter K. Molony, Philip D. Gregory, Zhonghua Ji, Bo Lu, Michael P. Köppinger, C. Ruth Le Sueur, Caroline L. Blackley, Jeremy M. Hutson, and Simon L. Cornish. Creation of ultracold $^{87}Rb^{133}Cs$ molecules in the rovibrational ground state. *Phys. Rev. Lett.*, 113:255301, Dec 2014.

[173] Frauke Seeßelberg, Nikolaus Buchheim, Zhen-Kai Lu, Tobias Schneider, Xin-Yu Luo, Eberhard Tiemann, Immanuel Bloch, and Christoph Gohle. Modeling the

adiabatic creation of ultracold polar ^{23}na^{40}K molecules. *Phys. Rev. A*, 97:013405, Jan 2018.

[174] Mingyang Guo, Bing Zhu, Bo Lu, Xin Ye, Fudong Wang, Romain Vexiau, Nadia Bouloufa-Maafa, Goulven Quéméner, Olivier Dulieu, and Dajun Wang. Creation of an ultracold gas of ground-state dipolar ^{23}Na^{87}Rb molecules. *Phys. Rev. Lett.*, 116:205303, May 2016.

[175] Piotr S. Żuchowski and Jeremy M. Hutson. Reactions of ultracold alkali-metal dimers. *Phys. Rev. A*, 81:060703, Jun 2010.

[176] Goulven Quéméner, John L. Bohn, Alexander Petrov, and Svetlana Kotochigova. Universalities in ultracold reactions of alkali-metal polar molecules. *Phys. Rev. A*, 84:062703, Dec 2011.

[177] M. Aymar and O. Dulieu. Calculation of accurate permanent dipole moments of the lowest +1,3 states of heteronuclear alkali dimers using extended basis sets. *The Journal of Chemical Physics*, 122(20):204302, 2005.

[178] M. Aymar and O. Dulieu. Calculations of transition and permanent dipole moments of heteronuclear alkali dimers nak, narb and nacs. *Molecular Physics*, 105(11-12):1733–1742, 2007.

[179] Jee Woo Park, Sebastian A Will, and Martin W Zwierlein. Two-photon pathway to ultracold ground state molecules of 23na40k. *New Journal of Physics*, 17(7):075016, jul 2015.

[180] Min-Jie Zhu, Huan Yang, Lan Liu, De-Chao Zhang, Ya-Xiong Liu, Jue Nan, Jun Rui, Bo Zhao, Jian-Wei Pan, and Eberhard Tiemann. Feshbach loss spectroscopy in an ultracold ^{23}Na $-^{40}$ K mixture. *Phys. Rev. A*, 96:062705, Dec 2017.

[181] Kai K Voges, Philipp Gersema, Torsten Hartmann, Torben A Schulze, Alessandro Zenesini, and Silke Ospelkaus. A pathway to ultracold bosonic 23na39k ground state molecules. *New Journal of Physics*, 21(12):123034, dec 2019.

[182] Luigi De Marco, Giacomo Valtolina, Kyle Matsuda, William G. Tobias, Jacob P. Covey, and Jun Ye. A degenerate fermi gas of polar molecules. *Science*, 363(6429):853–856, 2019.

[183] Xing-Yan Chen, Andreas Schindewolf, Sebastian Eppelt, Roman Bause, Marcel Duda, Shrestha Biswas, Tijs Karman, Timon Hilker, Immanuel Bloch, and Xin-Yu Luo. Field-linked resonances of polar molecules. *Nature*, 614(7946):59–63, Feb 2023.

[184] B. Damski, L. Santos, E. Tiemann, M. Lewenstein, S. Kotochigova, P. Julienne, and P. Zoller. Creation of a dipolar superfluid in optical lattices. *Phys. Rev. Lett.*, 90:110401, Mar 2003.

[185] Fabian Böttcher, Jan-Niklas Schmidt, Jens Hertkorn, Kevin S H Ng, Sean D Graham, Mingyang Guo, Tim Langen, and Tilman Pfau. New states of matter with fine-tuned interactions: quantum droplets and dipolar supersolids. *Reports on Progress in Physics*, 84(1):012403, dec 2020.

[186] U. Ernst, A. Marte, F. Schreck, J. Schuster, and G. Rempe. Bose-einstein condensation in a ioffe-pritchard trap. pages 48–, 1998.

[187] K M F Magalhães, S R Muniz, E A L Henn, R R Silva, L G Marcassa, and V S Bagnato. Achievement of quantum degeneracy in a na-quic trap in brazil: an in situ observation. *Laser Physics Letters*, 2(4):214, dec 2004.

[188] Eugene Hecht. *Optics*. Pearson, Upper Saddle River, NJ, 5 edition, December 2015.

[189] Eric D. Black. An introduction to pound–drever–hall laser frequency stabilization. *American Journal of Physics*, 69(1):79–87, 2001.

[190] Carl Wieman, Gwenn Flowers, and Sarah Gilbert. Inexpensive laser cooling and trapping experiment for undergraduate laboratories. *American Journal of Physics*, 63(4):317–330, 1995.

[191] J. Fortagh, A. Grossmann, T. W. Hänsch, and C. Zimmermann. Fast loading of a magneto-optical trap from a pulsed thermal source. *Journal of Applied Physics*, 84(12):6499–6501, 1998.

[192] Umakant D. Rapol, Ajay Wasan, and Vasant Natarajan. Loading of a Rb magneto-optic trap from a getter source. *Phys. Rev. A*, 64:023402, Jun 2001.

[193] K. Moore, T. Purdy, K. Murch, Sabrina R. Leslie, S. Gupta, and D. Stamper-Kurn. Collimated, single-pass atom source from a pulsed alkali metal dispenser for laser-cooling experiments. *Review of Scientific Instruments*, 76:023106, 2004.

[194] Bartalini, S., Herrera, I., Consolino, L., Pappalardo, L., Marino, N., D'Arrigo, G., and Cataliotti, F. S. Full characterization of the loading of a magneto-optical trap from an alkali metal dispenser. *Eur. Phys. J. D*, 36(1):101–104, 2005.

[195] Peter D. McDowall, Tzahi Grünzweig, Andrew Hilliard, and Mikkel F. Andersen. An atomic beam source for fast loading of a magneto-optical trap under high vacuum. *Review of Scientific Instruments*, 83(5):055102, 2012.

[196] B. P. Anderson and M. A. Kasevich. Loading a vapor-cell magneto-optic trap using light-induced atom desorption. *Phys. Rev. A*, 63:023404, Jan 2001.

[197] C. Klempt, T. van Zoest, T. Henninger, O. Topic, E. Rasel, W. Ertmer, and J. Arlt. Ultraviolet light-induced atom desorption for large rubidium and potassium magneto-optical traps. *Phys. Rev. A*, 73:013410, Jan 2006.

[198] Gustavo Telles, Tetsuya Ishikawa, Matthew Gibbs, and Chandra Raman. Light-induced atomic desorption for loading a sodium magneto-optical trap. *Phys. Rev. A*, 81:032710, Mar 2010.

[199] Lara Torralbo-Campo, Graham Bruce, Giuseppe Smirne, and Donatella Cassettari. Light-induced atomic desorption in a compact system for ultracold atoms. *Scientific Reports*, 5, 10 2015.

[200] S. Kang, K. R. Moore, J. P. McGilligan, R. Mott, A. Mis, C. Roper, E. A. Donley, and J. Kitching. Magneto-optic trap using a reversible, solid-state alkali-metal source. *Opt. Lett.*, 44(12):3002–3005, Jun 2019.

[201] K Stam, Eikbert Van Ooijen, R Meppelink, Johannes Vogels, and Peter van der Straten. Large atom number bose-einstein condensate of sodium. *The Review of scientific instruments*, 78:013102, 02 2007.

[202] J. Catani, P. Maioli, L. De Sarlo, F. Minardi, and M. Inguscio. Intense slow beams of bosonic potassium isotopes. *Phys. Rev. A*, 73:033415, Mar 2006.

[203] Sean Ravenhall, Benjamin Yuen, and Chris Foot. High-flux, adjustable, compact cold-atom source. *Opt. Express*, 29(14):21143–21159, Jul 2021.

[204] G. Lamporesi, S. Donadello, S. Serafini, and G. Ferrari. Compact high-flux source of cold sodium atoms. *Review of Scientific Instruments*, 84(6):063102, 2013.

[205] Stefan Kuhr, Wolfgang Alt, Dominik Schrader, Martin Müller, Victor Gomer, and Dieter Meschede. Deterministic delivery of a single atom. *Science*, 293(5528):278–280, 2001.

[206] Till Klostermann, Cesar Cabrera, Hendrik Raven, Julian Wienand, Christian Schweizer, Immanuel Bloch, and Monika Aidelsburger. Fast long-distance transport of cold cesium atoms. 09 2021.

[207] T. L. Gustavson, A. P. Chikkatur, A. E. Leanhardt, A. Görlitz, S. Gupta, D. E. Pritchard, and W. Ketterle. Transport of bose-einstein condensates with optical tweezers. *Phys. Rev. Lett.*, 88:020401, Dec 2001.

[208] Julian Leonard, Moonjoo Lee, Andrea Morales, Thomas Karg, Tilman Esslinger, and Tobias Donner. Optical transport and manipulation of an ultracold atomic cloud using focus-tunable lenses. *New Journal of Physics*, 16, 09 2014.

[209] G. Unnikrishnan, C. Beulenkamp, D. Zhang, K. P. Zamarski, M. Landini, and H.-C. Nägerl. Long distance optical transport of ultracold atoms: A compact setup using a moiré lens. *Review of Scientific Instruments*, 92(6):063205, 2021.

[210] Markus Greiner, Immanuel Bloch, Theodor W. Hänsch, and Tilman Esslinger. Magnetic transport of trapped cold atoms over a large distance. *Phys. Rev. A*, 63:031401, Feb 2001.

[211] Thomas Salez. *Towards quantum degenerate atomic Fermi mixtures*. Theses, Ecole Normale Supérieure de Paris - ENS Paris, September 2011.

[212] Stefan Minniberger, Fritz Diorico, Stefan Haslinger, Christoph Hufnagel, Christian Novotny, Nils Lippok, Johannes Majer, Stephan Schneider, and Jörg Schmiedmayer. Magnetic conveyor belt transport of ultracold atoms to a superconducting atomchip. *Applied Physics B*, 340, 03 2014.

[213] Thomas Badr, Dany Ben Ali, Joseph Seaward, Yanliang Guo, Fabrice Wiotte, Romain Dubessy, Hélène Perrin, and Aurélien Perrin. Comparison of time profiles for the magnetic transport of cold atoms. *Applied Physics B*, 125(6), May 2019.

[214] H. J. Lewandowski, D. M. Harber, D. L. Whitaker, and E. A. Cornell. Simplified system for creating a bose–einstein condensate. *Journal of Low Temperature Physics*, 132(5):309–367, Sep 2003.

[215] S. Händel, A. L. Marchant, T. P. Wiles, S. A. Hopkins, and S. L. Cornish. Magnetic transport apparatus for the production of ultracold atomic gases in the vicinity of a dielectric surface. *Review of Scientific Instruments*, 83(1):013105, 2012.

[216] Tobias G. Tiecke. *Properties of Potassium*. 2011.

[217] Or Katz, Or Peleg, and Ofer Firstenberg. Coherent coupling of alkali atoms by random collisions. *Phys. Rev. Lett.*, 115:113003, Sep 2015.

[218] John H. Moore, Christopher C. Davis, Michael A. Coplan, and Sandra C. Greer. *Building Scientific Apparatus*. Cambridge University Press, 4 edition, 2009.

[219] Carl E. Wieman and Leo Hollberg. Using diode lasers for atomic physics. pages 772–791.

[220] G. C. Bjorklund, M. D. Levenson, W. Lenth, and C. Ortiz. Frequency modulation (fm) spectroscopy. *Applied Physics B*, 32(3):145–152, Nov 1983.

[221] Devang Naik. Bose-einstein condensation: Building the testbeds to study superfluidity. 2006.

[222] T. W. Hänsch, I. S. Shahin, and A. L. Schawlow. High-resolution saturation spectroscopy of the sodium *d* lines with a pulsed tunable dye laser. *Phys. Rev. Lett.*, 27:707–710, Sep 1971.

[223] R. Muhammad, J. Ramirez-Serrano, K.M.F. Magalhães, R. Paiva, R. Shiozaki, J. Weiner, and V.S. Bagnato. Efficiency in the loading of a sodium magneto-optical trap from alkali metal dispensers. *Optics Communications*, 281(19):4926–4930, 2008.

[224] William D. Phillips and Harold Metcalf. Laser deceleration of an atomic beam. *Phys. Rev. Lett.*, 48:596–599, Mar 1982.

[225] Mark Kasevich and Steven Chu. Atomic interferometry using stimulated raman transitions. *Phys. Rev. Lett.*, 67:181–184, Jul 1991.

[226] Kai Bongs, Michael Holynski, Jamie Vovrosh, Philippe Bouyer, Gabriel Condon, Ernst Rasel, Christian Schubert, Wolfgang P. Schleich, and Albert Roura. Taking atom interferometric quantum sensors from the laboratory to real-world applications. *Nature Reviews Physics*, 1(12):731–739, Dec 2019.

[227] Masao Takamoto, Feng-Lei Hong, Ryoichi Higashi, and Hidetoshi Katori. An optical lattice clock. *Nature*, 435(7040):321–324, May 2005.

[228] N. Hinkley, J. A. Sherman, N. B. Phillips, M. Schioppo, N. D. Lemke, K. Beloy, M. Pizzocaro, C. W. Oates, and A. D. Ludlow. An atomic clock with 10^{–18} instability. *Science*, 341(6151):1215–1218, 2013.

[229] Wolfgang Ketterle and N.J. Van Druten. Evaporative cooling of trapped atoms. 37:181–236, 1996.

[230] K M R van der Stam, E. D. van Ooijen, R. Meppelink, J. M. Vogels, and P. van der Straten. Large atom number bose-einstein condensate of sodium. *The Review of scientific instruments*, 78 1:013102, 2007.

[231] K. Dieckmann, R. J. C. Spreeuw, M. Weidemüller, and J. T. M. Walraven. Two-dimensional magneto-optical trap as a source of slow atoms. *Phys. Rev. A*, 58:3891–3895, Nov 1998.

[232] J. Schoser, A. Batär, R. Löw, V. Schweikhard, A. Grabowski, Yu. B. Ovchinnikov, and T. Pfau. Intense source of cold rb atoms from a pure two-dimensional magneto-optical trap. *Phys. Rev. A*, 66:023410, Aug 2002.

[233] Saptarishi Chaudhuri, Sanjukta Roy, and C. S. Unnikrishnan. Realization of an intense cold rb atomic beam based on a two-dimensional magneto-optical trap: Experiments and comparison with simulations. *Phys. Rev. A*, 74:023406, Aug 2006.

[234] T. G. Tiecke, S. D. Gensemer, A. Ludewig, and J. T. M. Walraven. High-flux two-dimensional magneto-optical-trap source for cold lithium atoms. *Phys. Rev. A*, 80:013409, Jul 2009.

[235] Armin Ridinger, Saptarishi Chaudhuri, Thomas Salez, Ulrich Eismann, Diogo Fernandes, Kilvia Farias, David Wilkowski, C. Salomon, and Frédéric Chevy. Large

atom number dual-species magneto-optical trap for fermionic 6li and 40k atoms. *The European Physical Journal D*, 65, 03 2011.

[236] E Pedrozo-Peñafiel, F Vivanco, P Castilho, R R Paiva, K M Farias, and V S Bagnato. Direct comparison between a two-dimensional magneto-optical trap and a zeeman slower as sources of cold sodium atoms. *Laser Physics Letters*, 13(6):065501, may 2016.

[237] Dallin Durfee. Dynamic properties of dilute bose-einstein condensates. 1999.

[238] Michael A. Joffe, Wolfgang Ketterle, Alex Martin, and David E. Pritchard. Transverse cooling and deflection of an atomic beam inside a zeeman slower. *J. Opt. Soc. Am. B*, 10(12):2257–2262, Dec 1993.

[239] Ananth Chikkatur. Colliding and moving bose-einstein condensates: Studies of superfluidity and optical tweezers for condensate transport. 10 2004.

[240] Devang Naik. Bose-einstein condensation: Building the testbeds to study superfluidity. 01 2006.

[241] R. S. Williamson and T. Walker. Magneto-optical trapping and ultracold collisions of potassium atoms. *J. Opt. Soc. Am. B*, 12(8):1393–1397, Aug 1995.

[242] John Weiner, Vanderlei S. Bagnato, Sergio Zilio, and Paul S. Julienne. Experiments and theory in cold and ultracold collisions. *Rev. Mod. Phys.*, 71:1–85, Jan 1999.

[243] Torsten Hartmann, Torben A. Schulze, Kai K. Voges, Philipp Gersema, Matthias W. Gempel, Eberhard Tiemann, Alessandro Zenesini, and Silke Ospelkaus. Feshbach resonances in ^{23}Na $+^{39}$ K mixtures and refined molecular potentials for the nak molecule. *Phys. Rev. A*, 99:032711, Mar 2019.

[244] Kevin M. Jones, Eite Tiesinga, Paul D. Lett, and Paul S. Julienne. Ultracold photoassociation spectroscopy: Long-range molecules and atomic scattering. *Rev. Mod. Phys.*, 78:483–535, May 2006.

[245] Andrew Truscott, Kevin Strecker, William McAlexander, Guthrie Partridge, and Randall Hulet. Observation of fermi pressure in a gas of trapped atoms. *Science (New York, N.Y.)*, 291:2570–2, 04 2001.

[246] Z. Hadzibabic, C. A. Stan, K. Dieckmann, S. Gupta, M. W. Zwierlein, A. Görlitz, and W. Ketterle. Two-species mixture of quantum degenerate bose and fermi gases. *Phys. Rev. Lett.*, 88:160401, Apr 2002.

[247] M. S. Santos, P. Nussenzveig, A. Antunes, P. S. P. Cardona, and V. S. Bagnato. Hyperfine-changing collision measurements in trap loss for mixed species in a magneto-optical trap. *Phys. Rev. A*, 60:3892–3895, Nov 1999.

[248] M. W. Mancini, A. R. L. Caires, G. D. Telles, V. S. Bagnato, and L. G. Marcassa. Trap loss rate for heteronuclear cold collisions in two species magneto-optical trap. *The European Physical Journal D - Atomic, Molecular, Optical and Plasma Physics*, 30(1):105–116, Jul 2004.

[249] M. Prentiss, A. Cable, J. E. Bjorkholm, Steven Chu, E. L. Raab, and D. E. Pritchard. Atomic-density-dependent losses in an optical trap. *Opt. Lett.*, 13(6):452–454, Jun 1988.

[250] D. Sesko, T. Walker, C. Monroe, A. Gallagher, and C. Wieman. Collisional losses from a light-force atom trap. *Phys. Rev. Lett.*, 63:961–964, Aug 1989.

[251] Béatrice Bussery, Yamina Achkar, and Monique Aubert-Frécon. Long-range molecular states dissociating to the three or four lowest asymptotes for the ten heteronuclear diatomic alkali molecules. *Chemical Physics*, 116(3):319–338, 1987.

[252] Daniel Steck. Sodium d line data. 2003.

[253] Tim Dinneen, K Vogel, John Hall, and A Gallagher. Cold collisions of sr[*]-sr in a magneto-optical trap. (59), 1999-01-01 00:01:00 1999.

[254] U. Schlöder, H. Engler, U. Schünemann, Rudolf Grimm, and Matthias Weidemüller. Cold inelastic collisions between lithium and cesium in a two-species magneto-optical trap. *The European Physical Journal D*, 7:331–340, 10 1999.

[255] G. D. Telles, W. Garcia, L. G. Marcassa, V. S. Bagnato, D. Ciampini, M. Fazzi, J. H. Müller, D. Wilkowski, and E. Arimondo. Trap loss in a two-species rb-cs magneto-optical trap. *Phys. Rev. A*, 63:033406, Feb 2001.

[256] C. G. Townsend, N. H. Edwards, C. J. Cooper, K. P. Zetie, C. J. Foot, A. M. Steane, P. Szriftgiser, H. Perrin, and J. Dalibard. Phase-space density in the magneto-optical trap. *Phys. Rev. A*, 52:1423–1440, Aug 1995.

[257] Thad Walker, David Sesko, and Carl Wieman. Collective behavior of optically trapped neutral atoms. *Phys. Rev. Lett.*, 64:408–411, Jan 1990.

[258] David J. Griffiths. *Introduction to Quantum Mechanics (2nd Edition)*. Pearson Prentice Hall, 2nd edition, April 2004.

[259] Min Sung Yoon. *Experiments on magnetic transport, magnetic trapping, and Bose-Einstein Condensation*. Theses, University of Oxford, 2013.

[260] Bertrand Mercier. Conductance measurement of a conical tube and calculation of the pressure distribution. *Journal of Vacuum Science and Technology*, 24:529–536, 2006.

[261] David J Griffiths. Introduction to electrodynamics. 2013.

[262] T. Bergeman, Gidon Erez, and Harold J. Metcalf. Magnetostatic trapping fields for neutral atoms. *Phys. Rev. A*, 35:1535–1546, Feb 1987.

[263] Alan L. Migdall, John V. Prodan, William D. Phillips, Thomas H. Bergeman, and Harold J. Metcalf. First observation of magnetically trapped neutral atoms. *Phys. Rev. Lett.*, 54:2596–2599, Jun 1985.

Appendix A

Ultra-high vacuum system and 2D$^+$MOT

In this chapter, I will give an brief overview on the considerations and the calculations involve to design a ultra-high vacuum system.

A.1 Calculations to design a ultra-high vacuum system

Figure-A.1 shows a schematic diagram of a differential pumping scheme. A high pressure region ('chamber 1'), at pressure P_1, is separated from the low pressure region ('chamber 2'), at pressure P_2 (where, $P_1 \gg P_2$) by a differential pumping tube.

The effect of the differential pumping tube can be understood by calculating the conductance of the tube, it is a measure of the particle flow through the tube. For the cylindrical geometry of the tube the following formula is used to calculate the conductance [218],

$$C = 12\frac{d^3}{L} \tag{A.1}$$

in unit of litres/sec, where L is the length of the tube (in cm) and d is the diameter of the tube (in cm). This specific form of the conductance has been devised for air at 20^0C. Which is a valid assumption in our case, since we would like to calculate the

conductance of the background thermal gas through the differential pumping tube and the lab temperature is typically maintained at 20^0C.

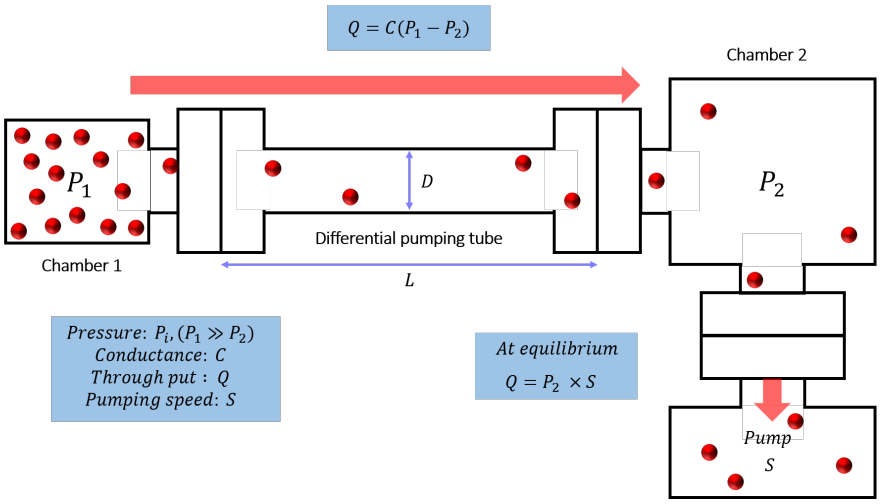


Figure A.1: A schematic diagram of a vacuum setup. The higher pressure and low pressure chambers are separated by a differential pumping tube.

The through put is a measure of the mass flow across the tube. The through put from the 'chamber 1' to 'chamber 2' is given by [218],

$$Q = C \times (P_1 - P_2) \tag{A.2}$$

The 'chamber 2' is pumped by a pump with a pumping speed of S l/s to maintain the pressure at P_2. At steady state condition,

$$Q = P_2 \times S \tag{A.3}$$

Therefore, we could write,

$$Q = C \times (P_1 - P_2) = P_2 \times S \tag{A.4}$$

In the limit, $P_1 \gg P_2$, C$\times P_1 \approx P_2 \times$ S, therefore $\frac{P_2}{P_1} \approx \frac{C}{S}$. Equipped with this basic calculation of a differential pumping scheme, now I will determine the effective pumping speed

at the 3DMOT chmaber by the ion pumps we have employed in our systems.

Figure-A.2 shows a simplified schematic diagram of the vacuum assembly we have designed. We have one ion pump, with pumping speed 75 l/s, connected near the 3DMOT chamber and two more ions pumps of pumping speed 75 l/s and 40 l/s, respectively, are connected near the science cell. In the following, I will estimate the net pumping speed at the 3DMOT chamber due to the combined effect of all of these pumps. Due to the geometry of the construction, each of the pumps have an effective pumping speed, which is determined by the vacuum components installed in the path of the of the 3DMOT chamber and the respective ionpump.

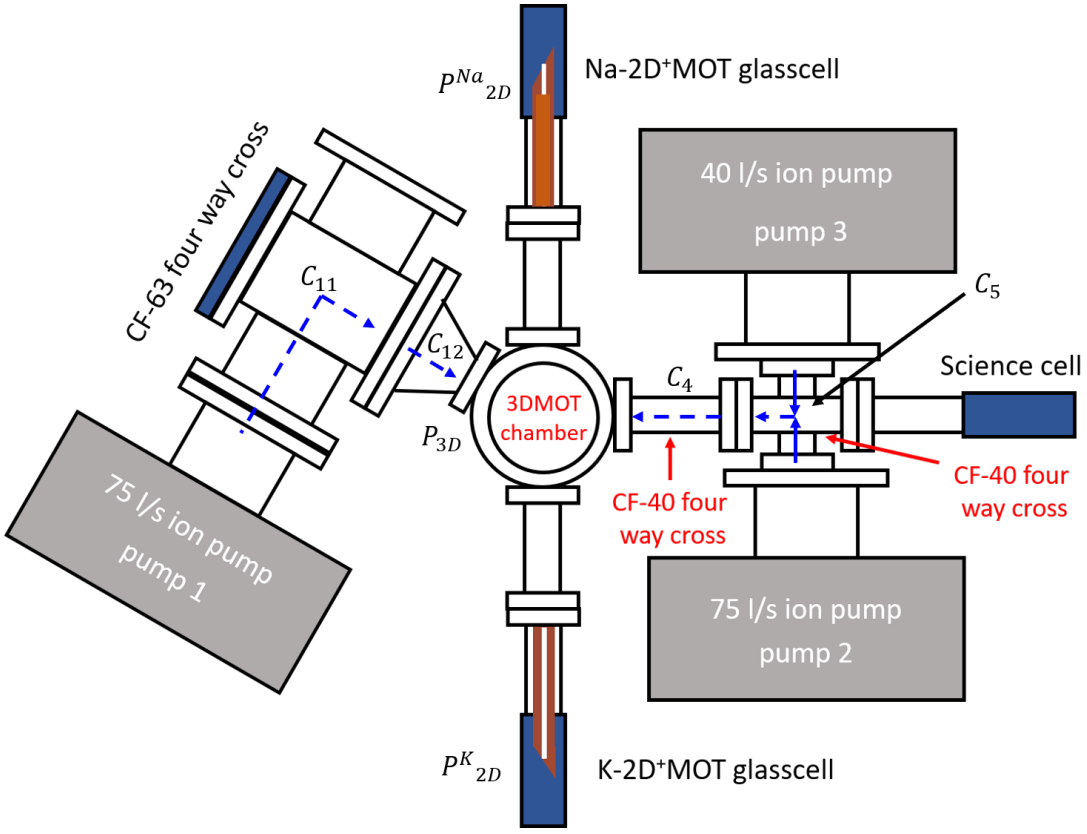


Figure A.2: A simplified schematic diagram of the vacuum setup.

The 75 l/s ionpump ('pump 1') is connected to the 3DMOT chamber through a DN63CF 4-way cross and a DN63CF-DN40CF conical reducer, we define the conductance of the sections as C_{11} and C_{12} respectively.

Note that, the magnitude of the conductance of a straight connector of length L and diameter D and the 90^o elbow of length L and diameter D are the same. This can be easily verified by using the Eqn.A.1. The dimensions of these vacuum components and the value of their conductance are listed in Table-A.1.

Connector	denoted by	Length cm	Diameter cm	Conductance l/sec
DN63CF 4-way cross	C_{11}	10.5	6.2	136
DN63CF-DN40CF conical reducer [260]	C_{12}	7.5	d_1=3.4 and d_2=6.2	150

Table A.1: The dimensions of the vacuum components and their conductance.

Note that, to calculate the conductance of DN63CF-DN40CF conical reducer, we have used the formula given in the reference [260].

These two vacuum components (listed in Table-A.1) connected in series, therefore, the resultant conductance between the 'pump 1' and the 3DMOT chamber will be,

$$C_1 = \frac{C_{11} \times C_{22}}{C_{11} + C_{22}} \tag{A.5}$$

As a result, the effective pumping speed of the 'pump 1' (S_1 = 75 /s) at the 3DMOT chamber will be,

$$S_1' = \frac{S1 \times C_1}{S_1 + C_1} = 36\, l/s \tag{A.6}$$

The 75 l/s ion pump ('pump 2') and 40 l/s ion pump ('pump 3') are connected to the opposite end of a DN40CF 4-way cross, and the combined assembly is connected to the 3DMOT through a DN40CF full nipple straight connector. The conduction of the full nipple connector (C_4) and the 4-way cross connector (C_5) will have same conductance. Therefore, we can assume each of pumps is connected to the 3DMOT chambers effectively through two DN40CF full nipple straight connectors. We can further consider, the connectors are in series connection, this assumption will simply the calculation.

The dimensions and conductance DN40CF full nipple and DN40CF 4-way cross connectors are listed in Table-A.2.

Connector	denoted by	Length cm	Diameter cm	Conductance l/sec
DN40CF full nipple	C_4	12.5	3.4	37
DN40CF 4-way cross	C_5	12.5	3.4	37

Table A.2: The dimensions of the vacuum components and their conductance.

The conductance of the vacuum components between the 3DMOT chamber and both the ion pumps is $C_2 = \frac{C_4 \times C_5}{C_4 + C - 5} = 18\, l/s$. Therefore, the effective pumping speed of the 'pump 2' ($S_2 = 75 l/s$) at the 3DMOT chamber will be, $S_2' = \frac{S_2 \times C_4}{S_2 + C_4} \approx 15 l/s$ and the effective pumping speed of 'pump 3' will be $S_3' \approx 12\, l/s$. The net pumping speed at the 3DMOT chamber due to all the three ion pumps will be $S_{eff} = S_1' + S_2' + S_3' \approx 69 l/s$.

Determination of the conductance of the differential tubes

The 2D$^+$MOT of sodium and potassium atoms are connected to the 3DMOT chamber through their respective differential pumping tubes. We have used Oxygen-free high conductive (OFHC) copper slabs to manufacture differential pumping tubes. The engineering drawings of the differential pumping tubes are shown in Figure-A.3 and Figure-A.4 for sodium and potassium 2D$^+$MOTs respectively. The differential pumping tubes have a centered aligned hole that starts at the surface of the 45^o polished angle surface and runs along the entire length of the tube. The 45^o polished angle surface is inserted inside the 2D$^+$MOT glasscell and ends at the 3DMOT chamber. The hole is having specific diameters over specific lengths. In order to calculate the conductance of the differential tubes, we assume each diameter and corresponding length as independent tubes and calculate the conductance using Eqn.A.1 . The resultant conductance is given by the series combination of all the conductance of the independent tubes.

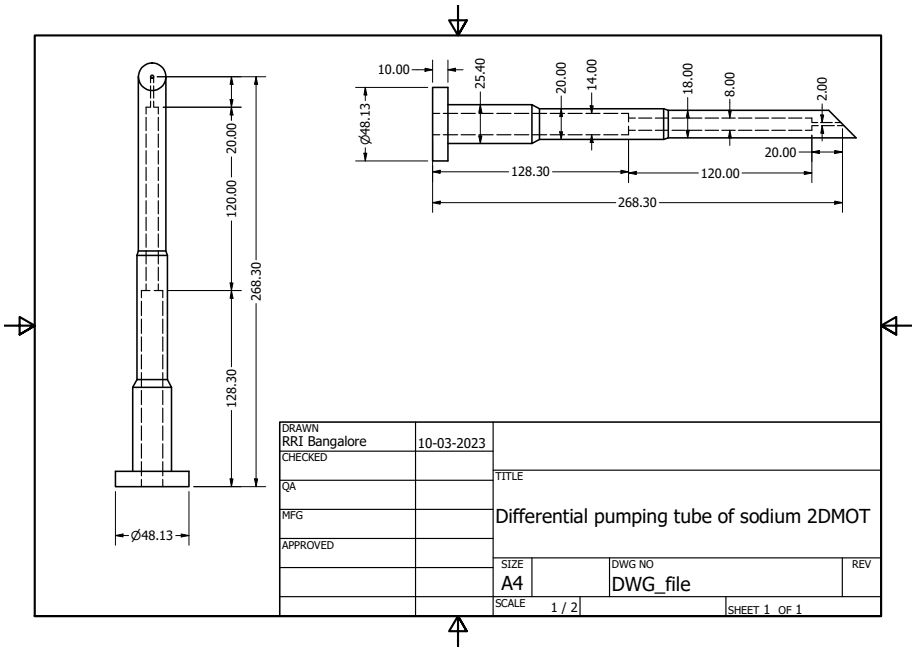


Figure A.3: The engineering drawing of differential pumping tube of the sodium 2D$^+$MOT.

The dimensions and the value of the conductance of each part of the differential pumping tube Na-2D$^+$MOT is listed in Table-A.3. In the conductance calculations, we have used the Eqn.A.1.

Part	Conductance denoted by	Diameter cm	Length cm	Conductance l/sec
1	c_1^{Na}	0.2	2	0.048
2	c_2^{Na}	0.8	12	0.512
3	c_3^{Na}	1.4	12.83	2.53

Table A.3: The dimensions of different parts of the differential pumping tube of the sodium 2D$^+$MOT.

The conductance of the differential pumping tube of Na-2D$^+$MOT, c^{Na} is given by,

$$\frac{1}{c^{Na}} = \frac{1}{c_1^{Na}} + \frac{1}{c_2^{Na}} + \frac{1}{c_3^{Na}} \tag{A.7}$$

The resultant conductance is given by $c^{Na} \approx 0.043 l/s$.

The engineering drawing of the differential pumping tube of K-2D$^+$MOT is shows in Figure-A.4.

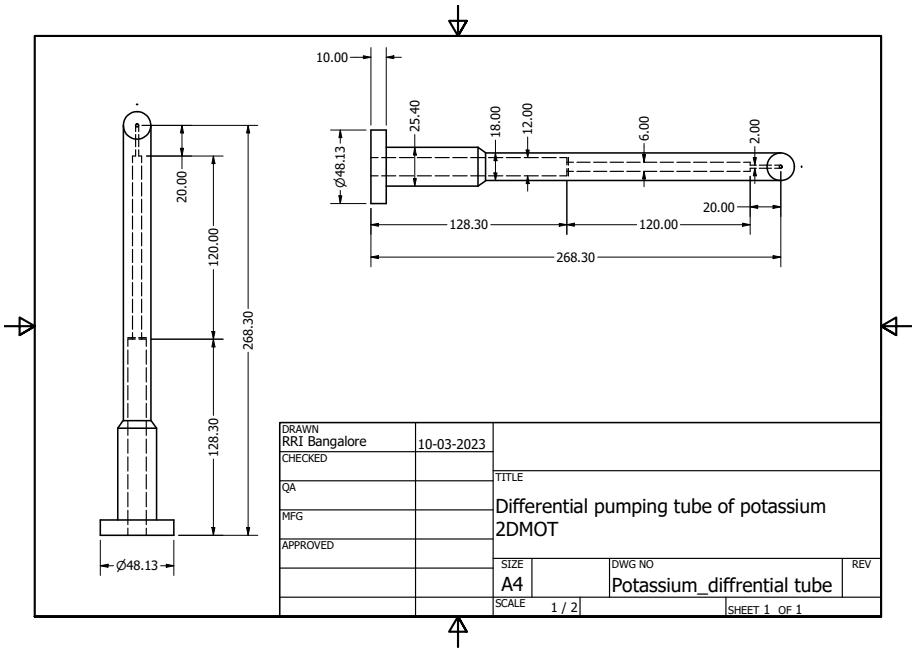


Figure A.4: The engineering drawing of differential pumping of the potassium 2D$^+$MOT

The dimensions and the value of the conductance of each part of the differential pumping tube K-2D$^+$MOT is listed in Table-A.4.

Part	Conductance denoted by	Diameter cm	Length cm	Conductance l/sec
1	c_1^K	0.2	2	0.048
2	c_2^K	0.6	12	0.216
3	c_3^K	1.2	12.83	1.60

Table A.4: The dimensions of different parts of the differential pumping tube of the sodium 2D$^+$MOT.

The conductance of the K-2D$^+$MOT c^{Na} is given by,

$$\frac{1}{c^K} = \frac{1}{c_1^K} + \frac{1}{c_2^K} + \frac{1}{c_3^K} \tag{A.8}$$

The resultant conductance is given by $c^K \approx 0.038 l/s$.

We denote the pressure in the Na-2D$^+$MOT and Na-2D$^+$MOT by P_{2D}^{Na} and P_{2D}^K respectively, as shown in Figure-A.2.

We determine the effective pumping speed at the 3DMOT chamber and the conductance of the Na-2D$^+$MOT and K-2D$^+$MOT. Now we would be able to calculate the pressure difference maintained by the differential pumping tubes between the 2D$^+$MOT and the 3DMOT chamber. At steady state, using conservation of mass, we can write for the differential pumping tube connecting Na-2D$^+$MOT and 3DMOT,

$$c^{Na} \times (P_{2D}^{Na} - P_{3D}) = S_{eff} \times P_{3D} \tag{A.9}$$

Therefore, $\frac{P_{3D}}{P_{2D}^{Na}} \approx \frac{c^{Na}}{S_{eff}} \approx 6 \times 10^{-4}$.

Similarly, following same procedure, for ^{39}K atoms, we can determine the pressure difference between the K-2D$^+$MOT and the 3DMOT as, $\frac{P_{3D}}{P_{2D}^K} \approx \frac{c^K}{S_{eff}} \approx 5 \times 10^{-4}$.

A.2 UHV compatible glasscells of the vacuum setup

We have used total three glasscell in our vacuum setup. The 2D$^+$MOT of the sodium and potassium atoms are performed in two cuboidal shaped glasscells of dimension 40 mm x 40 mm x 85 mm as shown in Figure-A.5. For the 'science cell' we have used a cuboidal shape glasscell of dimension 40 mm x 40 mm x 85 mm as shown in Figure-A.6

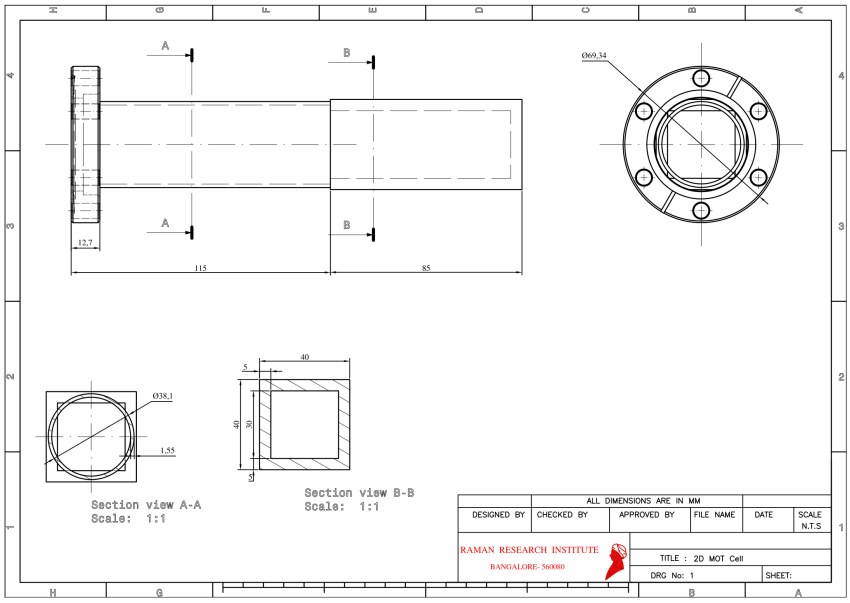


Figure A.5: Engineering drawing of the 2D$^+$MOT glasscell.

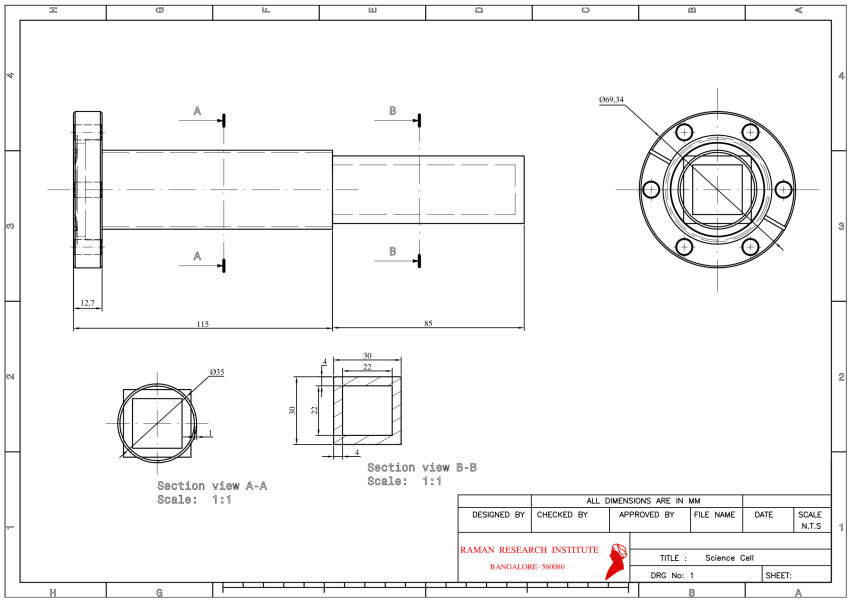


Figure A.6: Engineering drawing of the 'science cell'.

A.3 Two dimensional (2D) quadrupole magnetic field for the 2D$^+$MOT

The engineering drawing of the frame of 2DMOT magnetic is shown in Figure-A.7. We have manufactured aluminium frames according to the design and had wound the coils on the frames.

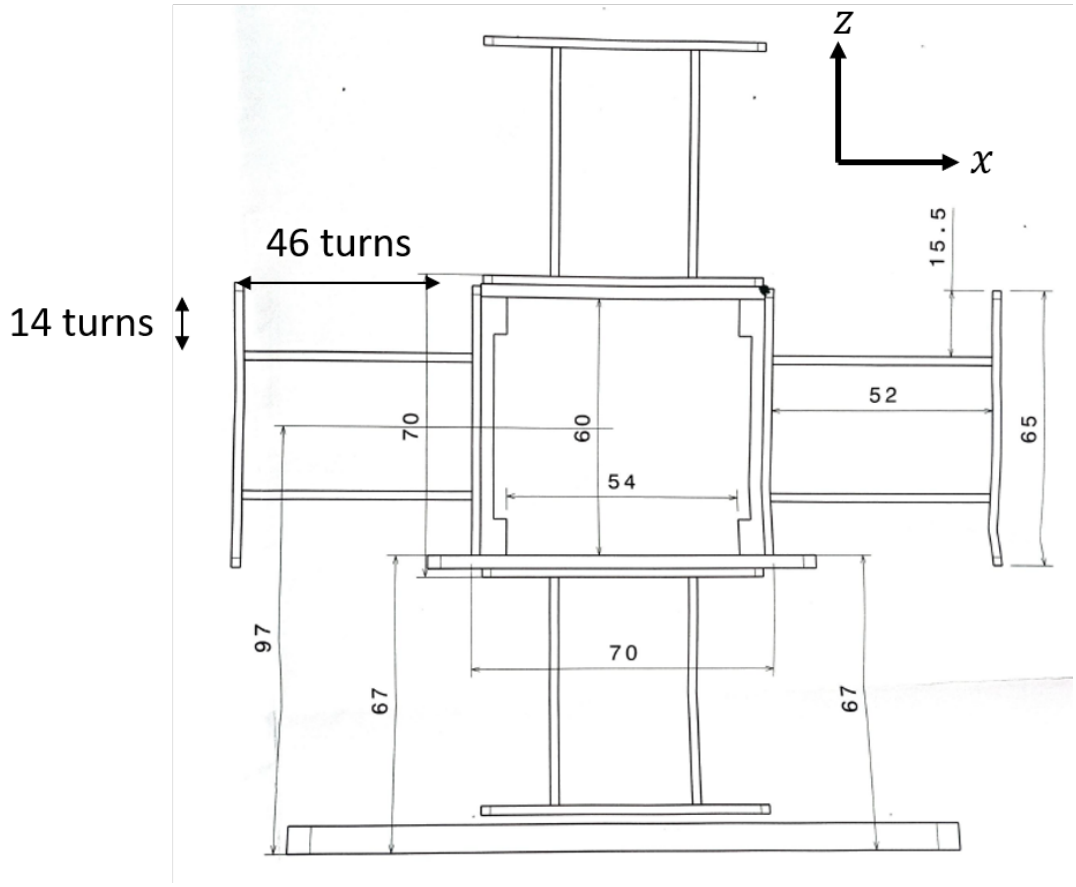


Figure A.7: The dimension of the frame of the 2D$^+$MOT racetrack coils.

We have used 1mm diameter enamelled coated copper wire to make the coils. In each coil, we had wound around $\sim$ 646 turns. In our experiment, the co-ordinates are defined as, x-axis is the horizontal direction (magnetic transport direction), z-axis is along the vertical direction (gravity), and y-axis is along the axis of the 2D$^+$MOT coil, which is also the direction of the atomic beams. We have mounted all the four coils on the

aluminium frames. The mounting frame has appropriate openings to allow the transverse and longitudinal beams for the 2D$^+$MOT. We send the currents in each of the coils to produce 2D-quadrupolar magnetic field configuration around the center on xz plane.

We have measured the magnetic field gradient of the 2DMOT coils using a Hall effect Gaussmeter (Lake Shore: Model 460 3-channel). We performed the measurement by sending 1 Ampere of current in each of the coils. We obtain a magnetic field gradient of $\sim$ 19 Gauss/cm along the transverse direction. Figure-A.8 shows the measurement of the magnetic field along $\hat{x}$.

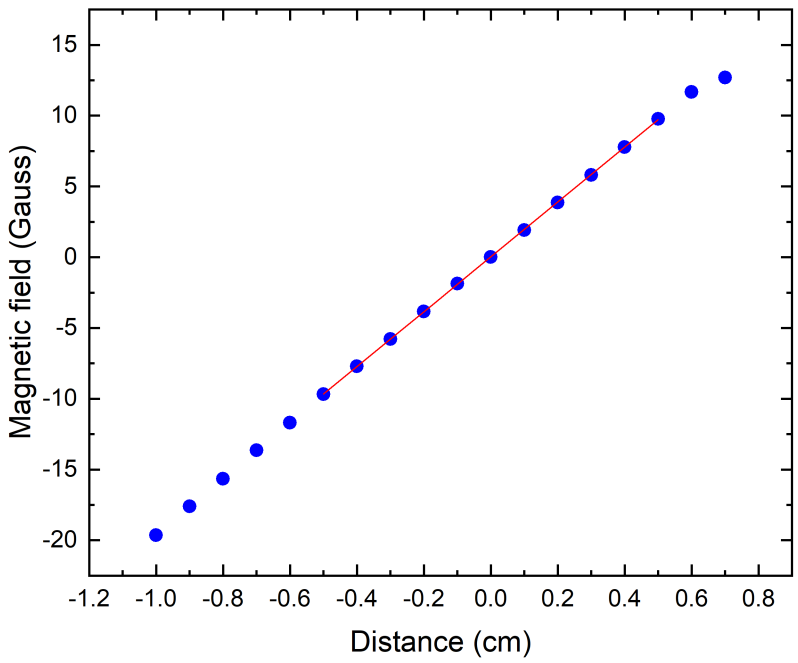


Figure A.8: The experimentally measured magnetic field of the 2D$^+$MOT racetrack coils along one of the transverse axis ($\hat{x}$). The fitting of the experimental data points by a linear function yields a magnetic field gradient $\sim$ 19Gauss/cm at 1 Ampere of current.

The rise and fall of the current in the MOT coils is shown in Figure-2.28.

The independent control of the current in each of the coils is advantageous, by tuning the currents in each of the coils we could change the position of the zero-magnetic field

point (on xz-plane) and aligned with the hole of the differential pumping tube of the 2D$^+$MOT. The tuning of the currents, provides an excellent experimental control during the optimization of the 3DMOT loading using the cold atomic beam from 2D$^+$MOT.

Appendix B

Fast switching of current in the magnetic coils based on IGBT

The circuit diagram of the IGBT based switching circuit of current is shown in Figure-B.1.

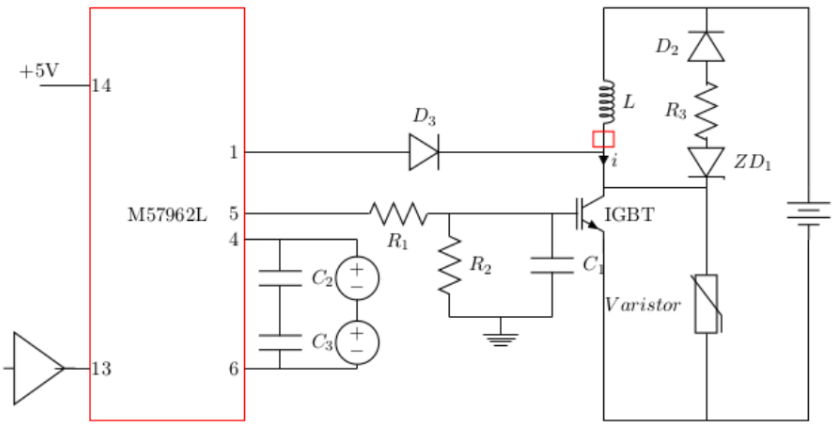


Figure B.1: The schematic of the circuit diagram of IGBT based switching circuit of current in magnetic coils

We have used Mitsubishi CM600HA-24H IGBTs. The gate of the IGBTs are driven by Powerex hybrid integrated gate driver module (M57962L). In Table-B.1, I have listed the components have been used in the fast current switching circuits.

components	part number
IGBT	CM600HA-24H, Mitsubishi
Gate driver	M57962L, Powerex
R1	10Ω (1 W)
R2	1 Ω (1/4 W)
R2	Varierd during the opimization of the circuit
C_1	100pF
C_2 and C_3	47pF (63V)
ZD_1	V_z =9.4 V
D_2 and D_3	pn junction diode 1N4007
Varistor	according to requirement (typically V =220 V or 330 V)

Table B.1: The list of the components have been used in the IGBT based switching circuit.

The IGBT is a fast switch for the current through the magnetic coils. The circuit can be simplified as shown in Figure-B.2.

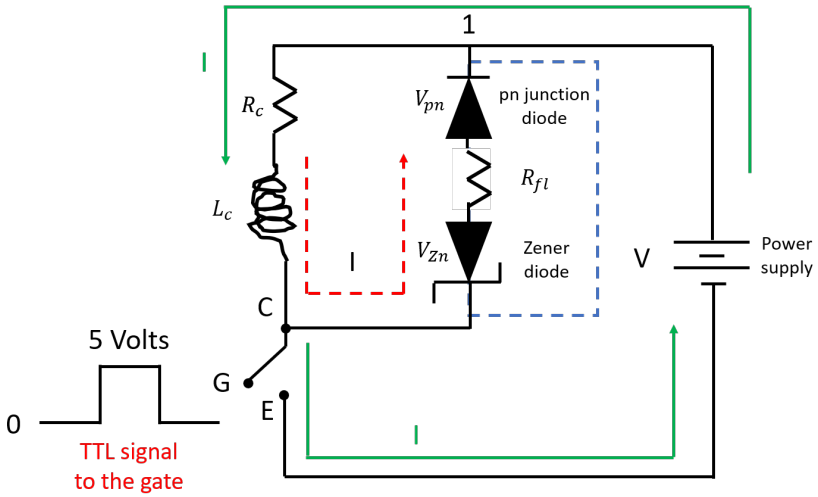


Figure B.2: A simplified schematic diagram of the switching circuit.

A TTL signal is applied to the gate (G). When TTL is low, the path collector (C) to

the emitter (E) connected via G is open, and no current flows through the circuit. When TTL high is applied to G, the path mentioned above is closed via G. A current flows through the coil followed by the C-E path. The amount of current is determined by the applied voltage (V) and the total resistance of the coils (R_c). There is a small amount of voltage drop across CE. Now the circuit behaves as a simple LR circuit, and the current in the coils increases exponentially with a time constant of the rise is given by, $\tau_R = \frac{L_c}{R_c}$, where R_c is the resistance and L_c is the inductance of the coils.

In case of our MOT coils, the total resistance $\sim 0.55\,\Omega$ and the total inductance is 6 mH. The calculated exponential rise time of the MOT coils is ∼11 msec.

If we would like to switch off the magnetic field in a very short time (∼100 usec), then we need to apply TTL low to the gate, which will open the path C-E and no current will flow through the circuit. But, according to Lenz law, this fast switch-off current results in a very high back electro-motive force (EMF). The value of the back EMF would be ∼ 1200 Volts for our MOT coils. The back EMF will be directly applied across the power supply, and it would easily damage the power supply. Therefore, while we are switching off the current in the magnetic coils, special care must be taken to avoid the generation of the back EMF. By providing an alternating path to the current, we could avoid the generation of back EMF. This is achieved by using a protection circuit (fly-wheel circuit). The fly-wheel circuit is connected across the coils as shown in Figure-B.1.

The fly-wheel circuit is composed a pn-junction diode, a resistance (R_{fl}), and Zener diode. The connection of each components to the IGBT circuit is shown in Figure-B.2. The pn-junction diode is in reverse bias, therefore when the TTL is high the current didn't flow through the fly-wheel part and it flows through the coils and followed by the C-E path and completes the circuit as indicated by the green arrows.

When the TTL is low, the current couldn't flow through the circuit and circulates in the alternating path, shown by the red dashed arrow. The current dissipates as heat across the resistance (R_{fl}). The IGBT based switching circuit provides us a very a fast switching off the current ($\sim 130\,\mu s$) in the magnetic coils.

Appendix C

Opto-coupler

Impedance mismatch between the analog and digital cards and the interfacing ports may generate a high back EMF. To protect the control computer and the NI PXIe-1062Q system from over-voltage spikes, it is required to transfer the voltage signals from the PXIe system to the instruments without any direct physical connections.

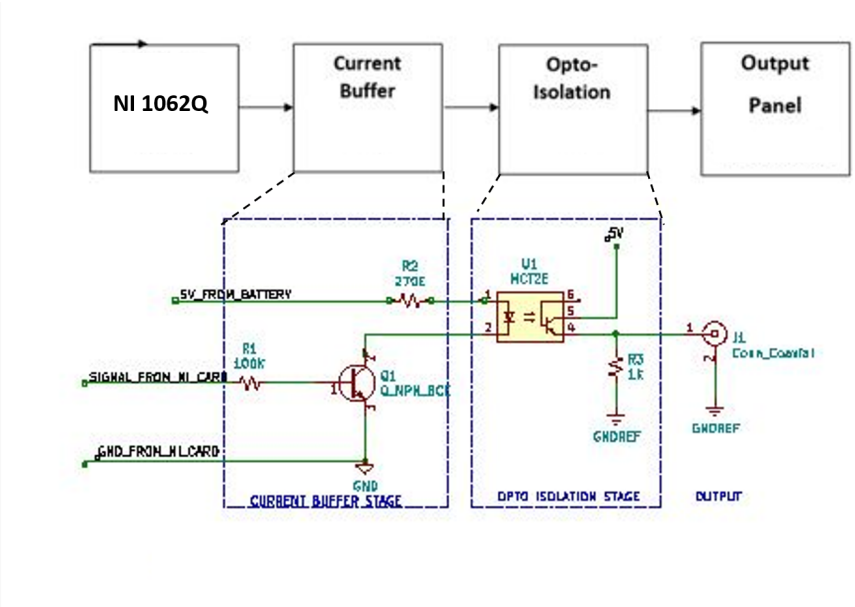


Figure C.1: The circuit diagram of the opto-coupler. The output voltage from the NI 1062Q is send though a current buffer followed by the opto-coupler circuit.

For this purpose we send the voltage signals from the analog and voltage cards of the

NI PXIe-1062Q through the opto-coupler. The output of the opto-coupler is fed to the instruments. Figure-C.2 shows diagram of the opto-coupler circuit.

The response the opto-coupler to rise and fall of a square input voltage signal .

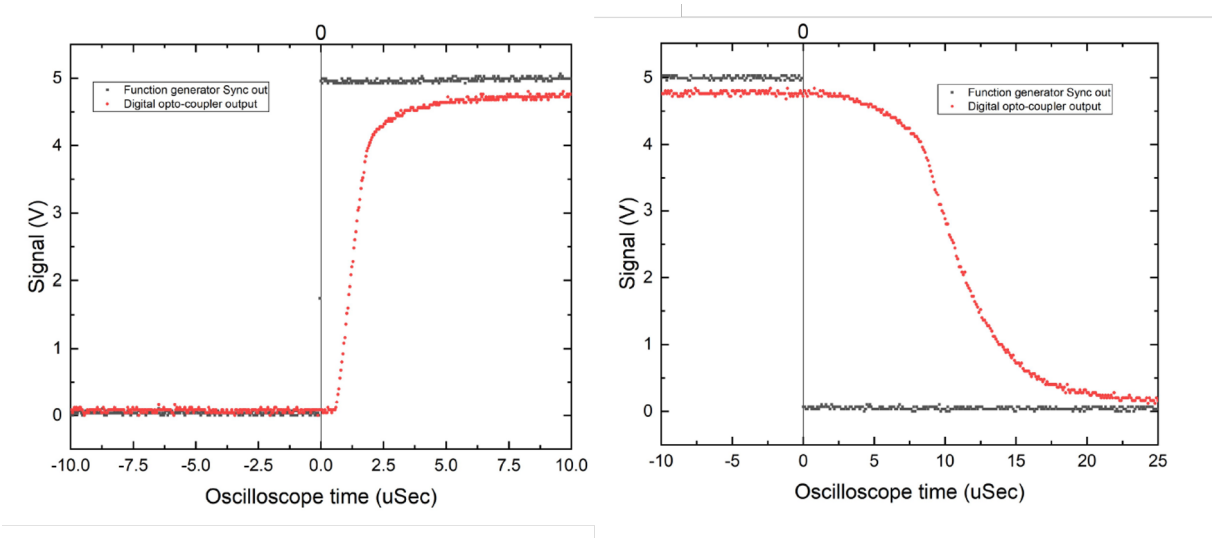


Figure C.2: The response of the opto-coupler to the (a) rise and (b) fall to a square voltage signal.

Appendix D

3DMOT

As mentioned in Section-4.2.1, the photons emitting from the cold and trapped atoms of the 3DMOT due to fluorescence incident on the pixels of a CCD camera. Each of the pixels generate electronic counts and the generation of the electronic counts depends on the number of photons incident on the pixel over the exposure time of the CCD camera and the quantum efficiency of the pixels for the given wavelength of the incident photons. Therefore, by knowing the total number of electronic counts generated by the CCD camera, we could determine the number of photons incident on the CCD camera. The number of captured photons by the CCD camera is determined by the solid angle (Eqn.4.3) subtended by the first lens of the imaging system on the 3DMOT center (Figure-4.5). Thus, by knowing the solid angle and the number of the incident photon on the CCD camera, we could determine the total number of photons emitted from the cold and trapped atoms in the 3DMOT. Afterwards, using of Eqn.4.7, we can determine the number of trapped atoms in the 3DMOT.

D.1 Calibration of the total number of counts generated by the CCD camera for an incident laser beam

As mentioned above and in Section-4.2.1, it is essential to calibrate the CCD camera. Determining the number of trapped atoms requires a priori knowledge of the total count generated by the CCD camera for a given number of incident photons.

To calibrate the camera, we use a probe beam of small diameter and power P_{cal} and let it incident on the CCD camera. The schematic of the experimental arrangement to perform the calibration is shown in Figure-D.1.

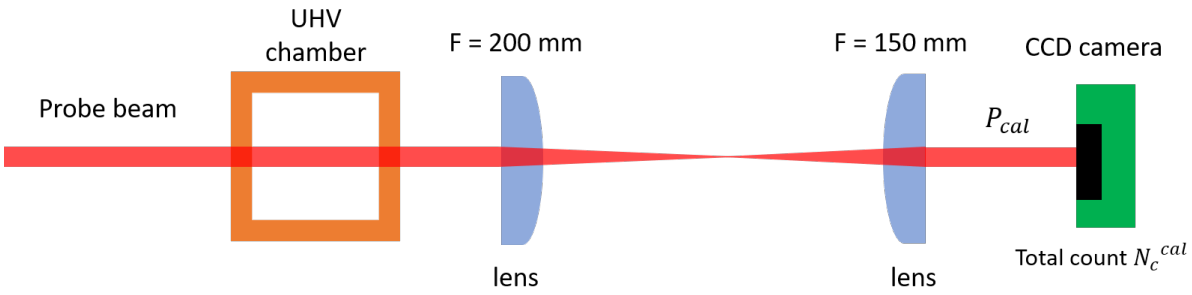


Figure D.1: A probe laser beam is incident on the CCD camera. We measure the power of the laser beam in front of the CCD camera and determine the total count generated by the CCD camera.

First, we determine the number of photons of the probe beam incident on the camera per second using the relation,

$$N_{ph} = \frac{P_{cal}}{E_{ph}} \tag{D.1}$$

Where, $E_{ph} = \frac{hc}{\lambda}$ is the energy of each photon and h is the Planck's constant, c is the velocity of the light, and λ is the wavelength of the probe beam.

We determine the total count generated by the CCD camera when the probe light is blocked for the given exposure time (τ) of the CCD camera and we call it the background count (C_{bg}). After that, we allow the probe light to fall on the CCD camera over the same exposure time of the camera and determine the total count (C_T) generated by the

camera.

Therefore, the number of counts generated by the CCD camera due to the probe light is given by,

$$C_{cal} = C_T - C_{bg} \tag{D.2}$$

The number of photons incident on the CCD camera over the duration of the exposure time (τ) is given by,

$$N_{ph}^{\tau} = N_{ph} \times \tau \tag{D.3}$$

Therefore, we can relate the total number of counts generated by the CCD camera due to N_{ph}^{τ} number of the photons fall on the camera over the duration of the exposure time τ as,

$$C_{cal} = \alpha_{CCD} \times N_{ph} \tag{D.4}$$

Where, α_{CCD} is the conversion factor. In Table-D.1, we quoted the experimentally obtained conversion factor of the photon to the generated count by the CCD camera,

Probe light	Exposure time ms	Conversion factor %
sodium	5	37
potassium	1	13

Table D.1: The calibration of the CCD camera. We are listing the experimentally obtained conversion factor of the number of photons to the counts generated by the CCD camera.

D.2 Determine the atoms number from the counts of the CCD pixel

The solid angle Ω_{MOT} subtended by the fluorescence collection lens (first lens of the imaging system) on the 3DMOT is calculated using Eqn.4.3. Then we calculate the total

intensity (I_{tot}) of the six 3DMOT beams and determine $\frac{I_{tot}}{I_{sat}}$. After that, we determine the scattering rate, R_s using the formula $R_s = \frac{\Gamma}{2}\frac{\frac{I_{tot}}{I_{sat}}}{1+\frac{I_{tot}}{I_{sat}}+(\frac{2\delta_L}{\Gamma})^2}$ where δ_L is the detuning of the 3DMOT cooling beam .

The quantity $\frac{\Omega_s}{4\pi}$ and typical parameters of the cooling beam of the experiment are listed Table-D.2. With the listed parameters of the cooling beams, the scattering rate (R_{sc}) is determined. For N^{at} number of trapped atoms in the 3DMOT, the total number of photons scattered from the 3DMOT over the duration τ is given by, $N^{at} \times R_{sc} \times \tau$. The expression for the total number of trapped atoms in the 3DMOT given by Eqn.4.7, $N^{at} = \frac{4\pi}{\Omega_s}\frac{N^{ph}_{det}}{R_s \times \tau}$. N^{ph}_{det} number of photons from the 3DMOT fluorescence incident on the CCD camera and CCD camera generates total count C_{det}. Then, we have the following relation,

$$N^{ph}_{det} = \frac{C_{det}}{\alpha_{CCD}} \tag{D.5}$$

Therefore, the we have the expression of the number of trapped atoms in the 3DMOT as,

$$N^{at} = \frac{4\pi}{\Omega_s}\frac{1}{\alpha_{CCD}}.\frac{C_{det}}{R_s \times \tau} \tag{D.6}$$

This equation determines the number of trapped atoms in the 3DMOT in terms of the total count generated by the CCD camera.

The quantity ($\frac{\Omega_s}{4\pi}$) and the parameters of the cooling beams of K-3DMOT have been listed in, Table-D.2.

$\frac{\Omega_s}{4\pi}$	0.034
detuning of the cooling beam (Γ)	-6.8
total cooling beam intensity (I_{sat})	22.7
Scattering rate (R_{sc})	6.17×10^5 s^{-1}

Table D.2: The value of the solid angle subtended by the imaging system and the properties of the cooling beams of K-3DMOT.

With a typical fluorescence count of $C_{det} \approx 5 \times 10^9$, we obtain the number of trapped

atoms in the 3DMOT, $N^{at} \sim 1.8 \times 10^{10}$.

The quantity ($\frac{\Omega_s}{4\pi}$) and the parameters of the cooling beams of the Na-3DMOT have been listed in, Table-D.3.

$\frac{\Omega_s}{4\pi}$	0.034
detuning of the cooling beam (Γ)	-1.4
total cooling beam intensity (I_{sat})	7.5
Scattering rate (R_{sc})	1.1×10^7 s^{-1}

Table D.3: The value of the solid angle subtended by the imaging system and the properties of the cooling beams of Na-3DMOT.

With a typical fluorescence count of $C_{det} \approx 10^{10}$, we obtain the number of trapped atoms in the 3DMOT $N^{at} \sim 1.5 \times 10^8$

D.3 Determination the intraspecies collisional loss rate for single species 3DMOT

The density evolution of atoms in a single-species 3DMOT is described by Eqn.4.15. Let us recall the equation,

$$n = n_{ss} \frac{1 - e^{-\Gamma t}}{1 + \zeta e^{-\Gamma t}} \tag{D.7}$$

Where n_{ss} is the steady state density.

The quantities Γ and ζ are expressed as,

$$\Gamma = \gamma + 2\beta n_{ss} \tag{D.8}$$

and

$$\zeta = \frac{\beta n_{ss}}{\beta n_{ss} + \gamma} \tag{D.9}$$

We fit the above equation independently to the experimentally obtained density evo-

lution data Figure-D.3(a) for potassium and Figure-D.3(b) for sodium 3DMOTs.

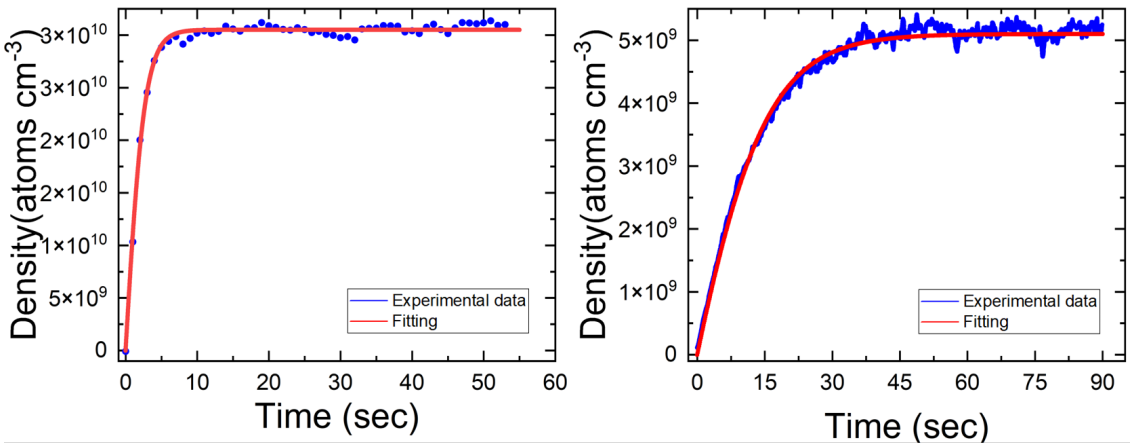


Figure D.2: The density evolution of the atoms in (a) potassium and (b) sodium 3DMOTs. We fit Eqn.D.7 to the data of (a) and (b) and obtained the respective intra-species collisional rates (β).

As mentioned earlier, we have determined the background scattering length γ from the decay curve of the 3DMOTs. We obtained γ‘ ≈0.03. Therefore, β is the only remaining free parameter in Eqn.D.7.

Therefore, the fitting of the experimental data of Figure-D.3(a) and Figure-D.3(b) by the Eqn.D.7 yields the value of the intra-species collisional rates, $\beta_{KK} = 3\times10^{-11}$ cm^3/sec and $\beta_{Na} = 2 \times 10^{-11}$ cm^3/sec, respectively.

D.4 Determination of interspecies collisional loss rate

A detail description of the mechanisms of the interspecies collisional dynamics is given in Section-4.5. The expression of the interspecies collisional loss rate is given by eqn4.26. We recall the equation,

$$\beta_{NaK} = \left[\frac{\pi(w'^2_{Na} + w^2_K)}{2}\right]^{3/2} \times \frac{1}{N_K N'_{Na}} \left\{\gamma(N_{Na} - N'_{Na}) + \beta_{NaNa}\left[\left(\frac{1}{\pi w^2_{Na}}\right)^{3/2} N_{Na} - \left(\frac{1}{\pi w'^2_{Na}}\right)^{3/2} N'_{Na}\right]\right\} \tag{D.10}$$

Where, N_{Na} and N'_{Na} are the number of sodium atoms in the steady state of the Na-3DMOT in the absence and in the presence of the K-3DMOT. w_{Na} and w'_{Na} are the $\frac{1}{e^2}$ radius of the Na-3DMOT in the steady state in the absence and presence of the K-3DMOT. N_K is the number of the potassium atoms and w_K is $\frac{1}{e^2}$ radius of potassium atoms in the steady state of the K-3DMOT.

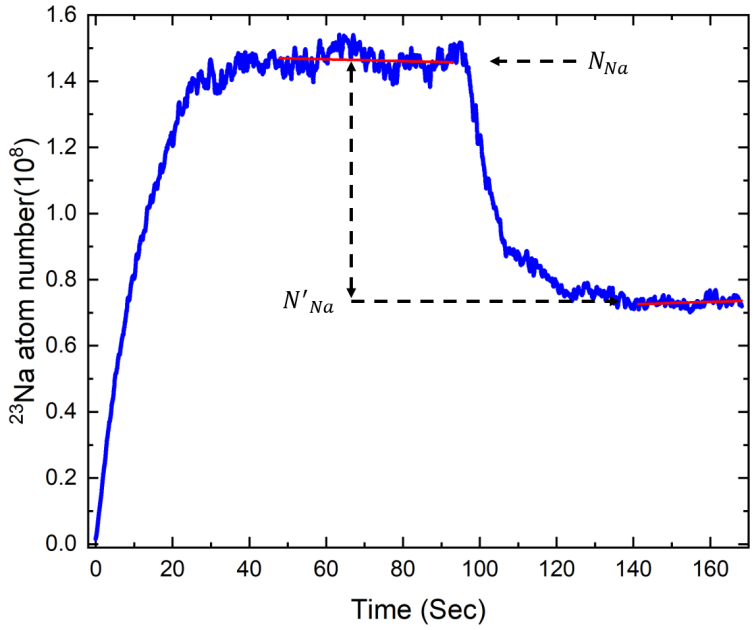


Figure D.3: The loading dynamics of sodium atoms in the 3DMOT in the absence and the presence of K-3DMOT. We load Na-3DMOT from the atomic beam from the Na-2D$^+$MOT and obtain a steady state at ∼20 sec. We allowed the K-3DMOT loading at ∼95sec and observed a gradual decrease of sodium atoms. We obtained a steady state of the Na-3DMOT again at ∼120 sec. We observed a significant loss of sodium atoms as large as 50%. N_{Na} and N'_{Na} are the steady state number of the sodium atoms in the Na-3DMOT in the absence and presence of the potassium 3DMOT.

In the experiment, we load the sodium atoms in the 3DMOT and monitor the fluorescence by a Femto Watt photodiode. When the number of trapped atoms in the 3DMOT reached a steady state, we allowed the potassium atomic beam to load K-3DMOT. During this entire duration, we observed the fluorescence of the Na-3DMOT. The Na-3DMOT

reaches a steady state in the presence of K-3DMOT. From the experimental data, we determine Na and Na'. The size of the Na-3DMOT remains the same in the absence and presence of the K-3DMOT. Therefore, $w'_{Na} \approx w_{Na}$. From the loading of single species 3DMOT of sodium and potassium atoms, we determined β_{NaNa} and β_{KK}, respectively (following the procedure of Appendix-D.3). For typical parameters of the Na-3DMOT and K-3DMOT, we obtained the interspecies $\beta_{NaK} \approx 2 \times 10^{-12}$ cm^3/sec.

D.5 Determination of the excited state population of the potassium atoms in K-3DMOT

Figure-D.4 schematic diagram showing the cooling and repumping beams are interacting with ^{39}K atoms in the 3DMOT.

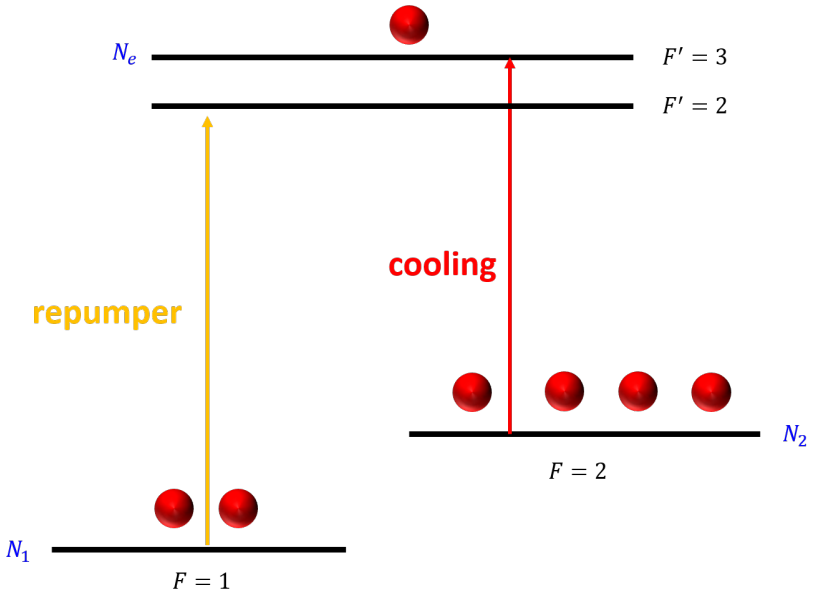


Figure D.4: The schematic diagram shows the distribution of atoms in different hyperfine states. The cooling beam is tuned to the transition $|F = 2\rangle \rightarrow |F' = 3\rangle$. While interacting with the cooling beam, the atoms could make a transition to the hyperfine state $|F = 1\rangle$ and would be out of the cooling transition. Therefore, the repumper beam is employed, which is tuned to the transition $|F = 1\rangle \rightarrow |F' = 2\rangle$. The repumper beam is optically pumps the atoms again to the hyperfine state $|F = 2\rangle$.

During the 3DMOT operation, the distribution of the atoms in different hyperfine states are shown at any given instant of time.

We denote the number of atoms in the ground hyperfine states, $|F = 1\rangle$ by N_1, in $|F = 2\rangle$ by N_2, and in the excited hyperfine state $|F' = 3\rangle$ by N_e. The total number of atoms, $N_T = N_1 + N_2 + N_e$.

In this discussion, we would like to calculate the fraction of the total number of atoms in the excited atoms in the given condition of the 3DMOT, and we defined the quantity

as $\epsilon_e = \frac{N_e}{N_T}$.

The excited state population is given by [50],

$$\rho_{ee} = \frac{1}{2}.\frac{s}{1+s+(\frac{2\delta}{\Gamma})^2} \tag{D.11}$$

Where s is the saturation parameter, given by $s = \frac{I_{tot}}{I_{sat}}$, I_{tot} is the total intensity of the cooling beam of the 3DMOT, I_{sat} is the saturation parameter for the cooling transition, and δ is the detuning of the cooling beam from the cooling transition. For potassium atoms, with the 3DMOT parameters, $s = 7$ (I_{sat} is given by [**?**]), and $\delta = 7\Gamma$, where $\Gamma = 6\pi \times 6$MHz, we obtained, $\rho_{ee} = .018$.

In other words, we could write, $N_e = \rho_{ee} N_2$. Therefore,

$$\epsilon_e = \rho_{ee}\ \frac{N_2}{N_T} \tag{D.12}$$

We obtained the number of atoms (N_2) in the state $|F = 2\rangle$ from the florescence measurement. In the limit, $N_e << N_1$, and N_2, we assume $N_T \approx N_1 + N_2$.

We have observed the reduction of the fluorescence of the 3DMOT, as we reduced the intensity of the 3DMOT repumper beams. Consequently, the fluorescence measurement determines less number of atoms trapped in the 3DMOT. But, the reduction of the fluorescence with reduction of th intensity of the 3DMOT repumper beam doesn't necessarily mean that the total number of atoms trapped in the 3DMOT also reduces at the same rate.

As the intensity of the 3DMOT repumper beam is reduced, less number of atoms, trapped in the hyperfine state $|F = 1\rangle$ are optically pumped to the hyperfine state $|F = 2\rangle$. The trapped atoms in the hyperfine state $|F = 2\rangle$ interact with the 3DMOT cooling beam. In the fluorescence measurement, we capture the photons emitted by the atoms that are experiencing $|F = 2\rangle \rightarrow |F' = 3\rangle$ transition by the cooling beam. As a result, the number of atoms calculated from the fluorescence measurement (N_2) is less than the actual number of atoms($\sim N_1 + N_2$) trapped in the 3DMOT.

As depicted in Figure-D.4, the total number of atoms in a 3DMOT is shared among the three quantum states: $|F = 1\rangle$, $|F = 2\rangle$, and $|F' = 3\rangle$ in the limit $N_e << N_1 \, and \, N_2$. To ensure the fact, we performed an experiment, we send two pulses of a probe beam of equal power and equal duration through the atomic cloud and measured the transmission of the probe beam on a fast photodiode. We monitor the signal generated by the photodiode on a oscilloscope. The frequency of the probe beam is tuned to $|F = 2\rangle \rightarrow |F' = 3\rangle$ transition. Therefore, the absorption of the probe beam through the atomic cloud is a measure of the number atoms in the hyperfine state $|F = 2\rangle$.

We sent the first pulse: call it 'probe 1', of duration 100 μs when the 3DMOT reached the steady state. Then, we turn off the 3DMOT cooling beam and kept the 3DMOT repumper beam on for another 50 μs. After 100 μs we send another pulse of the probe beam, termed as 'probe 2', of duration 100 μs. The enhancement of the absorption of the pulse 'probe 2' w.r.t to the pulse 'probe 1' is a measure of the number of atoms were optically pumped from the hyperfine state $|F = 1\rangle$ to $|F = 2\rangle$. The sequence of the entire measurement sequence is depicted in Figure-D.5. In the given schematic diagram, the enhancement of the absorption of 'probe 2' measured by the photodiode (shown by the deep green plot) of amount ΔV is a measure of the number of the atoms trapped in the hyperfine state $|F = 1\rangle$.

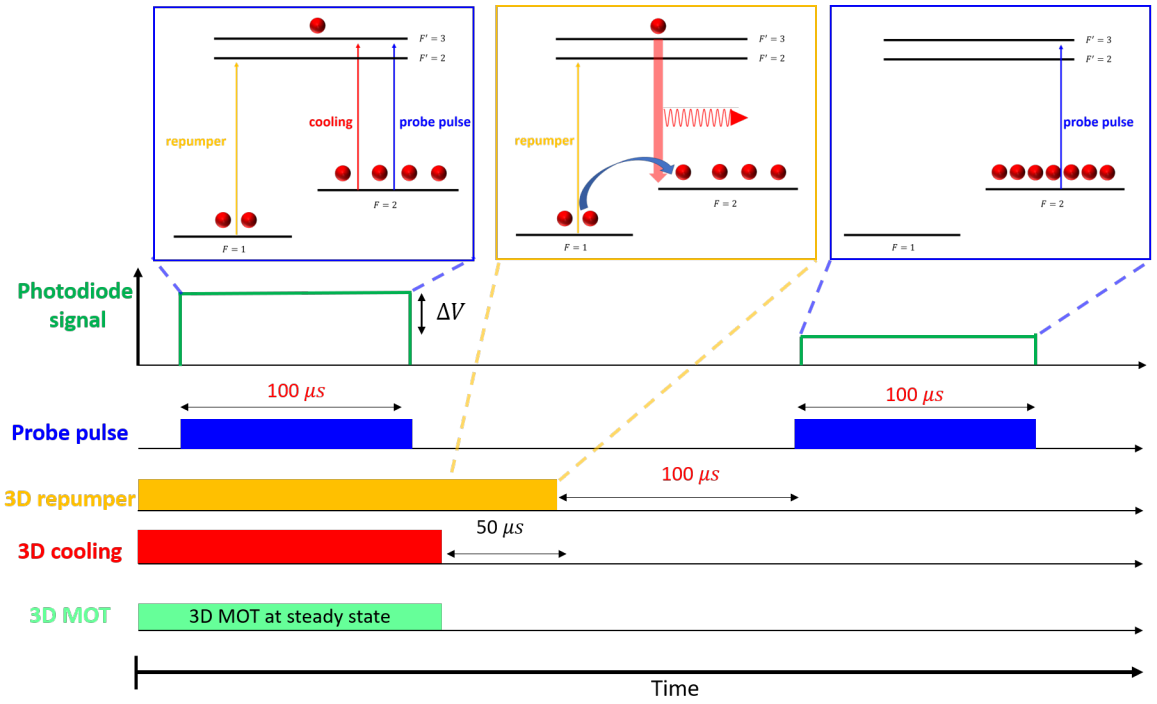


Figure D.5: The schematic diagram shows the measurement scheme of the excited state population of the potassium atoms in the 3DMOT. We send the first pulse, 'probe 1' in the steady state of the 3DMOT. The transmission of the probe is shown by the photodiode signal(green). The distribution of the atoms in different hyperfine states is shown in the inset. Afterward, we turned off the cooling beam of the 3DMOT, and after 50 μs, we turned off the repumper beam of the 3DMOT. This scheme optically transfers the atoms in the hyperfine state $|F = 1\rangle$ to $|F = 2\rangle$. After 100 μs, we sent another pulse, 'probe 2', through the atomic cloud. The transmission of the probe is shown by the photodiode signal(green). The difference(ΔV) between the two consecutive signals is a measure of the optically pumped atoms to $|F = 2\rangle$.

The schematic of the experimental arrangement is shown in Figure-D.6. We send two pulses of the probe beam through the center of the atomic cloud and measured the transmission of the probe beam by a fast photodiode.

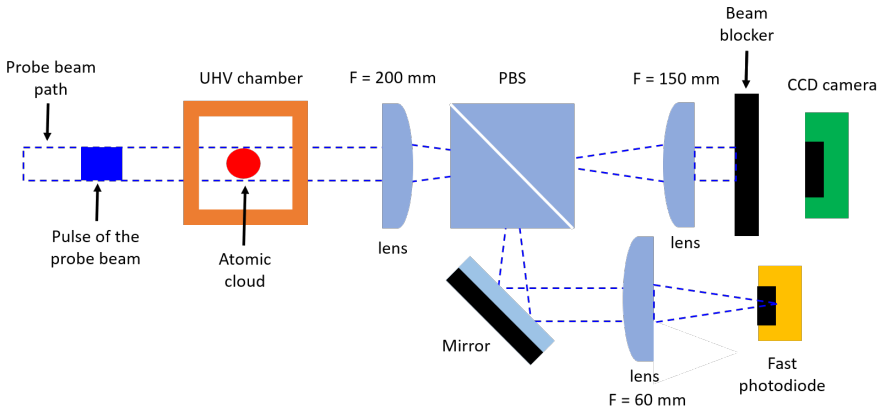


Figure D.6: The schematic diagram of the experimental arrangement. We first aligned the probe beam through the center of the atomic cloud. Thereafter, we sent the two pulses of the probe beams as describe in the text. The transmission of the pulses of the probe beam has been measured by a fast photodiode. The blue dashed lines shows the path traversed by the probe beam and blue solid block represent the pulse of the probe beam.

We have sent both the pulses; 'probe 1' and 'probe 2', of equal power (P_{probe}) 5 μW and of diameter 3 mm over a duration (τ_p) of 100 μs through the atomic cloud. The intensity of the probe beam is, I_{probe}=0.071 mW/cm^2 = 0.019I_{sat}. Figure-D.7 shows enhancement in the absorption of the 'probe 2' pulse w.r.t the absorption of 'probe 1' pulse beam as we varied the intensity of the 3DMOT repumper beams.

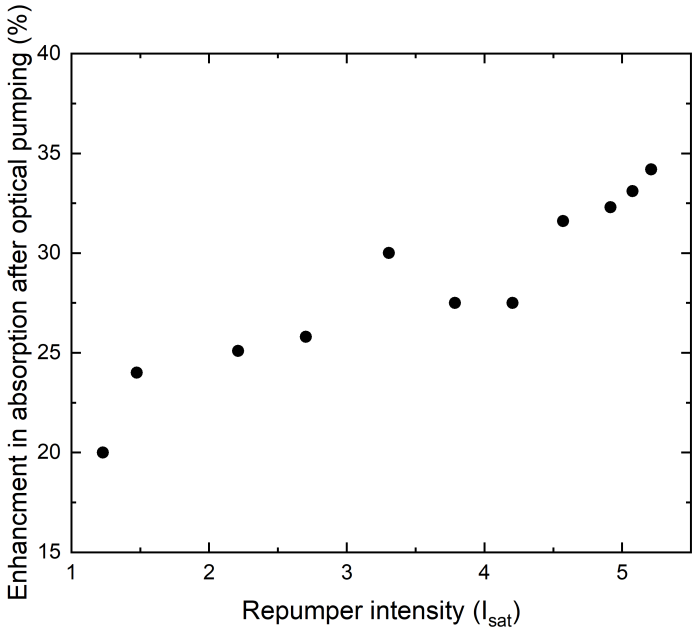


Figure D.7: The enhancement in the absorption of the 'probe 2' pulse w.r.t the 'probe 1' pulse as we varied the intensity of the 3DMOT repumper beams.

In the optical pumping scheme, as outline in Figure-D.5, the repumper beams pumped the atoms trapped in the hyperfine state $|F = 1\rangle$ to the hyperfine state $|F = 2\rangle$. As a result, we have seen an increase in absorption of the 'probe 2' pulse compared to the 'probe 1' pulse as we increased the intensity of the repumper beams.

To validate our argument, stated above, we will demonstrate that, as we reduce the intensity of the 3DMOT repumper beams, the rate of decrease of the number of atoms, N_2 is faster than the decrease of the number of atoms ($\approx N_1 + N_2$) trapped in the 3DMOT. In this regard, we compare the number of fluorescence photons emitted from the atoms trapped in hyperfine state $|F = 2\rangle$ with the additional number of the photons absorbed from the probe beam after the optical pumping.

The expression of energy of each photon is given by, $E_{ph} = \frac{hc}{\lambda}$, Where, λ is the wavelength of the D_2 transition of potassium ^{39}K atoms, λ=767.701 nm. Therefore, the energy of each photon corresponding to $E_{ph} = 2.57 \times 10^{-19}$ Joule. The number of photons

of the probe beam falls on the detector in each second is, $N_{ph} = \frac{P_{probe}}{E_{ph}} = 1.93 \times 10^{13}$.

With the maximum intensity in the K-3DMOT repumper beam, we obtained $\sim 34\%$ enhancement in the absorption as shown in Figure-D.7. Therefore, additional number of photons absorbed by the atomic cloud after the optical pumping is $N_{abs} = 0.34 \times N_{ph} = 6.59 \times 10^{12}$/sec.

The scattering rate experienced by the atoms in the 3DMOT by the cooling beams,

$$R_{scatt} = \Gamma \, \rho_{ee} \tag{D.13}$$

With the cooling beam parameters, as mentioned earlier, we obtain, $R_{scatt} = 6.5 \times 10^5$/sec. Using fluorescence imaging, we determined $N_{at} = 5.4 \times 10^8$ number of atoms were trapped in the 3DOT with the maximum intensity in the 3DMOT repumper beams. Therefore, the total number of fluorescence photons emitted from the trapped atoms in 3DMOT by the cooling beam is given by, $N_{fluo} = N_{at} \times R_{scatt} = 3.5 \times 10^{14}$/sec.

At this point we make the assumption that, with the maximum possible intensity in the 3DMOT repumper beams, in the steady state condition of the 3DMOT, all the atoms are pumped to the $|F = 2\rangle$ state. In the statement, we are keeping a room for the error, since from the probe beam measurement, we have already observed that 34% of the total number of atoms are trapped in the hyperfine state $|F = 1\rangle$. We are assuming that, at this maximum intensity of the 3DMOT, all the atoms are experiencing $|F = 2\rangle - |F' = 3\rangle$ transition. Therefore, our assumption allows us to state that, at the maximum intensity of the 3DMOT repumper beams, the number of atoms participate in the absorption of the 'probe 2' pulse is equivalent to the number of atoms trapped in the 3DMOT (calculated using the fluorescence measurement).

In other words, the number of photons absorbed, N_{abs} at the maximum intensity of the 3DMOT repumper beams and the number of photons scattered from the 3DMOT (N_{fluo}) at the maximum intensity of the 3DMOT repumper are equivalent. So we find out a scaling factor, $c = \frac{N_{abs}}{N_{fluo}}$. With this scaling factor, we scale down the number of

photons scattered from the 3DMOT due to the fluorescence at the lower intensities of the 3DMOT repumper beams. We determined the number of additional photons absorbed from 'probe 2' each of the data points of Figure-D.7.

We plot the additional number of photons absorbed after the optical pumping (termed as 'shelved absorption', $N_{shelved}$) together with the scaled down number of photons ('Fluorescence', N_{Fluor}) obtained from the fluorescence measurement in Figure-D.8.

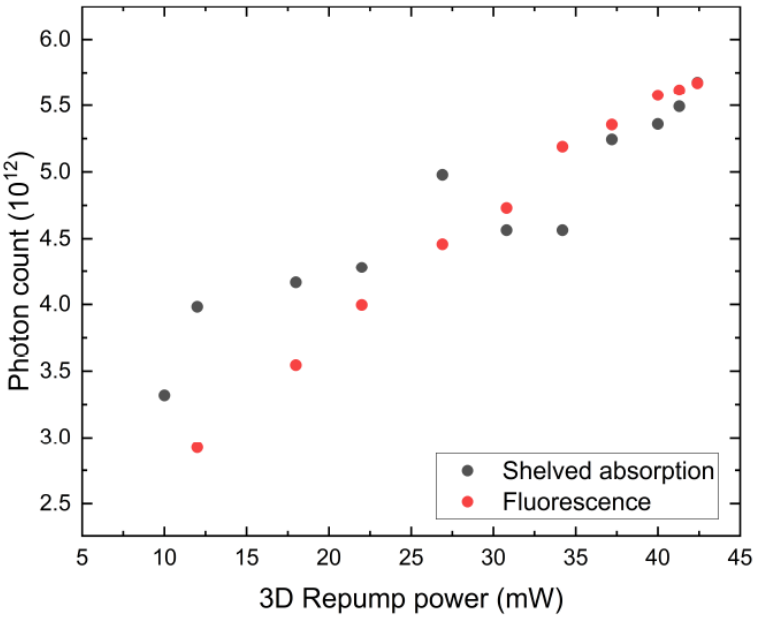


Figure D.8: The additional number of photons absorbed after the optical pumping (black) and the number of photons emitted from the trapped atoms in the 3DMOT due to the fluorescence(red).

We fit the 'shelved absorption' data points with a linear curve and re-plot the graph, we obtained, Figure-D.9,

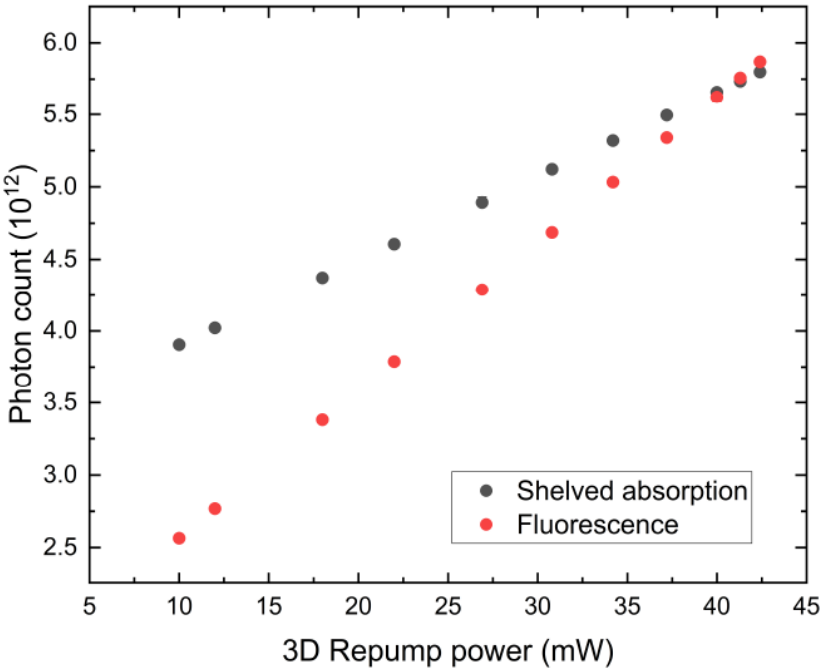


Figure D.9: The additional number of photons absorbed after the optical pumping, calculated from the linear fitting as mentioned in the text and the number of photons emitted from the trapped atoms in the 3DMOT due to the fluorescence.

The above graph shows the photon count of the 'Fluorescence' reduces at faster rate compared to the photon count of the 'Shelved absorption' as the power (or the intensity) of the 3DMOT repumper is reduced. This prove the fact that, the total number of trapped atoms $(N_1 + N_2)$ in the 3DMOT is reduced at a slower rate than the number of trapped atoms , N_2 trapped in the hyperfine state $|F = 2\rangle$, as determined by the fluorescence measurment technique.

Therefore, fraction of the atoms in the excited state as mentioned in Eqn.D.12 could be written in terms of the photon counts of 'Fluorescence' and 'Shelved absorption' as,

$$\epsilon_e = \rho_{ee} \times \frac{N_{Fluo}}{N_{Shelv}} \tag{D.14}$$

During the entire measurement, we kept the 3DMOT cooling parameters the same, therefore, the value of ρ_{ee} remains the same as 0.018. At the maximum intensity of

the 3DMOT repumper, we have $N_{Fluo} = N_{shel}$, for the lower intensities of the 3DMOT repumper, the value of ϵ_e is determined by the quantity $\frac{N_{Fluo}}{N_{shelv}}$, obtained from Figure-D.9. With all the above considerations, we obtained the variation of excited state fraction with the the power (or the intensity) of the 3DMOT repumper beams, as shown in Figure-D.10.

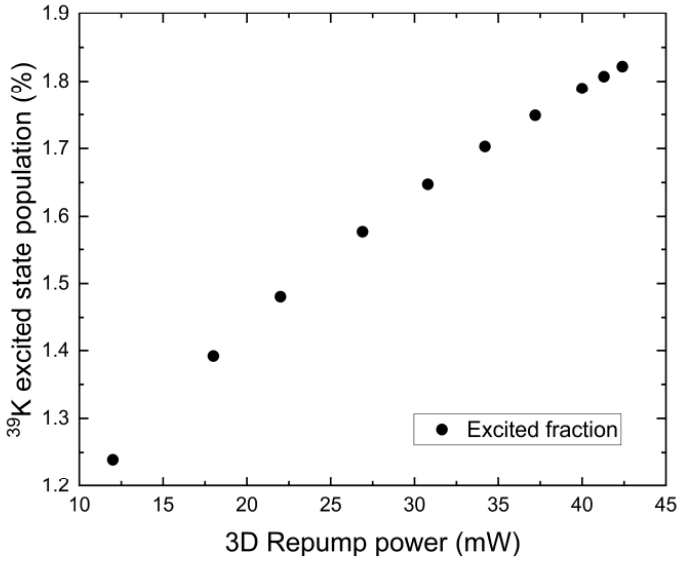


Figure D.10: The variation of the excited state population of the potassium atoms in K-3DMOT with the power of the repumper beams.

Appendix E

Magnetic transport

Magnetic fields of circular coils

The magnetic field generated by a current carrying element is given by Biot-Savart law [261],

$$d\vec{B} = \frac{\mu_0}{4\pi}\frac{I\vec{dl}\times\vec{r}}{|r|^2} \tag{E.1}$$

Where, $\vec{dl}$ is the infinitesimal length vector of the current element carrying current I and $\vec{r}$ is the unit vector specifying the direction of the field point from the current element.

Figure-E.1 shows a schematic diagram of a current carrying loop on $z = A$ plane and generating a magnetic field at position $P(x, y, z)$. The loop has a radius R.

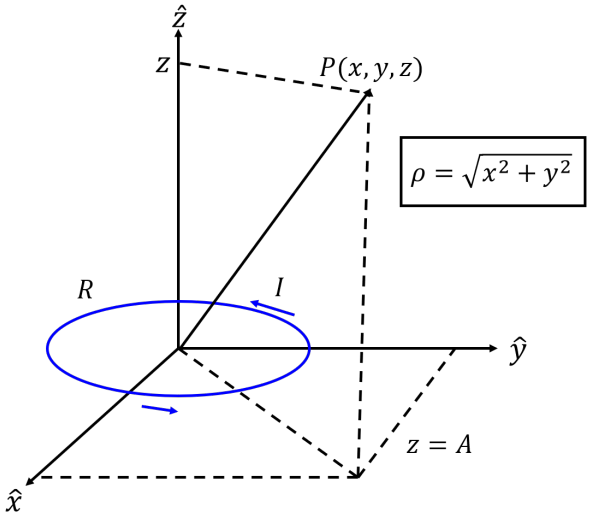


Figure E.1: A schematic of a current carrying single loop generating magnetic field at position $P(x, y, z)$ in the cylindrical cor-ordinate. The loop has a radius R and carrying current I and $\rho = \sqrt{x^2 + y^2}$, is the radial distance of the point.

The magnetic field components in cylindrical polar coordinates is given by [262],

$$
\begin{aligned}
B_\phi &= 0 \\
B_z &= \frac{\mu I}{2\pi(R+\rho)^2 + (z-A)^{2}{}^{1/2}} \{K(k^2) + \frac{R^2 - \rho^2 - (z-A)^2}{(R-\rho)^2 + (z-A)^2} E(k^2)\} \\
B_\rho &= \frac{\mu I (z-A)}{2\pi\rho(R+\rho)^2 + (z-A)^{2}{}^{1/2}} \{-K(k^2) + \frac{R^2 + \rho^2 + (z-A)^2}{(R-\rho)^2 + (z-A)^2} E(k^2)\}
\end{aligned}
\tag{E.2}
$$

The argument of the complete integrals K and E is $k^2 = \frac{4a\rho}{(a+\rho)^2 + (z-z_0)^2}$. In air, $\mu = \mu_0 = 4\pi \times 10^{-7}$ H/m. We have used equations in numerical simulation to calculate the total magnetic field of a thick circular coil of a large number of turns by summing the fields produced by each of the single loops which make the large coil.

Anti-Helmholtz coil configuration

Figure-E.2 shows an anti-Helmholtz magnetic field configuration, produces by two coils placed at positions $z = \frac{d}{2}$ and $z = -\frac{d}{2}$. The arrows indicate the direction of currents in the respective coils. An anti-Helmholtz configuration produces a zero magnetic field on the axis of symmetry at the midway between the two coils and a gradient magnetic field.

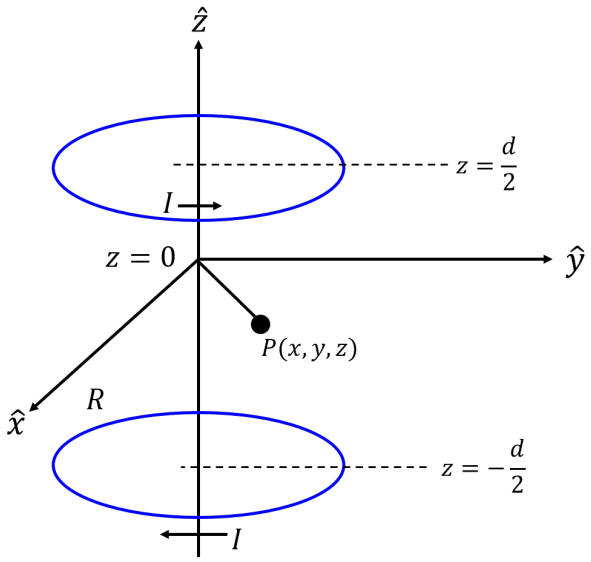


Figure E.2: A schematic of a current carrying single loop generating magnetic field at position $P(x, y, z)$ in the cylindrical cor-ordinate. The loop has a radius R and carrying current I and $\rho = \sqrt{x^2 + y^2}$, is the radial distance of the point.

A linear quadrupole magnetic field configuration requires a locally uniform magnetic field gradient to provide spatially dependent Zeeman shift for the trapping of a cloud atoms as used to trap magnetically neutral atoms by Migdall et.al [263]. The expression of magnetic field B along the z-axis (axis of symmetry) of a pair of anti-Helmholtz coils yields,

$$B(z) = \frac{\mu_0 I a^2}{2}\left(\frac{1}{\{a^2 + (z - d/2)^2\}^{3/2}} - \frac{1}{\{a^2 + (z + d/2)^2\}^{3/2}}\right) \tag{E.3}$$

We have used the set of Eqn.E.2 in numerical simulation to find out the magnetic field produces by a pair of coils in anti-Helmholtz configuration. Thereafter,I have designed the numerical simulation. I have written the code in Wolfram Mathematica. As discussed

earlier, for the purpose of the magnetic transport, I designed a series of magnetic coils as listed in Table-E.1. Following the algorithm of the magnetic transport, I have determined the optimized parameters (Table-E.1) required to obtain a considerable amount of currents during the transport as shown Figure-5.5.

coils	**x-center** cm	**z-height** cm	**inner radius** cm	**turns**	**layers**	**wire width** cm	**wire height** cm
Push	-11.2	0	5	5	20	0.2	0.2
Additional	10.9	14.8	1.5	55	4	0.11	0.5
MOT	0	8.7	3	20	10	0.45	0.45
T1	11.2	6.5	1.5	55	4	0.11	0.5
T2	19.1	3.6	1	55	4	0.11	0.5
T3	26.9	6.4	1	55	4	0.11	0.5
T4	35	5.05	1	55	2	0.11	0.32
T5	42.9	6.2	1	52	4	0.11	0.5
Quadrupole	52	2.55	2.2	26	4	0.45	0.45
T6	62.3	5.2	1.5	55	6	0.11	0.5

Table E.1: parameters of the magnetic transport coils

Magnetic field measurement

To calibrate and comparison with the simulation, we have measured the magnetic field components generated by the coils pair in anti-Helmholtz configuration using a Hall effect Gaussmeter (Lake Shore: Model 460 3-channel). Figure-E.3 shows field measurement of the MOT coils in anti-Helmholtz configuration. The Gaussmeter sensor is placed horizontally on a a supporting mount with the long axis of the probe along the magnetic transport axes. The sensor is mounted on three axes micrometer translational stage such a way that we would get finer displacement along $X, Y, and\ Z$ axes respectively. The entire

assembly is placed on a LM rail-block to have coarse displacement along the transport axes (X-axis).

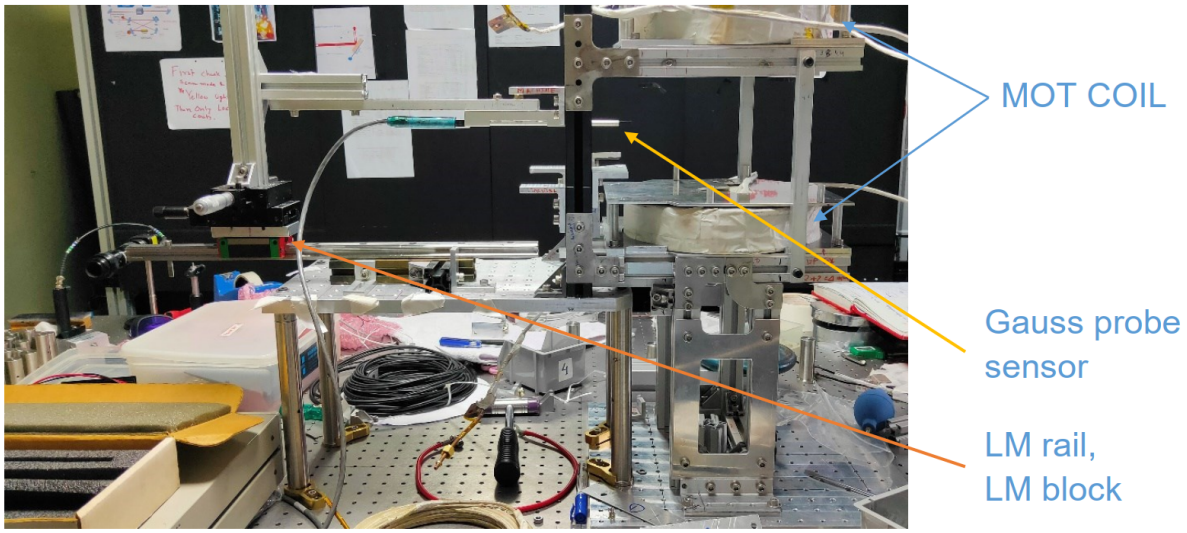


Figure E.3: The arrangement for the measurement of the magnetic field generated by the coils in anti-Helmholtz configuration.

In the following, I will show the measured data of the magnetic field components of the coils of the magnetic transport and the comparison with the numerical simulation.

Additional coils

The measured magnetic field and comparison with the simulation of the magnetic field components of the additional coils.

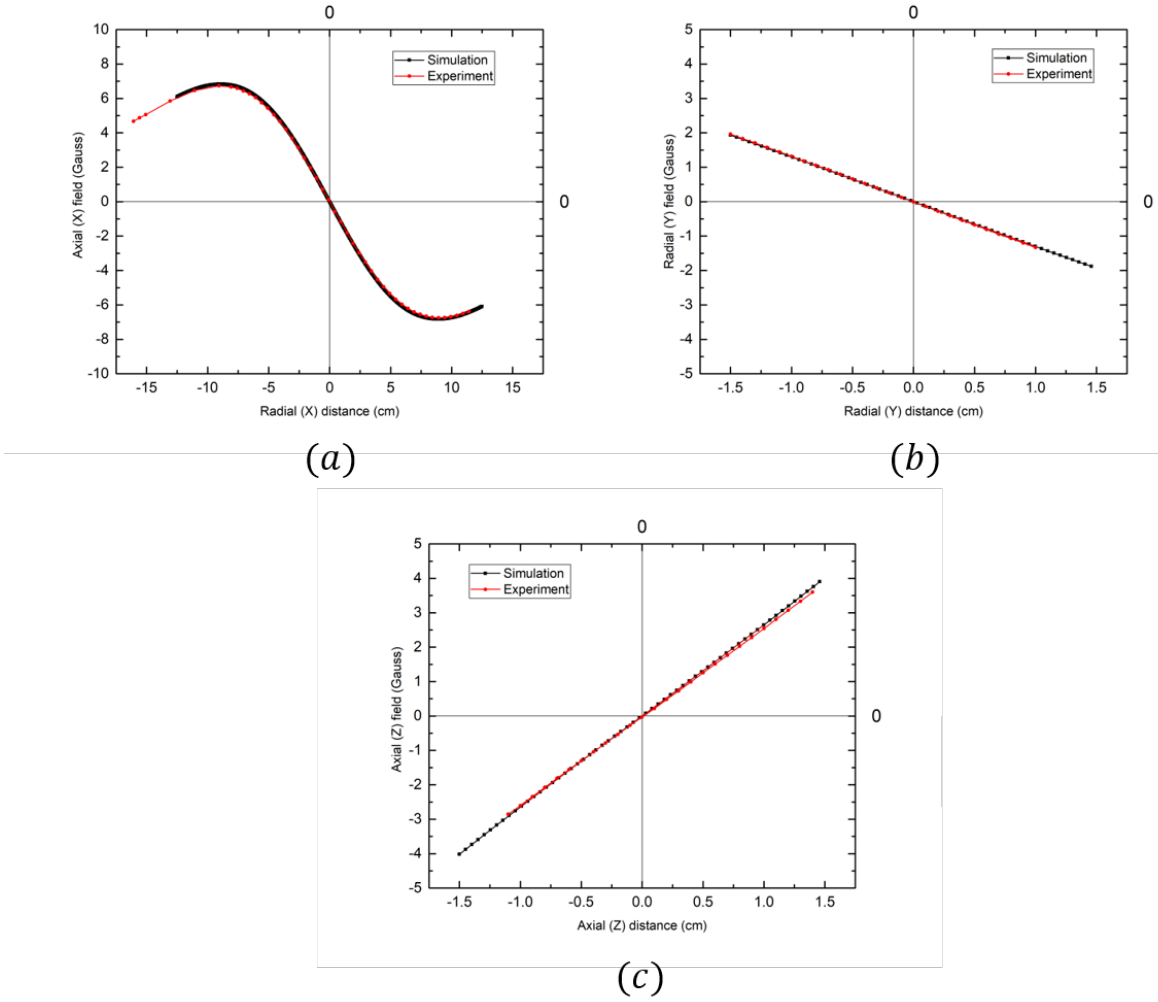


Figure E.4: The measured magnetic field and the comparison of the magnetic field components along (a) x-axis, (b) y-axis, and (c) z-axis of the additional coils at 10 Amps of current.

The comparison of simulated and measured gradient of the magnetic field components,

axis	**simulation**	**experiment**
	Gauss/cm	Gauss/cm
x	-1.30	-1.27
y	-1.30	-1.33
z	2.63	2.56

Table E.2: Magnetic field gradients of additional coils pair at 10 Amperes of current

MOT coils

The measured magnetic field and comparison with the simulation of the magnetic field components of the MOT coils.

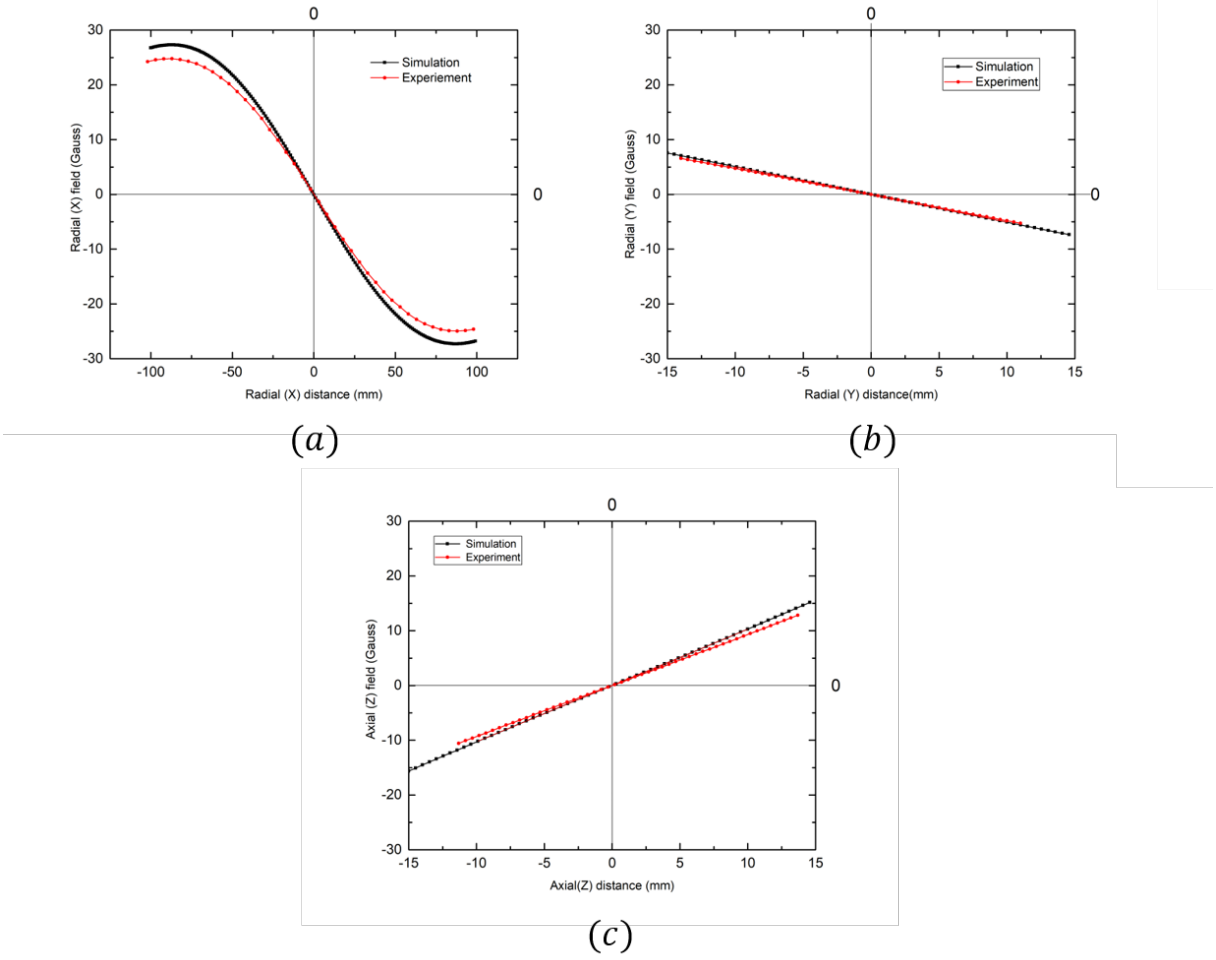


Figure E.5: The measured magnetic field and the comparison of the magnetic field components along (a) x-axis, (b) y-axis, and (c) z-axis of the MOT coils at 10 Amps of current.

The comparison of simulated and measured gradient of the magnetic field components,

axis	**simulation**	**experiment**
	Gauss/cm	Gauss/cm
x	-5.09	-4.59
y	-5.09	-4.78
z	10.27	9.27

Table E.3: Magnetic field gradients of MOT coils pair at 10 Amperes of current

T1 coils

The measured magnetic field and comparison with the simulation of the magnetic field components of the T1 coils.

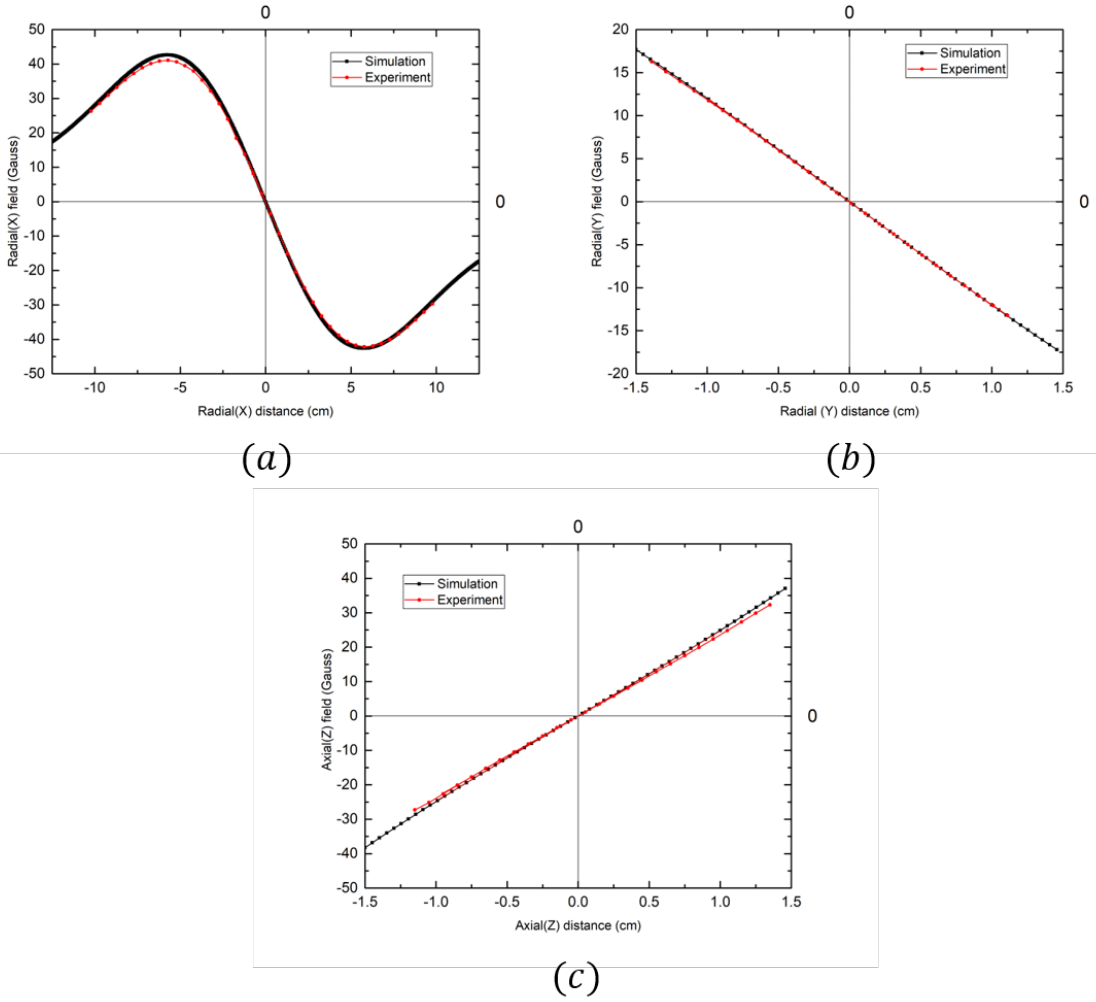


Figure E.6: The measured magnetic field and the comparison of the magnetic field components along (a) x-axis, (b) y-axis, and (c) z-axis of the T1 coils at 10 Amps of current.

The comparison of simulated and measured gradient of the magnetic field,

axis	**simulation**	**experiment**
	Gauss/cm	Gauss/cm
x	-12.07	-11.57
y	-12.07	-11.99
z	24.68	23.49

Table E.4: Magnetic field gradients of T1 coils pair at 10 Amperes of current

T2 coils

The measured magnetic field and comparison with the simulation of the magnetic field components of the T2 coils.

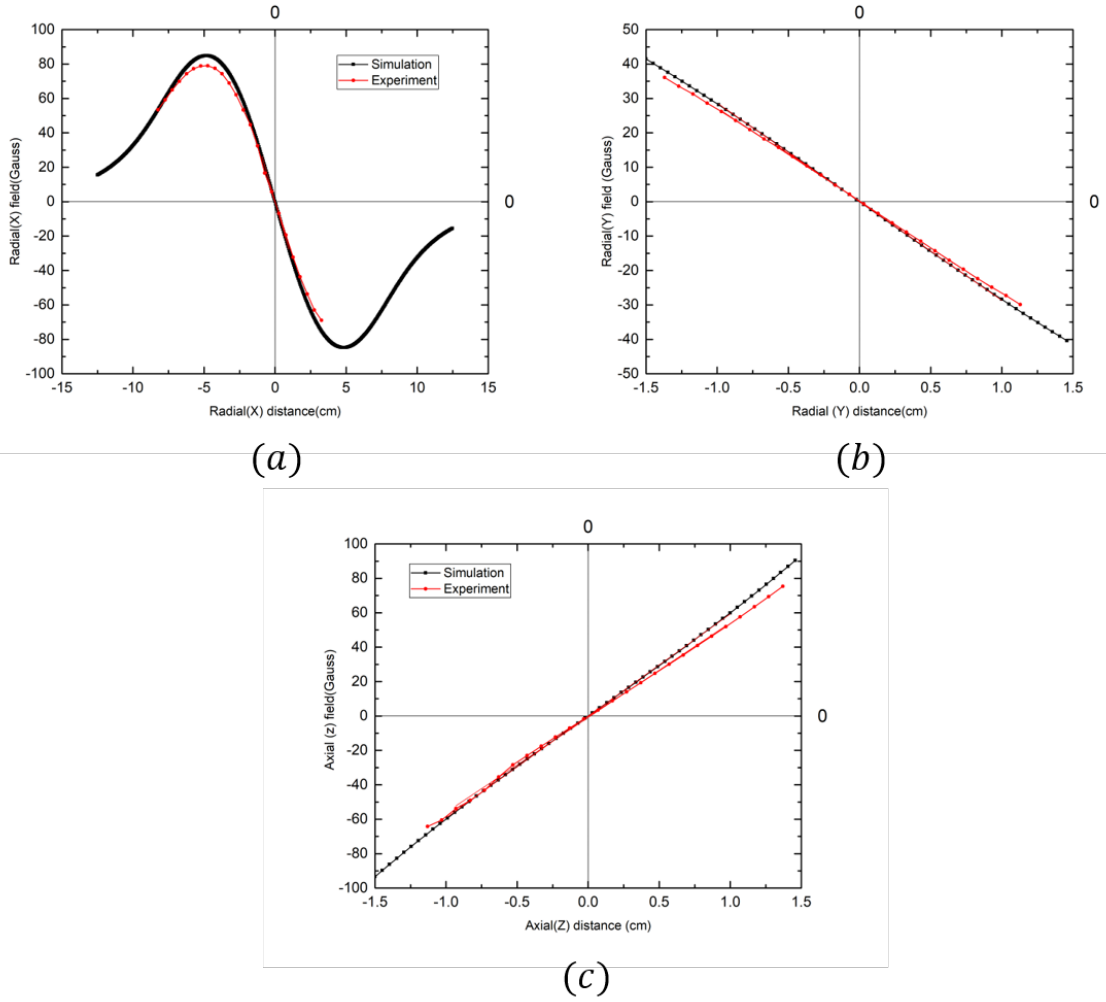


Figure E.7: The measured magnetic field and the comparison of the magnetic field components along (a) x-axis, (b) y-axis, and (c) z-axis of the T2 coils at 10 Amps of current.

The comparison of simulated and measured gradient of the magnetic field,

axis	**simulation**	**experiment**
	Gauss/cm	Gauss/cm
x	-28.69	-25.38
y	-28.69	-27.08
z	59.25	55.09

Table E.5: Magnetic field gradients of T2 coils pair at 10 Amperes of current

T3 coils

The measured magnetic field and comparison with the simulation of the magnetic field components of the T3 coils.

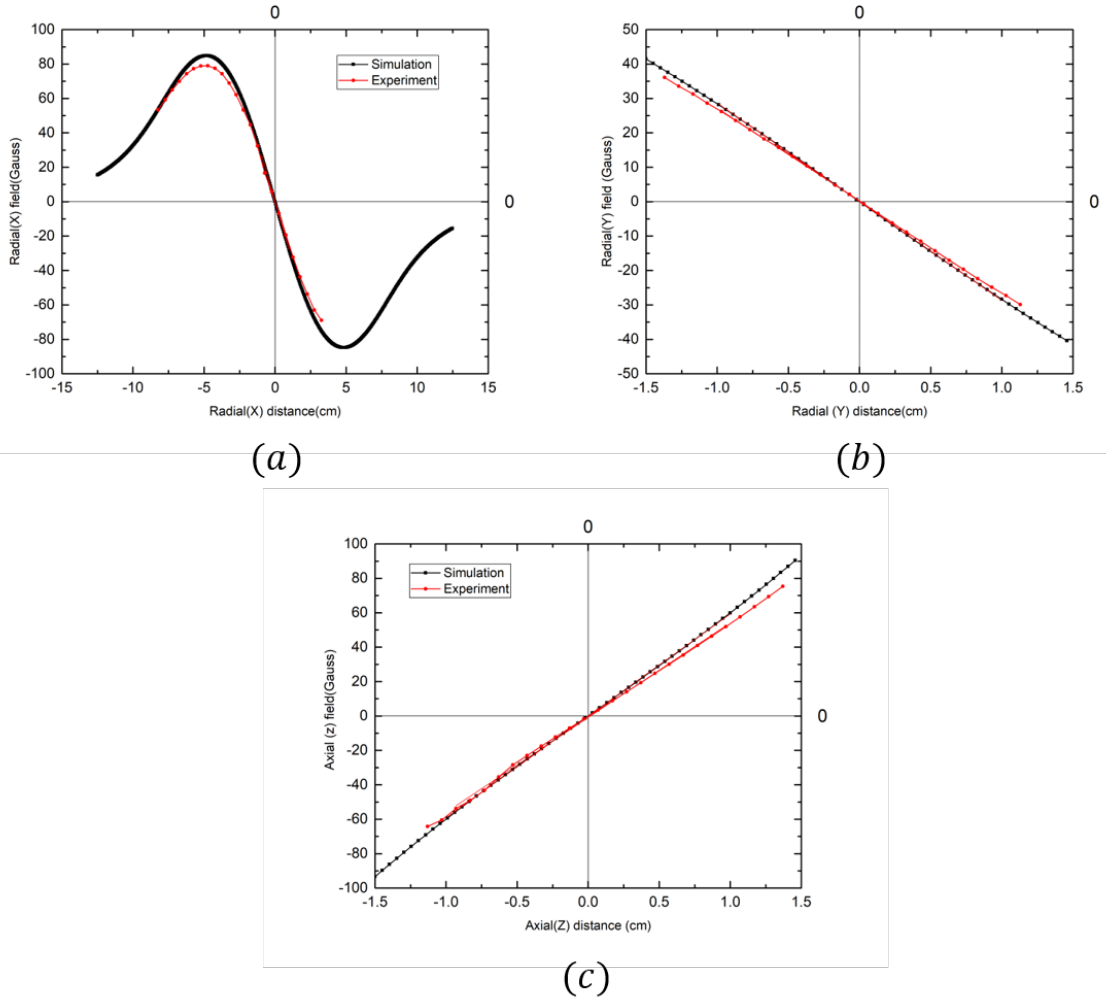


Figure E.8: The measured magnetic field and the comparison of the magnetic field components along (a) x-axis, (b) y-axis, and (c) z-axis of the T3 coils at 10 Amps of current.

The comparison of simulated and measured gradient of the magnetic field,

axis	**simulation**	**experiment**
	Gauss/cm	Gauss/cm
x	-8.7	-8.6
y	-8.7	-9.17
z	18.7	18.10

Table E.6: Magnetic field gradients of T3 coils pair at 10 Amperes of current

T4 coils

The measured magnetic field and comparison with the simulation of the magnetic field components of the T4 coils.

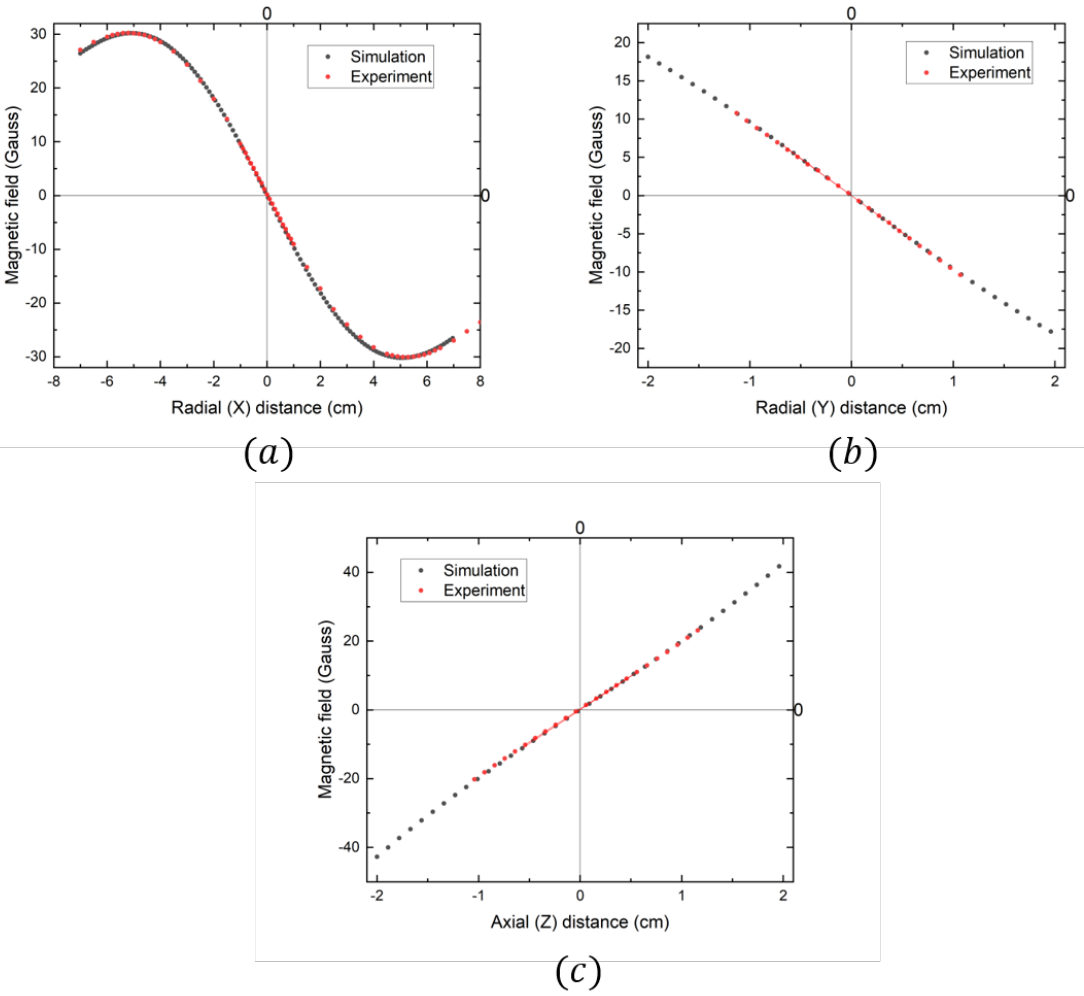


Figure E.9: The measured magnetic field and the comparison of the magnetic field components along (a) x-axis, (b) y-axis, and (c) z-axis of the T4 coils at 10 Amps of current.

The comparison of simulated and measured gradient of the magnetic field,

axis	**simulation**	**experiment**
	Gauss/cm	Gauss/cm
x	-9.6	-9.5
y	-9.6	-9.60
z	19.5	19.19

Table E.7: Magnetic field gradients of T4 coils pair at 10 Amperes of current

T5 coils

The measured magnetic field and comparison with the simulation of the magnetic field components of the T5 coils.

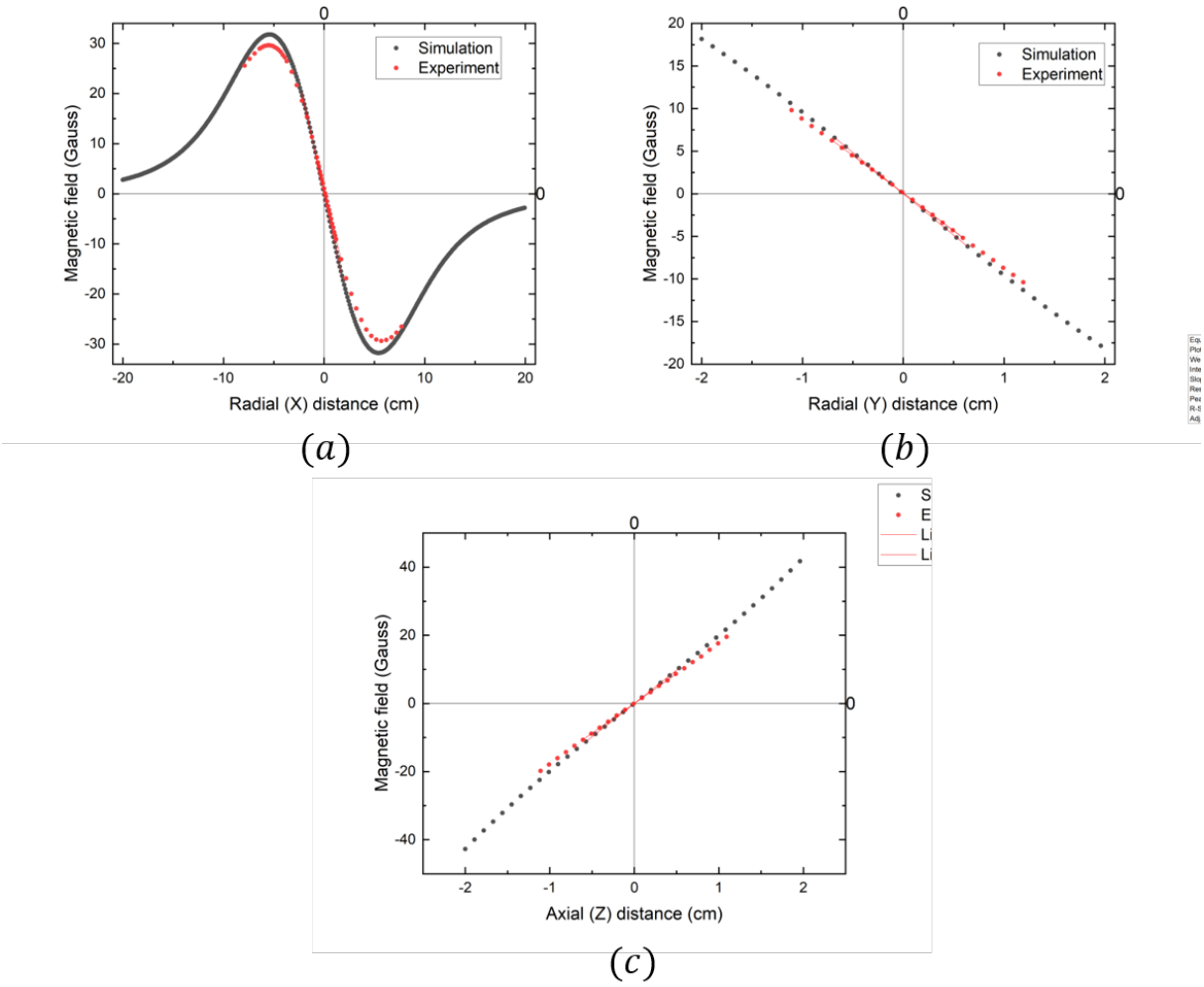


Figure E.10: The measured magnetic field and the comparison of the magnetic field components along (a) x-axis, (b) y-axis, and (c) z-axis of the T5 coils at 10 Amps of current.

The comparison of simulated and measured gradient of the magnetic field,

axis	**simulation**	**experiment**
	Gauss/cm	Gauss/cm
x	-9.30	-8.3
y	-9.30	-8.8
z	19.5	17.4

Table E.8: Magnetic field gradients of T5 coils pair at 10 Amperes of current

Quadrupole coils

The measured magnetic field and comparison with the simulation of the magnetic field components of the Quadrupole coils.

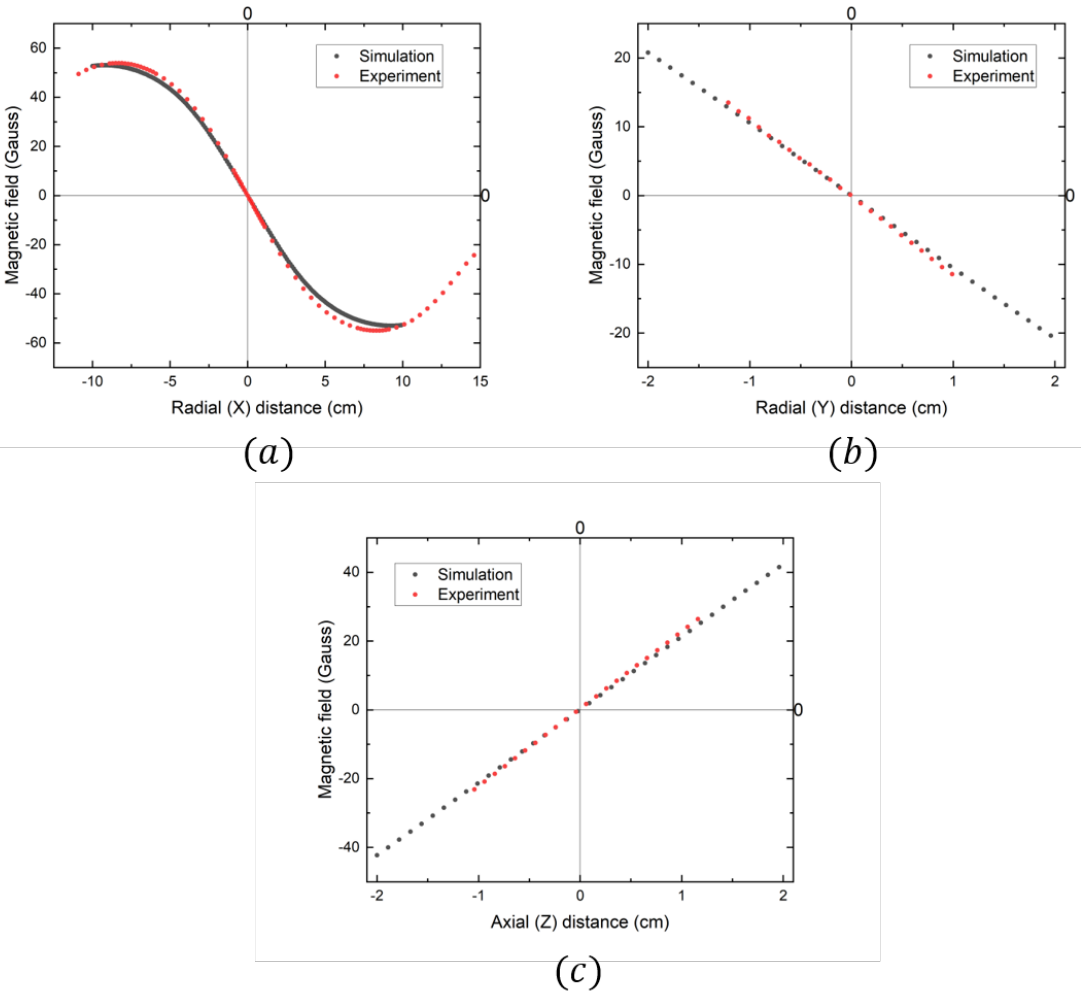


Figure E.11: The measured magnetic field and the comparison of the magnetic field components along (a) x-axis, (b) y-axis, and (c) z-axis of the Quadrupole coils at 10 Amps of current.

The comparison of simulated and measured gradient of the magnetic field,

axis	**simulation**	**experiment**
	Gauss/cm	Gauss/cm
x	-10.5	-11.48
y	-10.5	-11.29
z	21.19	22.50

Table E.9: Magnetic field gradients of Quadrupole coils pair at 10 Amperes of current

T6 coils

The measured magnetic field and comparison with the simulation of the magnetic field components of the T6 coils.

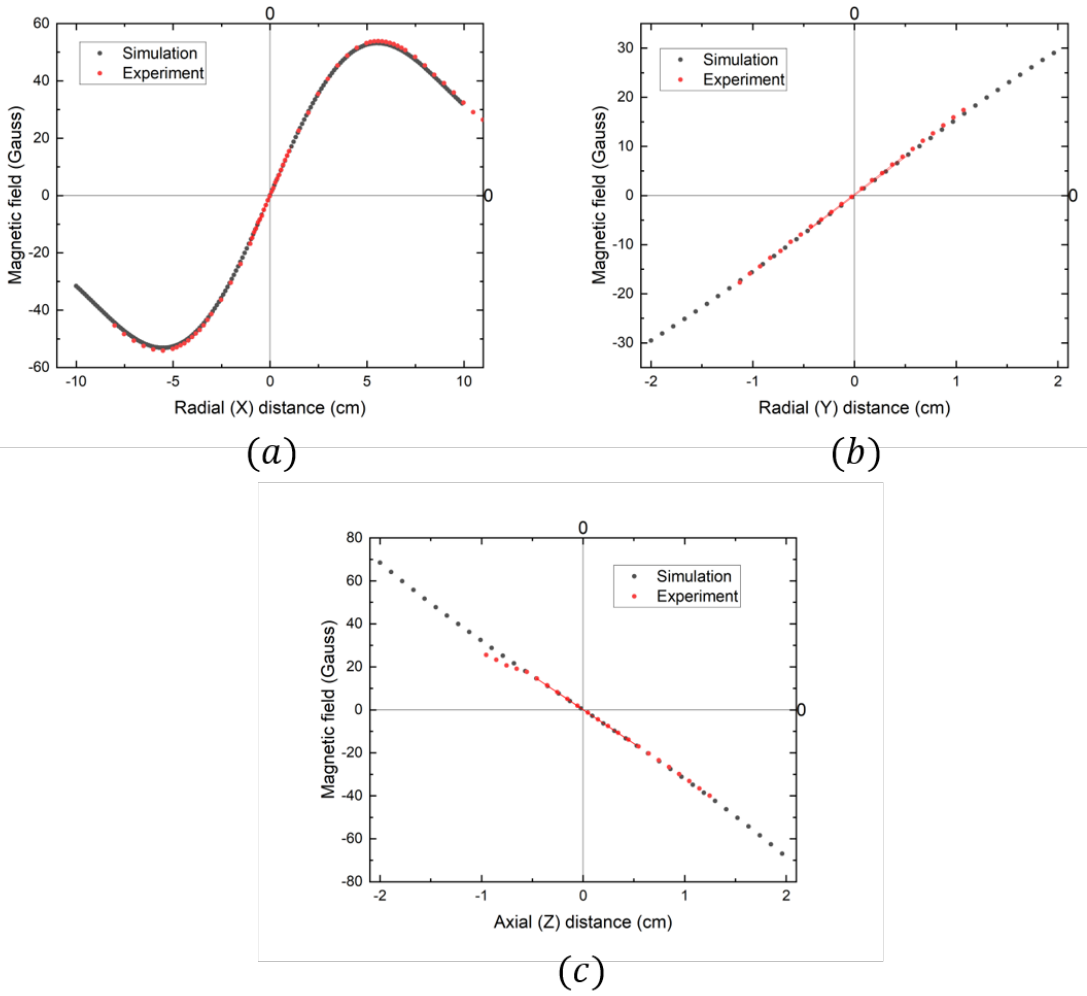


Figure E.12: The measured magnetic field and the comparison of the magnetic field components along (a) x-axis, (b) y-axis, and (c) z-axis of the T6 coils at 10 Amps of current.

The comparison of simulated and measured gradient of the magnetic field,

axis	**simulation** Gauss/cm	**experiment** Gauss/cm
x	15.5	15.8
y	15.5	15.8
z	-31.5	31.5

Table E.10: Magnetic field gradients of T6 coils pair at 10 Amperes of current

Parameters of the Ioffe coil

coils	**x-center** cm	**z-height** cm	**inner radius** cm	**turns**	**layers**	**wire width** cm	**wire height** cm
Ioffe	54.3	0	0.75	10	3	0.2	0.2

Table E.11: parameters of the Ioffe coils of the QUIC trap.